Investigation of UV and IR Laser Processing of Single-Crystalline 4H:SiC and Characterisation of Laser Grown Graphene Derivatives

being a thesis submitted in partial fulfilment of the requirements for the degree of
Doctor of

Mathematics and Physical Sciences

in the University of Hull

by

Arina Faraj Mohammed
BSc and MSc
February 2021

Copyright © Arina F Mohammed, 2021. All rights reserved

Dedication

To my Father…

You will always be with me

To my Mother…

To my Family…

Acknowledgement

This thesis would not have been possible without the inspiration and support of some wonderful individuals, my thanks and appreciation to all of them for being part of this journey and making this thesis possible.

First, I would like to express my gratitude towards my country represented by the Higher Committee of Education Development in Iraq (HCED) for the opportunity they provided me to pursue my dream and complete my PhD. As well, I thank my supervisors Chris D. Walton and Neil T. Kemp for their support and guidance. Special thanks to Chris Walton for the confidence, reassuring that he gave me to fulfil my potential. Not to forget his pastoral care when I needed it.

Being a part of the physics department for years, I was privileged with the help of a number of the academic staff, thank you all for any help you gave me from your time and knowledge. I would also like to thank the technician team for the designs and equipment they facilitate for my work to move forward.

Special thanks to Thiago Amaral for his help with some SEMs and Raman measurements in INM Germany. We also acknowledge support from the Air Force Research Laboratory, UES, Inc., the Air Force Office of Scientific Research (C. C. Perry. via FA9550-13-1-0040) for Raman measurements. Special gratitude to my fellow postgraduates: Andy Clarke, Alex Gee, Charlotte Elling, Abdullsattar Easa, Qassim Al-Jarwani, Ayob Jaafar, Jack Eden, Alex Bridgwater, Francesco Viscomi and Addison Marshal who share me my journey and contributed their knowledge and experience towards my work. It has been an honour.

With love, I am forever indebted to my parents for giving me the opportunities and experiences that have made me who I am. They selflessly encouraged me to explore new directions in life and seek my own destiny. This journey would not have been possible if not for them, and I dedicate this milestone to them and my siblings and my friends for all their moral support.

Finally, my deep and sincere gratitude to my family and friends for their continuous and unparalleled love, help and support.

Publications and Conferences

- Ablation Threshold Measurements and Surface Modifications of 193 nm Laser Irradiated 4H-SiC. Published paper. Chemical physics letters 2018.
- Morphology studies of 193 nm excimer laser irradiated 4H-SiC. ILAS conference, Grantham 2017.
- Emergence of Electrically Conductive Layers on Laser Silicon Carbide. European workshop on laser ablation. France 2018.
- Realisation of a sub-wavelength dimple using a 193 nm wavelength photonic nano jet, accepted paper. Chemical physics letters 2020.

Ongoing publication

- Enhance the electrical conductivity of SiC by excimer and CO_2 lasers.
- Laser Processing of Silicon Carbide: Laser-Induced Growth of Graphene Derived Structures.

Abstract

The formation of graphene (G) on the surface of silicon carbide (SiC) has gathered interest over recent years as a potential component in high power nano and microdevices. However, it is still in the early stages of research, therefore there are many challenges to overcome. Among the existing problems, the formation of good quality graphene/SiC is one of the most critical factors that determine the behaviour of this heterostructure. Here we report a full study of the formation of graphene and its derivative structures on SiC using different laser systems with different controlled irradiation conditions.

Laser ablation experiments on polished 4H-SiC wafers using a 193 nm ArF laser over a fluence range of 0.3 Jcm^{-2} – 5 Jcm^{-2} are reported. An onset of material modification was measured at a laser fluence of 925 ± 80 $mJcm^{-2}$, and a concomitant etch rate of ~200 pm per pulse. Laser ablation sites have been analysed using optical microscopy, scanning electron microscopy (SEM), atomic force microscopy (AFM), Raman microscopy and white light interferometry (WLI). Different surface modifications were observed. The influences of the laser fluence, number of pulses, and scanning velocity on the position of the microchannel are discussed. At a laser fluence in the region of 1.0 Jcm^{-2}, the irradiated site removed material forming a uniform crater. At a higher laser fluence, in the region of 2.7 Jcm^{-2}, nodule-like structures form on the base of the ablation crater. An increased fluence led to a smoother surface with higher etched depth and ripple formation. The dissociation of laser irradiated 4H-SiC was discussed. Graphene oxide (GO) and reduced graphene oxide (rGO) formed on the SiC surface by 193 nm laser-induced high-temperature thermal decomposition of the SiC substrate. The decomposition resulted in the presence of silicon (Si), especially on the edge of the irradiated site.

Graphene formation on the 4H:SiC surface by high power CO_2 laser. Two distinct ablation threshold energies of 4.3 mJ and 73 mJ were found. The etch rate was dependent on the applied pulse duration, laser power, the scanning velocity and the number of pulses. High temperature thermal decomposition of the SiC substrate was achieved with a CO_2 laser over a power range of 1-30 W. The structure was different from the structure obtained from the UV laser irradiated samples. More rough surfaces were prepared with small islands of graphene, GO and rGO on SiC in addition to the ripples. Monolayer and

Multilayer graphene was also achieved. The laser-induced surface decomposition of the SiC was controlled spatially. The processing was held at room temperature, and the operation carried out in either a vacuum chamber or at atmospheric pressure. A fast graphene growth rate was achieved. This method is achievable, scalable and compatible with semiconductors technology due to the onsite direct writing of graphitic structure formed by the laser. This method is cost-effective as it does not necessitate SiC pre-treatment, there is no need for a processing vacuum chamber, and it can be achieved on the nano/microsecond time scale.

Analytical and Finite element simulations using COMSOL™ MetaphySiCs, 5.3 have been used to calculate laser-induced temperature rise of 4H-SiC as a function of laser fluence. The simulated temperature was always less the temperature anticipated analytically. The 193 nm laser fluence required to reach the melting points of silicon, silicon carbide, and carbon, have been calculated and correspond to ~0.97, 1.95 and 2.6 Jcm^{-2}, respectively. Extreme heating and cooling rates controlled the growing process of graphene and its derivatives. The CO_2 laser-induced temperature rise was also estimated. The CO_2 laser acted as a heat source for the SiC. High power was used to reach the high temperature needed to decompose the SiC. Pulse duration also played a significant role in controlling the temperature and the depth distribution inside the SiC.

This work reports the graphene formation on the surface of SiC by laser-induced thermal decomposition for electrical characterisation. Current-voltage (I-V) measurements show a decrease of the electrical resistance per unit length by nine orders of magnitude. The lowest resistance per unit length was obtained using a laser fluence of ~1.5 Jcm^{-2}, a pulse repetition frequency of 10 Hz and using a sample translation speed of 0.01 mms^{-1}. Temperature simulations have been performed using the finite element method (FEM) to assist in understanding the dissociation mechanisms of SiC and hence optimise the experimental variables. 2D axis-symmetric FEM calculations predict a surface temperature of ~2500K at a laser fluence of 1.5 Jcm^{-2}. Laser-irradiated 4H:SiC is an efficient and controllable method of producing highly reproducible electrically conducting tracks. An increase in the conductivity was observed when the graphitic structure was produced with the CO_2 laser. However, the conductivity was less than the graphitic structure produced by the 193 nm laser. It is expected that the different graphene interfaces, including Ohmic contact and Schottky contact, was created.

Contents

Dedication i

Acknowledgement ii

Publications and Conferences iii

Abstract iv

Contents vi

List of Figures xii

List of Tables xxiii

Chapter 1 Introduction 1

1.1 Introduction 1

1.2 Thesis Structure 3

Chapter 2 Materials and Literature Review 4

2.1 Introduction 4

2.2 Silicon Carbide 4

2.2.1 SiC Properties 4

2.2.2 SiC Application 8

2.3 SiC Laser Processing 8

2.4 Graphene 10

2.4.1 Graphene Production Techniques 12

2.5 Decomposition of SiC 14

2.6 Laser induced Decomposition of SiC 15

2.7 Applications of Graphene on SiC 16

Chapter 3 Theoretical Background 19

3.1 Introduction 19

3.2 Light-Matter Interaction 19

3.2.1 Optical Properties of Material 19

3.2.2 Carrier Behaviour 22

3.3 Laser Heating and Heat Transfer 24

3.3.1 Surface Melting (Heterogeneous Melting) 25

3.3.2 Enthalpy Model of Melting 26

3.3.3 Laser Ablation and Material Removal 28

3.3.4 Laser Vaporisation 33

3.4 Nanosecond and Microsecond Pulsed Laser Ablation 34

3.5 Characterisation Methods 35

3.5.1 Raman Spectroscopy 35

3.5.2 Carrier Transport in Semiconductors 36

3.5.3 Sheet Resistance Measurements 38

Chapter 4 Methodology 39

4.1 Methodology 39

4.2 Material 39

4.2.1 Preparation Process 39

4.3 Laser Micromachining of SiC and Setup 40

4.3.1 ArF Excimer Laser Processing 40

4.3.2 CO_2 Laser Processing ... 43

4.4 Laser Irradiation under Low Pressure ... 49

4.5 Characterisation Techniques ... 49

4.5.1 Tauc Plot ... 49

4.5.2 Surface Imaging ... 50

4.5.3 Temperature Calculations ... 51

4.5.4 Raman Spectroscopy ... 51

4.5.5 Current-Voltage I-V Measurements ... 53

Chapter 5 Theoretical Modelling of Laser Heat Transfer ... 55

5.1 Introduction ... 55

5.2 Heat Transfer Theory ... 55

5.2.1 Thermal Conduction ... 55

5.2.2 Thermal Convection ... 59

5.2.3 Thermal Radiation ... 61

5.3 Analytical Solution of Laser Heating Source ... 64

5.4 Semi-Analytical Heat Equation Solution ... 65

5.4.1 Flat-Top Laser Profile Heat Equation Solution ... 65

5.4.2 Gaussian Laser Profile Heat Equation Solution ... 66

5.5 COMSOL Multiphysics ... 68

5.5.1 Simulation Methodology ... 69

5.5.2 Silicon Carbide Parameter ... 71

5.5.3 Other Parameters ... 73

5.6 Results and Discussion 75

5.6.1 Analytical and Numerical Modelling Comparison for ArF and CO_2 Lasers 75

5.6.2 Numerical Modelling of Excimer Laser on SiC 77

5.6.3 Numerical Modelling of CO2 Laser on SiC 80

5.7 Summary 85

Chapter 6 : Ablation Threshold Measurements and Surface Modifications of 193 nm Excimer Laser Irradiated 4H:SiC 86

6.1 Result and Discussion 86

6.1.1 Laser-Induced Modification and Threshold Measurements 86

6.1.2 Excimer Laser Micromachining of 4H:SiC using a Stationary Sample ... 93

6.1.3 Travelling Micromachining of 4H:SiC 101

6.1.4 Raman Investigation and Laser Surface decomposition of SiC 107

6.2 Discussions 114

6.2.1 Light-Matter Interaction 114

6.2.2 Laser Ablation 115

6.2.3 Heat Transfer 116

6.2.4 Enthalpy Model of Melting 116

6.2.5 Material Vaporisation 117

6.3 Summary 117

Chapter 7 CO_2 Laser Micromachining of Single Crystalline 4H-SiC 119

7.1 Introduction 119

7.2 Laser Ablation Threshold of SiC by CO_2 Laser 119

7.3 Raman Investigation for Stationary Laser Surface Decomposition of 4H:SiC 122

7.4 Effect of Laser Pulse Duration on the Structure and Decomposition of SiC . 125

7.4.1 Structural Characteristics 125

7.4.2 Raman Characteristics 127

7.5 Effect of Laser Power on the Surface of SiC 131

7.5.1 Surface Characteristics 131

7.5.2 Raman Investigation 135

7.6 Effect of Travelling Laser Speed on the Surface of 4H:SiC 137

7.6.1 Surface Characterisation 137

7.6.2 Raman Characterisation 142

7.7 Irradiation under Controlled Atmosphere 146

7.8 Summary 148

Chapter 8 Electrical Properties Characterisation of the grown graphene structure on SiC 149

8.1 Introduction 149

8.2 Results and Discussion 150

8.2.1 Excimer Laser Direct Written Graphitic Channels 150

8.2.2 Effect of Laser Power and Travelling Speed on the I-V Measurements. 156

8.2.3 CO_2 Laser Direct Written Graphitic Channels 159

8.3 Summary 163

Chapter 9 Conclusion and Future Work 164

9.1 Conclusion 164

9.2 Future Work 169

References 170

List of Figures

Figure 2.1: a) The lattice structure of the basic unit of SiC. Dark atoms are C, and light atoms are Si. The length between Si and Si of two C is 3.08 Å and the distance between Si and C is 1.89 Å. b) Stacking sequences of 4H-SiC polytypes in c-axis. 6

Figure 2.2: Graphene structure a) the orbitals b) the planes. 11

Figure 3.1: Electron excitation and relaxation in material coupled with intense laser light[156]. In semiconductors, absorption of wavelengths between 0·2–10.0 μm causes an interband transition (valence to conduction). The absorbed energy converted to heat through (a) excitation of electrons in valence and/or conduction band, (b) interaction between excited electron-phonon within a span of 10^{-11}–10^{-12} s, (c) electron-electron or electron-plasma interaction, and (d) electron-hole recombination within 10^{-9}–10^{-10} s. 22

Figure 3.2: electronic excitations in insulators and semiconductors[158]. 23

Figure 3.3: Different interaction and mechanisms involved in Pulse laser ablation. Ablation can be based on thermal activation only (left path), on direct bond breaking (photo-chemical ablation; right path), or on a combination of both (photophysical ablation; intermediate path)[158] 30

Figure 3.4: Jablonski Diagram Representing Quantum Energy Transitions for Rayleigh and Raman Scattering[180]. 36

Figure 3.5: two-point method to measure the resistivity of slab shape material............. 37

Figure 4.1: Schematic of the 193 nm ArF excimer laser system. Samples were translated using Aerotech (fibre align) motion control stages relative to a stationary beam. The laser imaged using different shapes of masks... 41

Figure 4.2: photograph of 193 nm laser system. 42

Figure 4.3: Schematic diagram of the experimental CO_2 system set up. It used for the processing of SiC and the ablation threshold measurements. 44

Figure 4.4: The average power of CO_2 laser for different pulse duration as a function of the pulse repetition rate. 46

Figure 4.5: Averaged power as a function of the duty cycle controlled by the pulse repetition rate and for different pulse width. 46

Figure 4.6: Averaged power as a function of the attenuator transmission percentage. .. 47

Figure 4.7: Tauc's plots obtained through the applications of standard equations. It indicates an Eg of 3.34 eV 50

Figure 4.8: Two probe I-V measurements on graphitic channel written directly on 4H:SiC. The schematic shows the probe positioning on the irradiated channels of the produced channels and the change of the space between the tips. 54

Figure 5.1: Total heat flux toward and out of the volume dV=dxdydz 56

Figure 5.2: Convection energy transfer and the hydrodynamic formation at the boundary. 59

Figure 5.3: Thermal Radiation a) at the surface and b) at the surface surrounded by matter. 62

Figure 5.4: COMSOL general steps to simulate physical processing. 70

Figure 5.5: Schematic of the sample irradiated by ArF laser. 70

Figure 5.6: The boundary condition and the geometry of the 1D and 2D axisymmetric model 71

Figure 5.7: Calculated Refractive index of 4H:SiC from Equations (5.42) and (5.43) for both ordinary and extraordinary refractive index[208] 72

Figure 5.8: Temperature-dependent specific heat of 4H:SiC. It shows the increase of specific heat with temperature. 73

Figure 5.9: The change in the thermal conductivity of 4H:SiC as a function of temperature. 73

Figure 5.10: Measured temporal shape of the excimer laser of 193 nm. The shape of our laser pulse measured with a photodetector......74

Figure 5.11: Normalized extracted temporal shape of the CO_2 Laser pulse. The data was provided as a picture from the Rofin Sinar Company. The data was extracted using the Origin software......74

Figure 5.12: Temperature rise conducted with different models of COMSOL, Duley and El-Adawi at 0.97 Jcm^{-2} laser fluence. 76

Figure 5.13: Temperature change for an applied CO_2 laser of 10.6 µm wavelength with 100 µsec (FWHM) and Gaussian laser pulse of peak incident power 4.5 W, and the beam radius FWHM point is 79 µm. The temperature is plotted at the beam centre for z = 0, i.e. at the surface. 76

Figure 5.14: Temperature rise with one dimensional and two dimensional axisymmetric for laser fluence of 0.97 Jcm^{-2}......77

Figure 5.15: Temperature rise in time as a function of the applied laser fluence. The fluence was determined depending on the experimental values where there was a modification on the surface......78

Figure 5.16: Linear relation between the applied laser fluence and the temperature rise solved with 2D-axisymmetric model. 78

Figure 5.17: Temperature simulations of 193nm laser irradiated carbon, 4H:SiC and silicon using finite element modelling, COMSOL MultiPhySiCs™5.3. The laser pulse duration used in the simulations is 11.5 ns FWHM. Each curve has been calculated using the corresponding laser fluence required for the peak temperature to reach the corresponding melting point. 79

Figure 5.18: Heat profile inside the material due to the laser irradiation of different fluences. 79

Figure 5.19: Temperature rise in time with different laser pulse duration using 4.5 W power......80

Figure 5.20: Evolution of the temperature as a function of the irradiated laser power at 79 μm beam diameter. The tuned pulse duration was 100 μsec for the left side graph and 150 μsec for the right-hand graph. 81

Figure 5.21: Peak temperature predicted for various power using both 100 μsec pulse duration and the 150 μsec pulse duration. 82

Figure 5.22: Evolution of the thickness peak temperature profile. The used laser power was 15 W tuned at 100 μsec pulse width. 82

Figure 5.23: The peak temperature for a series of the number of pulses. The simulation was conducted for 4.5 W laser power and at a pulse duration of 100 μsec. 83

Figure 5.24: The peak temperature of a SiC during laser irradiation. It combines both the temperature rise using Al as a substrate and without the substrate. The laser power was 4.5 W with 150 μsec pulse duration. 84

Figure 5.25: Temporal peak temperature of different spot sizes with the same power density of 4.5 W. the calculation was conducted for single pulse laser with 150 μsec pulse duration. 84

Figure 5.26: The spatial peak temperature of the irradiated laser power 4.5 W with different mean diameter. 85

Figure 6.1: Laser ablation etches rates versus laser fluence. The top axis corresponds to the calculated temperature using a finite element method, software COMSOL Multiphysics 5.3. Each ablation site was irradiated with 100 laser pulses, and the data averaged. 87

Figure 6.2: Optical micrographs of laser irradiated 4H:SiC. Sample irradiated at a laser fluence of 1.5 Jcm^{-2} and a sample translation speed 0.01 mms^{-1} (a) and laser fluence 2.7 Jcm^{-2} and a sample translation speed of 0.005 mms^{-1} (b). The floor of the ablation craters can be seen to have a different surface topology. 88

Figure 6.3: SEM micrographs of the redeposited debris outside of the ablation crater depicted in Figure 6.2(b). The approximate size of the particulates ranges between ~ 800 nm to ~1.4 μm diameter. Although not in view, the redeposited material extends away from the edge of the ablation crater out to a distance of about 300 μm. 89

Figure 6.4: Cross-sectional one stylus profile measurement of laser ablated 4H:SiC channel. The channel was created using a laser fluence of 2.7 Jcm^{-2} and a scan speed of 0.005 mms^{-1}. Redeposited debris resides in the regions between 150-440 μm and 950-1250 μm. Note the channel region consists of structures protruding above the surface of the un-irradiated sample. 90

Figure 6.5: SEM micrograph of the laser irradiated 4H:SiC using a 193 nm laser at fluence 2.7 Jcm^{-2}.The sample was translated relative to a stationary beam along the long direction at a speed of 0.005 mms^{-1}. The irradiated sample received 1000 overlapping laser pulses. 91

Figure 6.6: High-resolution SEM micrographs of 193 nm laser ablated 4H:SiC site. Laser ablation was carried out at a laser fluence of 2.7 Jcm^{-2} applying 100 laser pulses, a) structures on the crater floor close to the crater edge, b) magnified view of the structures, c) a single microstructure decorated with nano-sized particles, d) increased magnification showing the microstructure consists of spherical droplet-like particles and the formation of ripples. 92

Figure 6.7: WLI 2D profile of the irradiated SiC with different laser fluence with 100 pulses per site. 93

Figure 6.8: SEM micrographs of laser squared imaged sites on 4H:SiC surface at 100 pulses with different laser fluence (a) 1.2, (b) 1.4, (c) 1.8, (d) 2.2, (e) 2.6, (f) 3.0, (j) 3.4 and (h) 3.8 Jcm^{-2}........ 94

Figure 6.9: Histogram of the nanoparticle distribution on the irradiated site of SiC under Excimer laser. (a) At laser fluence of 2.6 Jcm^{-2} and (b) 5 Jcm^{-2}........ 96

Figure 6.10: Raman Spectra of a reference 4H:SiC (bottom layer) and surface irradiated 4H:-SiC with 193 nm laser at different fluences (top layer). 97

Figure 6.11: Optical micrographs of the laser irradiated SiC using a circular mask at 1.2 Jcm^{-2}. It shows the effect of different number of laser pulses (a) 1 pulse, (b) 10 pulses, (c) 100 pulses and (d) 1000 pulses 99

Figure 6.12: 3D surface mapping of the SiC irradiated with different number of laser pulses (a) 10 pulses and (b) 1000 pulses 100

Figure 6.13: Raman spectra of the irradiated SiC sites as a function of the number of applied laser pulses on SiC (a) at the centre of sample (b) at the edge of the sample. . 100

Figure 6.14: Optical micrographs (left side) and the corresponding SEM images (right side) of irradiated 4H:SiC with different travelling speed (a) 0.5 mms^{-1} (b) 0.1 mms^{-1} and (c) 0.02 mms^{-1}. 102

Figure 6.15: Raman spectra of irradiated SiC with 193 nm laser at laser fluences of 1.6 Jcm^{-2} at different travelling speed with a reference of un-irradiated SiC 103

Figure 6.16: Optical micrographs of SiC ablated with fluence of 1 Jcm^{-2} (top row) and 1.4 Jcm^{-2} (low row) with different overlapping pulses (a,d) 10, (b,e) 100 and (c,f) 1000 pulses per site. 104

Figure 6.17: AFM images of SiC irradiated with 193 nm laser at a fluence of 1 Jcm^{-2} with different overlapped number of pulses (a) 10, (b) 100 and (c) 1000. 105

Figure 6.18: AFM images of SiC irradiated with 193 nm laser at a fluence of 1.4 Jcm^{-2} with different overlapped number of pulses (a) 10, (b) 100 and (c) 1000. Table 6-5: AFM characteristic for irradiated SiC under different fluences and different overlapping pulses. 106

Figure 6.19: SEM micrographs of 193 nm laser ablated 4H:SiC irradiated at a laser fluence of 1.7 Jcm^{-2} and receiving 100 laser pulses at a pulse repetition frequency of 1 Hz. Positions 1-5 indicate the spatial locations of the micro Raman measurements. 108

Figure 6.20: Micro Raman spectra of the 193 nm laser irradiated 4H:SiC at a laser fluence 1.65 Jcm^{-2}. The numbers in the right-hand corner correspond to the positions shown in the SEM in. Micro Raman measurements were acquired using an integration time of 300 seconds, and two measurements were averaged. Excitation using a 632.8 nm He-Ne laser at a power of 12 mW and a 100 × microscope objective. 109

Figure 6.21: Micro Raman spectra of the 193 nm laser irradiated 4H:SiC at a laser fluence 1.65 Jcm^{-2}. The numbers in the right-hand corner correspond to the positions shown in the SEM in. Micro Raman measurements were acquired using an integration time of 300 seconds, and two measurements were averaged. Excitation using a 632.8 nm He-Ne laser at a power of 12 mW and a 100 × microscope objective. 110

Figure 6.22: Micro-Raman spectra of 193 nm laser irradiated SiC with a fluence of 1 Jcm^{-2} and different overlapped laser pulses during scanning processing (a) 10, (b) 100 and (c) 1000 overlapped pulses. Micro Raman measurements were acquiescing an integration time of 10 seconds, and two measurements were averaged. Excitation using a 784.92 nm at a power of 10 mW and a 50× microscope objective. 112

Figure 6.23: Raman spectra of irradiated SiC at 1.4 Jcm^{-2} with different overlapped laser pulses during laser scanning processing starting from bottom to top (1) SiC (2)10, (3) 100 and (4) 1000 overlapped pulses.. 113

Figure 7.1: The multi-shot of theoretical ablation threshold measurements of SiC irradiated by 10.6 µm CO_2 with 150 µsec pulse duration. The plot represents a natural logarithmic dependence of the squared ablated diameter with the applied laser fluence. The slope shows the minimum laser ablated squared radius. The extrapolation to zero gives the ablation threshold fluence. 121

Figure 7.2: A typical irradiated spot of SiC by CO_2 laser at 150 µsec and 500 pulses repetition rate. The attenuator set the applied power to 8.5 W. 121

Figure 7.3: SEM micrographs of CO_2 laser ablated 4H:SiC. It was irradiated at a laser power of 4.2 W, pulse duration of 100 µsec and laser pulse repetition frequency of 500 Hz. Positions 1-5 indicate the spatial locations of the micro Raman measurements. ... 122

Figure 7.4 Average normalised Raman spectra of irradiated 4H:SiC substrate. It was irradiated at a laser power of 4.2 W, pulse duration of 100 µsec and laser pulse repetition frequency of 500 Hz. Layers attributed to 4H: SiC, location one, location 2, after background subtraction of location 3, location 4 and location 5, respectively as illustrated in Figure 7.3. 124

Figure 7.5: Tilted SEM micrographs of the irradiated SiC with different pulse widths of 100, 200 and 400 µsec. 125

Figure 7.6: SEM micrograph of SiC irradiated with 8.5 W and 500 pulse repetition rate with 150 µsec pulse width. The period of the formed ripples (Λ) was measured using ImageJ software to be 8.5 µm. 126

Figure 7.7: Optical and SEM micrograph of 4H:SiC irradiated with 1.9 W and 100 pulse repetition rate with 100 μsec pulse width and stage speed of 2 mms^{-1}. Λ was measured using ImageJ software to be 4 μm...127

Figure 7.8: Raman spectra of SiC and multilayer graphene are grown on single crystalline 4H-SiC (0001) at a different laser pulse duration of 20, 50, 100, 200, and 400 μsec at the centre of the irradiated channel. The x2 at the above three layers shows double magnification...128

Figure 7.9: Raman spectra of SiC and multilayer graphene and reduced graphene oxide grown on single crystalline 4H-SiC (0001) at a different laser pulse duration of 100, 200, and 400 μsec. The spectra collected at the edge of the irradiated channel. 130

Figure 7.10: SEM micrograph and EDX map of the irradiated site with 1.9 w of 10.6 μm laser at a pulse duration of 400 μsec at 100 Hz frequency (a) SEM, (b) SiK, (c) OK and (d) CK. 130

Figure 7.11: Microscopic depth and channel width measurements of the irradiated spots as a function of the applied laser power..132

Figure 7.12: A channel produced by 14 W laser power with the processed profile using origin software. Three areas of the sample shows; the surface, the redeposited material on the edge and the track. The two lateral areas are above the surface 132

Figure 7.13: Cross-sectional one stylus profile Dektak measurements of laser ablated 4H:SiC channels. Central channel depth and the protruding structure's height above the surface of the SiC surface measured as a function of the applied laser power ranged between 3 and 12.5 W..133

Figure 7.14: SEM micrographs of CO_2 laser-irradiated 4H:SiC surface with 500 Hz pulse repetition rate and 150 μsec pulse width and a different power (a) 3 W and (d) 15 W.134

Figure 7.15: Raman spectra of CO_2 irradiated 4H:SiC at different laser power. The bottom layer is a reference 4H:SiC surface, then 3W, 6.2 W, 10 W and 15 W, respectively...136

Figure 7.16: Raman spectra of CO_2 ablated SiC at a 15 W with 150 μsec and 500 Hz pulse repetition rate at different locations of the beam. Red colour represents the spectra collected near the edge and the black colour related to the centre of the beam. 137

Figure 7.17: Microscopic measurements of the channel width of the irradiated channels as a function of the stage motion.. 138

Figure 7.18: Cross-sectional one stylus profile Dektak measurements of protruding height above the surface of the irradiated channels as a function of travel speed ranged between 3 and 21 mms^{-1}. 138

Figure 7.19: SEM micrographs of SiC irradiated with various Aerotech stage speed ranging from (a) 5 mms^{-1}, (b) 9 mms^{-1}, (c) 17 mms^{-1} and (d) 21 mms^{-1}........................ 139

Figure 7.20: Optical micrograph of SiC irradiated at different Aerotech stage speed of 3, 11 and 19 mms^{-1} starting from left to right, respectively. 140

Figure 7.21: Cross-sectional view at the bottom edge of un-irradiated 4H:SiC (a), irradiated SiC with different travel speed at (b) 21, (c) 19, (d) 17, (e) 11 and (f) 7 mms^{-1}. 141

Figure 7.22: SEM micrograph of SiC edge irradiated at 10 W and 7 mms^{-1} speed...... 142

Figure 7.23: EDX of SiC irradiated with different travel speed. 142

Figure 7.24: Raman spectra of CO2 irradiated 4H:SiC at different travelling sample speed. The bottom layer is an un-irradiated 4H:SiC surface, then 3, 7, 11, 15 and 19 mms^{-1}, respectively. The data were normalised and subtracted. 145

Figure 7.25: SEM micrograph of CO_2 irradiated SiC under controlled atmosphere. The applied laser fluence was ~57 Jcm^{-2} with a pulse width of ~100 μsec and a pulse repetition rate of 3 kHz. 146

Figure 7.26: Single point Raman spectra of graphene grown on 4H:SiC using CO_2 laser under low pressure at different locations. The bottom layer shows the pristine SiC, middle layer represents the collected Raman from the spot centre and the top layer collected from the spot edge. 147

Figure 8.1: I-V characteristic of the graphitic channels produced by 11.5 nsec 193 nm laser at a fluence of 1.56 ± 0.08 Jcm^{-2}. The sample speed was 0.01 mms^{-1} with 5 Hz pulse repetition rate. The black data represent the un-irradiated SiC while the coloured data

shows the irradiated channel with probes spacing changing from 1 mm to 5 mm, respectively. 151

Figure 8.2: The linear relation between the reduced resistance and the changing spacing distance between the probes measured on the channel produced with 1.56 Jcm^{-2}. 152

Figure 8.3: Optical micrograph of the gap width between two tracks on SiC (the left) and the corresponding AFM image (right) 152

Figure 8.4: The linear relation between the reduced resistance and the changing spacing distance between the probes measured on the channel produced with 1.56 Jcm^{-2}. The probes were either together on one track or each on one track. 153

Figure 8.5: Temperature rise as a function of time for the laser fluence 1.56 ±0.08 Jcm^{-2}. It shows that the temperature exceeds 2250 K for the pulse duration of the laser of 11.5 nsec. 154

Figure 8.6: Micro-Raman spectra of 4H:SiC before irradiation (top layer) and after irradiation with 193 nm laser (bottom layer). Excitation laser was 784 nm at the power of 1 mW. 155

Figure 8.7: Optical micrograph of the irradiated channel by ArF laser with 1.56 Jcm^{-2}. a) is X100 magnification and b) is higher magnification. 156

Figure 8.8: AFM images of 4H:SiC before laser processing a) semi-insulating SiC and after 193 nm laser processing, (b) conductive SiC. 156

Figure 8.9: I-V measurements of graphitic/SiC junction produced by 193 nm at 1.4 Jcm^{-2} laser fluence with different speed or overlapped dosage. 157

Figure 8.10: Top row represents the optical micrographs, and the bottom row is the AFM graphs of the graphitic structure produced on SiC irradiated by 193 nm laser at 1.4 Jcm^{-2} with different overlapped laser pulses (a, d) 10 pulses (b,e) 100 pulses and (c,f) 1000 overlapped pulses. 158

Figure 8.11: I-V measurements of graphitic/SiC junction produced by 193 nm at 1 Jcm^{-2} laser fluence with different speed or overlapped dosage. 159

Figure 8.12: I-V measurements of the graphitic/SiC surface produced by CO_2 laser as a function of the applied laser power. 160

Figure 8.13: SEM micrograph of graphene/SiC junction produced with different laser power (left side) 6.2 W (right side) 14 W 160

Figure 8.14: I-V measurements of the graphitic/SiC junction produced by CO_2 laser as a function of the travelling speed. 161

Figure 8.15: I-V measurements of the graphitic/SiC junction produced by CO_2 laser as a function of the applied laser pulse duration. 162

Figure 8.16: SEM micrographs of the graphene derivatives/SiC tracks produced with different laser pulse duration (a) 100 μsec, (b) 200 μsec and (c) 400 μsec.......... 162

List of Tables

Table 2-1: The optical properties of the used 4H-SiC at 193 nm and 10.6 μm wavelengths[8]. 5

Table 2-2: The thermal, electrical and mechanical properties of the used 4H-SiC at 193 nm wavelength along with some properties of Si and 6H:SiC[13–18]........ 7

Table 2-3: Laser processing of SiC for different applications. 9

Table 2-4: Graphene properties[88–95]. 13

Table 2-5: A review of all the production of graphene by laser. 18

Table 3-1: Photon source and their energy in eV. 31

Table 6-1: Partial vapour pressures of silicon carbide (atm). 88

Table 6-2: Roughness measurement of the irradiated SiC with 193 nm laser conducted at different laser fluences. The measurements were taken by WLI. 95

Table 6-3: WLI roughness measurements of SiC samples irradiatedwith different pulse numbers near threshold fluence. 99

Table 6-4: WLI depth measurements for the 10000 overlapped pulses at different fluences around the threshold. 99

Figure 6.18: AFM images of SiC irradiated with 193 nm laser at a fluence of 1.4 Jcm^{-2} with different overlapped number of pulses (a) 10, (b) 100 and (c) 1000. Table 6-5: AFM characteristic for irradiated SiC under different fluences and different overlapping pulses. 106

Table 7-1: Calculated thermal and optical penetration depth of CO_2 laser at room temperature with different pulse durations. 120

Table 7-2: The relation between the applied laser power and the defect ratio of $I_D/I_{D`}$. 135

Table 7-3: Speed effect on the surrounding redisposition at the edge of the irradiated channel. 138

Table 7-4: The relation between the applied laser power and the defect ratio of ID/ID`. 143

Chapter 1 **Introduction**

1.1 Introduction

Recent researchers reported the production of different carbon-based films on silicon Carbide (SiC) surface by thermal decomposition. SiC is a wide gap semiconductor and it is well known for its exceptional properties over Si. As a material, SiC and its properties will be discussed in detail in chapter 2. 4H-hexagonal polytype of SiC (4H:SiC) was considered as a semiconductor of choice from 200 polytypes in the thesis. It is commercially available in high quality wafers, has a high electron mobility and low anisotropy. SiC has a high electric field breakdown resulting in lower losses. 4H:SiC would compete with Si and 6H:SiC. It can be applied in high temperature. SiC is able to withstand temperatures as high as 650 °C. It is radiation hard, and it is preferable at microwave frequencies. In comparison, silicon can only withstand temperatures up to 150 °C, due to the low temperature breakdown. In addition to all the above, SiC has a wide window of optical transparency, 350-1100 nm, and a high optical damage threshold.

The ability to process SiC is not an easy task due to its hardness. However, laser was used as a versatile tool to process SiC efficiently and control the formation of a Graphitic layer/SiC junction resulting in a huge potential for high power, high temperature and high-frequency applications. The connection between SiC and graphene with its derivatives can be utilised. Graphene, the wonder material will also be discussed in details in Chapter 2. In general, Graphene can be formed on SiC by thermal annealing. It can be grown as a monolayer or multilayer.

Here, we explore the feasibility of laser-assisted graphitisation of micron-sized SiC particles. Laser-mediated SiC decomposition is demonstrated at nearly ambient conditions, which can result in a manifold of graphene structures, e.g. SiC particles covered by few-layer epitaxial graphene up to highly porous graphene-like structures (froth morphology). SiC particles coated by few-layer graphene films are considered for

applications in macro- and nano-electromechanical systems owing to their very high electrical conductivity. More specifically, the realisation of spatially locating electrically conductive tracks by laser direct-write (LDW) methods is attracting attention. Lasers are especially useful, as high temperatures are required to transform silicon carbide to graphene, typically in the temperature region of ~ 1700 K. The production of electrically conductive tracks via LDW methods is a relatively fast and efficient process and therefore desirable from a technological perspective.

In this work, we report results for the first time on laser processing and ablation characteristic of 4H:SiC using an ArF 193 nm excimer laser. We are especially interested in identifying the laser parameters and understanding how 193 nm radiation couples with 4H:SiC, specifically, to identify the onset of modification of 4H:SiC. To aid the analysis, we carry out temperature simulations using the Finite Element Method (FEM), COMSOL™ Multiphysics 5.3. The motivation behind this work is to report the laser ablation threshold of 4H:SiC at 193 nm and secondly study the decomposition as a function of laser fluence.

This work presents studies about the growth and characterisation of graphene layers on crystalline SiC substrate using heating by a 10.6 μm CO_2 laser beam. We report the decomposition structure of a (0001) SiC. We were especially interested in identifying the effect of the used laser parameters, how the beam couples with 4H:SiC, and how to identify the modification of 4H:SiC. The processing includes the use of controlled atmosphere and in ambient conditions.

It is essential to highlight the advantage of this technique. It creates tracks or any complex shapes of graphene on SiC surface without the need for prior preparation. However, the investigations of this process are in the early stage. Thus, many characterisation methods were employed to investigate the produced graphene.

Moreover, 193 nm and 10.6 μm lasers were used to reduce the resistivity of the graphitic layer. The electrical properties behaviour of the produced Graphene derivatives layer/SiC junction resulting in a massive potential for high power, high temperature and high-frequency applications. The charge carriers and the mobility of the produced graphene/SiC junction were even higher. Mainly, femtosecond lasers were employed to

modify the conduction properties and study the current-voltage (I-V) characteristic of the produced graphitic/SiC interface.

1.2 Thesis Structure

This thesis is organised into nine chapters. Chapter 1 shows the introduction and thesis structure. Chapter 2 deals with the literature review on SiC laser processing for microelectronic and then specialised in the production of graphene/SiC junctions. Chapter 3 shows the fundamental theory of laser processing. Chapter 4 shows the experimental work and the methodology used to complete this work. Chapter 5 focuses on thermal behaviour under laser processing using different methods, including numerical and analytical processing. Numerical solution using finite element analysis by COMSOL™ Multiphysics 5.3. Chapter 6 deals with excimer laser ablation and micromachining of single-crystal 4H:SiC for the formation of carbon-based material/SiC junction. Chapter 7 shows the ablation study and micromachining of single crystal 4H-SiC using a CO_2 laser. It demonstrates the efficacy in fabricating graphene structure on SiC. Chapter 8 deals with electrical and I-V characteristics of the produced junctions. Chapter 9 is on Conclusion and future work.

Chapter 2 **Materials and Literature Review**

2.1 Introduction

This chapter gives the literature review on laser proceeding of SiC to produce graphene and graphitic structures. It also shed a light on both the SiC and graphene with their properties.

2.2 Silicon Carbide

2.2.1 **SiC Properties**

Silicon carbide, the gemstone that was first predicted then synthesised. It was initially theorised in 1824 by Jöns Jakob Berzelius. SiC was first manufactured as black crystals in 1885 and 1892[1]. It has been known as an abrasive material as well as non-oxide ceramic. SiC was artificially synthesised before being found in nature. In 1905[2], it was discovered as a transparent mineral by the Nobel Prize winner Henri Moissan and named moissanite in his honour. It gained such broad interest that even NASA considered it the future of electronic devices[3].

It has many fascinating properties, mostly due to the covalent bonding and the 12% ionic chemical bonds. This ionicity is related to the mismatch in electronegativity between the carbon (C=2.55) and the silicon (Si=1.5); meaning different potential strength of Si and C will have an asymmetric distribution of the electronic charge. These strong bonds allow the material to have a high melting temperature[4].

Silicon Carbide is tetrahedron of SiC_4 or CSi_4, and this is the building unit of SiC, see Figure 2.1[5]. The Si and C connected with sp^3 hybridised bonds[6]. In addition, the ionic bonds will produce polarity to the surface since one of the Si-C bonds in the building unit will be longer than the other three. This is known as a Si and C terminated surface (Si-

face and C-face) when the polar is along c-axis. C-face has higher surface relaxation and lower surface free energy than Si-face[7].

Table 2-1: The optical properties of the used 4H-SiC at 193 nm and 10.6 μm wavelengths[8].

Property	193 nm	10.6 μm
Absorption coefficient (cm^{-1})	1.47×10^{6}	6584
The imaginary part of the refractive index	2.267	0.55538
The real part of the refractive index	2.49	2.7081
Reflectivity (%)	42	23

Although it has the same stoichiometry, the structure could be formed in more than 200 polytypes by managing its one-dimensional layer arrangement; this is referred to as polytypism. The crystal could be either cubic polytype (β-SiC) such as 3C-SiC, hexagonal or rhombohedral (both known as α-SiC) such as 4H-SiC, 6H-SiC and 2R-SiC, respectively. The commercially available types are the 4H-SiC, 6H-SiC and 3C-SiC. The initial numbers, Ramsdell notation, refers to the number of layers in a unit cell while the letter relates to the structure of the crystal[9]. The stacking of these layers will be in three positions named A, B, and C. Therefore, each polytype will have different orders of these positions. For 4H-SiC, the stacking order will be ABCB. Both hexagonal SiC displays isotropic properties and a relatively higher band gap (over 3 eV) than the 3C-SiC (less than 3 eV)[10] see Table 2-1 and Table 2-2.

The main issue with mass SiC production is the quality of the prepared crystals due to the high density of different kind of defects[11], such as stacking fault, twin boundaries, dislocation and presence of another polytype[9]. However, it is relatively cheaper and more available than before.

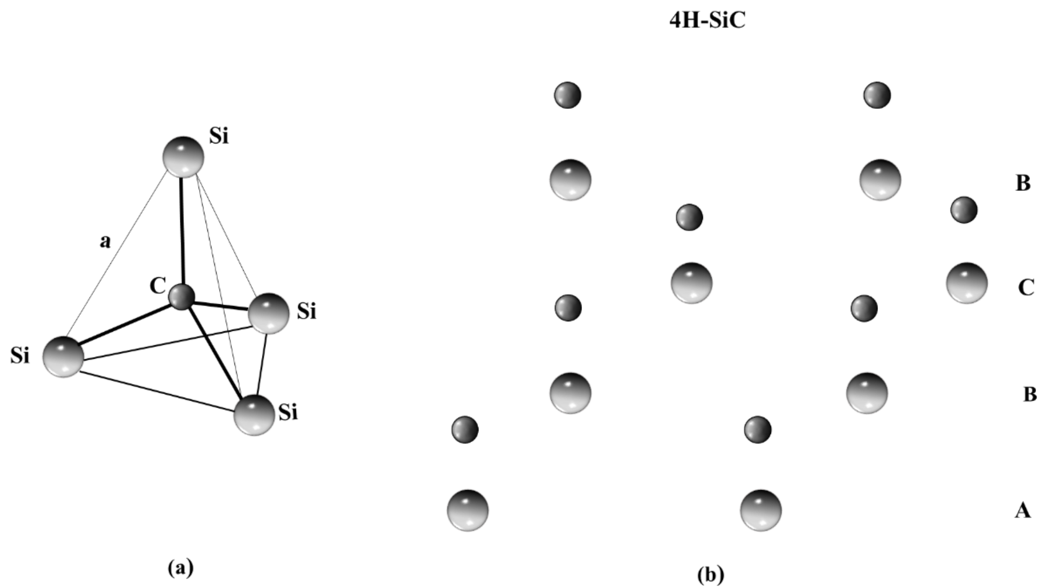

Figure 2.1: a) The lattice structure of the basic unit of SiC. Dark atoms are C, and light atoms are Si. The length between Si and Si of two C is 3.08 Å and the distance between Si and C is 1.89 Å. b) Stacking sequences of 4H-SiC polytypes in c-axis.

It is considered a super material with all its unique properties. In summary, it is a wide band gap material with high breakdown field, so it is preferable for harsh conditions such as high temperature, high radiation environments and high-power devices. Also, it is hard and mechanically strong, which can be seen from Young's modulus, and its high yield strength. Additionally, SiC has preferred tribology properties such as wear-resistance and lubrication.

For more unique properties, see Table 2-2, which demonstrate properties such as low density, high thermal conductivity, high hardness, high elastic modulus, excellent thermal shock resistance, chemical inertness, high strength, and low thermal expansion.

4H-SiC is typically preferred for microelectronics applications over 6H-SiC because of its higher carrier mobility and its favourable mechanical properties. SiC is almost as hard as diamond; it is similar to that of Al_2O_3 on the Moh's scale (9)[12]. Its hardness is approximately three times greater than silicon.

Table 2-2: The thermal, electrical and mechanical properties of the used 4H-SiC at 193 nm wavelength along with some properties of Si and 6H:SiC[13–18].

Property	4H-SiC	6H-SiC	Si
Thermal diffusivity (m^2sec^{-1})	1.7×10^{-4}	2.2×10^{-4}	9×10^{-5}
Thermal conductivity at 300 K (WmK^{-1})	370	490	105
Working temperature (K)	1513	1513	573
The melting point (K)	3100 (at 35 atm)	3100 (at 35 atm)	1700
Latent heat of melting	5000 Jcm^{-3}		50.55×10^3 $Jmol^{-1}$
Latent heat of Evaporation ($Jmol^{-1}$)	4×10^5		384.22×10^3
Electron mobility (cm^2/Vs)	800-1000	370-600	1400-1500
Breakdown Field E_B (Vcm^{-1})$\times10^6$	3-5	3-5	0.3
Saturation Drift Velocity V_s (cms^{-1})$\times10^7$	3.3-8	2.7	2
Band gap (eV) (indirect)	3.26	3.0	1.12
Lattice Constant of SiC (Å)	a=3.0730 b=10.053	a=3.080 c = 10.1	5.431
Electron affinity (V)	3.08	3.34	4.07
Moh's Hardness	9	9	6.5
Density (kgm^3)	3200	3200	2300
Specific Heat C_p (Jg^{-1} $^oC^{-1}$)	0.7	0.69	0.69
Atomic weight (Da)	44	46	28

2.2.2 SiC Application

For SiC, various applications can be achieved depending on their properties. Interest in using the material for mechanical applications grew because it is hard material with high thermal conductivity, which is similar to the thermal conductivity of copper. It can be used in aerospace space crafts[19], engines[20], car brakes and many other wear resistance parts in cars and abrasive material by shaping the SiC powder[21]. Moreover, due to its electronic and optical properties (especially the variety with a large band gap), SiC have been used in electronic applications. It can be used in power electronics such as Thyristors[22], Schottky diodes[23], MOSFETs[24], gas sensors[25], and even optical mirrors in some lasers[26].

2.3 SiC Laser Processing

Laser micro and nano machining of SiC is appealing due to a large number of potential applications. Laser processing of this material has advantages over conventional methods. It is a fast process with minimum steps and can be controlled precisely. SiC has been treated with lasers since the 1980s, but due to the lack and cost of the SiC material, it did not take on its full potential. Laser-SiC interaction can be classified into subtractive and additive categories. Each one of them can be divided into different processing mechanism, see. Table 2-3 Some processing mechanisms are annealing, crystallisation, electroless metallization, surface re-constructing, and ablation as drilling.

Moreover, different types of lasers have been used in micromachining SiC for different applications and purposes. CO_2 lasers[27–29], excimer Laser[30–39], Nd:YAG[40–43], Ar^+ laser[44,45] , femtosecond lasers[46–48], Picoseconds lasers[49], copper vapour laser[50], and even Nitrogen lasers[15] were employed to process SiC for different purposes. Most used lasers were excimer lasers such as KrF (248 nm), XCl (308 nm) and ArF (193 nm). These lasers are preferable as they work in the ultraviolet (UV) region, where the SiC has high optical absorption to their wavelengths whether it has a crystalline or an amorphous structure and due to the popularity of these lasers.

Table 2-3: Laser processing of SiC for different applications.

Laser Processing	Laser type	Wavelength (nm)	SiC type	Comments
Annealing and Crystallization	Excimer	193, 248 and 308	α-SiC, 4H	Ion implantation damage and Crystallization[44,51–55]
	Ar	514.5	β-SiC, 6H, and 4H	Form an Ohmic contact on SiC[56–58]
	Excimer and Nd:YAG	248, 355 and 1060	4H	Restore the structure after annealing[59] .
	Nd:YAG	265 and 1240	a-SiC	Annealing after production[60–63]
Electroless Metallization	Excimer Cu vapour	193, 308 510	SiC and ceramic	Both Ni and Cu deposits show good adherence to the SiC surface up to 0.5 N/mm^2 [32,64,65]
Surface Structuring	N_2 Ti-Sapphire Excimer Dye	340 800 193, 248 1040, 1026	3C-SiC, 4H-SiC 6H-SiC 6H-SIC, 3C-SiC	Formation of nanoparticles on the treated surface [15,66,67]. Micromachining on surface[46,68]
Doping	Excimer Nd:YAG	193 1064	4H and 6H	n-type and p-type doing[69,70]

SiC is very reflective for the mid-infrared (IR) wavelength and almost transparent to the visible spectra. On the other hand, amorphous SiC, couples differently with the light, it absorbs in the visible and near-infrared (NIR) wavelengths[44,58,62].

For IR Lasers processing of material, the mechanism will be different from the UV laser processing. The IR wavelengths will interact with the material and coupled with the lattice rather than the electrons as in the UV lasers[28,29].

Recently, ultrashort Lasers such as femtosecond pulses and picosecond lasers have been used to micromachine SiC regardless of the wavelength. This is due to the limitation of the heat-affected zone (HAZ) and the high peak energy delivered to the sample[71].

With using ultrashort pulsed lasers, nanostructures formed on the surface as ripples and spherical structures, an effect of the light polarisation[72,73]. Although other theories are proposed, such as coulomb explosion[66] self-assembly[74], and laser beam interference with the plasma[75].

2.4 Graphene

One of the main outcomes of laser processing of SiC is the decomposition of the SiC surface resulting in a pattern of carbon or one of its derivatives such as graphene. Graphene, with its unique properties, represents a breakthrough in material science. What makes it unique is the combination of these properties that can not be found in any other material. It has, therefore, been proposed as an alternative material for some applications. Graphene is a chiral two-dimensional carbon. It arranges in a hexagonal structure, see Figure 2.2. It is a hybridised carbon structure with strong sp^2 covalent bonds in order to be stable. This will be formed by the s, p_x, p_y orbitals with C-C-C bonds at a 120° angle between them. The lattice length of 1.42 Å; this is represented by the σ bond, responsible on the robustness of the lattice in all allotropes of carbon. The last p_z orbital will be overlapping with the adjacent carbon to produce the valence band (π filled orbitals) and the conduction band (π^* empty orbitals). π and π^* are responsible for all the distinctive graphene properties and stability.

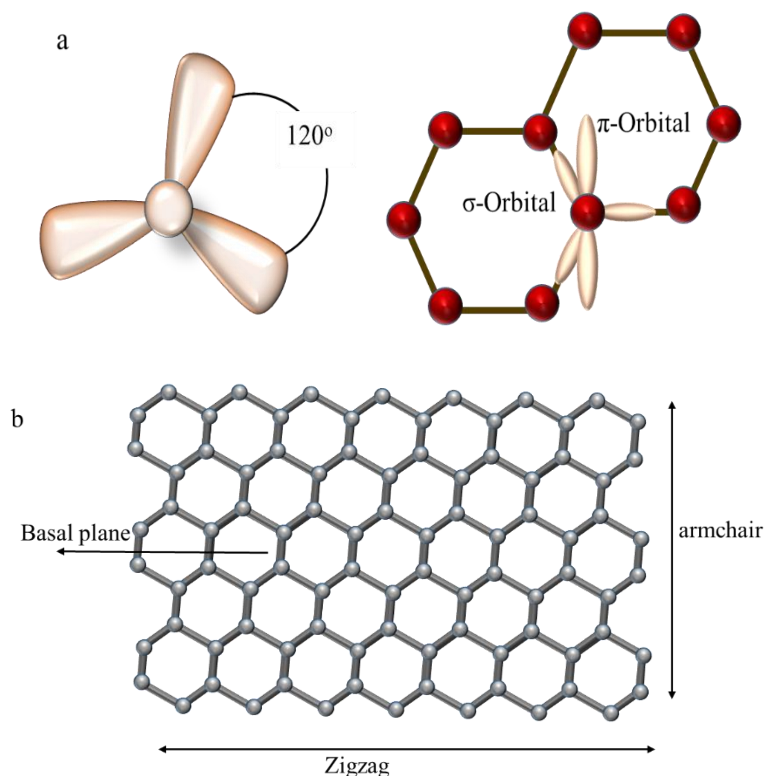

Figure 2.2: Graphene structure a) the orbitals b) the planes.

In general, graphene can be structured as *basal*, *zigzag* and *armchair* plane see Figure 2.2. The boundaries considered as defects (represented in Raman spectra by D peaks) and minimise the unusual properties. However, these are yet to be controlled. Graphene has an atomic thickness, it is flexible and could be folded to produce different allotropes, it can be stacked to form 3D graphite, rolled to one Dimensional nanotube or wrapped for zero Dimension fullerenes[76]. It was first investigated theoretically in 1947[77]. However, it took more than half a century to produce it experimentally by Geim and Novoselov in 2004, for which they received a Nobel Prize in Physics in 2010[78].

Electronically, graphene is considered to have a zero band gap since its conduction and valence bands meet up in six points (Dirac points)[79]. Recently, the structure of graphene was modified to establish a band gap, and that could be used as an electron-phonon superconductor for high-frequency applications[80]. Furthermore, electrons in graphene behave almost as massless particles. The above will lead to very high mobility. Hence the sheet resistance is about 30 Ω cm^{-1} at 90 % transparency[81]. This will also depend on the symmetrical honeycomb lattice.

Mechanically, graphene is one of the most durable material in the world, yet it is elastic up to 20%[76]. This will introduce graphene as a potential reinforcement for other composites increasing the tensile strength up to 150 %[82].

Optically, it is a transparent material due to the two-dimensional aspect and to the lack of band gap. Single-layer graphene absorbs 2.3% of the light, and that is true for each added layer[83]. It combines some desired properties like transparency and electrical conductivity. Many others are shown in Table 2-4.

Graphene was first defined in 1986 by Boehm[87.] Since 2004, many techniques were used to produce Graphene such as the mechanical exfoliation of crystalline graphite one must mention that the graphene quality defines the properties significantly, and that is directly related to the synthesis method.

In addition to the unique electronic properties, the vibrational properties of the 2D layer are fascinating too. Graphene is very light (one atom layer), but with strong bonds, it will have a high sound velocity leading to high thermal conductivity. We can also use the vibrational behaviour to determine the optical properties of the layer[84] through the scattered phonons.

In general, all carbon allotropes are good heat conductors but, for graphene, it could be as high as 5300 $W(mK)^{-1}$. This high thermal conductivity gives graphene advantages in optoelectronics, photonics and other applications. It also has a vast negative thermal expansion meaning it shrinks with temperature, which is rare. However, this is due to a large number of out of plane phonons[85]. Most of the properties discussed above are for single-layer graphene. Furthermore, it could be formed with a stack of layers connected by the Van der Waals weak bonds resulting in different properties. 3D graphene could be prepared and represented as graphene foam[86].

2.4.1 Graphene Production Techniques

Graphene was First defined in 1986 by Boehm[87]. Since 2004, many techniques were used to produce Graphene such as the mechanical exfoliation of crystalline graphite.

Table 2-4: Graphene properties[88–95].

Properties	Value	comments
C-C lattice (Å)	1.42	
Specific surface area (single sheet) (m^2g^{-1})	2630	
Young's modulus (TPa)	1	
Thermal conductivity (WmK^{-1})	2000-5300	
Thickness		Atomic thickness
Intrinsic strength (GPa)	130	
Optical absorbance Transmittance	2.3% 97.7%	
Energy gap (eV)	0-0.25	
Electron effective mass	0.012 m_o	m_o is the free electron mass
Electron mobility ($cm^2\ V^{-1}s^{-1}$) at 300 K	2×10^5	150 times greater than Si
Electron saturation mobility (10^7 cm s^{-1})	5	
Current Density (A/cm^2)	Up to 10^9	

This technique is time-consuming and produces small flakes, but very high quality[78]. Chemical vapour deposition (CVD) uses hydrocarbon gas on a metal surface by controlling the pressure and temperature of the furnace environment. However, this process will need the Graphene transferring to a different substrate[81]. Molecular beam deposition produces a large area of high quality Graphene on nickel[96]. Chemical production produces a gram scale of Graphene from Sodium-Ethanol[97]. Reduction of Graphene oxide can be achieved with different reduction methods. However, the produced structure is still under debate, and it only reduces the oxide and not producing pristine Graphene[98]. Another technique is narrowing carbon nanotubes, this can lead to pristine Graphene either due to the chemical reactions[99]. Thermal decomposition of SiC,

this technique could be used with a variety of heat sources and produces high quality graphene.

2.5 Decomposition of SiC

Thermal decomposition of SiC was investigated by Van Bommel in 1975[100]. The graphitic surface on SiC phenomenon initiated by Badami in 1965[101,102]. However, graphene on SiC was first observed in 2000[103]. Moreover, in 2004[104], a group revealed the production of two-dimensional epitaxial graphite. The whole process still undetermined[105], including the buffer layer bottom-up growth mechanism[106]. It requires heating the surface of SiC to high temperatures to sublime the silicon atoms leaving carbon of graphitic structure on the surface, which boosts the idea for graphene production[107]. The SiC surface faces and orientation can determine the number of layers produced. The C-face of SiC tends to give multilayer graphene while the Si-face of SiC results in single or bilayer graphene[108]. The main advantage of producing the graphene directly on the SiC is the ability to use it for different application [109]. With this technique, we could produce a full wafer of graphene, however, the mentioned above issues and the layers of graphene should be controlled[84,110]. Using this method decreases the side effect of transferring the produced graphene to other substrates and minimise the effect of other substrates on the produced graphene properties[108]. SiC sublimes under laser irradiation incongruently, producing different outcomes. It could produce oxidise surface [111], carbonised, or produce Si surface[64]. Silicon carbide is reported to sublime at ambient pressure, and melting takes place at pressures of ~35 atmospheres and above[112]. The sublimation and melting temperature of silicon and carbon reported to be 1670 K and 3870 K, respectively[60]. Other work stated that the sublimation temperature could be as low as 1300 K in vacuum[79]. Therefore, Si-C bonds will break under heating, and the Si atoms leave the carbon behind[113]. Eventually, the carbon layers prevents more Si sublimation[114]. Moreover, the melting temperature was declared to be above 3100 K[17], and the decomposed vapour will consist of Si, SiC_2 and Si_2C.

2.6 Laser induced Decomposition of SiC

Laser decomposition of SiC is preferable over other graphene growth due to the advantage of direct writing on the SiC surface. Absorption of laser radiation heats the surface rapidly providing a reduction of the incongruent decomposition. However, sublimation still occurs. The laser was used to experimentally define the melting temperature of 4H-SiC and 6H-SiC[38]. Melting was confirmed by reflectivity measurements[115]. Less work can be found on laser heating of SiC as a source for the thermal decomposition. Although different kinds of lasers were used, such as excimer laser (ArF, XeCl, and KrF)[32,116], where the treated surfaces were rich in Si and SiO_2 or disordered with oxidised regions, due to the incongruent sublimation of the surface[65]. Although others found that the surface structure depends on the applied laser fluence[117]. Other wavelengths, such as the Nd:YAG (1064 nm) and the $CO_{2,}$(wavelength)(10.6 μm) were found to act as a heat source and leave a carbon surface behind[118,119].

Several articles have pointed out the possibility for simultaneous synthesis and patterning of graphene using laser beams. Recently, Epitaxial Graphene (EG) was grown on the Si-face of SiC by UV laser radiation (248 nm) of an excimer pulsed laser[31]. The surface-induced laser decomposition of the Si surface led to spatially controlled and scalable, EG synthesis. Finally, in the pre graphene era, it was observed that irradiation of polycrystalline SiC with a pulsed near-infrared Nd:YAG laser (1064 nm) yields "crystallised" graphite on the SiC surface[120]. The graphitic structure of the irradiated area (~500 μm^2) was confirmed by Raman microscopy. Unfortunately, the spectra obtained at that time were not extended above 1800 cm^{-1} and the typical graphene spectral features were not observed.

It has been reported that non-congruent sublimation could be associated with laser processing unless the laser is used as a heating source. For this case, the optical properties of SiC will dominate coupling and removal of the surface material. In general, excimer lasers are reported to produce Si-rich regions. Nevertheless, IR lasers tend to produce C-rich regions. Table 2-5 represents an overview of various works accomplished to study the effect of laser processing on the surface and all the attempts of producing graphene by laser decomposition of SiC. Pehrsson and Kaplan[117] found that the surface

characteristics depend on the fluence of the used laser. They reported that multiple ArF pulses in the range of 0.4 – 0.6 J cm^{-2} produced a graphitic surface, and for higher fluences, a Si-rich region was produced. On the other hand, IR irradiation such as Nd:YAG with photon energy below the SiC band gap has a weak coupling with the SiC, mostly resulting in thermal effects leading evaporation of silicon. This is why Nd:YAG lasers at 1064 and 532 nm result in C-rich surfaces[121]. Unless they used for the formation of graphite surfaces a vacuum UV Raman cell with a frequency- quadrupled Nd:YAG laser (VUV-266 nm) on 6H-SiC[122]. Moreover, oxide formation will result on the SiC surface in the presence of oxygen, i.e., the surface oxide will be present in the case of excimer ablation in the range of 1-3.5 J cm^{-2} and an underlying Si-rich layer[64]. While the enrichment of Si was reported under high vacuum processing[57].

2.7 Applications of Graphene on SiC

Graphene has many potential applications due to its unique properties. However, for most applications, it needs to be supported by a substrate such as SiO_2 or semi-insulating SiC despite the fact of lowering the graphene electron mobility values[123]. Of special interest is graphene/SiC due to the longer electron mean free path compared to graphene/SiO_2 and also due to the option of avoiding the transfer of graphene to the required substrate surface while having the SiC substrate (semi-insulating or conductive) ready for device processing[94,123]. It has been reported that Graphene on SiC has ohmic properties[124]. Due to the atomic thickness and high carrier mobility attempts were conducted to for different devices such as Graphene FET transistors[125,126], however, these devices does not work as the traditional semiconductor's transistors because graphene is a zero band gap and it does not turn off entirely. Traditional on / off current ratios that accomplished by gating a graphene transistor seem to be on the order of 10 in a traditional configuration. Thus, high speed analogue electronics such as RF transistors[94,127,128] were achieved instead of graphene digital switch. Both the electrical and thermal conductivity are suitable, combined with the flexibility and transparency, allows this material to be an excellent source for electrodes in solar cells, Light Emitting Diode (LEDs), touch screens, smart windows, organic thin film transistors (OTFT)[79,91,129,130] and integrated circuits (IC), which was on a wafer scale "graphene broadband frequency mixer" on SiC[131].

Graphene/SiC detectors and sensors were also conducted successfully[94]. Magnetic sensor[132] and magnetic detectors were achieved as quasi-isolated graphene on SiC[133]. An ultraviolet detector was made by graphene on SiC heterojunction[134]. These devices have high performance in sensing.

In addition, the energy band structure and the Dirac points, make graphene very sensitive to chemical gating (using chemicals to tune charge transport). These properties allow graphene the potential of single molecule detection at room temperature[94,135,136]. Most of the above have been accomplished by epitaxial growth of graphene on SiC by decomposition under high temperature. This thesis presents experimental and computational work to understand the laser decomposition of SiC. Specifically, to identify optimum laser processing parameters necessary to form a graphene or graphitic layer directly on 4H:SiC and a device application are discussed.

Table 2-5: A review of all the production of graphene by laser.

Material	Laser wavelength (nm)	Surface	Comments	Reference
6H-SiC	CO_2 at 10,600	Large area homogeneous few monolayer graphene	No high vacuum.	[119]
4H-SiC	KrF at 248	Graphene with a structure as the thermally decomposed SiC. Wrinkle-free few-layer graphene	In vacuum. Room temperature.	[31,137,138]
4H and 6H-SiC	ArF at 193	Few layers Graphene and carbon nanostructures	The process implanted with ions	[139]
Poly SiC on Si	CO_2 at 10,600	Non-continuous graphene on the SiC surfaces	A thin film of SiC grown on Si wafers including AlN buffer layer. Sintered SiC.	[140] [141]
4H-SiC	Nd:YVO_4 at 1064	A nanocrystalline graphitic phase on SiC and Graphene	Ar Atmosphere Or Ultra high vacuum	[142]
SiC powder	KrF at 248	Graphene sheets as shells	Wet irradiation	[143]
Micron-sized α-SiC particles	CO_2 at 10,600	SiC particles covered by few-layer Graphene to free-standing 3D graphene froths	No vacuum	[86]
4H-SiC	XeCl at 308	n-doped Graphene	Vacuum includes solid dopant source	[144]
4H-SiC	9,300	Carbon layer containing Si	Low vacuum	[145]
SiC flakes	KrF at 248	ultrafine SiC@graphene nanocomposites and 1-3 layers of graphene	The SiC was dispersed in ethanol	[146]

Chapter 3 Theoretical Background

3.1 Introduction

This chapter deals with the theoretical background of interaction and coupling between the laser and the material. It focuses on laser interaction with semiconductor materials.

3.2 Light-Matter Interaction

Laser material interaction is a complicated process. Its complexity arises from the combination of several phySiCs processes, such as; heat transfer of the energy to the material lattice, the mechanism of fluid including the melted material and the dynamic of gas as the material vaporise, plasma science to describe the produced plasma at high laser fluences. A few concepts related to the laser material interaction can be found below to understand these processes.

3.2.1 Optical Properties of Material

By applying an electromagnetic wave, bound electrons will oscillate, while, free electrons will be accelerated. Electromagnetic waves interact with the electrons since atoms considered as heavy objects to react with, especially at high frequencies EM. Thus, the optical properties of the material will depend on the energy states of the molecules. Hence, the electric field and polarisation. The oscillated particles will "re-radiate" their energy or, they will get resonance with the material lattice because of the periodic behaviour of the applied field from the laser. In other words, the absorbed energy will be emitted again or transferred to the lattice[147,148]. The oscillation will be represented as a spring, see Equation (3.1)[149].

$$m\frac{d^2x}{dt^2} + m\Gamma\frac{dx}{dt} + m{\omega_o}^2x = e\vec{E}_{local} \tag{3.1}$$

Where m is the electronic mass, x is the displacement, $m\Gamma\frac{dx}{dt}$ is the damping factor, $m{\omega_o}^2x$ is the Hooke's law restoring force, e is the electronic charge magnitude and E_{local} is the local electric field acting on the electron as a driving force. Moreover, the light could be written as in Equation (3.2)

$$\vec{E}_{local} = \vec{E}_{o,local}\exp(i\omega t) \tag{3.2}$$

Where $\vec{E}_{\text{local}}$ is the electric field, ω is the angular frequency, t is the time.

Damping of the electrons' oscillation inside the matter is described by Lorentz theory [149]. The electrons change from the atomic rest where they oscillate symmetrically to the non-uniform oscillating mode by the laser wave electric field according to Equation (3.3) and the material response as dielectric function $\varepsilon(\omega)$ as in Equation (3.4)

$$\vec{E} = \vec{E}_o \exp\left(i\left(\frac{2\pi z}{\lambda} - \omega t\right)\right) \tag{3.3}$$

$$\varepsilon(\omega) = 1 + \omega_p\left(\frac{1}{(\omega_o^2 - \omega^2) - i\Gamma_c\omega^2}\right) \tag{3.4}$$

Where $\omega_p = \sqrt{\frac{Ne^2}{\varepsilon_o m}}$ the frequency of the plasma, Γ_c is the damping constant and ω_o is the resonance frequency. The intraband resonance ΔE can be written as;

$$\Delta E = \frac{\omega_o h}{2\pi} \tag{3.5}$$

When the material changes phase into a liquid, the optical properties change, and the behaviour of the material can be considered metallic[150].

The incident wavelength is much larger than atomic lattice. Therefore material reaction could be explained by the complex refractive index, $N = n \mp ik$, where n is the real part of the refractive index($n = c/v$) and c is the speed of light in vacuum, ν is the light speed in the matter and k is the imaginary part (known as the extension coefficient, represents the damping factor of the wave)[148,151]. These quantities will define the reflectivity R and the absorption coefficient α as in Equations (3.6) and (3.7)[152,153].

$$R = \frac{(n-1)^2 + k^2}{(n+1)^2 + k^2} \tag{3.6}$$

$$\alpha = \frac{4\pi k}{\lambda} \tag{3.7}$$

Where α is the previously defined optical absorption coefficient, and λ is the wavelength. The optical absorption coefficient can be used to quantify the exchange of electromagnetic (EM) energy with the material. According to Equation (3.7) when $k > 0$ the optical processes are dominated by absorption.

The absorbed light will penetrate inside the material according to Lambert-Beer law, Equation (3.8), where the light intensity decreases exponentially into the material thickness z[154],

$$I(z,t) = I_o(t)(1 - R)\exp(-\alpha z) \tag{3.8}$$

Where I_o is the incident laser intensity and z is the material thickness.

3.2.2 **Carrier Behaviour**

In semiconductors, the interaction between the laser and the material is dominated by the density of electronic excitation and the flux density of the photon field. "The former is the volumetric density of electron-hole pairs created by the incident laser light while the latter is the volumetric density of photons per unit time capable of exciting products of the primary photon- solid interaction"[155]. The excitation and relaxation process of the electrons in the electronic states of semiconductor materials is shown in Figure 3.1. The dominant resonance in a semiconductor is the transition between two states or inter-band, from the valence band to conduction band. Initial laser interaction induces defects by altering the electronic and geometrical structure of the material, and by laser- induced particle emission. Defects grow in number, during one or multiple laser pulses, therefore, defects and defect clusters evolve on the surface and in the sub-surface bulk. The changing optical, topological and structural properties of the defect clusters then weaken the surface bonds and create the conditions for massive ejection of surface atoms, molecules and clusters[155].

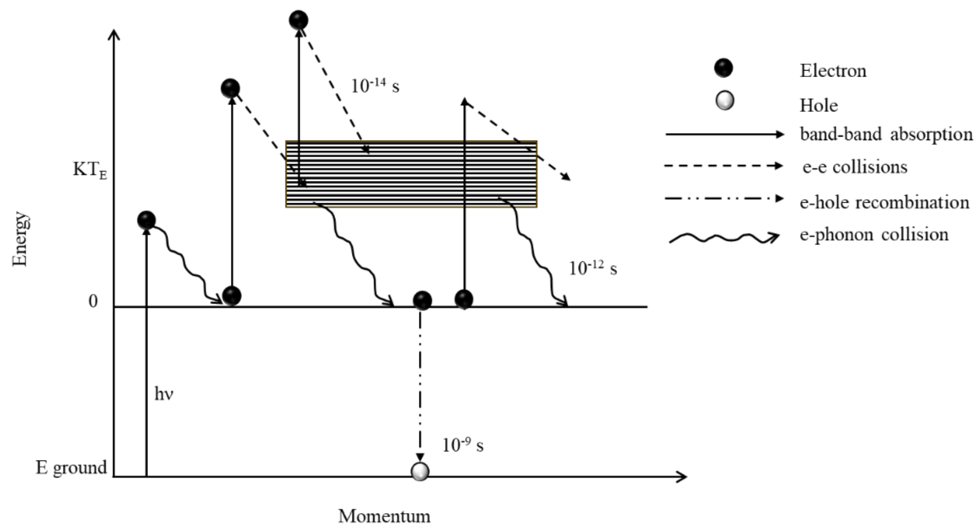

Figure 3.1: Electron excitation and relaxation in material coupled with intense laser light[156]. In semiconductors, absorption of wavelengths between 0·2–10.0 µm causes an interband transition (valence to conduction). The absorbed energy converted to heat through (a) excitation of electrons in valence and/or conduction band, (b) interaction between excited electron-phonon within a span of 10^{-11}–10^{-12} s, (c) electron-electron or electron-plasma interaction, and (d) electron-hole recombination within 10^{-9}–10^{-10} s.

There are many ways light and crystalline semiconductor structures can interact with one another. For example, (photon, phonon), (photon, electron) and (phonon, electron, photon) and even polaritons. Each interaction is dependent on each other, and they could be localised or not. Photon absorption is an essential outcome of these interactions. Increasing the photon energy, more electrons in the valence band will be excited to the conduction band even in deep sub-bands of both valence and conduction bands. In addition, photon absorption is temperature dependant process.

An interband optical transition can be direct or indirect. For an indirect transition, the difference in wave vector must be provided by the creation of a phonon. In indirect band gap semiconductors, phonons have a significant influence on the process of electron excitation due to energy and momentum conservation. Thus, phonons will influence the absorption process and high momentum phonons result in high lattice temperature[147,157,158].

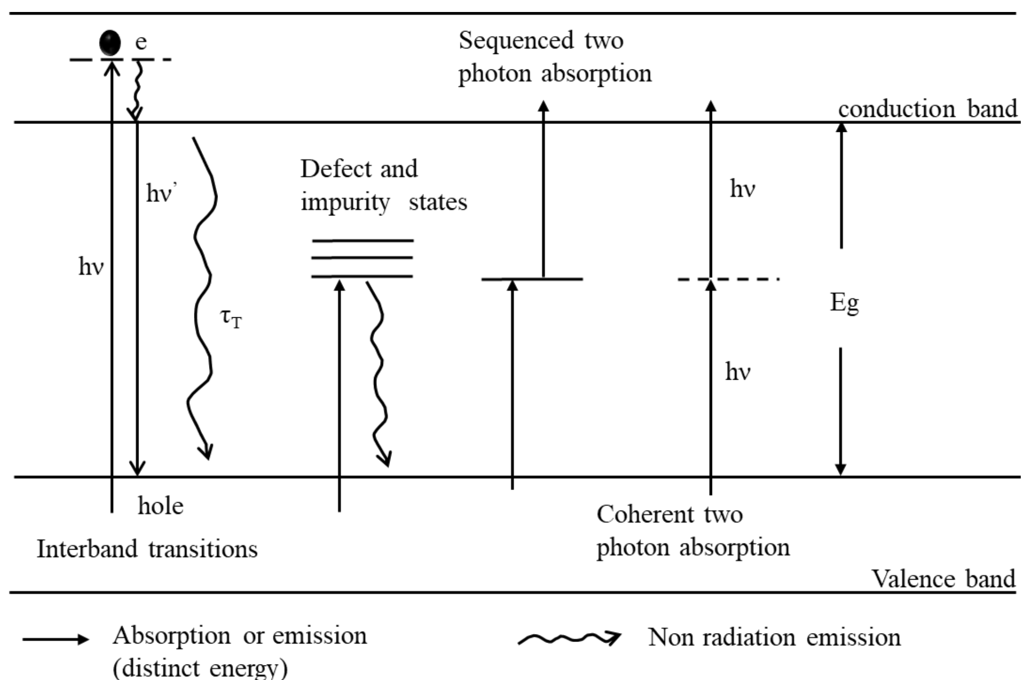

Figure 3.2: electronic excitations in insulators and semiconductors[158].

Schematic of different types of electronic excitation in a solid could be seen in Figure 3.2. In addition to the excitation explained previously, another transition occurs from the defects and the process of two-phonon absorption[158].

3.3 Laser Heating and Heat Transfer

In laser processing, the heating effect are all of great importance. The heat-affected zone (HAZ) (heat diffusion length (L_{therm}): the distance where the heat flux value will decrease to 1/e from the initial value) and the optical penetration depth (L_{opt}) are shown in Equations (3.9) and (3.10)[158]:

$$L_{opt} = \frac{1}{\alpha} \tag{3.9}$$

$$L_{therm} = 2\sqrt{D\tau_p} \tag{3.10}$$

Where D is the thermal diffusivity and τ_p is the pulse duration.

As discussed, the light absorption does not lead to direct heat. The extra energy will be distributed inside the material electronic states (bound electrons), the kinetic energy of free carriers and its interaction with the lattice (absorption and creation of phonons). This energy will be transformed into heat according to different processes and consequences:

- Collisions with electrons leading to random motion in space and in time of femtosecond scale towards the thermal equilibrium.
- Energy transformation to the lattice at an overall energy relaxation time of picosecond in most materials.
- Heat distributes from hot to a cool area, see Chapter 5.
- The energy gap reduces with temperature.
- Metallization leading to massive growth in R.

Heating of the material could involve melting which modifies the material, especially if it is combined by rapid solidification. Doping, surface alloying, recrystallization and

metallization would require melting. Temperature calculations (T) of an irradiated laser material discussed in detail in Chapter 5

In general, the primary process in semiconductors will be electron-hole formation and hole will act as an electron but with a positive charge. The absorption rises, leading to more heating, which will produce more free carriers and increasing the absorption. In a compound semiconductor, electronic structure and the bond's strength play an essential role in the ablation process[159].

3.3.1 **Surface Melting (Heterogeneous Melting)**

Fusion is the phase changing of the material to liquid. It is an essential part of laser processing that contributes to applications such as marking, welding and doping. Laser parameters need to be controlled to achieve the surface melting without building stress to avoid cracking and warping.

When uniform irradiation applied at a semi-infinite sample, the surface temperature increases and the irradiated laser energy will be spent on heating and melting (which require enthalpy). It will be increased after melting to a certain depth, and the maximum surface temperature will be reached at the laser pulse duration. After that, the cooling process and solidification take place. Clearly, the exact temporal behaviour of surface temperature depends on the material under consideration, on the intensity, duration and shape of the laser pulse, on convective flows and, if relevant, on the type of the ambient medium[158]. The calculation of the total spatial and temporal behaviours of the temperature distribution within the liquid and the solid material can be obtained only numerically.

Melting duration could be calculated from Equations (3.11) and (3.12) when the optical penetration depth is much larger than thermal penetration depth $l_{opt} >> l_{therm}$, and when $l_{opt} << l_{therm}$, respectively[158].

$$\tau_m \approx \frac{\Delta T_m K l_{opt}}{DI} \tag{3.11}$$

$$\tau_m \approx \frac{1}{D}\left(\frac{\Delta T_m K}{I}\right)^2 \tag{3.12}$$

Where $\Delta T = T_m - T(\infty)$ T_m is the melting temperature, K is the thermal conductivity, and I is the laser intensity[158]. Typically, at the end of the pulse duration, solidification will take place at the liquid-solid interface, beginning from the surface downward.

3.3.2 Enthalpy Model of Melting

To investigate the melting of a material by a laser, it is essential to understand the melting point (the heat required to reach melting) and the melting enthalpy. When the laser processing is thermal, the temperature and the total enthalpy could interrupt the system. Enthalpy is relevant if phase changes or chemical reactions occur[158].

For Semiconductors, the melting enthalpy is high, making it hard to melt. Semiconductors, when melted, solidify at a slower rate when compared to metals.

Unstable melting will dominate because of the liquid semiconductor. Liquid semiconductors form due to the high latent heat and high reflectivity (this happens during visible or infrared laser irradiation with relatively long pulse duration). “In reality, the temperature at the liquid–solid interface should exceed the equilibrium melting temperature (overheating), while in the case of solidification we should have (undercooling)”[158].

Furthermore, the melt temperature is dependant on the local pressure, and the melt of crystalline materials depends on the number of extrinsic and intrinsic defects. Defects are weakening the atomic bonds[160,161]. Quantifying an exact melt temperature is difficult, and a so-called *mushy* region is sometimes used when analysing enthalpy-temperature data[162]. Due to these challenges, a well defined free or moving boundary makes the Stefan problem “Within the frame of the Stefan problem, it is assumed that the temperature at the liquid–solid interface is continuous and equal to the melting temperature. The Stefan

model is often employed to describe melting and solidification in cases where the interface velocities are very small compared to the sound velocity, so that overheating (undercooling) at the liquid–solid interface can be ignored. From a physical point of view, this model is invalid, because it assumes that the phase transition takes place instantaneously"[158] and its associated Neuman solution less justified "Exact solutions of the Stefan problem can be found only in special cases; among those are the Neumann solutions" [158]. The Stefan statement is perhaps more appropriate to slow heat driven kinetics, for example, recrystallising of a melt phase. The conservation of energy in terms of an enthalpy model is an alternative method to understand temperature changes in materials undergoing phase changes with ill-defined moving interfaces[162]. In other words, one can solve the heat equation for the solid and liquid phase and include the heat of melting into the boundary condition for the moving interface. Alternatively, one can solve the (single) heat equation for the whole temperature region and include the heat of melting in $cp(T)$[158].This method overcomes the need to track a moving interface. For high-intensity laser pulses and focused laser-beam irradiation, liquid-phase expulsion and vaporization become important. Here, the deformation of the surface (deep-penetration melting, formation of droplets, etc.) must be taken into account. One assumes the enthalpy as an independent variable with temperature, and the rate of change of enthalpy can be written as[158]:

$$\frac{\partial \Delta H(T)}{\partial t} = V\frac{\partial \Delta H}{\partial z} + \frac{\partial}{\partial z}\left(K(T)\frac{\partial T}{\partial z}\right) - Q_{ab}(z,t) \tag{3.13}$$

Where H is the enthalpy per unit volume, the surface recession velocity can be calculated using,$V = \eta \dot{m_v}/\rho_l$, where, η is the ratio of the number of species escaping the surface to the number of species evaporating (neglecting re-condensation), $\dot{m_v}$is the mass flux of vapour evaporated from the liquid surface[158] and ρ_l is the density of the liquid, respectively. $K(T)$ is the thermal conductivity and $Q_{ab}(z,t)$ represent the heat source according to the Beer-Lambert law in equation (3.8).

$$\dot{m}_v(T_o) = P_o(T_o)\left(\frac{m_a}{2\pi k_B T_o}\right)^{1/2} \tag{3.14}$$

Where m_a is the atomic mass; k_B is Boltzmann's constant T_o is the initial temperature. The saturation pressure can be calculated from the Clausius-Clapeyron Equation (3.15) shown below.

$$P_o(T_o) = P_\infty \exp\left(\frac{L_v}{R_v T_2}\left(1 - \frac{T_2}{T_o}\right)\right) \tag{3.15}$$

Where P_∞ is the pressure, L_v is the latent heat of vaporisation, R_v is the specific gas constant.

3.3.3 Laser Ablation and Material Removal

Laser ablation describes the interaction between the laser beam and the material surface to remove material from the surface. We could define it as the process conducted by a laser to remove material, via melting, evaporation, sublimation and/or explosive phase ejection, from a solid surface. If the laser energy fluence is low, the temperature would be only sufficient for melting and the surface left behind would be smoother. While when higher fluence is applied to the surface, vaporisation occurs with noticeable rougher topography[163]. At high fluences, a plasma is formed slowing down the laser processing.[164]. It also depends on the laser wavelength and pulse duration. A laser irradiation will influence the material thermally and mechanically depending on the electronic states, surface morphology, surface roughness and the density of the defects of the target. Thus, the material temperature will be increased, and expansion takes place, leading to stress building. If the stress were above the damage threshold, the material would suffer plastic deformation or fractures. Stress and temperature will modify the properties of the material[165]. The material will be out of equilibrium and will try to reach a new balance[14]. The ambient environment and the plume or the ejected material during the process should also be considered i.e. “a non-reactive atmosphere may influence the transport of ablated

material, the attenuation of the laser light, and the development of surface instabilities. All of these effects become more pronounced with increasing gas pressure. While, a reactive atmosphere can increase the rate of material removal. This is known as dry etching. Additionally, such an atmosphere can change the physical and chemical properties of the ablated surface, which is the basis of many types of laser-induced surface modifications. A reactive atmosphere can also change the chemical composition of ablated species. This is of particular importance in Pulse Laser Deposition"[158].

3.3.3.1 Laser Ablation Models

Laser ablation can be grouped into different mechanisms named; photochemical, photo-thermal and photophySiCal, or a combination of any of these. It classified according to the laser wavelength, the pulse duration, and their influence on the interaction[166–168]. In the temporal domain, we can assign three-time scales associated with laser ablation mechanism, electron cooling time, τ_e (timescale of ps), lattice heating time, τ_h (timescale ns), and the laser pulse duration, τ_p . Below are the mechanisms of the ablation, as shown in Figure 3.3 :

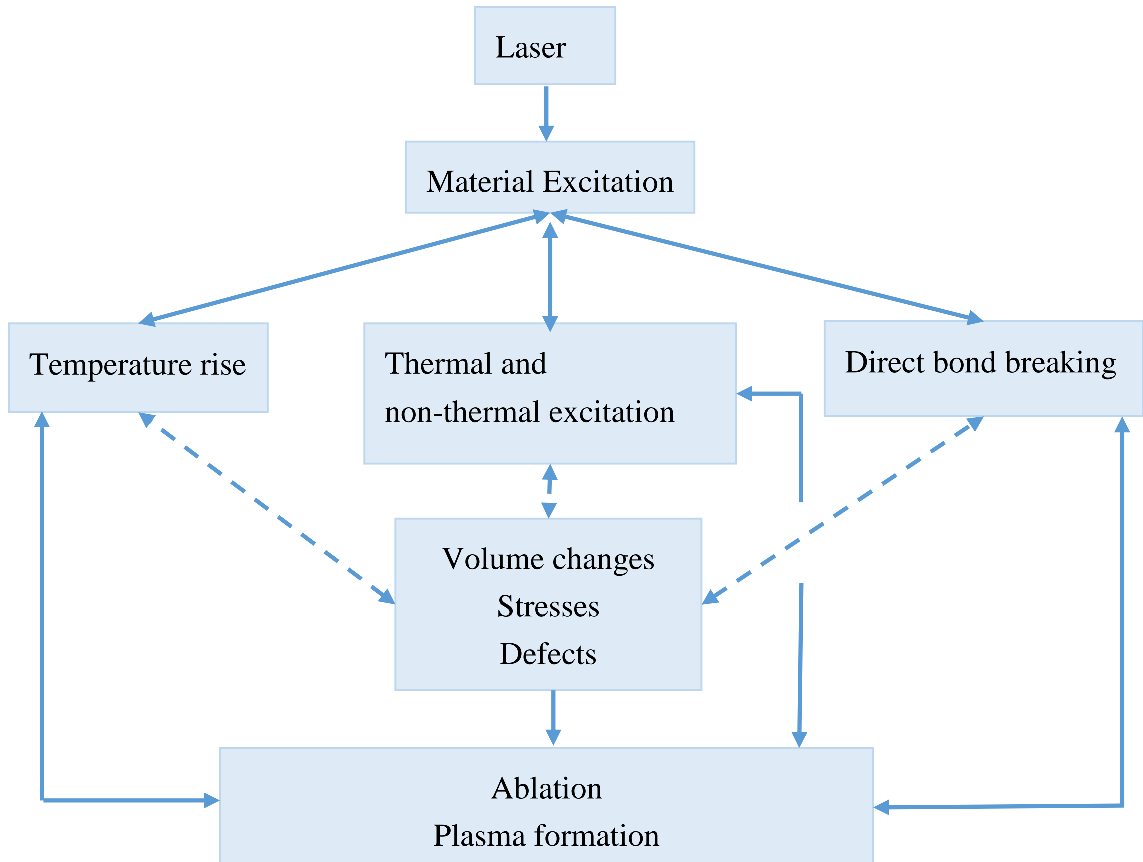

Figure 3.3: Different interaction and mechanisms involved in Pulse laser ablation. Ablation can be based on thermal activation only (left path), on direct bond breaking (photo-chemical ablation; right path), or on a combination of both (photophysical ablation; intermediate path)[158].

a) Photo-thermal processes

In general, this process is associated with longer wavelengths, for example, IR lasers. It utilises a laser beam as a heating source to induce melting or vaporisation. To explain this mechanism, the diffusion of the laser energy will be dominated by the "thermal relaxation time" τ_T and the inverse rate of excitation or the initial step (whichever smaller) τ_R . When $\tau_T \ll \tau_R$ the mechanism of excitation will be dealt with as a heating source. However, it is not the same procedure as a common heat source. This process is localised spatially and temporally reaching a very high temperature and large heating rates up to 10^{15} Ks^{-1}. These high heating rates are faster than the chemical relaxation, and any reaction will be out of equilibrium. Not to forgot the selectivity of certain particles as in

compounds[158]. To summarise, when the thermal relaxation time, τ_T, is very short, laser ablation simplified to be a thermal process. This is related Infrared and visible lasers in addition to UV laser processing with nanosecond and longer pulses. When melting takes place, thermal evaporation will dominate, in most cases. However, the processing gets more complicated if stress, phase expulsion or ejection of melted droplets participate to the processing. For a single uniform pulse the model can be represented as below:[158]

$$F_{thr} = \frac{\Delta H(T)}{A}\left((D(T)\tau_p)^{\frac{1}{2}} + L_{opt}\right) \quad (3.16)$$

Where F_{thr} is the ablation fluence, $\Delta H(T)$ is the enthalby atmelting ppoint, A is the absorptivity, $D(T)$ is the temperature dependent thermal diffusivity, τ_p is the laser pulse duration and L_{opt} is the optical penetration depth. This model gives a good approximation for fluences $F \approx F_{thr}$.

b) Photochemical effects (Photolytic):

The photochemical process typically associated with non-thermal light-matter interactions utilising relatively high photon energies and short wavelengths. It is a straight interaction with the electronic structure to initiate a chemical reaction between the excited particles and with the surface. It takes place when $\tau_T \geq \tau_R$. In this case, τ_R represent the charge (electron) transfer time. The process does not involve any temperature rise when it is entirely photochemical. High-energy lasers are suitable for this type of processing and also the lasers with short pulse duration[158]. Table 3-1 shows the lasers used in this work with their photon energy.

Table 3-1: Photon source and their energy in eV.

Laser	*Wavelength (nm)*	*Frequency (THz)*	*Energy (eV)*
ArF	193	1553.328	6.42
CO_2	10600	28.28	0.1169

Furthermore, plasma will be formed when high energy light absorbed by the particles creating an enormous number of electrons in the conduction band.

Two conditions must be applied to start the photochemical process in semiconductors such as: $n_{photon} \geq n_{atomic}$ and $h\nu \geq E_{gap}$. Where n_{photon} is the photon density, n_{atomic} is the material atomic density, h is Plank constant, and v is photon frequency, this could be expressed as in Equation (3.17) :

$$\frac{E}{V} = h\nu n_{photon} \geq h\nu n_{atomic} \tag{3.17}$$

Where E is the absorbed energy per pulse and V is the volume of the irradiated target, and the ablation fluence could be written as in Equation (3.18)[169].

$$F_{thr} = \left(\frac{E}{S}\right)_{\min} = \frac{h\nu n}{\alpha\eta(1-R)} \tag{3.18}$$

R the reflection coefficient, α the absorption coefficient, n the number of molecular bonds which must be broken per unit volume and η is the quantum yield for chain scission.

c) Photo-physical effects

Photophysical ablation is the process where thermal and non-thermal mechanisms take part to the overall ablation rate i.e. a material in which the lifetime of electronically excited species or of broken bonds is so long that species desorb from the surface before the total excitation energy is dissipated into heat. The desorption process enhances by the temperature rise. Thermally or non-thermally generated defects, stresses, and volume changes may again influence the overall process. Thermal ablation and photochemical ablation can be considered as limiting cases of photophysical mechanisms. It is a second step physical process of the produced excited species escaping the surface. Therefore, it has a straight impact on the ablation-etching rate. The ablation process may be linked with a combination of bond session and thermal degradation[155,158].

3.3.3.2 Laser Ablation Threshold

Ablation threshold is the minimum energy fluence that will affect the target surface and remove at least a monolayer. Therefore, below the threshold, there is no significant ablation, but surface modification and emission can take place. While for higher fluences, the etching rate might tend to saturate[167,170–172]

Ablation rate could be calculated by Equation (3.19)[158]:

$$D_{EF} = \alpha^{-1} \ln\left(\frac{EF}{EF_{thr}}\right) \tag{3.19}$$

Where D_{EF} is the ablation rate, and EF_{thr} is the threshold energy fluence. It is worth mentioning that Equation (3.19) is general and does not depend on the ablation mechanism.

3.3.4 Laser Vaporisation

Evaluating the amount of material transported away from a laser irradiated site can be approached using a surface vaporisation model. The above is justified as opposed to volumetric evaporation when we have a powerful absorption such as the 193 nm UV radiation with the 4H-SiC, $\alpha^{-1} \sim 7$ nm. We estimate the flux of species transported away from the sample surface using the Hertz-Knudson (H-K) and Clausius-Clapeyron (C-C) equations[173]. We assume clasSiCal kinetic theory (Maxwell Boltzmann) to calculate the flux of species leaving the surface.

$$j_{ev} = n_l \left(\frac{K_B T_l}{2\pi m_a}\right)^{1/2} \exp\left(\frac{-L_v}{K_B T_l}\right) - \theta_s n_v \left(\frac{K_B T_v}{2\pi m_a}\right)^{1/2} \tag{3.20}$$

Where n_l, represents the atomic density near surface, T_l, is the temperature of the surface, T_v is the evaporation temperature and θ_s is the sticking coefficient. The sticking coefficient represents the fraction of species returning to the liquid vapour interface as the species changes phase from their initial liquid or vapour state. Pinning down a value for the sticking coefficient is non-trivial. Strictly speaking, the H-K equation is valid only under equilibrium conditions but is frequently used for near-equilibrium conditions[174]. It has been debated whether one should assign two coefficients', that is, evaporation and condensation (mass accommodation) coefficients. However, quantifying the coupling mechanism between evaporating and condensing species is non-trivial. In this work, we simplify the analysis and use a single sticking coefficient for the entrapment of species returning to the melt of $\theta_s \sim 20\%$[175]. Acknowledging these simplifications, we estimate the depth of material removed as a result of absorption of UV laser radiation.

$$\delta_{ev} = \int_0^\infty j_{ev}(t) \frac{m_a}{\rho} dt \tag{3.21}$$

Mass transported away from irradiated materials at a known laser fluence is essential in laser processing and especially the depth of an ablation per laser pulse.

3.4 Nanosecond and Microsecond Pulsed Laser Ablation

When a nanosecond laser pulse is applied, there will be enough time for the photons to be absorbed by the electrons and then the energy transferred to the material lattice. The process will then reach thermal equilibrium. Moreover, the nanoseconds regime will be long enough to accomplish the melting of the surface not only at the irradiated site but could reach the surrounding area, see Equations (3.9) and (3.10) forming the HAZ, micro size cracks, shock waves and debris[176]. Thus, in a nanosecond laser ablation, there will be changes in the material's optical properties in addition to the interaction and relaxation modes during and after the pulse duration, and that is why a vast number of weak bonds will be produced. These bonds will be broken even with a moderate laser energy fluence [155].

The output wavelengths of the used excimer lasers vary from 193 nm. Excimer lasers can be operated only in the pulsed regime. The pulse duration is in the range of several tens of nanoseconds, and the pulse energy is on the order of hundreds of millijoules[177].

Hence, an excimer laser operates differently from CO_2 lasers. It will ablate the material through high spatial resolution and instant decomposition of the material bonds because of the photolytic process (decompose of bonds caused by absorption of photons) and pyrolytic (decompose of bonds caused by a thermal effect). Besides, processing material using Excimer lasers will minimise the thermal damage and the heat-affected zone around the irradiated site depending on the thermal diffusivity of the irradiated material “Ultraviolet laser sources can initiate both photochemical and photo- thermal effects in condensed media”[14].

These advantages are related to the parameters of excimer laser such as their short wavelengths, high energy, and ns pulse duration. In targets with covalent bonds such as a polymer or organic, photo-lytic process takes place, while this process is partial in ionic bond’s material[73,178]. While, Pyrolytic process takes place in other materials.

3.5 Characterisation Methods

3.5.1 Raman Spectroscopy

Raman spectroscopy presents a non-contact tool to characterise materials. It can be used to identify materials, analyse the structure of the material and its bonding, so all the rotational, vibrational and electronic information could be revealed.

It uses the inelastic scattering of an incident single-frequency laser wavelength. The scattered light will be in two groups as a Rayleigh scattering or Raman scattering. Raman scattering occurs when there is a collision between the incident photon and the molecule. As a result of the collision the vibrational or rotational energy of the molecule is changed by an amount of energy[179]. If the energy transferred from the incident photon to the molecule when the material absorbs the irradiation, then the scattered light will have less energy (Stokes scattering). While, if the energy transferred from the molecule to the scattered photon, the material lost energy, the scattered light will have more energy so

this is anti-stokes scattering. The stokes is dominant due to the relaxed population in the ground vibration state at room temperature. See Figure 3.4.

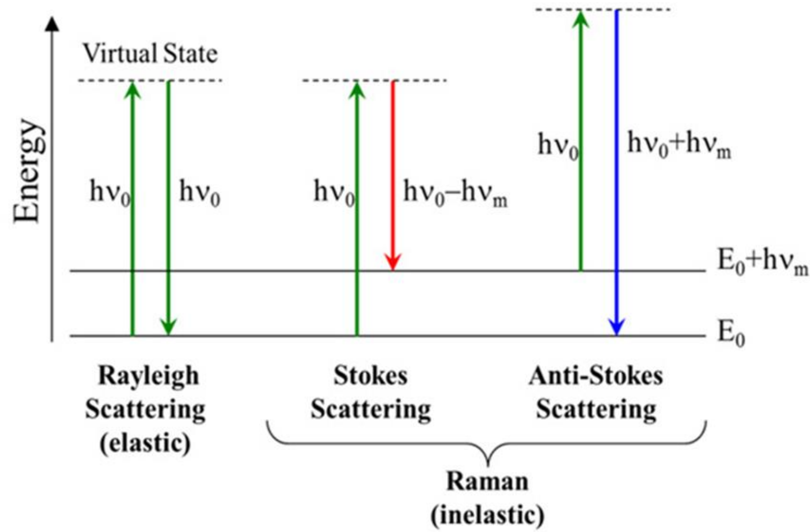

Figure 3.4: Jablonski Diagram Representing Quantum Energy Transitions for Rayleigh and Raman Scattering[180].

Raman shift (cm^{-1}) is determined by Equation (3.1)[179],

$$Raman \quad Shift = \frac{10^7}{\lambda_{excitation}} - \frac{10^7}{\lambda_{scattered}} \tag{3.22}$$

Where $\lambda_{excitation}$, $\lambda_{scattered}$ are the wavelengths (nm) of the incident light and scattered light, respectively.

3.5.2 Carrier Transport in Semiconductors

A simple model of electrical resistivity can be defined as how the material resist the current flow. The electrical conductivity represents the inverse of the resistivity, $\sigma = 1/\rho_r$ where σ is the conductivity and ρ_r is the resistivity.

For a homogenous isotropic material, resistivity, according to Ohm's law will be $\vec{E}_{field} = \rho_r \vec{J}$ where E_{field} is the electric field and J is the current density. For a slab of 3D

material, see Figure 3.5, the electric field will be written as $E = \frac{V_o}{l}$ and $J = \frac{I_c}{A}$ from the above, voltage (V_o), resistance (R_s) and electrical current (I_c) can be written as in equations below, respectively.

$$V_o = \frac{I_c \rho_r l}{A} \tag{3.23}$$

$$R_s = \frac{\rho_r l}{A} \tag{3.24}$$

$$I_c = \frac{V_o}{R_s} \tag{3.25}$$

Resistance is dependent on the dimension while the resistivity is independent of the geometry of the sample. All the above represented the simple model while resistivity in the microscopic model would be[181]:

$$\rho_r = \frac{m_e}{ne^2 \tau} \tag{3.26}$$

Where m_e is the mass of an electron, n is the number of electrons per volume e is the electric charge and τ is the average time of free path between the electrons and atoms [181].

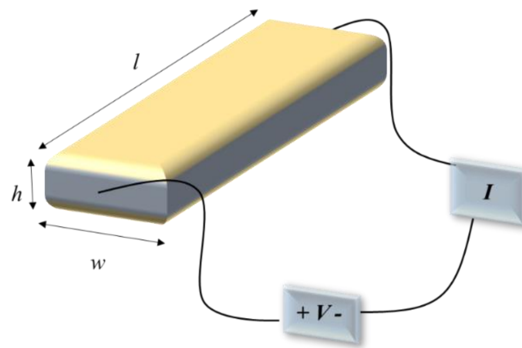

Figure 3.5: two-point method to measure the resistivity of slab shape material

3.5.3 **Sheet Resistance Measurements**

Sheet resistance is used when we need to study the resistivity of a thin film, preferably in a square shape so we can apply Equation (3.27)[181];

$$\rho_s = \frac{V_o h_i}{I_c} \tag{3.27}$$

Where ρ_s is the sample sheet resistivity, V represents the voltage, h_i the thickness of the sample, and I_c is the current flowing through the sample.

However, sheet resistivity is independent of the size of the square film. Hence, it is more suitable to compare different materials.

Chapter 4 **Methodology**

4.1 Methodology

This chapter explains the experimental work of this thesis.

4.2 Material

Different sizes and specification of single and double polished 4H-SiC wafers were used in this work. For the surface studies and the decomposition process, n-type semiconducting 4H:SiC (0001) ± 0.5 wafers with 10 mm^2 diameters and 330 ± 25 µm thick and Micro Pipe Density < 7/cm^2 was used. These samples were made by Xiamen. For the electrical characterisation processing, we have used semi-insulated 4H:SiC with a resistivity of 10^7 and 10^5 Ω.cm. Polished 2 inches' vanadium (V) doping and n doped 4H:SiC <0001> were used to conduct these experiments. The wafer thickness was 330 ± 25 µm. To make the maximum of the sample, it was cut into smaller samples of 10×10 mm^2 area. These samples were double face polished with the roughness of < 0.5 nm.

4.2.1 **Preparation Process**

4H-SiC wafers were provided with different sizes ranging from 10 mm^2 square pieces to 50.8 mm diameter wafer. For the 50.8 mm diameter samples, wafers were diced into ~10 × 10 mm samples using an 800 nm wavelength Ti-sapphire laser of 155 femtosecond pulse duration and peak power of 4.83 GW. This powerful laser was applied to overcome the hardness of the SiC material. The Ti-sapphire laser was used to cut the sample directly or dice it and then it was cut.

Due to the cutting process and the redepositing of debris on the surface, the samples needed to be cleaned before any further processing. Four steps cleaning process carried out.

The samples were immersed for ten minutes in four separate solutions inside an ultrasonic bath; Decan 90, acetone, isopropyl and distilled water, in the respective order. Finally, the samples were dried using a Nitrogen gun.

4.3 Laser Micromachining of SiC and Setup

Different set-ups were used depending on the laser system. We have conducted work with both ArF Excimer laser of 193 nm wavelength and 10.6 µm CO_2 laser. Another classification of the processing is whether we conducted a static processing or scanning irradiation using both systems. These experiments were repeated to investigate the reproducibility of the processing.

4.3.1 **ArF Excimer Laser Processing**

Laser processing of 4H:SiC surface was carried out in an ambient environment using a 193 nm ArF excimer laser (Lambda Physik, LPF202, retrofitted rear reflector and output coupler). The experimental set-up for the laser system is shown in Figure 4.1 and Figure 4.2. Laser pulse duration, 11.5 ns full-width-half-maximum (FWHM) at a charging voltage of 26 kV, was measured using a LeCroy WP960 oscilloscope. Most experiments were carried out using a pulse repetition frequency ranging from 1-20 Hz. The beam was steered using dielectric mirrors that were optimised for operation at 45 degrees. The laser fluence was controlled using a variable angle dual plate attenuator (ML2110-Metrolux-Germany). A stainless-steel object aperture (produced by photofabrication) was imaged onto the sample surface using an MgF_2 bi-convex lens having a radius of curvature 45.9 mm. The laser fluence was increased using a 1/10 magnification. Laser energy was measured after the lens using a Joulemeter (Molectron). For the pulse temporal shape measurement, a fast photodiode (Hamamatsu, S7911) connected to an oscilloscope was used. For the static ablation processing, experiments were conducted using a circular, square and triangle object apertures with different sizes

ranging from 1 mm diameter for circles and 1 mm length for the square to the aperture of 4 mm of a rectangle shape. The site then reduced to 10% of the aperture to produce sites of micrometre scale on the sample. A set of non-static experiments were carried out by translating the sample relative to a stationary laser beam using high-resolution motion control stages (Aerotech, fibre align). A different mask was also utilised to produce a channel of different sizes as 1.5 mm length and 500 μm diameter.

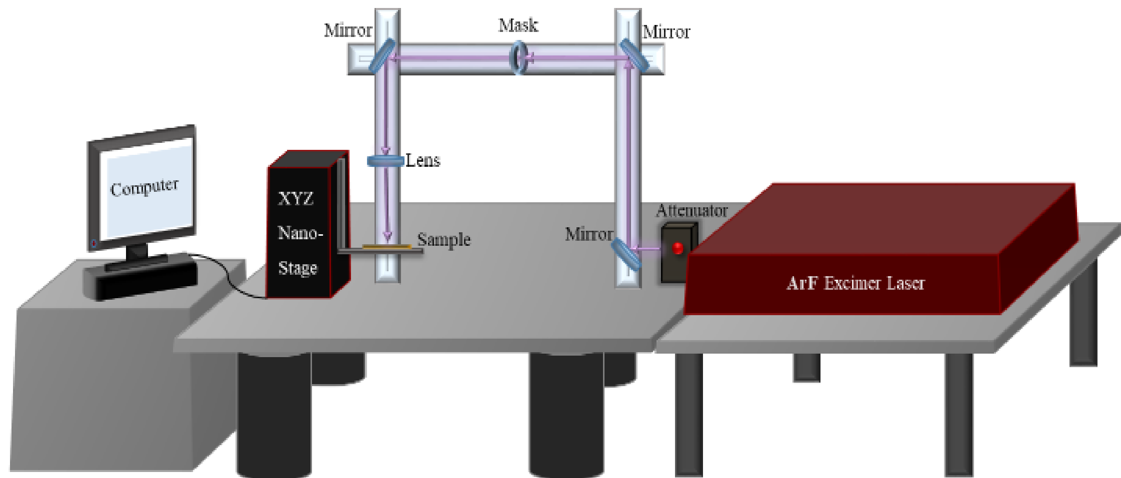

Figure 4.1: Schematic of the 193 nm ArF excimer laser system. Samples were translated using Aerotech (fibre align) motion control stages relative to a stationary beam. The laser imaged using different shapes of masks.

4.3.1.1 Laser Beam Delivery System

The delivery system of the ArF laser (Lambda Physik LPF 202), the maximum energy of 285 mJ and maximum repetition rate of 20 Hz, has been held on three construction rails (Thorlabs) one of 750 mm and 95 mm and the other two are 2000 mm and 66 mm dimensions. These were used to hold the optical component to steer the laser from the aperture to the samples. Three of 25 mm diameter dielectric coated fused silica mirrors (Edmund Co. and CVI Co.) were employed. The laser beam was then passing a photomask with different shapes to image them on the SiC surface using a plano-convex fused silica lens (Newport Co.) of 81.8 mm focal length.

The static process will be discussed later, including the ablation threshold measurements. While the second set of experiments used scanning irradiation ablation of SiC. It has been irradiated with different energy fluences ranging from 0.3 to 5 Jcm^{-2}. In addition, different

travelling speed for each energy fluence was conducted. The magnification and PRR were 10 and 10 Hz, respectively for most procedures to guarantee the high fluence. The scanned processing meant that the ablation site has varying overlapping pulses. That was employed to study its effect on the sample and the behaviour of the channel. Therefore, the chosen scanning velocity was calculated as in Equation (4.1):

Figure 4.2: photograph of 193 nm laser system.

$$V_{stage} = \frac{F_{prr} w_c}{N_p} \tag{4.1}$$

Where F_{prr} is pulse repetition rate, w_c is the ablation channel width or diameter and N_p number of pulses.

The samples were characterised by employing various instruments such as; White Light Interferometer, optical microscope, and Horiba Raman spectroscopy.

4.3.1.2 Ablation Threshold

Ablation threshold of SiC at 193 nm wavelength laser was measured experimentally. In addition to the characterisation of the samples after stationary processing. The static set-up was used to carry out the etch rate of the 200 µm site produced using a 2 mm circular

aperture mask. The shape has been fixed along with all the laser parameters except the energy fluence, which was varied by the attenuator. The corresponding energy fluences were in the range of 0.3 Jcm^{-2} and 5 Jcm^{-2}. Each site was irradiated with 100 pulses. Ablation etching rates profiles were obtained using White Light Interferometer (WLI) (WYCO NT1100 from VEECO). Furthermore, an Optical microscope (LEICA DMLM) was employed to examine the surface damage. The depth per pulse was measured by dividing the total depth measured by the optical profiling system over the number of pulses (100).

4.3.2 **CO_2 Laser Processing**

High power 10.6 µm CO_2 laser (Rofin, OEM10iX), manufacturers manual averaged power range rated 5-115 W was employed to irradiate the SiC to study the effect of the IR radiation on the 4H-SiC surfaces. TTL controller (RS422) was used to enable and disable the RF power supply signal. This allows the pulse duration and the frequency to be variable with pulse width ranges between 2-400 µs and a maximum frequency of 130 kHz for 60% Duty cycle. The pulse was produced by a pulse generator and displayed on a 70 MHz oscilloscope (Keysight DSOX2002A). The processing was carried out in the atmosphere, as shown in Figure 4.3 and under a low-pressure environment. By controlling both the pulse width and the pulse repetition rate, we had the chance to choose the wanted duty cycle to ablate the SiC. A calibration processing was conducted to calibrate the output laser power with the input pulse width and the frequency. Both, the pulse duration and the frequency were controlled by a pulse generator as an input for the TTL to trigger the laser. This system was more challenging than the UV system due to its properties of invisibility and to its high output power.

Most experiments were carried out using a pulse repetition frequency ranging from 1-1000 Hz. The beam was steered using silicon mirrors coated with Supermax coating provided by ULO optics. They were optimised for operation at 45 degrees. The laser power was controlled by controlling either the pulse duration or the pulse repetition rate and/or by using the compact attenuator to get more control over the fluence of the beam. For the pulse duration measurements, it was provided by the manufacturer for all the used FWHM pulse durations here and in Chapter 5.

Laser power was measured by a high threshold damage power meter (COHERENT LabMaster Ultima). Stationary and scanning ablation were also conducted using G-code controlled nano-motion stage (Aerotech).

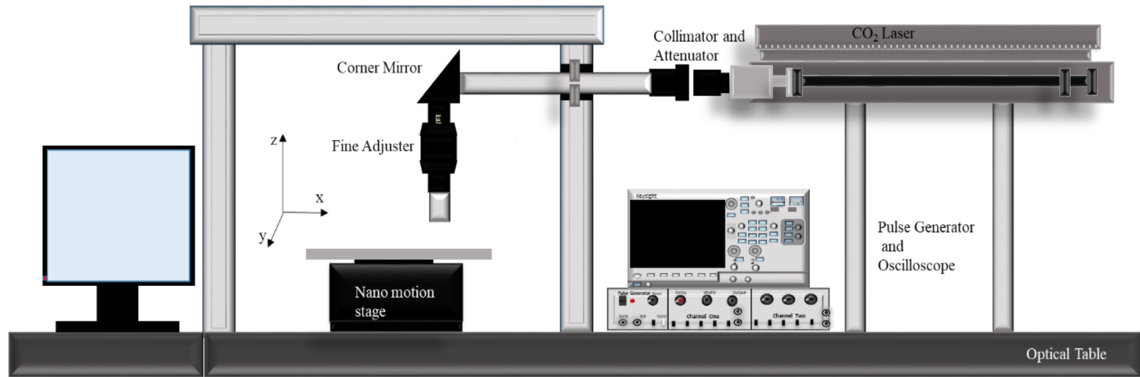

Figure 4.3: Schematic diagram of the experimental CO_2 system set up. It used for the processing of SiC and the ablation threshold measurements.

4.3.2.1 CO_2 Beam Delivery System

Due to the Properties of CO_2 laser, the invisibility and the high power of its output beam, a special delivery system was built around the beam to ensure the safety of the operator. It was built from multiple components of tubes and optical parts, mostly from ULO Optics that is suitable up to 500 W beams. We will describe it from the laser aperture to the sample. The laser aperture was attached to the rest of the system with a specialised tube.

Compact Beam expander of 1.6 magnification was used in reverse as a beam reducer bearing in mind the effect on the laser power and its far-field divergence. We were dealing with tubes of 19 mm inner diameter and according to the relation $D_{out} = mD_{in}$ where m is the magnification.

Manual Attenuator C-MA was used. It based on the principle of Brewster angle of two plates of ZnSe in the V configuration to adjust the beam displacement. The Brewster angle for the ZnSe plate depends on the refractive index as in the relation $\theta_B = \tan^{-1}(n)$ where *n* is the refractive index of the ZnSe plate. Since its two plates then we have four air-ZnSe interfaces, the limited transmittance would be 100% perpendicular polarisation

and 55.33 S polarisation. The transmittance calculated $T = 1 - 0.938\sin^2(\theta_B)$. This works only with linear polarisation beams.

Compact corner mirrors of silicon with Supermax coating. The clear aperture of these blocks is 16.4 mm. These mirrors are compact but controllable, and it is threaded both ways to fit with the other parts. These mirrors steered the laser beam in a different direction to the stage. The ZnSe lens with different focal lengths at the end of the delivery system to focus the laser onto the samples mounted at the nano-motion stage.

Fine focus adjustment provides a 20 mm of fine movement allocated in the z-direction of the laser, by rotating the notched ring. Both ends of the focusing unit have the thread to take the thread inserts. All the mentioned parts were put together using beam tubes, threaded in both ends. It was mostly used for health and safety. All for more security there was an enclosure of Pyrex to contain the CO_2 laser beam. This was also surrounding the Aerotech stage and the sample to prevent any reflected light from the sample surface.

4.3.2.2 Laser Power and Energy Calibrations

Laser average power was measured by COHERENT Labmaster Ultima. The averaged power was calibrated as a function of the laser repetition rate for different pulse durations. The power meter placed on the Aerotech stage and the beam was located on the centre of the power meter head. The measurements repeated and averaged, and it was in the error range of 3%, see Figure 4.4.

Power as a function of the duty cycle was also measured with different pulse widths as seen in Figure 4.5.

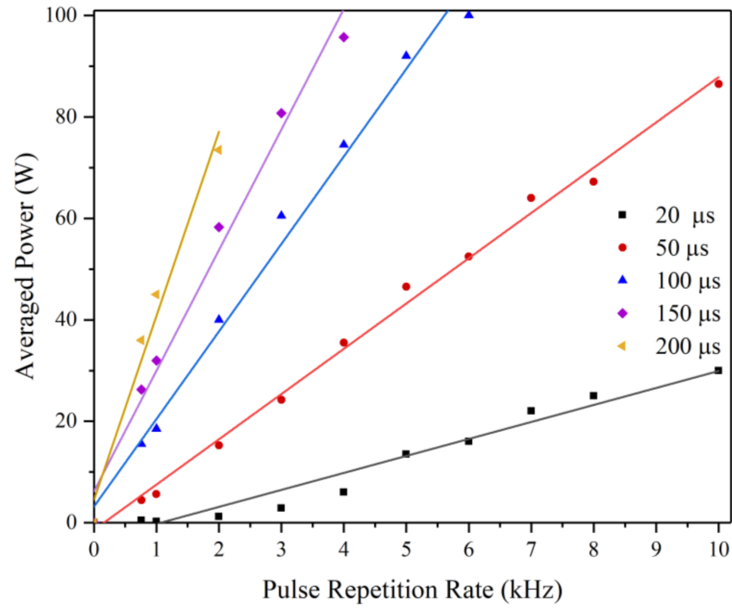

Figure 4.4: The average power of CO_2 laser for different pulse duration as a function of the pulse repetition rate.

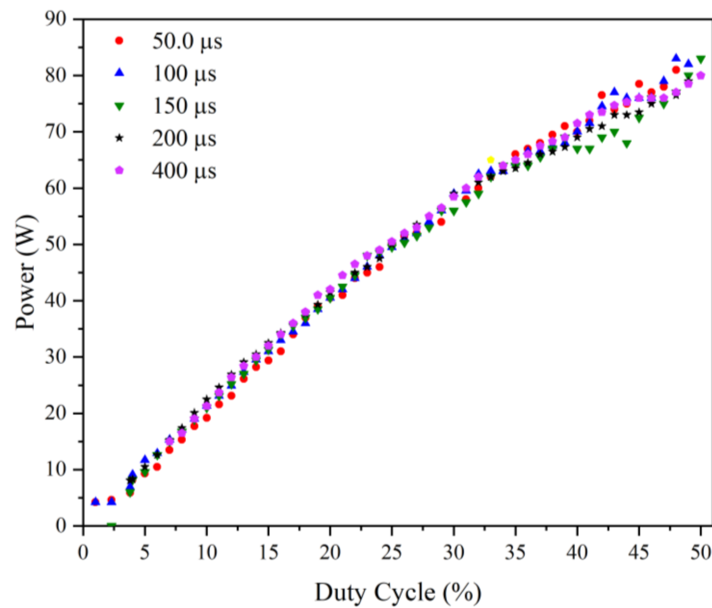

Figure 4.5: Averaged power as a function of the duty cycle controlled by the pulse repetition rate and for different pulse width.

In addition, the averaged power was measured as a function of the attenuator transmission as it can be seen in Figure 4.6.

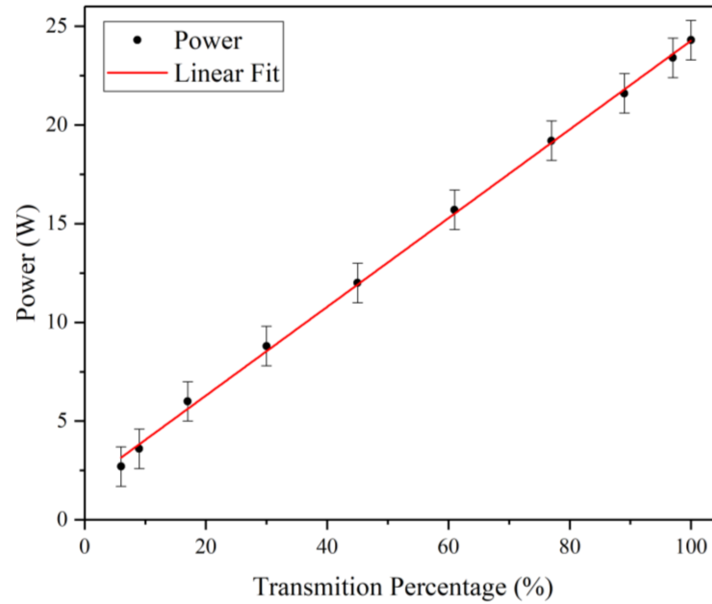

Figure 4.6: Averaged power as a function of the attenuator transmission percentage.

4.3.2.3 Gaussian Ablation Threshold Measurements

The effect of CO_2 laser threshold fluence and the surface modification of SiC was studied. The approach here was using the Gaussian definition: the distribution of the electric field as a function of the radial distance (r).

$$E(r) = E_O \exp\left(-\frac{r^2}{\omega_O}\right) \tag{4.2}$$

Where *E(r)* is the electric field at r distance, E_o is the maximum electric field, and ω_o is the laser spot size radius where the fluence will have the value F_o/e^2. Since the laser, irradiance could be linked to the electric field $I = 1/2\,\varepsilon_o c E_{\max}^2$. Equation (4.2) could be substitute with irradiance in Wcm^{-2}. In our work, the beam was time-averaged, and the Fluence F(r) was a substitute to the irradiance. For a Gaussian spatial beam profile with a $1/e^2$ laser beam radius ω_0 the radial distribution of the laser fluence is presented by:

$$F(r) = F_o \exp\left(-\frac{2r^2}{\omega_o}\right) \tag{4.3}$$

Equation (4.3) can be integrated into 2D to get the pulse energy (E), The peak laser fluence F_o is related to the total pulse energy E according to Equation (4.4), and it can be solved for (r) and $F(r) = F_{Th}$ as in Equations (4.5) Substituting $r=D/2$ and recognizing that the material cannot be ablated for laser fluences lower than the threshold (namely, $D=0$ at the threshold laser fluence, F_o peak $=F_{Th}$), we obtain (4.6) for the diameter (d) because E pulse is the integrated value of the Gaussian profile of laser fluence over the irradiated area with a radius ω_o. In the literature, most studies report the fluence in terms of an average value defined by $F_o^{av} = Epulse/\pi\omega_o$[182].

$$F_o = \frac{2E}{\pi\omega_o^2} \tag{4.4}$$

$$r^2 = \frac{1}{2}\omega_o^2 \ln\frac{F_o}{F_{Th}} \tag{4.5}$$

$$d^2 = 2\omega_o^2 \ln\frac{F_o}{F_{Th}} \tag{4.6}$$

This can be applied experimentally to determine the threshold and the spot size by plotting a graph between the squared of the diameter as a function of the natural logarithm of the pulse energy. The slope will equal $2\omega_o^2$, and the intercept will determine the threshold energy[183–185].

The same experimental set up was used, see Figure 4.3. The pulse repetition rate was set to 20 Hz. The laser was steered using the shown delivery system to finally be collimated by zinc selenide (ZnSe) plano-convex lens of 55 mm focal length. The laser travelled through the centre of the lens to minimise the aberration. The applied laser energy controlled by the ZnSe attenuator. The average power was measured using a power meter

calibrated with the pulse duration and the repetition rate. The samples were placed on the surface bracket attached to the Aerotech stage at the focus region. It was set to ensure the circular shape of the laser spot. Few measurements of the diameters were taken and then averaged. The diameter was then measured using an optical microscope (Leica DML with spot advanced software). The pulse duration was set to 150 μsec with a maximum power of 15 W. The ablation threshold will be discussed in Chapter 7.

4.4 Laser Irradiation under Low Pressure

Some of the SiC irradiation was conducted under controlled atmosphere. The low-pressure chamber was designed and prepared with the technical support of the engineering workshop. The chamber was small to be held on the displacement stages due to its weight limit. The chamber with all the fittings had to be less than 3 Kg. The fittings were designed to be able to use different gases into the system to study the effect of the gas on the surface during the irradiation. The sample placed on the bottom of the chamber and the lens was ensured, using the fine adjustment tube, to focus the laser so on the surface of the samples. It was also fitted with windows of relatively big diameter to be able to conduct the scanning processing of the SiC. A pressure gauge used to measure the pressure inside the chamber. It was also fitted with a connection to the different gas cylinders.

4.5 Characterisation Techniques

4.5.1 **Tauc Plot**

The characterisation process for the un-irradiated SiC was carried out using an optical spectrometry measurement (UV-Vis-NIR) from HORIBA; it was used to calculate the optical energy gap (*Eg*) of SiC by applying Tauc Plot [186]. Which confirmed that our sample is 4H:SiC with an Eg of 3.34 eV. This was carried out by calculating the absorption coefficient (α) as $\alpha = -\ln(T)/t$ Where T is the transmittance and t the SiC thickness. Then the plot utilised between $(\alpha hv)^{1/2}$ and hv where h is Plank constant and v

is the frequency as shown in Figure 4.7. In this plot, the intercept represents the material energy gap.

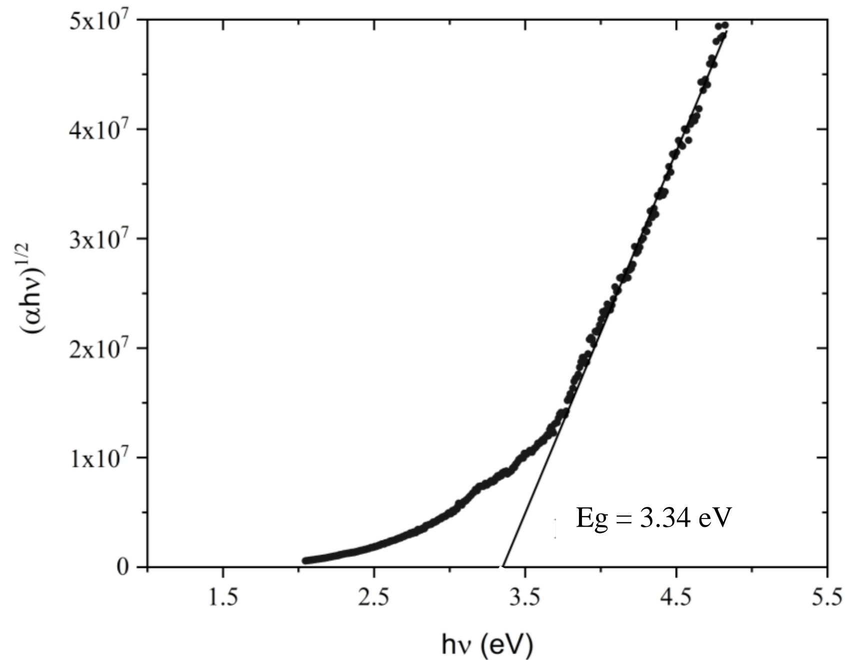

Figure 4.7: Tauc's plots obtained through the applications of standard equations. It indicates an Eg of 3.34 eV

4.5.2 **Surface Imaging**

Many techniques were employed to investigate the surface of SiC before and after irradiation. In addition to the mentioned optical microscope, surface modification was studied using scanning electron microscopy (SEM, Zeiss EVO60) and atomic force microscopy (AFM, Bruker edge). For the SEM, most of the samples were coated with a thin layer of carbon or gold for high-resolution imaging. Some samples were done without coating. The AFM measurements on the surface of the sample were obtained using the tapping mode with unmounted (for use on any AFM) high-quality pyramidal silicon tips (Tespa- V2 of 8 nm radius). These tips are 0.01- 0.025 Ω-cm Antimony (n) doped Si, resonance frequencies of 320 kHz and the backside is coated with Al. A Bruker Software called nanoscope analysis was used to analyse the measurements and produce three-dimensional images, 2D cross section, surface roughness and histogram of distribution.

For depth measurements, DektakXT (Bruker) was employed to provide 1D stylus profile. Furthermore, WLI (WYKO, NT1100) were applied to optically investigate the surface profile using vertical scanning interference (VSI).

4.5.3 Temperature Calculations

For more understanding of the irradiation process of SiC, the surface temperature was calculated by a finite element method (FEM) employed through COMSOL™ version 5.3. A two dimensions (2D) - axis-symmetric geometry was applied. One Dimension 1D numerical and analytical solutions were done to estimate the temperature rises, but it tends to overestimate surface temperature rises value. In 1D geometries, the mesh generator discretizes the domains (intervals) into smaller intervals (or mesh elements). While in 2D geometries, the mesh generator discretizes the domains into *triangular* mesh elements. If the boundary is curved, these elements represent an approximation of the original geometry. A mesh edge must not contain mesh vertices in its interior [187]. The software default solver settings were used for all models for time-dependent heat transfer studies except the time stepping, which was set to strict. Strict used to force the time-stepping method to take steps that end at the times specified in the times field in the general section. The solver takes additional steps in between these times if necessary[187]. This ensures that the solver will calculate at each manually defined individual time interval, as the solver could take any necessary intermediate steps. The used mesh was triangular in the 2D models. The used material properties were temperature-dependent. The geometry was designed as a two-layer system and was implemented as air at the front surface of bulk SiC. The simulations were done by both convection at the surface, and conduction, while the radiation losses were assumed negligible. The experimentally measured laser temporal pulse was used in the simulations. This will be discussed fully in chapter 5.

4.5.4 Raman Spectroscopy

The total area where the laser irradiation took place was monitored by micro-Raman spectroscopy. The site was mounted on the controlled calibrated *XYZ* stage of the microscope, and detailed measurements were performed at selected points superimposed on the profile. The measurements were repeated many times on other samples prepared

in a similar way. The majority of the spectra were collected with the Labram HR800 (Jobin–Yvon) micro-Raman system equipped with a He-Ne laser operating at 632.8 nm. Circumstantially, Raman spectra were recorded with the 784 nm laser line using the same system. Microscope objectives with magnifications 50× were used to focus the light onto ~2 µm spots. Calibration was conducted using Si samples whenever the instrument was started. Another micro-Raman System was used using 532 nm laser excitation. This system was built in the department using Symphony II Horiba charge-coupled device (CCD) cooled with liquid nitrogen to -130 °C. Rayleigh scattering was eliminated using two notch filters. The third Raman System was (LabRAM HR Evolution, Horiba Jobin Yvon, Germany). Two sequential scans were recorded and the average of the measurements plotted. An objective lens of 100×was used, and the excitation was carried using a HeNe laser 632.8 nm and an average power of 12 mW.

To understand how the crystallite sizes of the processed samples have been calculated, the known Raman peaks of graphite and grapheme must be briefed here. Raman spectra showed the G band at 1582 cm^{-1} and the 2D bands at approximately 2700 cm^{-1}. They are the main peaks of graphene. G band originating from the first-order Raman scattering is attributed with the E_2g phonon mode at the centre of Brillouin zone. While the 2D band is originating from second-order Raman. This associates two Brillouin zone boundaries. However, there are other peaks appear as a consequence of defects or structural disorders, D band at 1350 cm^{-1} and sometimes a weak peak at 1620 cm^{-1} and they originate from double resonance process [188,189]. Therefore, the ratio ID/IG was used to calculate the defect concentration of the graphene layers. The crystallite size (L_a) was also evaluated using Tuinstra Koenig Equation (4.7).

$$L_a\left(nm\right) = 2.4\times10^{-10}\lambda\left(\frac{A(D)}{A(G)}\right)^{-1} \tag{4.7}$$

Where L_a is the crystallite size, λ is the laser excitation wavelength, A(D)/A(G) is the relative integrated intensity (area) ratio of the D and G bands.

The integrated area ratio of A(D)/A(G) for D and G bands and the L_a crystallite size were calculated.

4.5.5 **Current-Voltage I-V Measurements**

Polished 2 inches Semi-insulating vanadium (V) doped and n-doped 4H-SiC were employed to conduct the I-V experiments. The wafer thickness is 330±25 μm. The processing of the SiC was carried out by 193 nm Excimer laser in the ambient atmosphere. Channels were produced through SiC samples of 10 mm^2 areas. The laser pulse duration (FWHM) was 11.5 ns at charging volts of 26 kV and a pulse repetition rate of 5 Hz. The laser fluence was increased by a 1/10 magnification. SiC channels were also produced using CO_2 laser of 10.6 μm with different laser power, sample travelling speed and pulse durations.

For the 193 nm laser, the main corresponding energy fluence was 1.56 Jcm^{-2}. However, different irradiation conditions were applied, including changing the fluence and the SiC travel speed. Electrical measurements were carried out using a fully motorised probe station attached to an Agilent B2912A source-measure unit. The probe station was used in a two-probe configuration with tungsten tips of 20 μm radius and fully triaxle cabling. The system series resistance (~3-4 Ohm) was negligible as compared to the resistance of the devices under test (in the order of kilo-ohms) hence the two-probe approach. The resistance of each track on the sample was measured by keeping one probe tip fixed at one end of the track, and moving the other probe at regular intervals of ~1 mm, starting from ~1 mm away and recording the current-voltage (I-V) characteristic at each of these positions, see Figure 4.8. The I-V measurements consisted in sweeping the voltage from 0 V bias up to 1 V at 0.1 V steps recording the current passing through the track. The accurate positioning of the probe tips and the measurements of the tips distances was achieved through a calibrated microscope with a ~50x magnification, and the estimated maximum error on the distances between the two probe tips on a track is less than 0.1 mm. For each track, this process was done at least in 5 locations. The above approach generated a resistance value for each track (by fitting the I-V characteristic) at each location along the track and the resistance vs track length curve. Ideally, a line, that was used to estimate the resistance per unit length of the track (slope) and the contact resistance between the tips and the SiC track (intercept). The former was consistent in the order of 2-2.5 kΩ/mm while the latter was of the order of 1 kΩ. In addition, Raman (Horiba/Germany) measurements were done on the irradiated channels.

Other I-V measurements set up were used. It consists of a probe station equipped with HP4140B source meter unit. The measurements were done at room temperature. With a metal contact at the edges of the irradiated channels. The I-V data were collected using a series programmed from -1 to 1 V.

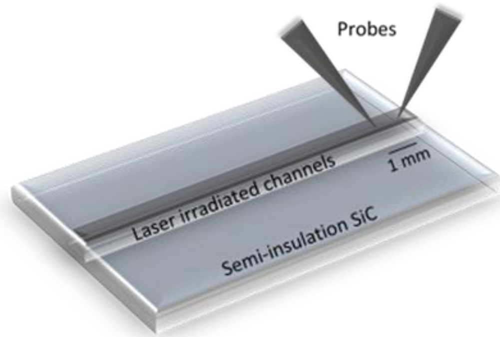

Figure 4.8: Two probe I-V measurements on graphitic channel written directly on 4H:SiC. The schematic shows the probe positioning on the irradiated channels of the produced channels and the change of the space between the tips.

Chapter 5 Theoretical Modelling of Laser Heat Transfer

5.1 Introduction

This chapter focuses on the use of a laser as a heating source. The theory is first explored. Analytical and numerical modelling then was performed.

5.2 Heat Transfer Theory

Heat is thermal energy that can transfer, in different ways, from one point to another within a body or a system. Different mechanisms can be used to interpret heat transfer, such as thermal conduction, thermal convection, thermal radiation, and phase change [190].

5.2.1 Thermal Conduction

Thermal conduction is the heat diffusion of molecules, atoms and electrons, transferring the heat due to their movements and colliding with one another. As temperature is directly related to the kinetic energy of a system this results in a change in the temperature distribution. For solids, the thermal conductivity depends on the electrical carriers (e or h), lattice vibration and other waves. The heat conduction in one dimension can be represented by Fourier's law as in Equation (5.1).

$$q = -K \frac{dT}{dx} \tag{5.1}$$

Where q is the heat flux normal to the cross-sectional area, K is the thermal conductivity and T is the temperature[190]. According to Incropera[190], in homogeneous solid an energy conservation applied. In three-dimensions, heat flux will be considered through each plane direction *dx, dy* and *dz* with the area see Figure 5.1.

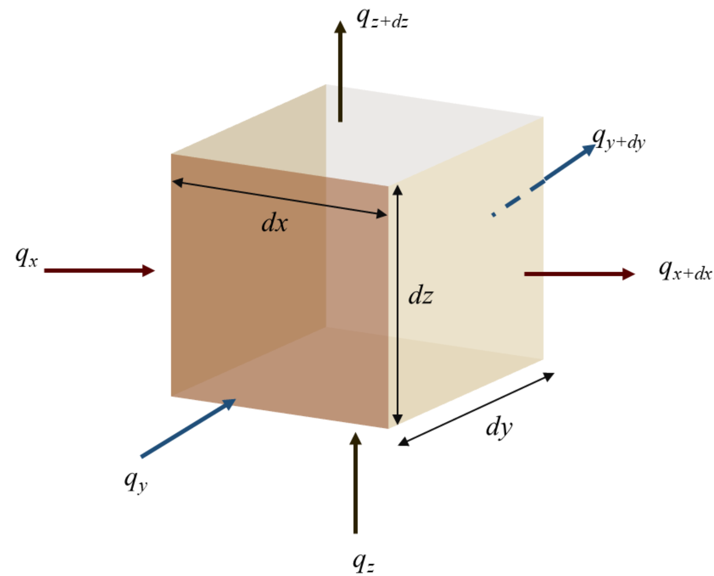

Figure 5.1: Total heat flux toward and out of the volume dV=dxdydz

First, the heat rate defined in indefinitely small volume:

$$dV = dxdydz \tag{5.2}$$

The outward conduction heat rate will be expressed in terms of the opposite surfaces employing Taylor expansion without the higher orders. Meaning, the heat transfer rate q in x-direction equals the heat rate in this direction, adding to the changes of q_x multiplied by dx, and the same was done for the other directions.

$$q_{x+dx} = q_x + \frac{\partial q_x}{\partial x} dx \tag{5.3}$$

$$q_{y+dy} = q_y + \frac{\partial q_y}{\partial y} dy \tag{5.4}$$

$$q_{z+dz} = q_z + \frac{\partial q_z}{\partial z} dz \tag{5.5}$$

The difference between the inlet and outlet heat will give the net energy flow in the three dimensions, while the overall net flow will be written as:

$$q_{NET} = -\left(\frac{\partial q_x}{\partial x} dx + \frac{\partial q_y}{\partial y} dy + \frac{\partial q_z}{\partial z} dz \right) \tag{5.6}$$

In the above, we considered the in and out energy while it could be that the system generates heat. The generated heat could be written as:

$$E_{Gen} = Qdxdydz \tag{5.7}$$

Where Q is the generated heat per unit volume of the system (Wcm^{-3}). Considering the heat balance, the total energy could be described as:

$$E_{stored} = E_{in} - E_{out} + E_{Gen} \tag{5.8}$$

From above, the internal energy change rate per unit mass could be written as in Equation (5.9), i.e. multiplying the temperature change rate by the specific heat capacity c_p.

$$\frac{du}{dt} = c_p \frac{dT}{dt} \tag{5.9}$$

Thus the enclosed system stored energy where no phase changes occur as below see Equation (5.11):

$$m = \rho dxdydz \tag{5.10}$$

$$E_{sto} = m\frac{du}{dt} = mc_p\frac{\partial T}{\partial t} = \rho c_p\frac{\partial T}{\partial t}dxdydz \tag{5.11}$$

Where $(\partial T/\partial t)$ is the time rate for changing temperature, *m* is the mass, ρ is the density, E_{sto} is the stored energy. By substituting Equations (5.6), (5.7) and (5.11) into Equation (5.8), we will have Equation (5.12) as below:

$$E_{sto} = \rho c_p\frac{\partial T}{\partial t}dxdydz = -\left(\frac{\partial q_x}{\partial x}dx + \frac{\partial q_y}{\partial y}dy + \frac{\partial q_z}{\partial z}dz\right) + Qdxdydz \tag{5.12}$$

From Fourier's law, the conduction energy rate could be represented as below:

$$q_x = -K(dydz)\frac{\partial T}{\partial x} \tag{5.13}$$

The same goes for *y* and *z*-direction. By combining both equations of (5.13) and the other directions into (5.12) and finally divide the equation terms on the volume (*dx, dy and dz*), we will end up with Equation (5.14)

$$\rho c_p\frac{\partial T}{\partial t} = K\left(\frac{\partial^2 T}{\partial x^2} + \frac{\partial^2 T}{\partial y^2} + \frac{\partial^2 T}{\partial z^2}\right) + Q \tag{5.14}$$

Where the term $K\left(\partial^2 T/\partial x^2\right)$ represents the net conduction heat flow in the system through *x*-direction. The solution of Equation (5.14) can identify the temperature as a function of *x, y* and *z* at a time, *t*. Most of the time, a simpler version can be used when the thermal conductivity equals a fixed value.

$$\frac{1}{D}\frac{\partial T}{\partial t} = \frac{\partial^2 T}{\partial x^2} + \frac{\partial^2 T}{\partial y^2} + \frac{\partial^2 T}{\partial z^2} + \frac{Q}{K} \tag{5.15}$$

5.2.2 **Thermal Convection**

Another example of heat transfer is *Thermal Convection*. It is the process involved when there are moving "bulk or macroscopic" fluids contributing to the heat distribution through the surface of the system, resulting in cooling the warm surface. Figure 5.2 shows the formation of the boundary convection layer at the system. It also shows that random particle diffusion takes place close to the surface where the fluid particle has low velocity. Considering a fluid flow over the heated surface, "a consequence of the fluid–surface interaction is the development of a region in the fluid through which the velocity varies from zero at the surface to a finite value u_∞ associated with the flow. This region of the fluid is known as the hydrodynamic, or velocity, boundary layer. Moreover, if the surface and flow temperatures differ, there will be a region of the fluid through which the temperature varies from at T_s at $y=0$ to in T_∞ the outer flow. This region, called the thermal boundary layer, may be smaller, larger, or the same size as that through which the velocity varies. In any case, if $T_s > T_\infty$, convection heat transfer will occur from the surface to the outer flow" [190]. Heat convection can be sorted by its nature into the natural flow, where the heat convection takes place due to the difference in temperature and forced flow, where an external method applies such as a fan.

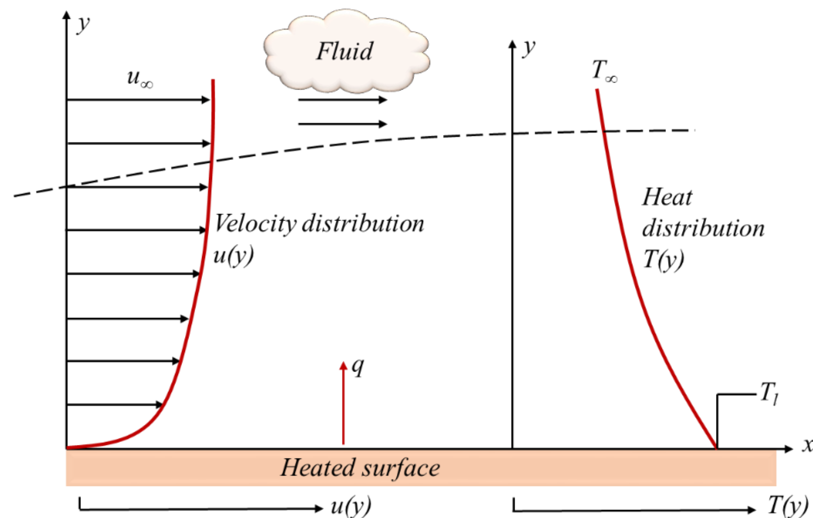

Figure 5.2: Convection energy transfer and the hydrodynamic formation at the boundary.

Moreover, due to the exchange of temperature between the surface and the fluid, the fluid velocity will decrease. Thus, the buoyancy force will dominate the fluid, pushing it up and replacing it with more cooling fluids. This cycling process will cool the surface. Convection also could happen in case of Latent heat exchange at the phase change between fluid and liquid. Phase change heat transfer is the way to transfer the energy when there is a boiling or fluid condensation with a constant temperature on the other side[191,192]. Convection heat transfer can be expressed as in Equation (5.16) "Newton's cooling law"[190–193].

$$q = h_c\left(T_l - T_{ext}\right) \tag{5.16}$$

Where q is the convective heat flux (Wm^{-2}), T_l is the surface temperature, and T_{ext} is external temperature while h_c represent the heat convection coefficient ($Wm^{-2}K$). This depends on the surface type, and in the case of a flat surface, h_c can be derived as in Equation (5.17) when the surface temperature is higher than the external temperature while Equation (5.18) is for the opposite case.

$$h_c = \begin{cases} 0.54\dfrac{K}{L}Ra_L^{1/4} & if \quad 10^4 \le Ra_L \le 10^7 \\ 0.15\dfrac{K}{L}Ra_L^{1/3} & if \quad 10^7 \le Ra_L \le 10^{11} \end{cases} \tag{5.17}$$

$$h_c = 0.27\frac{K}{L}Ra_L^{1/4} \quad if \quad 10^5 \le Ra_L \le 10^{10} \tag{5.18}$$

Where L is the "plate diameter represented by the area/perimeter", while Ra_L is Rayleigh number expressed as in Equation (5.19)[194,195]:

$$Ra_L = g\frac{\alpha_p \rho^2 c_p |T_l - T_{ext}| L^3}{K\mu} \quad (5.19)$$

Where g is the acceleration owing to gravity, α_p represent the thermal expansion coefficient, and μ is the dynamic viscosity[194,195]. The above is an approximation since it does not count the mass transfer due to the forced bulk convection (advection), which can be done by adding the velocity and calculate the heat transfer.

5.2.3 **Thermal Radiation**

In addition to heat conduction and convection, heat transfer can occur due to *thermal radiation***.** It is the process of producing electromagnetic radiation from its charged particles and their thermal vibration. It is neglected most of the time since it is much smaller than conduction and conviction[191,192] Any matter will emit energy when its temperature is exceeding zero Kelvin. The emitted energy will take the form of electromagnetic wave leading to cooling down the material. Radiation does not require the presence of other material.

In contrast, to thermal conduction and convection. Figure 5.3 shows surface heat transfer through convection and radiation. Stefan-Boltzmann explained the maximum limit of the emissive power of radiation as the energy rate emitted per unit area (Wm^{-2}) as in Equation (5.20). This is known as the blackbody surface.

$$E_b = \sigma_s T_s^4 \quad (5.20)$$

T_s is the surface absolute temperature (K), and σ_s is the Stefan-Boltzmann constant (5.67×10^{-8} $Wm^{-2}K^4$). While for other surfaces, Equation (5.21) should be used where ε is the emissivity ranging from 0 to 1. The heat flow radiation that can be described as in Equation (5.22)

$$E = \varepsilon\sigma_s T_s^4 \tag{5.21}$$

$$q = \varepsilon\sigma_{SB}\left(T_s^4 - T_{ext}^4\right) \tag{5.22}$$

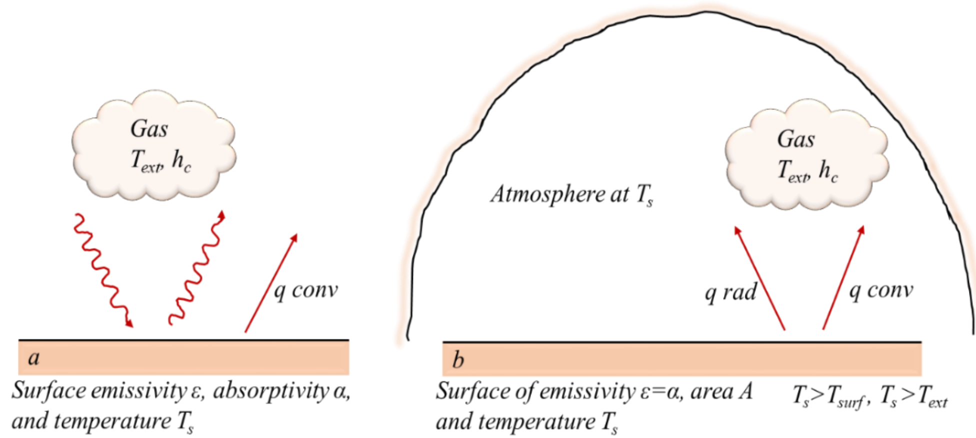

Figure 5.3: Thermal Radiation a) at the surface and b) at the surface surrounded by matter.

In reverse, there are the means to deliver heat energy to the surface. Moreover, since we are dealing with a laser, irradiation must be mentioned. Light-matter interaction was explained in detail in chapter three. Here it will be focused on the equations and options that have been used to simulate the temperature rise as a result of laser irradiation of the SiC surface. When the laser wave hits the surface, the effect can be modelled by applying both the material properties and the laser parameters. From the extinction coefficient *k,* it can be determined both the penetration depth and the surface reflectivity in addition to determining the absorption of the incident laser light as in Equation (5.23).

$$Q = \alpha I \tag{5.23}$$

Where α is the absorption coefficient, and *I* is the laser irradiance. Moreover, by applying Lambert-Beer law, we can calculate the exponential decay to account for the absorption and multiple reflection losses considered within the material thickness as in Equations (5.24) and (5.25) for the film and the substrate[196], respectively.

$$I_f(z) = I_o(1-R_1)\exp(-\alpha_f z)\left(\frac{\exp(2\alpha_f d_f - \alpha_f z) + R_2\exp(\alpha_f z)}{\exp(2\alpha_f d_f) + R_1 R_2}\right) \tag{5.24}$$

$$I_s(z) = I_o \frac{(1-R_1)(1-R_2)\exp(-\alpha_f d_f)}{1 - R_1 R_2 \exp(-2\alpha_f d_f)}\exp(-\alpha_s(z-d_f)) \tag{5.25}$$

Where I_o is the incident laser intensity, R_1 is the reflectivity at the film surface and air boundary, R_2 is the reflectivity between the sample and its substrate, d_f represents the film thickness, α_f and α_s are the absorption coefficient for the film and the substrate respectively. To use these equations, the peak intensity of the beam in space and time must be calculated Clarke 2017. The peak intensity for our systems, pulsed lasers, can be defined as the total energy of a single pulse. Moreover, to calculate these, Equations (5.26) and (5.27) could be applied according to the normalised spatial intensity *f(x,y)* and normalised temporal intensity *g(t)* of a pulse while *P* represents the beam power and *E* is the laser energy of a single pulse[196].

$$I_o = \frac{P}{\int_S f(x,y)dS} \tag{5.26}$$

$$I_o = \frac{E}{\int_S f(x,y)dS}\frac{1}{\int_0^\infty g(t)dt} \tag{5.27}$$

The integral takes place over the laser beam area. Thus the heat flux could be written as in Equation (5.28). It must be noticed that *h(z)* include the peak intensity as can be seen in the previous Equations (5.24) and (5.25). The h(z) term describes the laser intensity in the direction of beam propagation.

$$Q = \alpha(z) f(x, y) g(t) h(z) \tag{5.28}$$

Boundary conditions were needed to solve the heat equations. This leads us to the classification of the boundary conditions. Dirichlet (fixed boundary condition) and Neumann (heat flux boundary) were described as in Equations (5.29) and (5.30)[196]. The Neumann boundary employed for this work.

$$T = f(r,t) \tag{5.29}$$

$$\frac{\partial T}{\partial n} = f(r,t) \tag{5.30}$$

Where r is the radial vector, t is the time, and n is the perpendicular direction on the boundary.

5.3 Analytical Solution of Laser Heating Source

Most of these models relied on different assumption and conditions, especially when the system and model become complicated[148,158,197].

In general, analytical solutions were introduced by many researchers to model heat equations, as offered by Carslaw and Jeager[198]. Later on, these models were applied by others to model the laser as a heat source. J.F. Ready[199] reported the laser specific model for the uniform laser beam for a continuous or rectangular pulse, the distributed heat source and time-dependent irradiance[197]. Ready and Duley separately reported the finite sized Gaussian beam with a surface heat source in a semi-infinite solid with a varying intensity in time. Duley developed the solution for multiple layer subject. Lax followed this for the distributed source; the solution was for a time, depth and radial dependent temperature rise. He then introduced the solution with temperature-dependent material properties such as the thermal conductivity. This was useful for laser annealing of semiconductor[197,200,201].

El-Adawi provided a semi-analytical solution for the heat diffusion equation with the two-layer subject of a thin film attached on a substrate. This was a one-dimensional solution and solved using a computer[202]. Afterwards, computers evolved with numerical techniques predicting more precise spatial and temporal behaviour converge to the experimental results. This solution was achieved by applying a finite element technique. It is more common and considered the laser beam losses with its spatial and temporal behaviour, along with the temperature-dependent properties.

5.4 Semi-Analytical Heat Equation Solution

Here, It was focused on using a top hat excimer laser and a Gaussian pulse laser beam of CO_2. Different analytical heat equation solutions were applied depending on the beam profile. For excimer laser, the heat solution from Duley was applied[14], in addition to the two-layer by El-Adawi. This was employed to see the effect of a substrate on the temperature rise of the film[202]. For the CO_2 laser, Bechtel was used to estimating the temperature rise[203].

5.4.1 **Flat-Top Laser Profile Heat Equation Solution**

Initially, 1 Dimensional (1D) thermal model was implied for a free-standing bulk SiC. It was decided to apply an analytical model with a few assumptions from Duley[14]. For this study, the assumptions were considering the irradiation of the opaque surface by excimer laser of 193 nm. The penetration depth was controlled by the absorption coefficient in the range of 10^6 cm^{-1}. This is often smaller than the heat distribution presented in the linearised Equation (5.31)

$$\frac{\partial^2 T}{\partial x^2}(x,t) - \frac{1}{D}\frac{\partial T}{\partial t}(x,t) = -\frac{A(x,t)}{K} \tag{5.31}$$

Where x is the normal depth from the surface, $A(x,t)$ is the volumetric heat source, D is the thermal diffusivity, and K is the thermal conductivity. It approached over known steps of x as shown in Equation (5.32)[14]

$$A(x,t) = \alpha I_o(t)(1-R)\exp(-\alpha x) \tag{5.32}$$

Where R is the surface reflectivity for that wavelength, and $I_o(t)$is the time controlled laser intensity at the surface. Afterwards, the integral of $A(x,t)$ solved from zero to infinity and replaced in Equation (5.31).

For approximation, and since we are using excimer laser of 193 nm on a SiC surface, the light was strongly absorbed. The heat penetration depth is much larger than the optical penetration depth as in $\sqrt{D\tau_p} >> \alpha^{-1}$ and $I_o(t) = I_o$. The temperature rise can be written as in Equation (5.33).

$$T(x,t) = T_o + \frac{(1-R)I_o\sqrt{D\tau_p}}{K} ierfc\left(\frac{x}{2\sqrt{D\tau_p}}\right) \tag{5.33}$$

T_o is the environment temperature, and *ierfc* is error function integral. At the surface where x is set to zero, the temperature rise could be calculated from Equations (5.34) and (5.35) depending on if the laser intensity or laser fluence was used[14].

$$T(0,t) = T_o + 2\frac{1-R}{K} I_o \sqrt{\frac{D\tau_p}{\pi}} \tag{5.34}$$

$$T(0,t) = T_o + 2\frac{1-R}{K} E \sqrt{\frac{D}{\pi\tau_p}} \tag{5.35}$$

5.4.2 Gaussian Laser Profile Heat Equation Solution

For a Gaussian spatial laser profile, the radial term was introduced[203]. The heat equation solved for slab (semi-infinite) material where $z \geq 0$ in the same direction of laser

propagation. Bechtel assumed the material as an isotropic or cubic structure. The boundary and the initial conditions were considered for mathmatical convenience.

Bechtel considered “only a semi- infinite slab occupying the region $z \geq 0$. The slab is irradiated by a laser beam propagating in the z direction. In the absence of convective losses, the boundary condition for volume generation of heat is that the heat flux across the irradiated surface is equal to the thermal radiation loss”[203] see Equation (5.36). $T(r,t)$ is the temperature rise due to the laser irradiation. In pulsed lasers, we are interested in the temperature for time domain near the maximum irradiance. Thus, Equation (5.36) would be simplified to Equation (5.37).

$$K \left. \frac{dT(r,t)}{dz} \right|_{z=0} = \sigma_s \varepsilon \left(T^4 (z=0,t) - T_\infty^4 \right) \tag{5.36}$$

$$K \left. \frac{dT(r,t)}{dz} \right|_{z=0} = 0 \tag{5.37}$$

Also, it was assumed that the laser absorbed by the surface. Therefore, the boundary equation would be considered as in Equation (5.38).

$$K \left. \frac{dT(r,t)}{dz} \right|_{z=0} = -(1-R) I(r,t)\Big|_{z=0} \tag{5.38}$$

Where $I(r,t)$ is the laser irradiance. This solution was based on finding one point solution and then the superposition principle implied the solution on the different source distribution. Afterwards, Bechtel applied it in the agreement of Lambert-Beer law involving the spatial and temporal shape of the laser profile. Thus the source was presented as in Equation (5.39).

$$A(r,t) = I_{\max}(1-R)\alpha \exp(-\alpha z) f(r) q(t) \tag{5.39}$$

I_{max} is the maximum laser irradiance, *f(r)* is the normalised spatial dependent laser distribution, and *q(t)* is the normalised temporal behaviour of the laser pulse. The temperature rise was obtained as in Equation (5.40).

$$T(r,z,t) = \frac{I_{\max}(1-R)}{\sqrt{\pi K \rho c_p}} \exp\left(-\left(\frac{r}{d}\right)^2\right) \int_{\infty}^{t} \frac{\exp\left(-\left(\frac{t'}{\tau_p}\right)^2 - \frac{z^2}{\left(4D(t-t')\right)}\right)}{\sqrt{(t-t')}} \tag{5.40}$$

This can be represented in simple Equations (5.41).

$$\begin{aligned} \Delta T(0,t) &= 0, \quad t < 0 \\ \Delta T(0,t) &= \frac{2I_{\max}(1-R)}{K} \frac{\sqrt{Dt}}{\sqrt{\pi}}, \quad 0 \le t \le \tau \\ \Delta T(0,t) &= \frac{2I_{\max}(1-R)}{K} \frac{\sqrt{D\tau_p}}{\sqrt{\pi}} \left(\sqrt{(t-t')} - \sqrt{(t\tau_p^{-1} - 1)}\right), \quad t > \tau_p \end{aligned} \tag{5.41}$$

The drawback of the discussed semi-analytical solutions is they assume the absorption of all the incident laser at the surface, which is valid when the absorbed energy will take place in a very thin layer of the surface. Also, only 1D models could be applied, meaning ignoring the different beam shapes and the lack of scanning simulation. As stated, the losses due to the radiation and convection were neglected. Despite all the above, it has been used since it was a quick way to solve the heat equations and also for comparison

5.5 COMSOL Multiphysics

Having defined the heat equation and its analytical solution, numerical methods were introduced to solve the heat equation and to avoid the limitation of the semi-analytical solution. Consequently, the analytical and semi-analytical solution was less dominant. Numerical techniques are more powerful and precise due to the minimisation in the

assumptions. The model used here is the finite element method FEM. It is the prefered method to solve the heat equation on account of considering the thermal radiation and thermal convection more easily along with conduction energy. It can be used easily to solve partial differential equations[204,205], while more complicated temperature-dependent properties can be incorporated. COMSOL MultiphySiCs is the theoretical modelling presented in this work to determine the temperature rise at the sample irradiated with different laser beams. This programme is robust; it can be applied for solving various types of phySiCs and engineering problems. 1D, 2D, 2D axisymmetric and 3D [206] can be designed and modelled with COMSOL. Constant and temperature-dependent properties could be employed in the simulation. Optimised laser parameters and its temporal and spatial shapes could be considered to predict the temperature rise of the surface. Ambient conditions of material layers or air which could be inserted in the model since it affects the cooling process and generates more real volumetric heat solutions.

The genral COMSOL steps shown in Figure 5.4[187,206] was considered when building a model in COMSOL MultiphySiCs.

5.5.1 **Simulation Methodology**

To assist in the interpretation of the laser processing results, we calculate the surface temperature of laser irradiated SiC using a Finite Element Method (FEM) with commercially available software, COMSOL™ version 5.3. In this work, 1D and 2D axisymmetric have been used to simulate laser irradiation heating. The SiC of 1×1×0.03 cm^3 dimensions was introduced, see Figure 5.5. The sample was defined and divided into domains. This material was divided into elements using mesh. It is prefered to be fine to get accurate solutions, and the trial is the only method to determine if it was correct or not. However, it was determined by the laser pulse duration which is in the nanoscale for the ArF laser and microscale for the CO_2 laser. Since we modelled 2D axisymmetric, the mesh was used as a triangle[207].

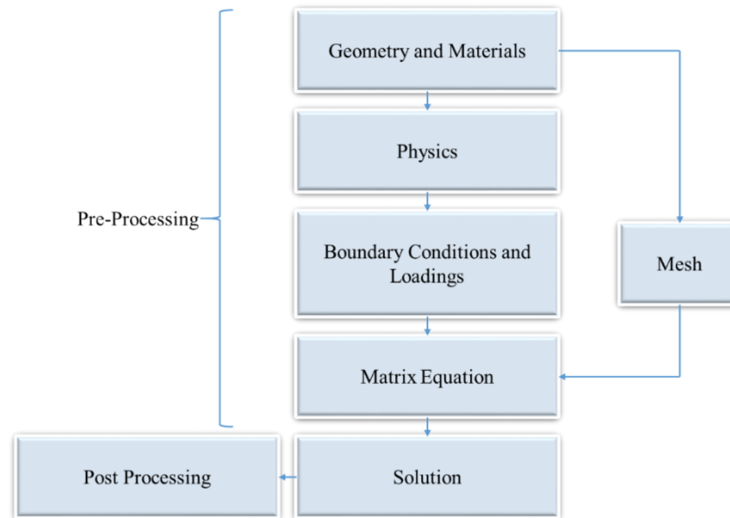

Figure 5.4: COMSOL general steps to simulate physical processing.

Time steps were controlled in the same way as the mesh to prevent any large jumps. However, COMSOL 5.3 was used in the default time-dependent heat transfer setting; only the time stepping was set to strict. This way, each chosen time step will be considered in addition to any intermediate time steps taken by the solver. Both convection and conduction at the surface were used in the simulation. Radiation losses were neglected. The Neumann boundary condition was considered in the simulation, see Equations (5.22) and (5.15). The boundary condition was applied on the outer boundaries to define a zero heat flux. This is usually defined by the heat penetration depth. Figure 5.6, represents the boundary condition and the used geometry in COMSOL. The initial temperature was set to 293.15 K. After that, a solution to Equation (5.28) should be reached for the volumetric heat source.

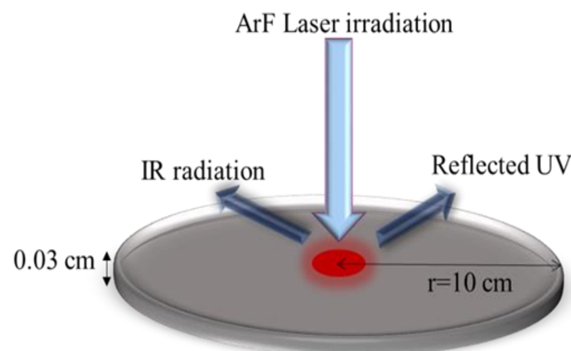

Figure 5.5: Schematic of the sample irradiated by ArF laser.

To make sure that the reached solution was correct, different models were built as mentioned earlier. This was compared with the analytical solutions. The 2D axisymmetry was dealing with realistic procedure. 2D-axisymmetric was restricted to the stationary situation, and the beam was circular.

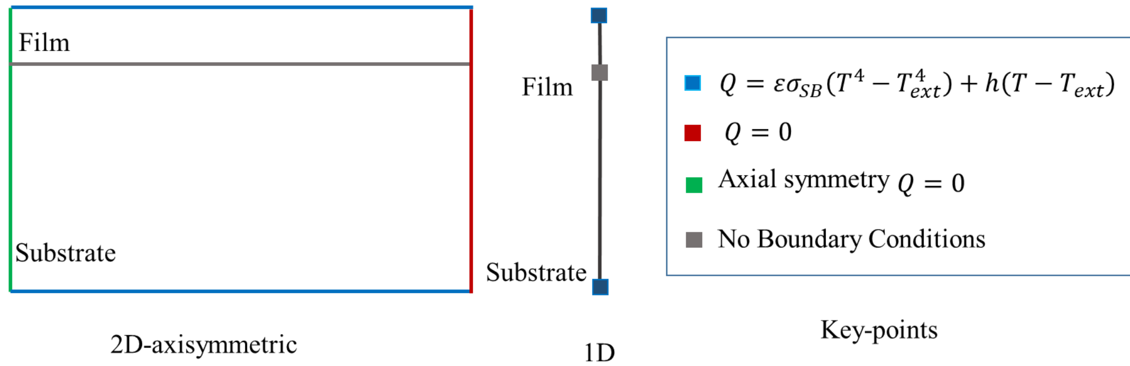

Figure 5.6: The boundary condition and the geometry of the 1D and 2D axisymmetric model

5.5.2 Silicon Carbide Parameter

Having defined the SiC properties in chapter two, more specific temperature-dependent parameters were considered in this chapter for the sake of accuracy. The refractive index of 4H:SiC was calculated by Naftaly using Equations (5.42) and (5.43)[208] as it can be shown in Figure 5.7, covering the wavelength range of 190 nm to 12 μm. Refractive index (n_o) was applied in the model for simplicity.

$$n_o^2(\lambda) = 9.90 + \frac{0.1364}{\lambda^2 - 0.0334} + \frac{545}{\lambda^2 - 163.69} \tag{5.42}$$

$$n_e^2(\lambda) = 10.52 + \frac{0.1701}{\lambda^2 - 0.0258} + \frac{729.2}{\lambda^2 - 194.72} \tag{5.43}$$

Temperature-dependent specific heat and thermal conductivity were also applied. Equation (5.44) describes the temperature-dependent specific heat for 4H:SiC, as it can be shown in Figure 5.8.

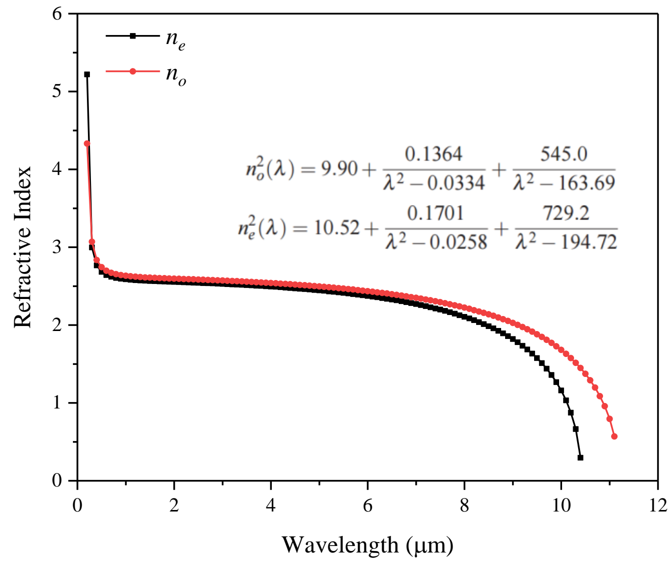

Figure 5.7: Calculated Refractive index of 4H:SiC from Equations (5.42) and (5.43) for both ordinary and extraordinary refractive index[208].

$$Cp(T) = A + BT + CT^2 + DT^3 + ET^4 \tag{5.44}$$

Where A=-126.97, B=3.73, C=-4.10×10^{-3}, D=2.10×10^{-6}, and E=-4.05×10^{-10}. Temperature-dependent thermal conductivity of 4H:SiC was calculated using Equation (5.45), see Figure 5.9 . Equations (5.44) and (5.45) have limits between 300 and 2300 K[209].

$$K(T) = 61100/(T - 115) \tag{5.45}$$

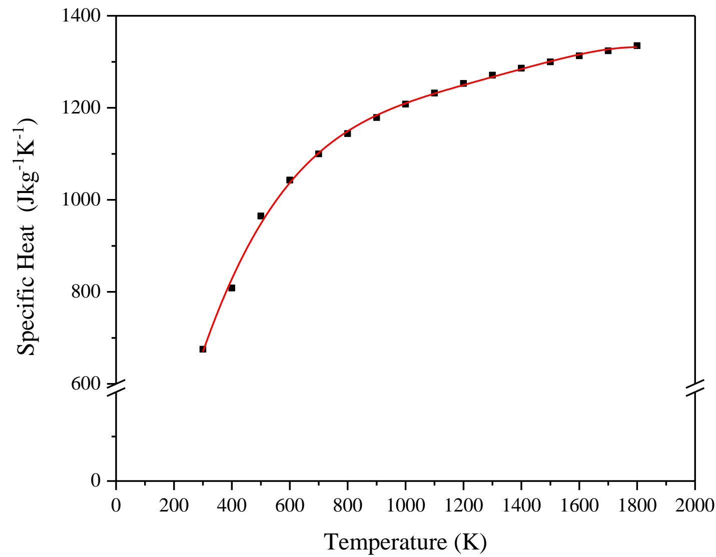

Figure 5.8: Temperature-dependent specific heat of 4H:SiC. It shows the increase of specific heat with temperature.

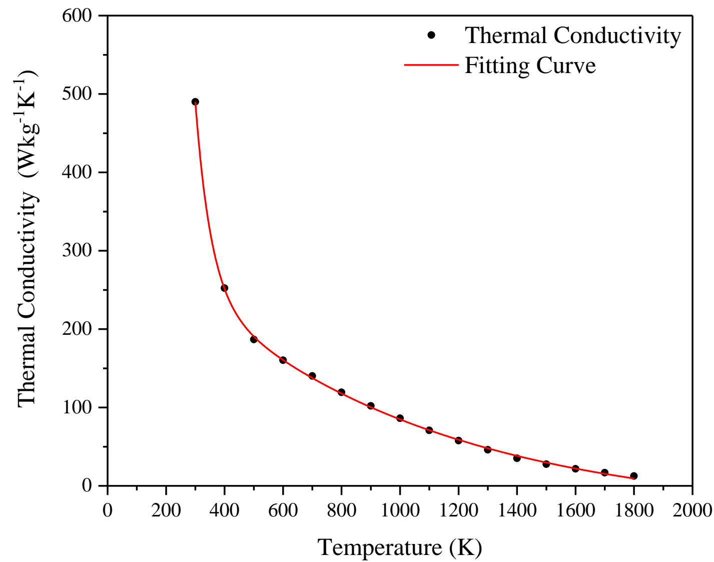

Figure 5.9: The change in the thermal conductivity of 4H:SiC as a function of temperature.

5.5.3 **Other Parameters**

Air properties were taken from the built-in library in COMSOL because it is well characterised. The refractive index equals one. Silica was modelled as the substrate for 193 nm radiation. However, the substrate was neglected here due to the limitation of both the optical and thermal penetration depth to the surface of the SiC. Silica was replaced

with Aluminium in the CO_2 processing, and the properties were taken from the COMSOL library. The laser temporal shape was considered for both laser systems. For the excimer laser, the pulse duration was measured as it can be seen in Figure 5.10.

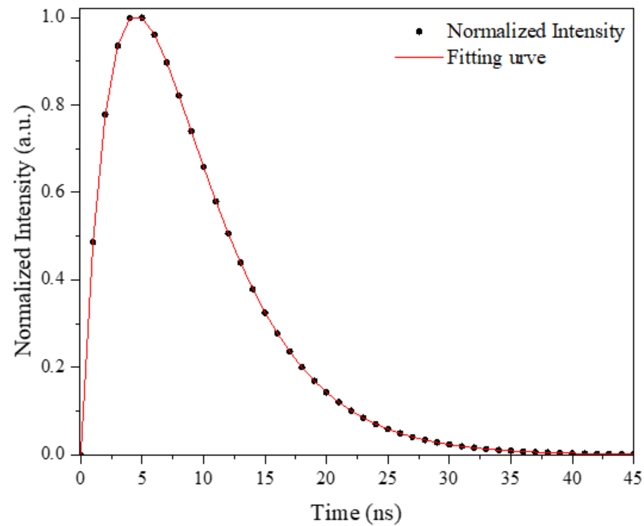

Figure 5.10: Measured temporal shape of the excimer laser of 193 nm. The shape of our laser pulse measured with a photodetector.

For the CO_2 laser, the temporal shape was measured by the manufacture of the laser (Rofin Sinar). The extraction of the data was conducted using Origin Pro Software see Figure 5.11.

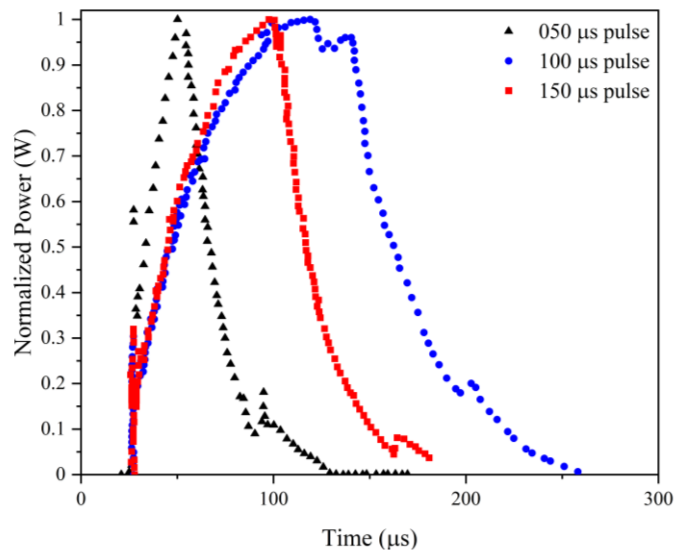

Figure 5.11: Normalized extracted temporal shape of the CO_2 Laser pulse. The data was provided as a picture from the Rofin Sinar Company. The data was extracted using the Origin software.

5.6 Results and Discussion

Pulsed laser processing of a surface has two significant advantages: high-speed heating up to the melting and evaporation temperature in the nanosecond time scale and efficient rapid solidification and cooling. The results show the surface temperature versus time and the temperature profile in depth (z) for the flat-top shape and Gaussian shape distribution. A comparison of analytical results and numerical solution were conducted. The effect of the substrate on the sample was computed and compared to the experimental results. The pulse repetition rate effect was also studied.

5.6.1 Analytical and Numerical Modelling Comparison for ArF and CO_2 Lasers

Analytical and numerical solutions were compared in this work. COMSOL simulations results compared with the analytical solutions of both Duley[14] and El-Adawi[202] models. A 0.97 Jcm^{-2} laser fluence was used to evaluate the mean temperature rise as it can be seen in Figure 5.12. Both analytical models gave almost the same results despite the presence of a substrate in El-Adawi's model. Furthermore, Bechtel[203] and COMSOL solutions were also compared in this work. A 4.5 W laser power was applied to evaluate the mean temperature (Figure 5.13). The analytical models gave higher results than the numerical models. Thus, the numerical simulation performed for the same laser power had lower temperature rise. This was justified by the fact that both the optical and thermal penetration depths were limited to the surface of SiC. However, the numerical simulation, which was calculated with the same laser fluence, had less temperature rise. This was expected because the numerical simulation uses more realistic parameters and conditions such as the temporal and spatial shape and of the applied laser and the temperature-dependent properties.

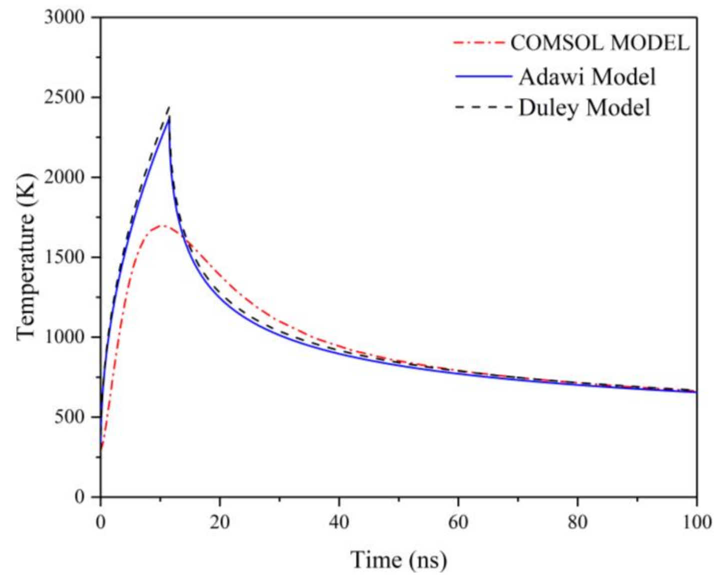

Figure 5.12: Temperature rise conducted with different models of COMSOL, Duley and El-Adawi at 0.97 Jcm^{-2} laser fluence.

The 1D model was constructed for simplicity and time efficiency. 2D-axisymmetric was applied next. A comparison of the 1D and 2D-axisymmetric models was studied at the threshold energy fluence Figure 5.14. The difference between the 1D and the 2D model was around 4 K.

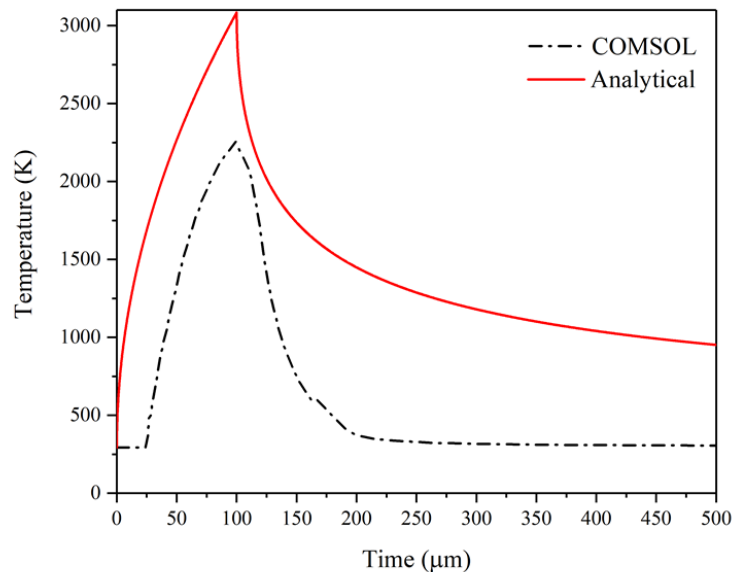

Figure 5.13: Temperature change for an applied CO_2 laser of 10.6 µm wavelength with 100 µsec (FWHM) and Gaussian laser pulse of peak incident power 4.5 W, and the beam radius FWHM point is 79 µm. The temperature is plotted at the beam centre for z = 0, i.e. at the surface.

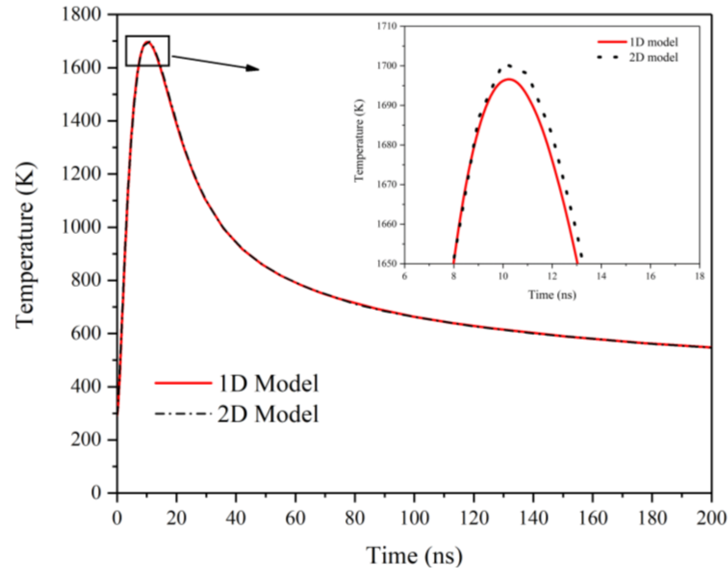

Figure 5.14: Temperature rise with one dimensional and two dimensional axisymmetric for laser fluence of 0.97 Jcm^{-2}.

5.6.2 Numerical Modelling of Excimer Laser on SiC

2D-axisymmetry simulations were conducted to the experimental values of the processing parameters. From the simulations, we were able to predict the spatial and temporal behaviour of the SiC surface temperature at the irradiated area. The temperature rises of the SiC surface as a function of the applied laser fluence can be seen in Figure 5.15. As expected, temperature increased linearly with increasing the applied fluence and flowing the temporal pulse shape, see Figure 5.16. At 0.97 Jcm^{-2} the temperature exceeded the Si melting point at 1700 K. Further increase in the applied fluence generates more heat. This was confirmed by the increase in the depth ablated in the irradiated site. Silicon carbide decompose at 3100 K while the equilibrium temperature of the crystal-liquid is 3500 K[34]. By applying the calculation on the experimental work, we could predict the behaviour of each of the SiC constituent, Si and C elements. Each temperature has been calculated using the corresponding laser fluence required for the peak temperature to reach the corresponding melting point (Figure 5.17). The reported melt temperatures of silicon, silicon carbide and carbon are ~1700K (Si), ~ 3100K (SiC) and 4200K (C) respectively [121,210]. The laser fluence that corresponds to these melt temperatures have been plotted, and temperature calculations correspond to laser fluences of 0.97 Jcm^{-2} (Si), 1.95 Jcm^{-2} (SiC) and 2.60 Jcm^{-2} (C).

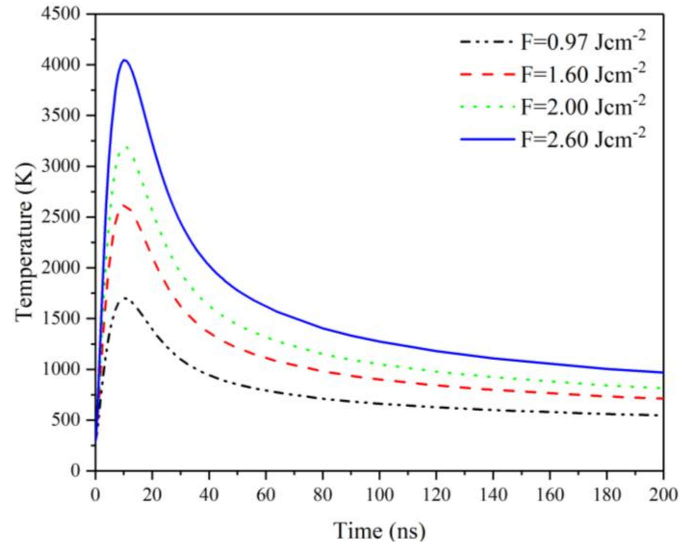

Figure 5.15: Temperature rise in time as a function of the applied laser fluence. The fluence was determined depending on the experimental values where there was a modification on the surface.

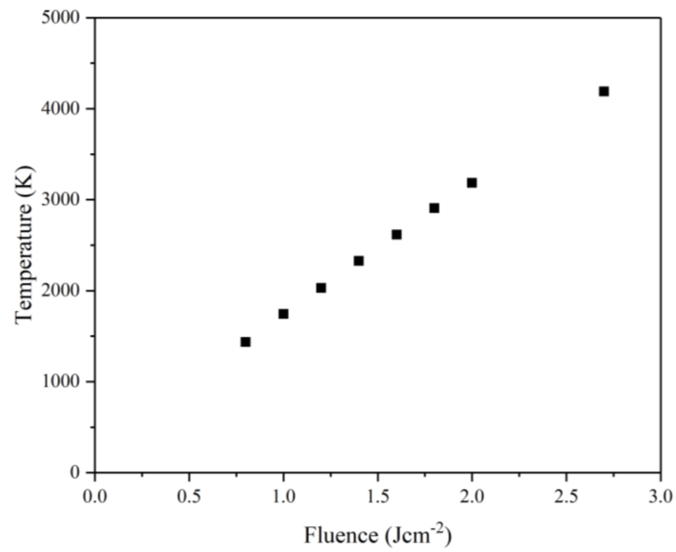

Figure 5.16: Linear relation between the applied laser fluence and the temperature rise solved with 2D-axisymmetric model.

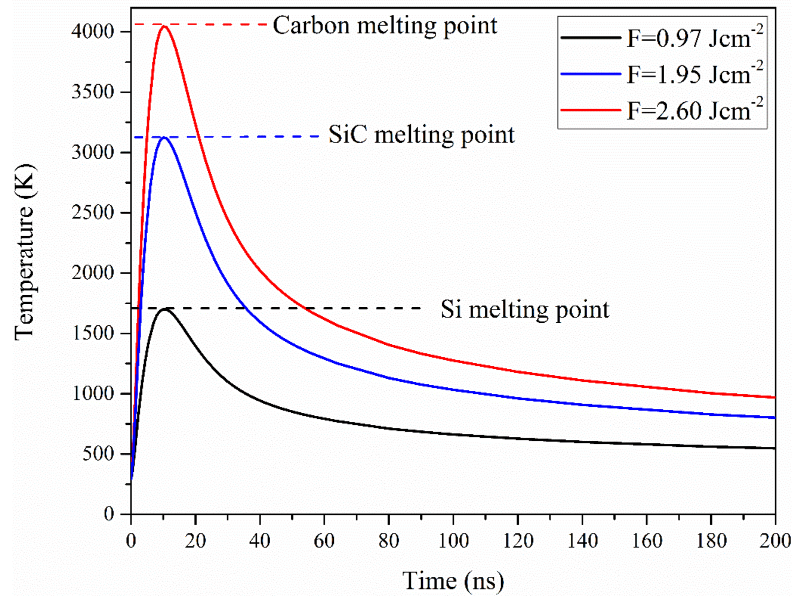

Figure 5.17: Temperature simulations of 193nm laser irradiated carbon, 4H:SiC and silicon using finite element modelling, COMSOL MultiPhySiCs™5.3. The laser pulse duration used in the simulations is 11.5 ns FWHM. Each curve has been calculated using the corresponding laser fluence required for the peak temperature to reach the corresponding melting point.

Furthermore, the spatial laser coupling with SiC was simulated not just at the surface but also normally beneath the surface in the z-direction as it can be seen from Figure 5.18. This is in agreement with our experimental etching rate depth. Using the threshold fluence, the effective temperature will be restricted to the surface. While the effective temperature will penetrate deeper inside the material with higher laser fluences.

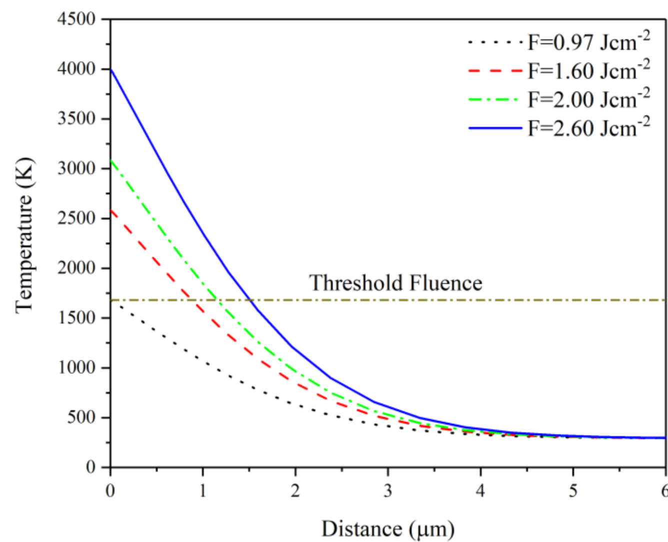

Figure 5.18: Heat profile inside the material due to the laser irradiation of different fluences.

5.6.3 **Numerical Modelling of CO2 Laser on SiC**

A systematic study was performed to understand the effect of the applied laser parameters on the spatial and temporal distribution of the temperature using a numerical model. This section deals with the CO_2 laser as the heat source of the SiC surface. We used a high power laser with a maximum power of 140 W. It is localised in time and space due to the Gaussian profile. It will reach its highest value at the centre and degrade toward the edge. Most of our calculations were done at the centre of the beam. When solid material absorbs the laser power, it will deposit energy in the electrons. These excited electrons will undergo collisions and then relax to phonons that are thermalised and distributed to increase the lattice temperature. These processes take place in the femto to picosecond range.

Our CO_2 laser has a long tuneable pulse width in the range of 2-400 µsec. However, it is powerful enough to accomplish a high temperature rise. The numerical solution was used to understand the effect of the pulse duration on the temperature rise (Figure 5.19). As previously mentioned, to overcome the behaviour of long pulse duration, a high power must be applied. These calculations conducted at the minimum spot size at a laser power of 4.5 W. It shows an increase in the surface temperature when it applied within shorter pulse duration.

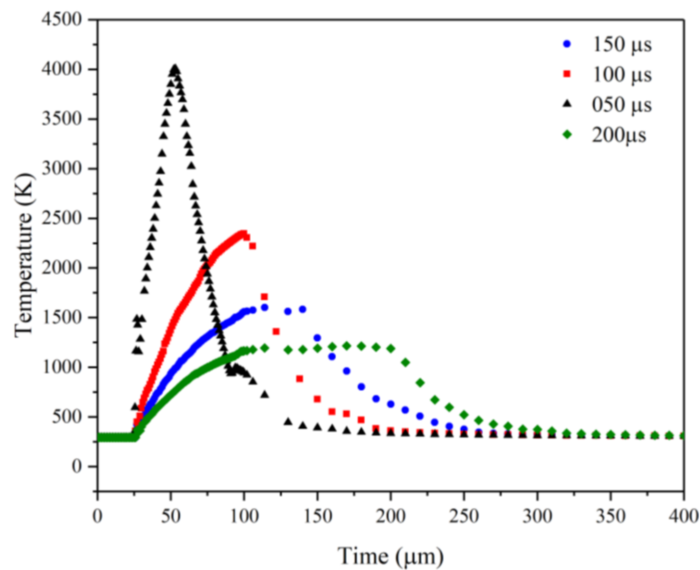

Figure 5.19: Temperature rise in time with different laser pulse duration using 4.5 W power.

To investigate the dominant influence on the temperature change, COMSOL was used to predict the heating of the SiC at different applied laser power, see Figure 5.20. These simulations were performed with 100 µsec and 150 µsec pulse durations at the minimum spot size of 79 µm. Other studies showed the effect of the pulse temporal shape on the outcome temperature rise and distribution [211,212]. However, for both pulse durations, there is a linear relationship between the peak temperature and the applied laser power (Figure 5.21).

The temperature of the surface increases with increasing laser power. This can be justified by the fact that for a higher laser intensity, more energy will be delivered to the system leading to increase the vibration of the states, causing the temperature to increase. However, too much temperature rise can result in damaging the samples. Therefore, for the high laser power, we can change other laser parameters as the pulse duration, the spot size or the number of pulses.

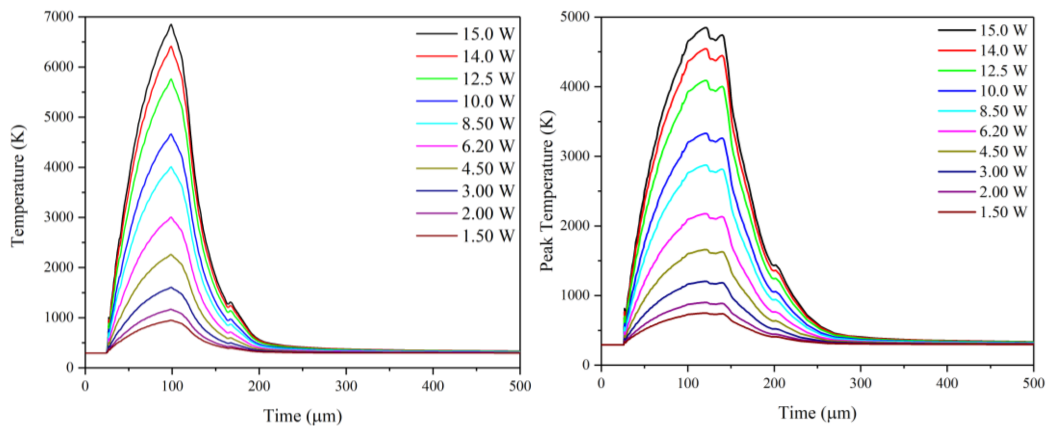

Figure 5.20: Evolution of the temperature as a function of the irradiated laser power at 79 µm beam diameter. The tuned pulse duration was 100 µsec for the left side graph and 150 µsec for the right-hand graph.

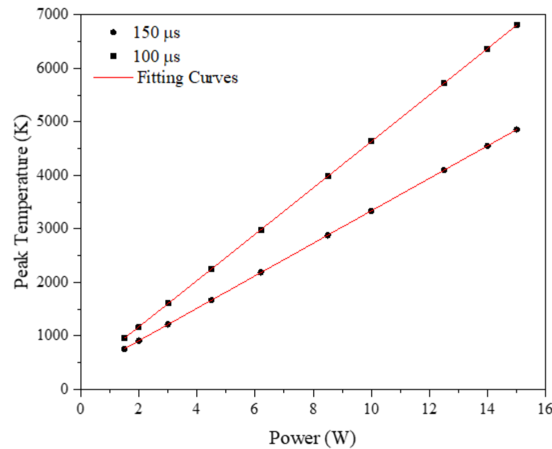

Figure 5.21: Peak temperature predicted for various power using both 100 µsec pulse duration and the 150 µsec pulse duration.

Figure 5.22 demonstrates the effect of laser power on temperature distribution within the SiC thickness normally in the z-direction. The temperature decreases dramatically to room temperature at 200 µm.

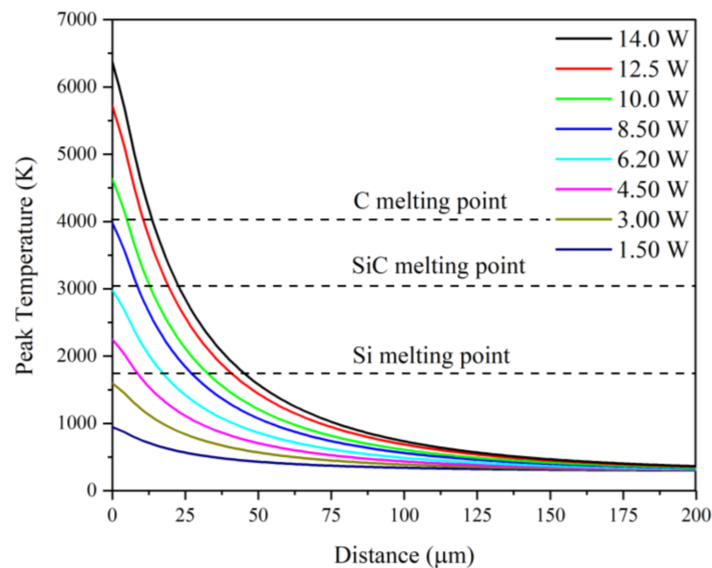

Figure 5.22: Evolution of the thickness peak temperature profile. The used laser power was 15 W tuned at 100 µsec pulse width.

However, the temperature rise above melting point is limited to a certain depth depending on the used laser power. For example, the applied 10 W power will penetrate deep to 200 µm while the sufficient temperature, in which an effect can show on the surface, will

penetrate to ~30 µm. The location of the sufficient temperature moves deeper inside the SiC as power increased.

The effect of using multiple pulses on the peak temperature rise was modelled (Figure 5.23). A pulse repetition rate of 500 Hz with a laser power of 4.5 W and a pulse duration of 100 µsec was employed. The cooling of the substrate is exponential, and it reaches room temperature before the start of the next pulse, which leads to a sub-degree increase in each pulse. The projection in Figure 5.23 is only for three pulses to make it more clear. The first peak reaches 2188 K while the second reach 2188.4 K indicating a difference of 0.4 K. The cooling process takes longer when the difference in temperature is low as it can be seen in Figure 5.20. Hence the increase of temperature at the next pulse.

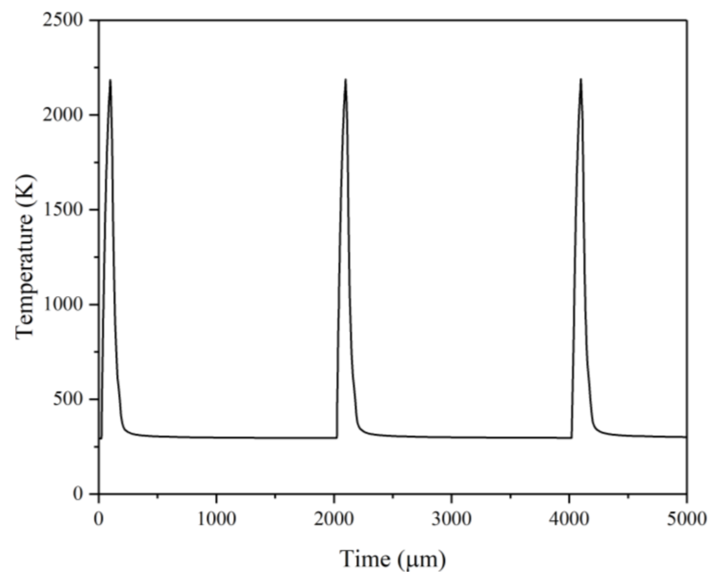

Figure 5.23: The peak temperature for a series of the number of pulses. The simulation was conducted for 4.5 W laser power and at a pulse duration of 100 µsec.

The effect of the presence of the substrate was also investigated. The presence of Al as a substrate under the SiC during the laser irradiation increases the temperature by 35 K at a laser power of 4.5 W and a pulse duration of 150 µsec. This is justified as the Al substrate will act as another heating source or simply it lowers the cooling rate in SiC.

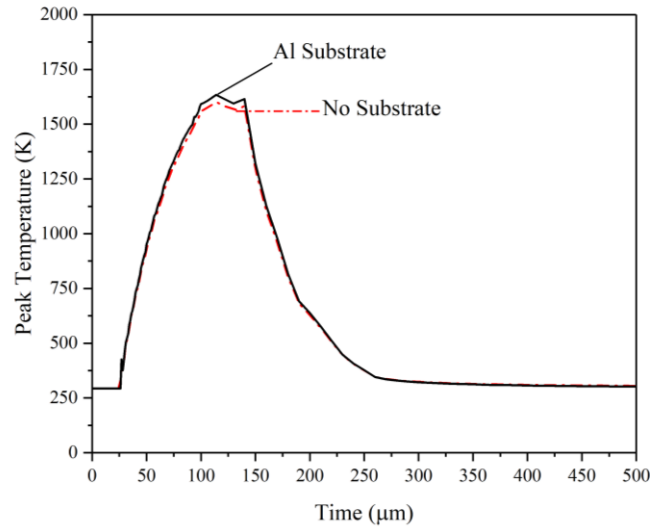

Figure 5.24: The peak temperature of a SiC during laser irradiation. It combines both the temperature rise using Al as a substrate and without the substrate. The laser power was 4.5 W with 150 µsec pulse duration.

Finally, the effect of the laser spot size was studied. We have fixed the power of the laser. The spot diameter influenced the power density of the laser directly. The smaller the spot size, the more concentrated the energy. The laser power was set to 4.5 W, and the pulse duration was set to 150 µsec. Both the temperature distribution in time and space was performed, as shown in Figure 5.25. The fact that the high temperature could be deep inside the SiC could explain the depth of the crater [194] check Figure 5.26.

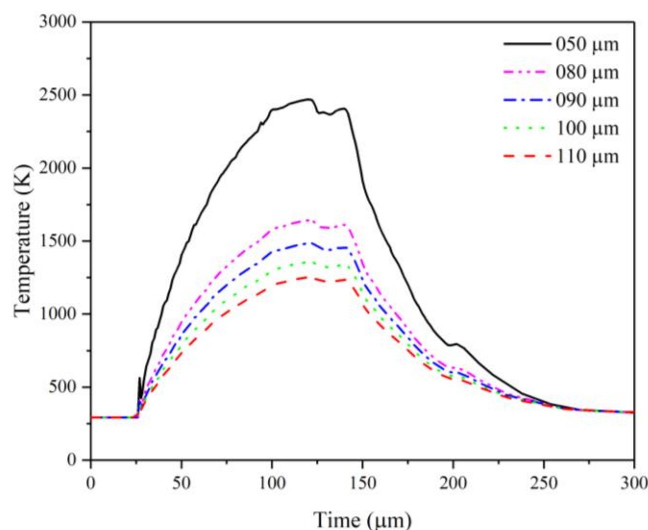

Figure 5.25: Temporal peak temperature of different spot sizes with the same power density of 4.5 W. the calculation was conducted for single pulse laser with 150 µsec pulse duration.

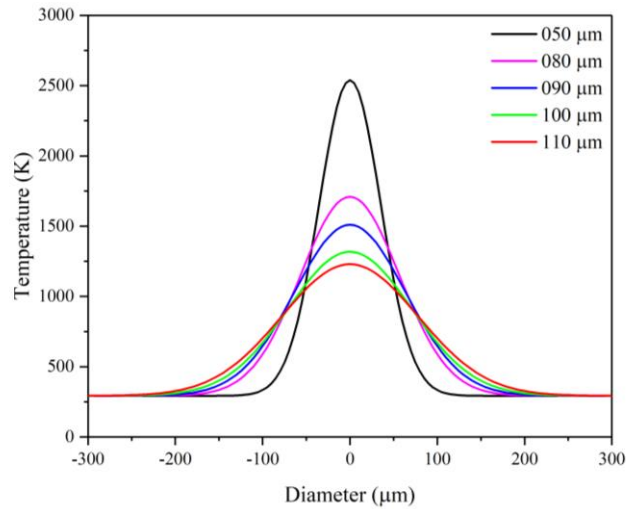

Figure 5.26: The spatial peak temperature of the irradiated laser power 4.5 W with different mean diameter.

5.7 Summary

Our measurements and simulations can be efficiently used to describe experiments involving laser heating by providing a useful basis for understanding its limitations.

The numerical solutions show a robust thermal gradient in the z-direction, which depends on the material properties.

SiC can be heated with the imaged ArF and focused CO_2 lasers to high temperature because of the optical and thermal properties of the SiC, such as the high thermal conductivity.

The laser parameters such as laser power, pulse duration, pulse repetition rate and spot radius were selected, and the combinations of these parameters were considered for the thermal analysis. The FE simulation results would be highly helpful to select the optimum laser parameters for laser-assisted machining.

Chapter 6 : Ablation Threshold Measurements and Surface Modifications of 193 nm Excimer Laser Irradiated 4H:SiC

6.1 Result and Discussion

This chapter reports the laser processing of polished single-crystalline 4H:SiC wafers using 193 nm ArF laser over a fluence range of 0.3–5 Jcm^{-2}. Two sets of scanning and stationary processing experiments were investigated. Laser-ablated sites have been analysed using optical microscopy, SEM, AFM, WLI and Raman microscopy. Finite element simulations using COMSOL™ Multiphysics, 5.3 have been used in this chapter to calculate laser induced temperature rise of 4H:SiC as a function of laser fluence.

6.1.1 Laser-Induced Modification and Threshold Measurements

It is therefore pertinent to establish the experimental parameters accurately to identify the laser ablation threshold. Experiments associated with graphene formation can then be carried out close to the ablation threshold. Laser etch rate measurements have been carried out to identify the ablation threshold fluence of 4H:SiC. Measuring the threshold laser fluence allows one to identify the upper fluence region for these studies. Figure 6.1 shows etch depth per pulse measurements of laser irradiated 4H:SiC in the laser fluence range of 0.9 Jcm^{-2} to 5 Jcm^{-2}.

As can be seen, there is a gentle onset of material removal that increases with laser fluence. On close inspection, the moderate increase in mass transported away from the surface does not necessarily warrant the name threshold [213]. Nevertheless, it is useful to identify a fluence in laser processing that indicates the onset of material removal. Using WLI measurements averaged over 100 laser pulses on a single site we identify an onset of material modification, at a wavelength of 193 nm, of F_T = 925 $\pm$ 80 mJcm^{-2} and a corresponding experimental etch rate of ~ 200 pm per laser pulse. We note that the laser

fluence that is identified as modifying the surface of silicon carbide is dependent, to some extent, on the sensitivity of the experimental technique used to measure the removal of material. When using an etch rate technique to determine the laser threshold fluence it may be pertinent to average over a large number of applied laser pulses so that the ablation crater can be measured. However, one should also keep in mind that the optical absorption coefficient should not be modified in the process. It is therefore important to select the optimum number of applied laser pulses so that one avoids near-surface material modification such as compaction effects [214] and to ensure, or try to prevent the introduction of defect states.

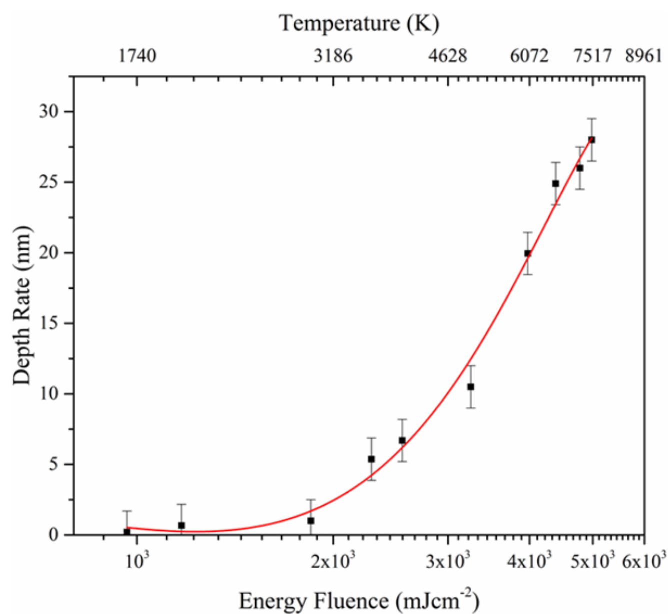

Figure 6.1: Laser ablation etches rates versus laser fluence. The top axis corresponds to the calculated temperature using a finite element method, software COMSOL Multiphysics 5.3. Each ablation site was irradiated with 100 laser pulses, and the data averaged.

In this work, the role of vacancies and defects either, intrinsic or laser induced that may affect the melt temperature have not been considered. Using the H-K and C-C relations, see Table 6-1 for the partial pressures, we estimate the crater depth due to evaporation from the near surface to be ~20 pm per laser pulse at a laser fluence of $F = 925\,\text{mJcm}^{-2}$. Increasing the laser fluence considerably above, F_T increases the etch rate from a sub-nanometre depth per pulse to ~28 nm per pulse at a fluence of 5.0 Jcm^{-2}. Absorption of relatively high photon energy laser pulse may induce defects, and it is not inconceivable that clusters, as well as mono-atomic species, will be removed from the surface. Silicon

carbide is reported to sublime at ambient pressure, and melting takes place at pressures of ~35 atmospheres and above[215]. As the laser energy is absorbed rapidly, on a nanosecond time scale, the pressure local to the irradiated area will be dependent on the intensity of the laser pulse.

Table 6-1: Partial vapour pressures of silicon carbide (atm).

Temperature (K)	**Si**	**SiC_2**	**Si_2C**
2149	2.1×10^{-5}	1.9×10^{-6}	1.4×10^{-6}
2196	4.1×10^{-5}	4.4×10^{-6}	3.9×10^{-6}
2316	2.0×10^{-4}	3.1×10^{-5}	2.2×10^{-5}

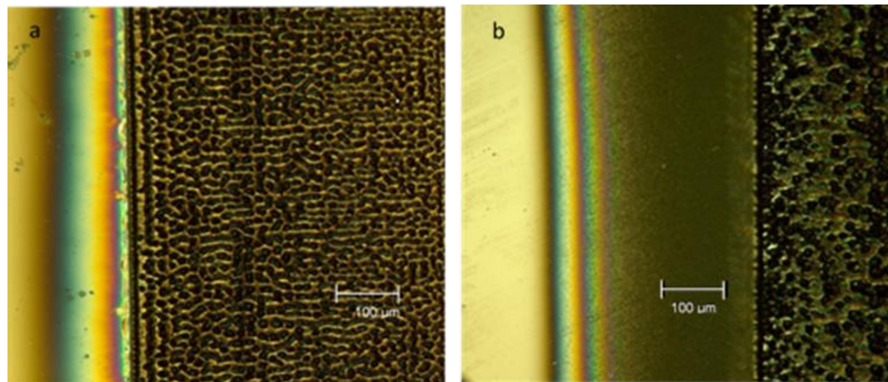

Figure 6.2: Optical micrographs of laser irradiated 4H:SiC. Sample irradiated at a laser fluence of 1.5 Jcm^{-2} and a sample translation speed 0.01 mms^{-1} (a) and laser fluence 2.7 Jcm^{-2} and a sample translation speed of 0.005 mms^{-1} (b). The floor of the ablation craters can be seen to have a different surface topology.

Figure 5.17 shows the temperature modelled for each constituent of Si and C in SiC compound due to laser-induced phase separation [216]. Optical microscopy measurements of laser-irradiated silicon carbide are shown in Figure 6.2. 4H:SiC samples were irradiated using a laser fluence of 1.5 Jcm^{-2} and 2.7 Jcm^{-2}. Samples were translated at speeds of 0.01 mms^{-1} and 0.005 mms^{-1} respectively. As can be seen, the ablation craters appear to be quite different. In Figure 6.2(a) the laser-ablated region shows a re-constructed surface that may be due to melting of the near surface. In contrast,

Figure 6.2(b) shows a different surface topology at the higher laser fluence and slower translation speed. Isolated structures appear to be agglomerating on the bottom of the channel.

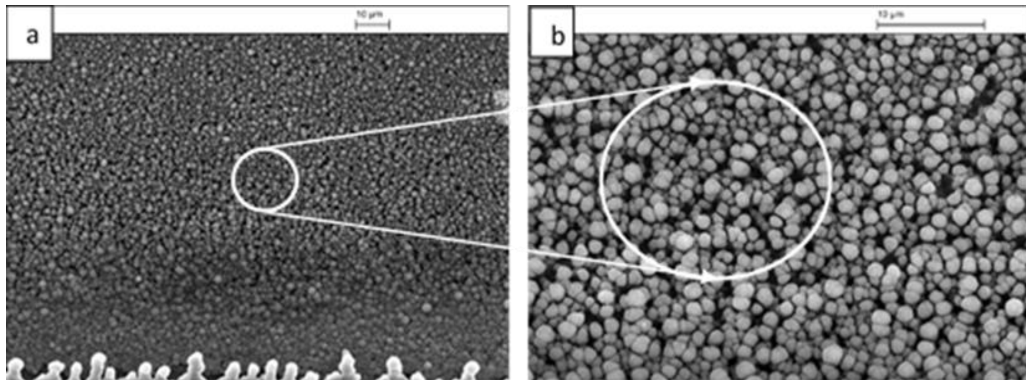

Figure 6.3: SEM micrographs of the redeposited debris outside of the ablation crater depicted in Figure 6.2(b). The approximate size of the particulates ranges between ~ 800 nm to ~1.4 μm diameter. Although not in view, the redeposited material extends away from the edge of the ablation crater out to a distance of about 300 μm.

In addition, as to be expected, there is a greater amount of redeposited material outside the ablation region. Figure 6.3 shows the SEM micrographs of redeposited material on the outer perimeter of the ablation crater. The approximate size of the particulates ranges between ~ 800 nm to ~1.4 μm. The particulates have been transported away from the irradiated zone to a distance of ~300 μm. A one-dimensional stylus profilometry measurement, measured orthogonal to the sample translation direction, is shown in Figure 6.4.

Three regions can be clearly identified. (1) The surfaces of the un-irradiated 4H:SiC, (2) a region of redeposited material between the un-irradiated region and the perimeter of the ablation crater. The height of the redeposited material ranges in height from ~2.5 μm at the edge of the crater and decreasing linearly down to the surface of the sample. (3) The ablated region. This region is unusual, to some extent, in that parts of the profile indicate structures protruding above the height of the un-irradiated sample surface. Whilst the stylus profile provides height and gradient information, the profile measurement lacks high-resolution lateral information.

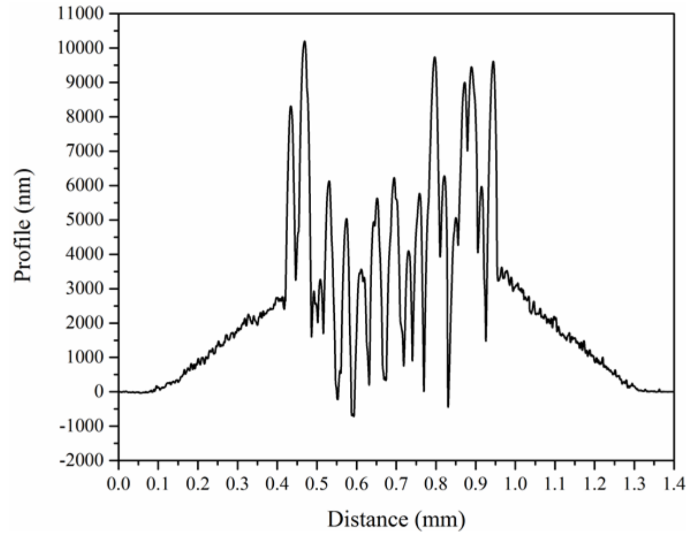

Figure 6.4: Cross-sectional one stylus profile measurement of laser ablated 4H:SiC channel. The channel was created using a laser fluence of 2.7 Jcm^{-2} and a scan speed of 0.005 mms^{-1}. Redeposited debris resides in the regions between 150-440 µm and 950-1250 µm. Note the channel region consists of structures protruding above the surface of the un-irradiated sample.

To observe the ablation crater in more detail, SEM measurements were carried out on the laser irradiated 4H:SiC samples, see Figure 6.5. By traversing the sample relative to the laser beam, a channel ~1.5 mm in length has been realised. As can be seen, the irradiated region consists of micron-sized features in the ablated region. Before discussing the result, we first note that there is some non-uniformity of the ablated channel. Observation of Figure 6.5 in a vertical direction one can see the features change in size. This is due to beam non-uniformities arising from non-uniform laser fluence. This spatial variation in the laser intensity manifests in a laser induced vertical temperature gradient across the channel.

Nodule-like structures appear to have grown on the floor of the crater that may have some correlation with the temperature gradient. Observing the channel, there appears to be a degree of quasi alignment of these nodule-like structures at the base of the crater. The nodules show some evidence of periodic growth. The horizontal bottom lip at the edge of the channel is more continuous than that of the top edge. This may be a result of a slightly higher temperature, causing melting and re-solidification to occur. We note that, under these experimental conditions, a laser fluence of 2.7 Jcm^{-2} is sufficiently high enough to induce melting in all three components, silicon, silicon carbide and carbon. SiC is a compound material that follows the phase separation due to laser irradiation[216].

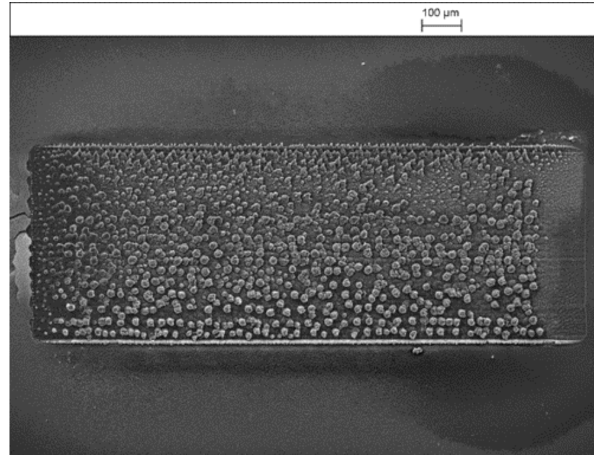

Figure 6.5: SEM micrograph of the laser irradiated 4H:SiC using a 193 nm laser at fluence 2.7 Jcm^{-2}.The sample was translated relative to a stationary beam along the long direction at a speed of 0.005 mms^{-1}. The irradiated sample received 1000 overlapping laser pulses.

Figure 6.6 shows a set of four SEM's of the same ablation site shown in Figure 6.5 but at different magnifications. The size of typical structures is ~15 µm across, and the nodules are decorated in places with nano-sized spherical particles. The micrograph shows the non-homogeneous laser beam effect on the surface. This was solved using a different part of the beam since the beam dimension was (4×20) mm. The spherical geometry of the nanoscale particles may also suggest the presence that melting has taken place. The spherical particles differ in size but are estimated to be in the range of about 500 nm to 1000 nm. Ripple-like features are also observed on the bottom of the crater; see Figure 6.6(d). The period of these ripples is estimated to be in the range of~ 600 nm to ~1400 nm. On heating, silicon carbide dissociates with the loss of silicon, followed by the loss of Si_2 and Si_2C[217,218].

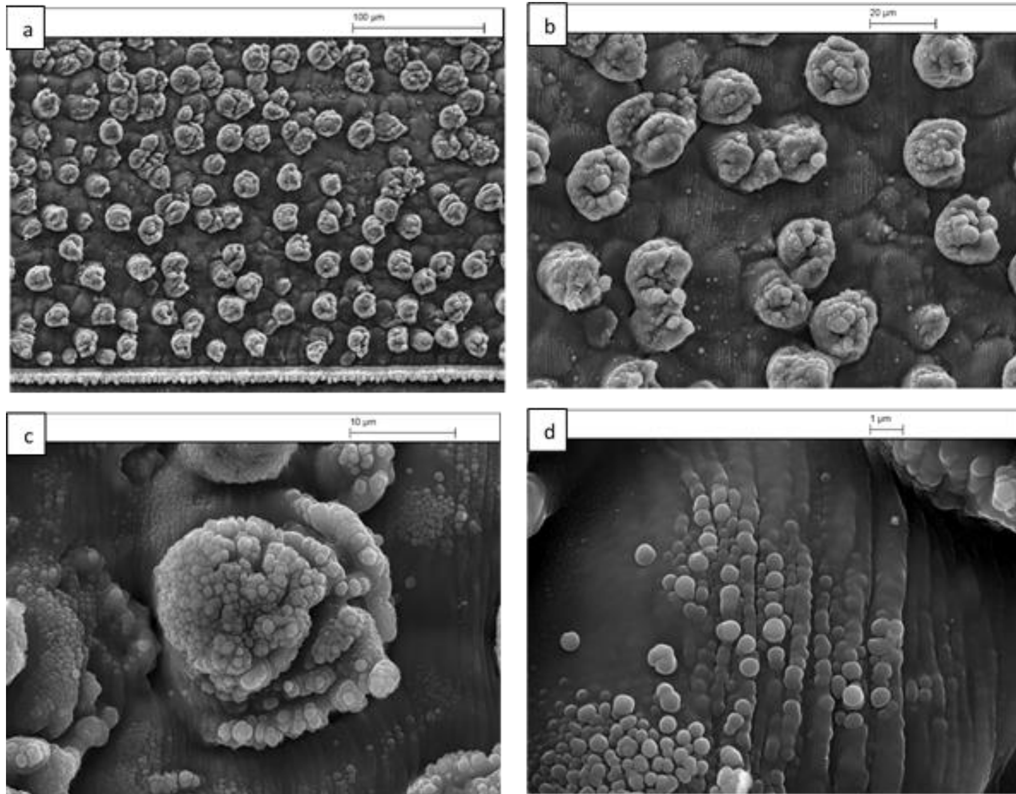

Figure 6.6: High-resolution SEM micrographs of 193 nm laser ablated 4H:SiC site. Laser ablation was carried out at a laser fluence of 2.7 Jcm^{-2} applying 100 laser pulses, a) structures on the crater floor close to the crater edge, b) magnified view of the structures, c) a single microstructure decorated with nano-sized particles, d) increased magnification showing the microstructure consists of spherical droplet-like particles and the formation of ripples.

It has been previously reported that as the temperature of laser irradiated 4H:SiC increases one experiences phase separation [216] forming regions rich in silicon and carbon. In crystalline materials, it has been found that surface modification by a laser beam is dependent on the specific crystallographic plane irradiated. The melt temperature of silicon is ~1700 K, and from the simulations in chapter 5, this corresponds to a laser fluence of 970 $mJcm^{-2}$, see (Figure 5-17). The existence of silicon-rich regions take place due to the melt temperature that is above 1700 K. Si has the highest vapour pressure of the three components to be evaporated from the surface. At a higher laser fluence of 2.7 $Jcm^{-2,}$ the surface temperature reaches ~4195K, which is above the melt temperature of silicon and silicon carbide and close to the melt temperature of carbon[210]. At this higher laser fluence, melting of the silicon carbide may lead to phase separation, clustering of silicon and the effusion of silicon-rich regions.

6.1.2 **Excimer Laser Micromachining of 4H:SiC using a Stationary Sample**

Here we report experiments carried on 4H:SiC using a range of laser fluences on a stationary sample.

6.1.2.1 Effect of Laser Fluence on the SiC Structure

The effect of laser fluence on the surface of 4H:SiC was investigated. Samples were irradiated at a 10 Hz repetition rate and 100 pulses with laser fluences ranging from 1 to 5 Jcm^{-2}. Figure 6.7 illustrates the decreasing depth of the ablation crater with decreasing laser fluence.

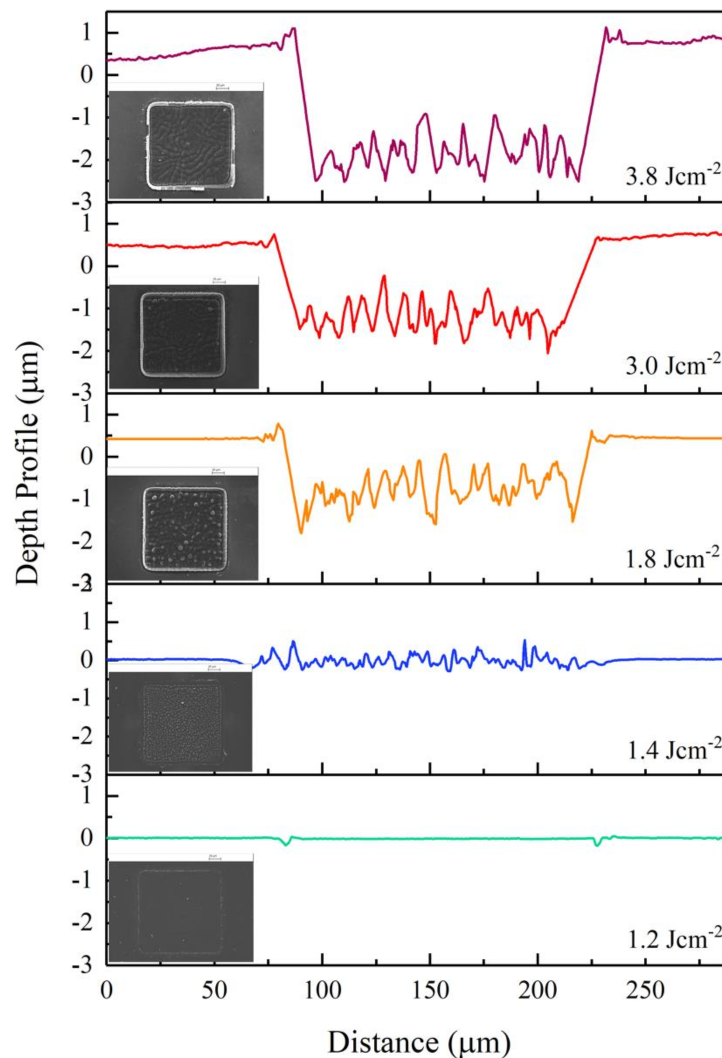

Figure 6.7: WLI 2D profile of the irradiated SiC with different laser fluence with 100 pulses per site.

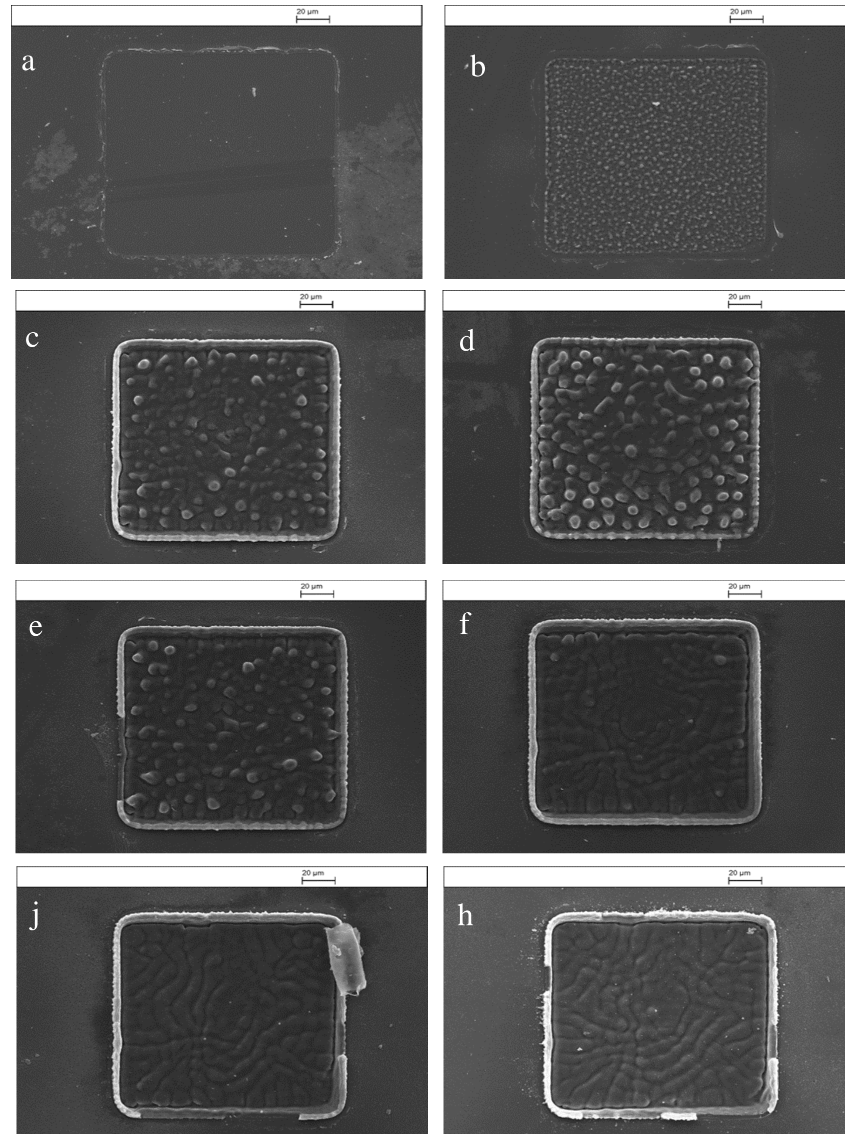

Figure 6.8: SEM micrographs of laser squared imaged sites on 4H:SiC surface at 100 pulses with different laser fluence (a) 1.2, (b) 1.4, (c) 1.8, (d) 2.2, (e) 2.6, (f) 3.0, (j) 3.4 and (h) 3.8 Jcm^{-2}.

Figure 6.8 shows an enlarged SEM micrograph corresponding to some of the insets in Figure 6.7. As a binary material, treating SiC with a laser will induce defect due to the fast and rapid solidification after melting, and the difference in evaporation on Si over C. This will alter the composition of the SiC. 100 Pulse with fluence close to threshold fluence caused almost no change in the surface of SiC neglecting the edges of the laser spot. By increasing the laser fluence, surface roughness was introduced by the incongruent melting of SiC. The Si-rich regions found to be the brighter, while the C-rich regions appears to be darker as suggested Raman. This indicates the segregation of both

Si and C with the loss of material by ablation or evaporation. With an increase in laser fluence, small bumps were distributed on the surface. However, these bumps will disappear, leaving a crater that is almost 3 μm in depth. As the laser fluence is increased, further an undulating surface topology begins to develop. This could be discussed as the generated heat with the laser duration would not have enough time to diffuse into the bulk. Thus, the heated layer will suffer sublimation or ablation. In addition, the rapid quenching speed of laser heated spots could induce regrowth of the melted layer into the metastable form of Si_xC_y or carbidic regions mixed with regions of pure Si and C[117]. In general, there will be an ordering of SiC before segregation of both C and Si. SiC-surface exposure to excimer laser leads to a surface and near-surface modifications, without bulk heating of SiC. The effects include the removal of surface oxide, reordering, surface graphitization, segregation of the components, and ablation[117].

The roughness also increased with the applied laser fluence, see Table 6-2. The roughness increased from 3.2 to 430 nm when the laser fluences increased from 1.2 to 2.2 Jcm^{-2}, while a further increase in the applied fluence reduced the roughness. A laser fluence of 2.6 Jcm^{-2} resulted in a temperature exceeding the melting temperature of SiC and its components. Increasing this laser fluence, further the measured surface roughness decreased.

Table 6-2: Roughness measurement of the irradiated SiC with 193 nm laser conducted at different laser fluences. The measurements were taken by WLI.

Fluence (Jcm^{-2})	1.2	1.4	1.8	2.2	2.6	3	3.4	3.8
Roughness Ra(nm)	3.2	123	390	450	430	409	395	370

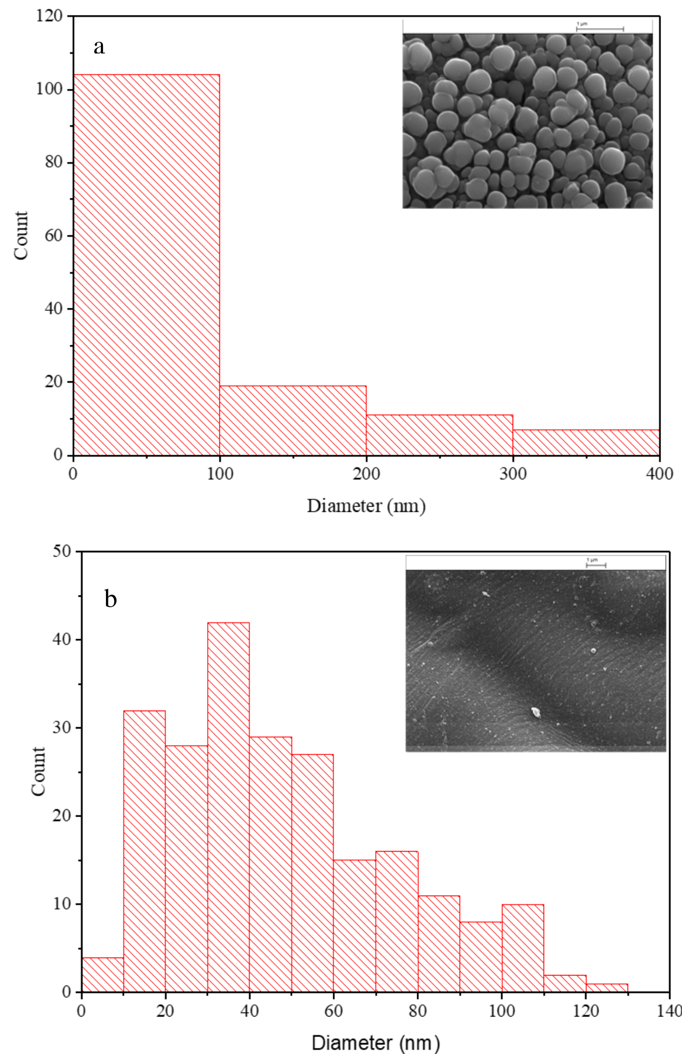

Figure 6.9: Histogram of the nanoparticle distribution on the irradiated site of SiC under Excimer laser. (a) At laser fluence of 2.6 Jcm^{-2} and (b) 5 Jcm^{-2}.

Furthermore, post experimental analysis of SEM's of the surface was conducted using Image J software. Figure 6.9(a) represents the histogram of particulate size distribution of that has been produced at a laser fluence of 2.6 Jcm^{-2}. While Figure 6.9(b) shows the histogram data for SiC irradiated at a laser fluence of 5 J.cm^{-2}. It shows that with 2.6 Jcm^{-2} laser fluence, the surface will be covered with nanoscale SiC particulates that are about 100 nm in size. Increasing the laser fluence to 5 Jcm^{-2} a smaller range of nanoparticles were distributed on the surface with notification of deeper crater formed by the laser.

To understand the decomposition of the formed nano-particles and ripples on the surface, Raman measurement was carried out, as shown in Figure 6.10. Raman spectra was

collected using an excitation wavelength of 532 nm. The Raman spectra shows the same peaks of bulk as received. 4H:SiC. It shows the planar modes E_1 and E_2 with the axial modes A_1 of SiC. The transverse optic peak, E_1(TO), was detected at 780 cm^{-1}, and the longitudinal optic peak, A_1(LO), appeared at 970 cm^{-1}. The folded transverse optical mode F_0(TO) was seen as a weak peak at 796 cm^{-1}. F_0(TO) band is Raman inactive using the (0001) face and it was activated by stacking faults of 4H:SiC. This mode could be used to monitor the stacking faults density. While other peaks were independent of the stacking faults density. Moreover, the C-C and Si bands were slightly observed in the spectrum, indicating slight damage on the surface.

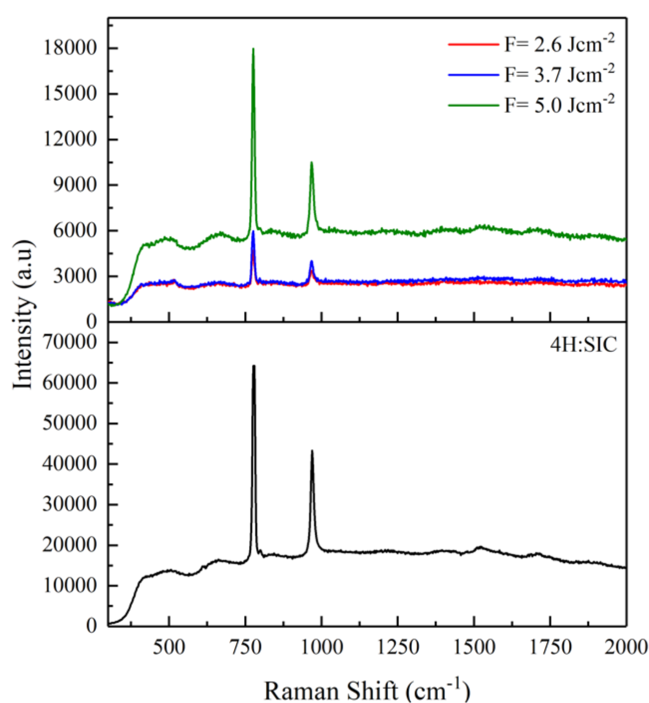

Figure 6.10: Raman Spectra of a reference 4H:SiC (bottom layer) and surface irradiated 4H:-SiC with 193 nm laser at different fluences (top layer).

In addition, the background effect observed, which is believed to be related to the excitation wavelength. The peaks intensity has dropped drastically after laser processing. In general, the intensity depends on the Raman excitation light source, the intensity and wavelength, and the sample concentration or the particle number and its scattering properties. Since the Raman source kept fixed; thus, the drastic drop in the Raman peaks was related to the formation of nanoparticles and the concentration of the material in addition to the modification of the sample crystallinity. Furthermore, changes in the

spectra were observed regarding the peak position, and it's FWHM[219]. The change in the peak position is a function of the structure, and its FWHM gives information on the crystallinity, defects and doping. Hence, when the defects increase, the LO phonons shift to a higher frequency and broadens asymmetrically. This is because of the electric field of the carriers and defects that interacts and modify the Raman cross section[220]. It appears from the above that by increasing the applied laser fluence, the LO peak position has a blue shift from 970 to 968 cm^{-1} corresponded with broadening the FWHM.

In summary, defects and doping create broadening and asymmetry since it induces a loss in periodicity and symmetry with disordered crystal. LO phonon is affected by the size confinement effect more than the TO phonon. Thus, it is logical that the LO mode intensity would enhance as the nano-crystallite size becomes larger.

6.1.2.2 Effect of the Number of Laser Pulses on the SiC Structure

The effect of the number of laser pulses 4H:SiC was investigated. The laser fluence was around the threshold fluence of ~1.2 Jcm^{-2}. The structure was studied optically by an optical microscope and WLI to observe the depth and the roughness.

Figure 6.11 shows the micrograph of the two regions in the irradiated spot, the centre and the outer ring with a rim. The centre region appears identical to un-irradiated SiC. The irradiation effect is limited to the surface as indicated by the WLI profiles, see Figure 6.12 and Table 6-3. The ring region was evident, and it was more noticeable with increasing the laser pulses number. The above effect was attributed to the diffraction of the used shadow mask. The rim believed to be created by the re-solidification of the molten material during the ablation at the edge. This can be justified despite the used laser fluence using the effect of wall reflection. Gower et al [169] used the Zemax optical ray tracing code to model the flux distribution at the sample. It showed that wall reflection will distribute the laser power away from the centre of the irradiated spot to the edges with up to 35% concentrated fluence [169]. The effect of the pulse was shallow; thus, the process conducted by overlapping 10,000 pulses to measure the average depth. The average depth was divided by the number of pulses to measure the effect of individual pulse experimentally. It was then compared to the theoretical depth measurements. The above study was repeated at laser fluences of 0.9, 0.95 and 1 Jcm^{-2}, see Table 6-4.

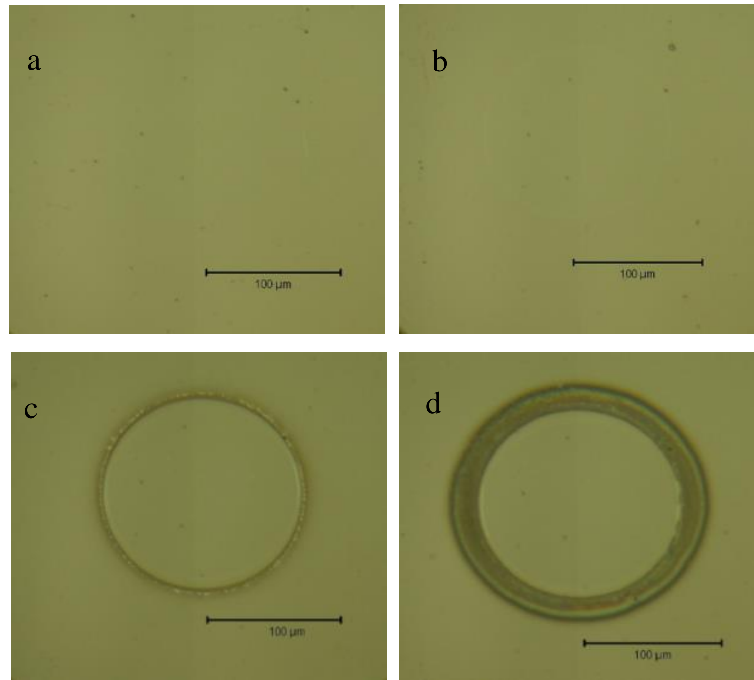

Figure 6.11: Optical micrographs of the laser irradiated SiC using a circular mask at 1.2 Jcm^{-2}. It shows the effect of different number of laser pulses (a) 1 pulse, (b) 10 pulses, (c) 100 pulses and (d) 1000 pulses

Table 6-3: WLI roughness measurements of SiC samples irradiatedwith different pulse numbers near threshold fluence.

No. of Pulses	Roughness Ra (nm)
1	3.26
10	2.8
100	3.9
1000	30

Table 6-4: WLI depth measurements for the 10000 overlapped pulses at different fluences around the threshold.

Fluence (Jcm^{-2})	$Depth_{ave}$ (µm)	Depth per pulse (pm)
0.90	0.13	13
0.95	0.466	46
1.00	0.65	65

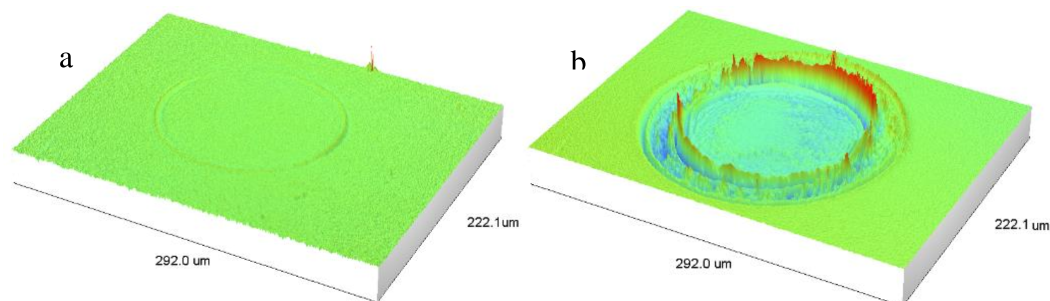

Figure 6.12: 3D surface mapping of the SiC irradiated with different number of laser pulses (a) 10 pulses and (b) 1000 pulses

Raman spectra collected at the centre and the outer ring of the sites, as it can be seen in Figure 6.13. Raman excitation laser was 784.92 nm. The insets in Figure 6.13 represents zoomed in images of the Raman peaks. The change in the peaks is almost negligible, indicating that no structure change takes place at the centre of the site. However, the difference between the centre and the edge of the site was indicating the change of structure, especially in the case of a high number of the pulse as in 1000 pulses. This difference was justified by the wall reflection as mentioned earlier[169]. The difference especially increased in the case of high number of pulses as in 1000 pulses due to the heat accumulation[221].

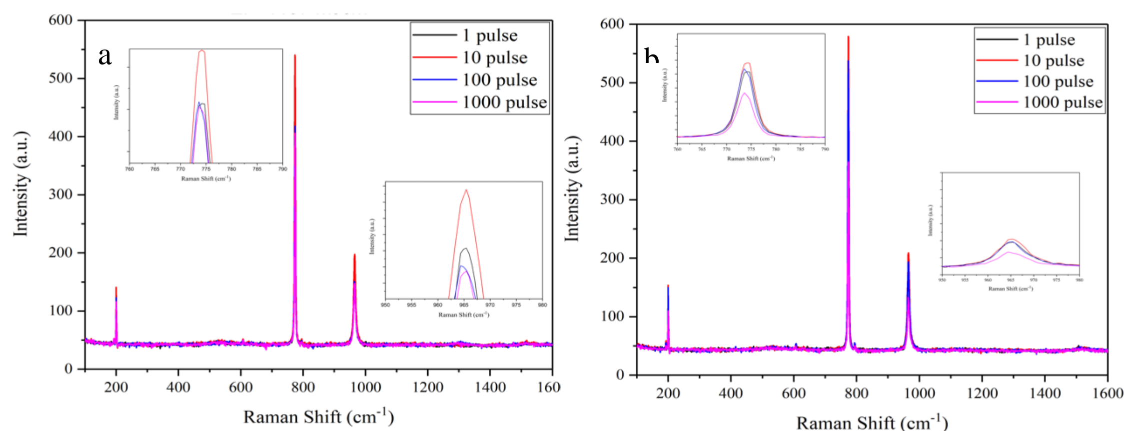

Figure 6.13: Raman spectra of the irradiated SiC sites as a function of the number of applied laser pulses on SiC (a) at the centre of sample (b) at the edge of the sample.

6.1.3 **Travelling Micromachining of 4H:SiC**

Moving laser processing is necessary for laser direct write on SiC surface, mainly for electronic applications. However, laser-travelling speed influences the laser interaction and the decomposition of SiC. In general, the total power will be the sum of the power necessary to heat the site (the melting power and the losses due to conduction and radiation). Considering melting, the heating depends on the processing speed while the heat losses depend on the cubic root of the travelling speed[222]. Meaning higher speed leads to less heat losses in the material. However, the number of overlapped laser pulses will play an important role in the outcome, as we will discuss.

Figure 6.14 shows the optical micrographs (left side) and the corresponding SEM images (right side) of the different number of overlapped pulses (3, 15 and 75 pulses per site of 150 μm). Different structure achieved as a function of the number of overlapped laser pulses. The surface roughness increased from 7.12 nm for reference SiC to 14, 12.3 and 145.7 nm at 0.5, 0.1 and 0.02 mms^{-1}. At low travel speed, more energy was absorbed, indicating further processing. Figure 6.15 shows the surface composition of the irradiated area as a function of the overlapped laser pulses. It is worth mentioning that the Raman spectra were taken for one identical point for all the tracks using a slit of 0.05 mm and a time of 0.5 s at an excitation laser of 532 nm. A huge decrease in the peak intensity took place with decreasing the travelling speed compared with Raman spectra of a reference SiC. Moreover, a Si Raman peak was noticed with low speed of 20 μms^{-1}. For the other travelling speeds of 0.5 and 0.1 mms^{-1}, the outcome was only a minor decrease in the Raman peaks with increasing the number of overlapped pulses.

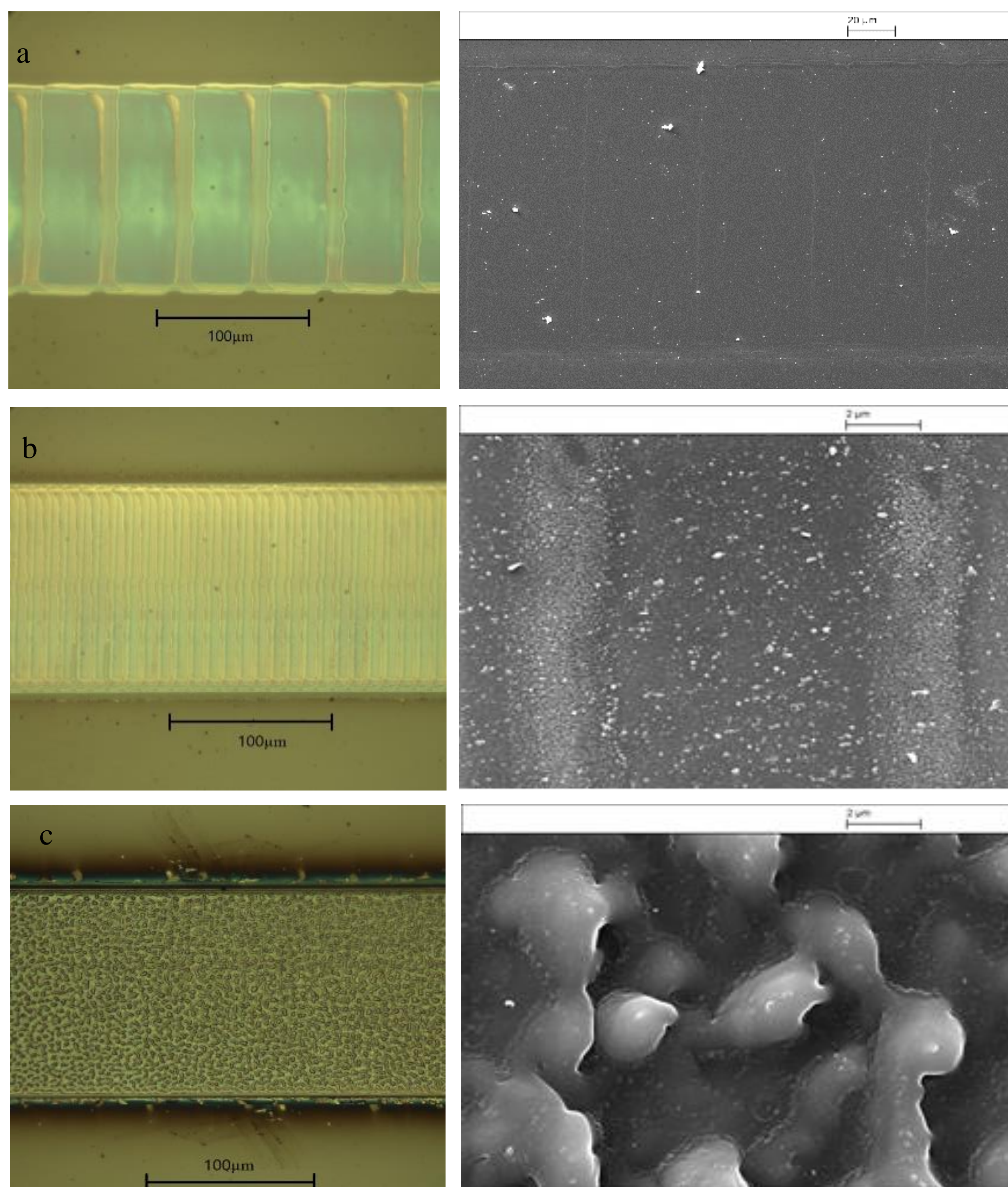

Figure 6.14: Optical micrographs (left side) and the corresponding SEM images (right side) of irradiated 4H:SiC with different travelling speed (a) 0.5 mms^{-1} (b) 0.1 mms^{-1} and (c) 0.02 mms^{-1}.

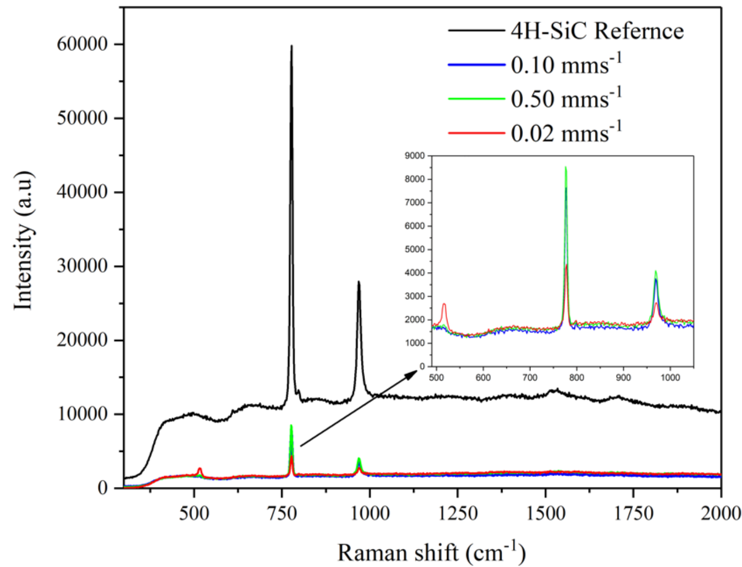

Figure 6.15: Raman spectra of irradiated SiC with 193 nm laser at laser fluences of 1.6 Jcm^{-2} at different travelling speed with a reference of un-irradiated SiC

Detailed investigation on the number of overlapping pulses carried out using a circular projection. The fluences were set to 1 and 1.4 Jcm^{-2}. The overlapped laser pulses calculated accordingly to be 10, 100 and 1000 pulses per site. The effect of using a circular mask was obvious on structure, see Figure 6.16.

For 1 Jcm^{2} fluence, the width of the irradiated track was roughly the same while for 1.4 Jcm^{-2}, an increase in the channel width takes place with increasing the number of overlapped pulses.

AFM was used to investigate the topography. The system has high spatial resolution and so it is useful to measure subtle laser induced surface modifications. The image analysis was conducted using the software, Nanoscope from Bruker. The analysis dimension was only 10×10 µm^{2}. Figure 6.17 shows the entire features extracted from the AFM images for both fluences, including the nanometre-dimension roughness, the highest Asperity "peaks or high spots on surfaces that come into contact during wear or friction"[223] and the bearing depth "which is essentially an integral of the height histogram from the top surface i.e., a plot of the percentage of data points at or above a given height" [224] for each scan area . For un-irradiated SiC the roughness was around ~1.45 nm, it shows as smooth sharp hills. After laser ablation, the roughness increased and the texture was similar to rounded hills. This may be an indication of the surface melting during the laser pulse.

From the roughness measurement, the roughness increased with laser irradiation. However, it fluctuated with the overlapped laser pulses. It increased with both fluences with both 10 and 100 pulses but decreased with the 1000 overlapped pulses.

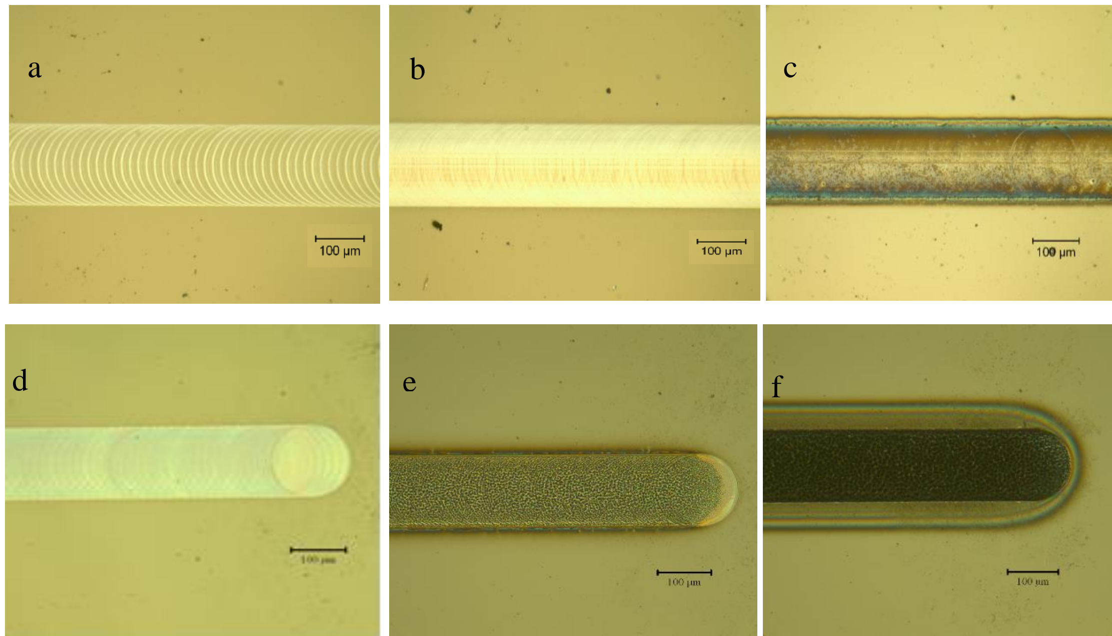

Figure 6.16: Optical micrographs of SiC ablated with fluence of 1 Jcm^{-2} (top row) and 1.4 Jcm^{-2} (low row) with different overlapping pulses (a,d) 10, (b,e) 100 and (c,f) 1000 pulses per site.

According to Figure 6.17, the shape of the SiC surface is valleys and hills. Moreover, the peaks or hills are dominant since the skewness has a positive value. For the fluence near the threshold, the 10 overlapped pulses have a uniform smooth surface with the edges of the mask. The size histogram was mostly around 50-60 nm. By increasing the pulses to 100, aggregations of material show on the surface with a size distribution around 85 and 100 nm. Further increase in the overlapped pulses produced doubled size dimensions on the surface (around 250 nm). For all the above, the shapes on the surface seem to have the same orientation. This could be related to the orientation of the irradiated SiC. In general, there is a tendency to form nanostructure SiC at the surface when it processed with low laser fluence (near the threshold).

Different morphology observed on the surface of SiC when irradiated with fluence of 1.4 Jcm^{-2} compared to sites processed with 1 Jcm^{2} laser fluence, see Figure 6.18. A smooth surface of R_a 1.9 nm was obtained when 10 laser pulses overlapped. This gave a

smoother surface than the 10 pulses with 1 Jcm^{-2}. By increasing the pulses to 100, a substantial relative increase in the surface roughness took place with R_a 179 nm. In addition, the size dimensions on the surface were measured in microscale. Interestingly, more overlapped pulses with 1000 lead to a decrease in both the surface roughness and the size histogram compared to 100 pulses, see Table 6-5.

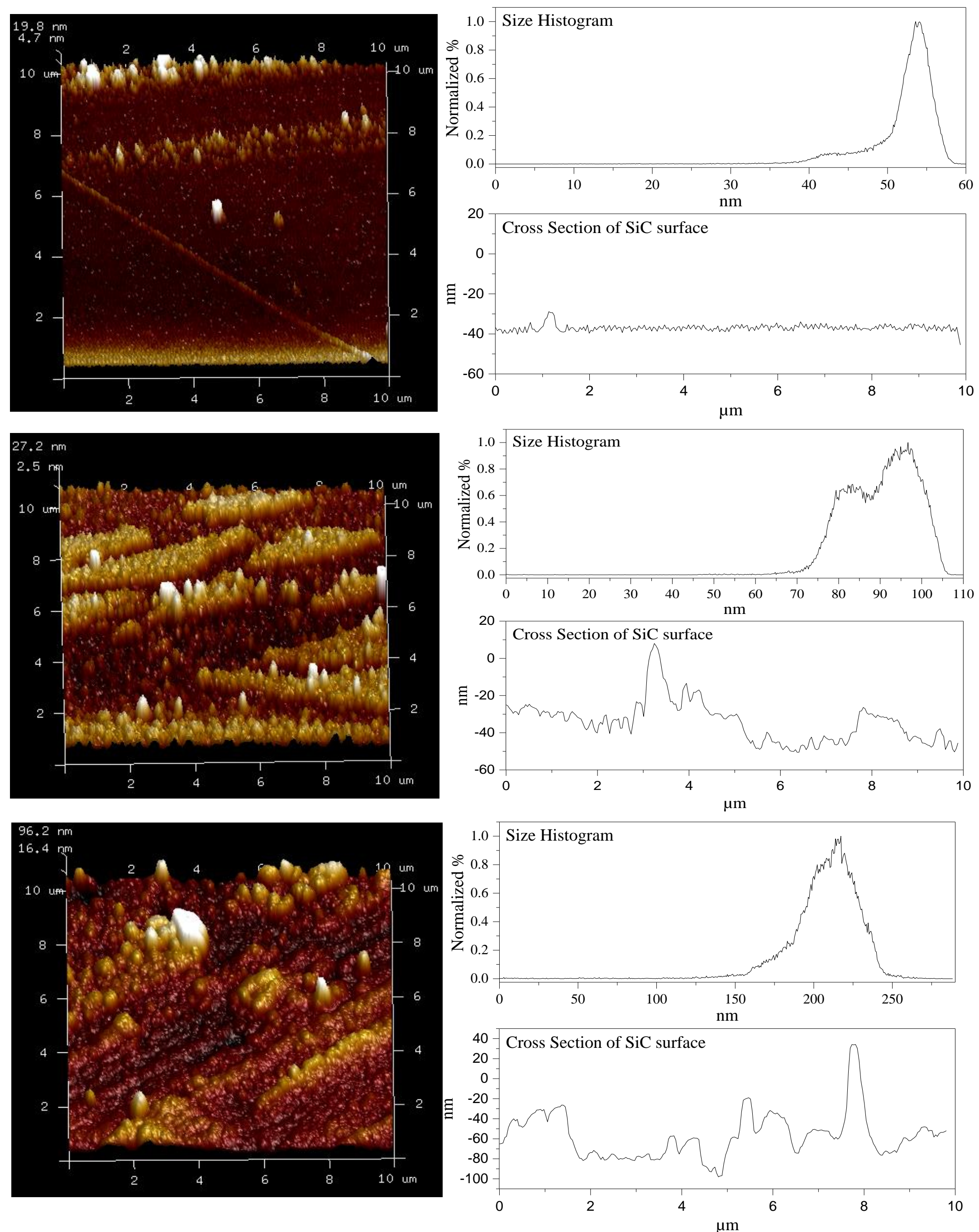

Figure 6.17: AFM images of SiC irradiated with 193 nm laser at a fluence of 1 Jcm^{-2} with different overlapped number of pulses (a) 10, (b) 100 and (c) 1000.

It appears that a higher temperature can stimulate the migration of grain boundaries and increasing the coalescence of more grains during the laser pulse, as suggested by Lin et al.[225]. While Fang et al.[226] explained that higher temperature leads the atoms to diffuse and fit in the lattice of the crystal. He also suggested that the smaller grains would aggregate into larger shapes with increasing temperature. Moreover, the surface roughness would increase[227].

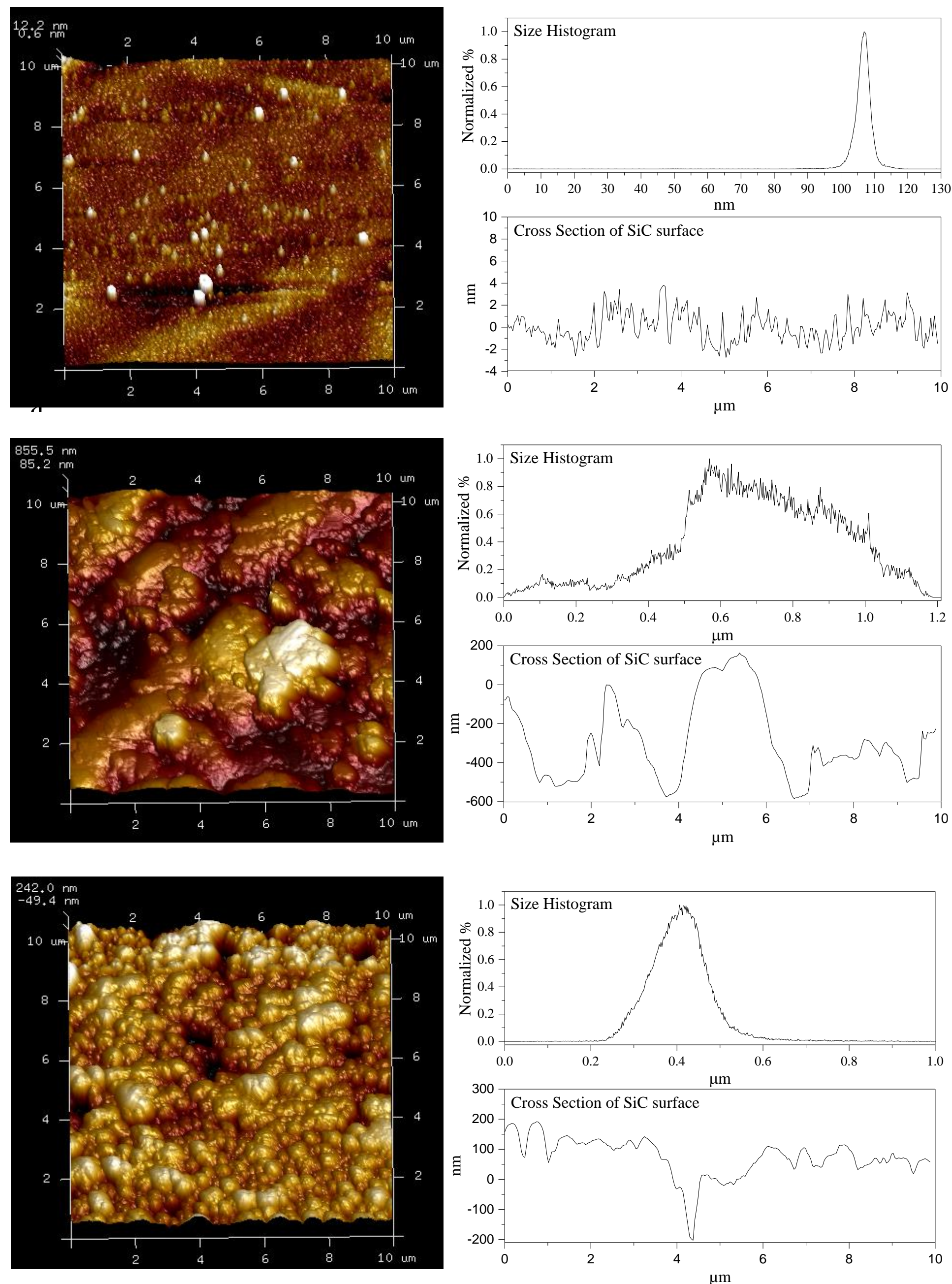

Figure 6.18: AFM images of SiC irradiated with 193 nm laser at a fluence of 1.4 Jcm^{-2} with different overlapped number of pulses (a) 10, (b) 100 and (c) 1000.

Table 6-5: AFM characteristic for irradiated SiC under different fluences and different overlapping pulses.

Fluence (Jcm^{-2})	**Overlapping pulse**	**Roughness Ra (nm)**	**Highest Asperity (Δz) (nm)**	**Bearing Depth (nm)**
Un-irradiated SiC	-	1.45	30.5	19.5
1.4	10	1.9	107	64
	100	179	569	590
	1000	53	40.5	490
1	10	2.9	53.5	30
	100	6.9	967	54
	1000	15.6	217	141

6.1.4 **Raman Investigation and Laser Surface decomposition of SiC**

6.1.4.1 Raman Spectra of the Stationary Laser Irradiated SiC

Micro Raman measurements were carried on a static ablation crater to investigate the decomposition of 4H:SiC.

Measurements were recorded at different locations inside and outside of a static ablation crater at five different spatial locations, see Figure 6.19 and Figure 6.20 show the results of the micro Raman measurements over different regions of the wavenumber. Micro Raman measurements were carried out on a clean silicon wafer and an as-received 4H:SiC sample for reference purposes. Both micro Raman reference signatures are shown at the bottom of Figure 6.20. The observed peaks at 204, 777, 798 and 970 cm^{-1} are related to silicon carbide and correspond to locations 2, 3, 4 and 5. Region 1 shows strong evidence of a silicon-rich region that slightly protrudes the floor of the ablation crater to form an island-like region. Region 2 is characteristic of silicon carbide with the presence of a small silicon peak at 520 cm^{-1}, which may suggest the agglomeration of silicon at the surface. Regions' 3 and 4 are the inner and outer perimeters of the ablation crater, respectively.

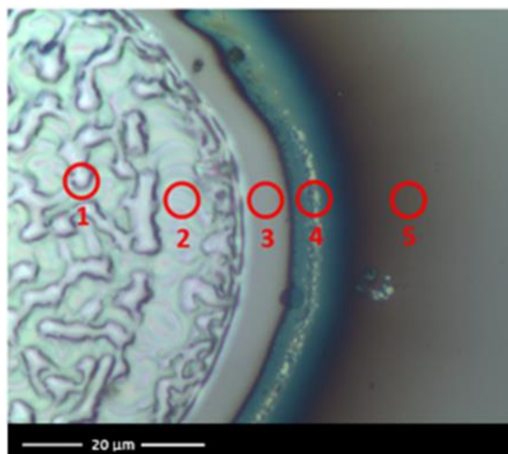

Figure 6.19: SEM micrographs of 193 nm laser ablated 4H:SiC irradiated at a laser fluence of 1.7 Jcm^{-2} and receiving 100 laser pulses at a pulse repetition frequency of 1 Hz. Positions 1-5 indicate the spatial locations of the micro Raman measurements.

The micro Raman spectra are very similar over the lower wavenumber range. However, the spectra are vastly different over the wavenumbers, 1000-3000 cm^{-1}. Figure 6.21 shows two intense peaks related to graphite at 1355 cm^{-1} and 1575 cm^{-1}. These peaks are the well-reported *D* (disorder) and *G* (graphite) peaks of graphite, respectively. Both *D* and *G* peaks are clearly observed at location sites 1-3. The emergence of these peaks is a result of 193 nm laser radiation and the formation of graphitic species on the surface of silicon carbide. However, the strength and widths of the *D* and *G* peaks differ between sites. At location 1, the signal intensity is much weaker compared with the peaks at locations 2 and 3, indicating the regions have a different structure. Micro Raman measurements were also carried out on the circumferential lips at positions 3 and 4. The inner and outer regions appear different in the SEM micrograph and are confirmed in the micro Raman measurement. At location 3 the spectra are characteristic of both silicon carbide and graphite whereas location 4 has a very broad *D* and *G* peaks, but they are less pronounced and buried within a very broad band. This band may arise from intermediary carbon species derived from initial steps of the silicon carbide decomposition process. In addition, the broadening of the *D* and *G* peaks is characteristic of amorphous materials. The origin of the *D* peak at 1335 is due to increased phonon density of states of disordered graphite. Turning our attention to the *G* peak that has been observed from measurements on the outer circumferential lip in position 4. This peak is centred at 1600 cm^{-1}. Broadening of the peak may be due to an increasing number and size of graphitic clusters. In addition, the broadening may also be an indication of laser-induced stress in the circumferential lip.

It has, however, been reported that the width of the *G* band increases linearly with stress in amorphous carbon[228].

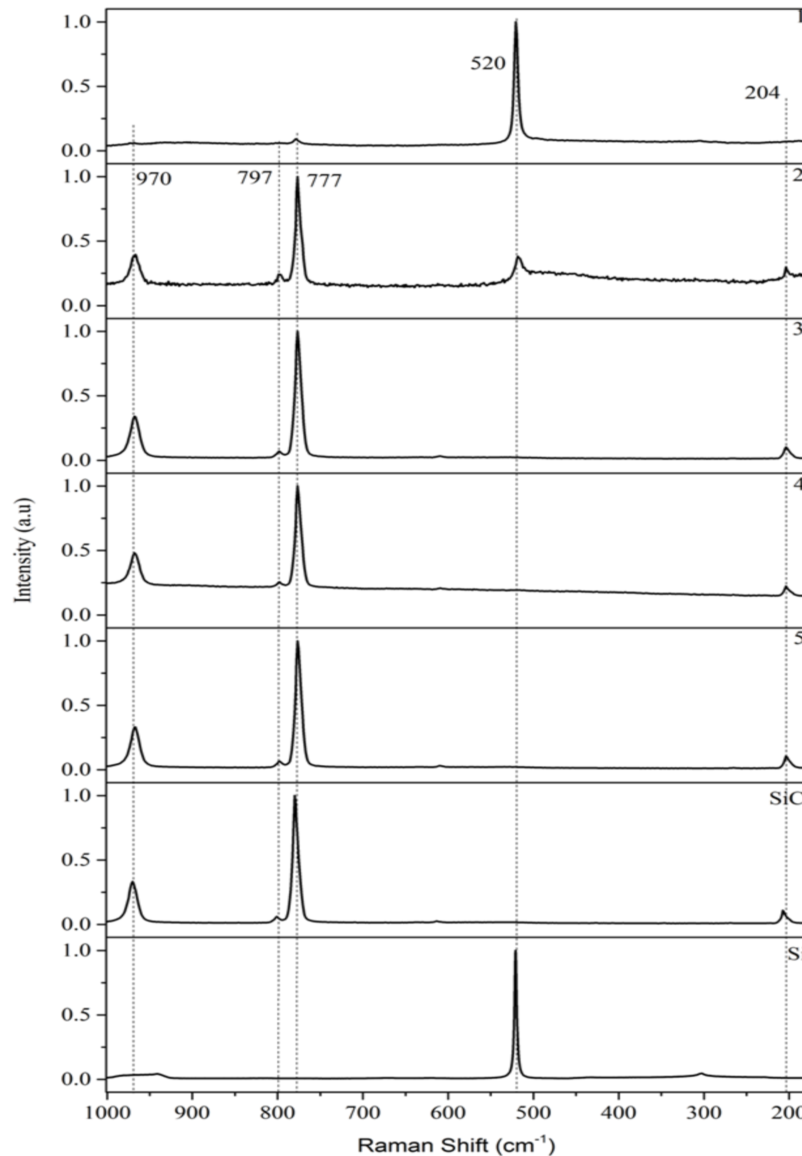

Figure 6.20: Micro Raman spectra of the 193 nm laser irradiated 4H:SiC at a laser fluence 1.65 Jcm^{-2}. The numbers in the right-hand corner correspond to the positions shown in the SEM in. Micro Raman measurements were acquired using an integration time of 300 seconds, and two measurements were averaged. Excitation using a 632.8 nm He-Ne laser at a power of 12 mW and a 100 × microscope objective.

At location 5, one can see evidence of re-condensed ablation debris on top of the silicon carbide substrate. The micro Raman data at this position is almost identical to that of the 4H:SiC reference measurement. This suggests that the debris consists of silicon carbide

or that the debris on top of the substrate is very thin such that the measured micro Raman signal is that of the underlying substrate. These results indicate the complexities of laser induced dissociation of 4H:SiC. A detailed study dedicated to Raman measurements are shown later.

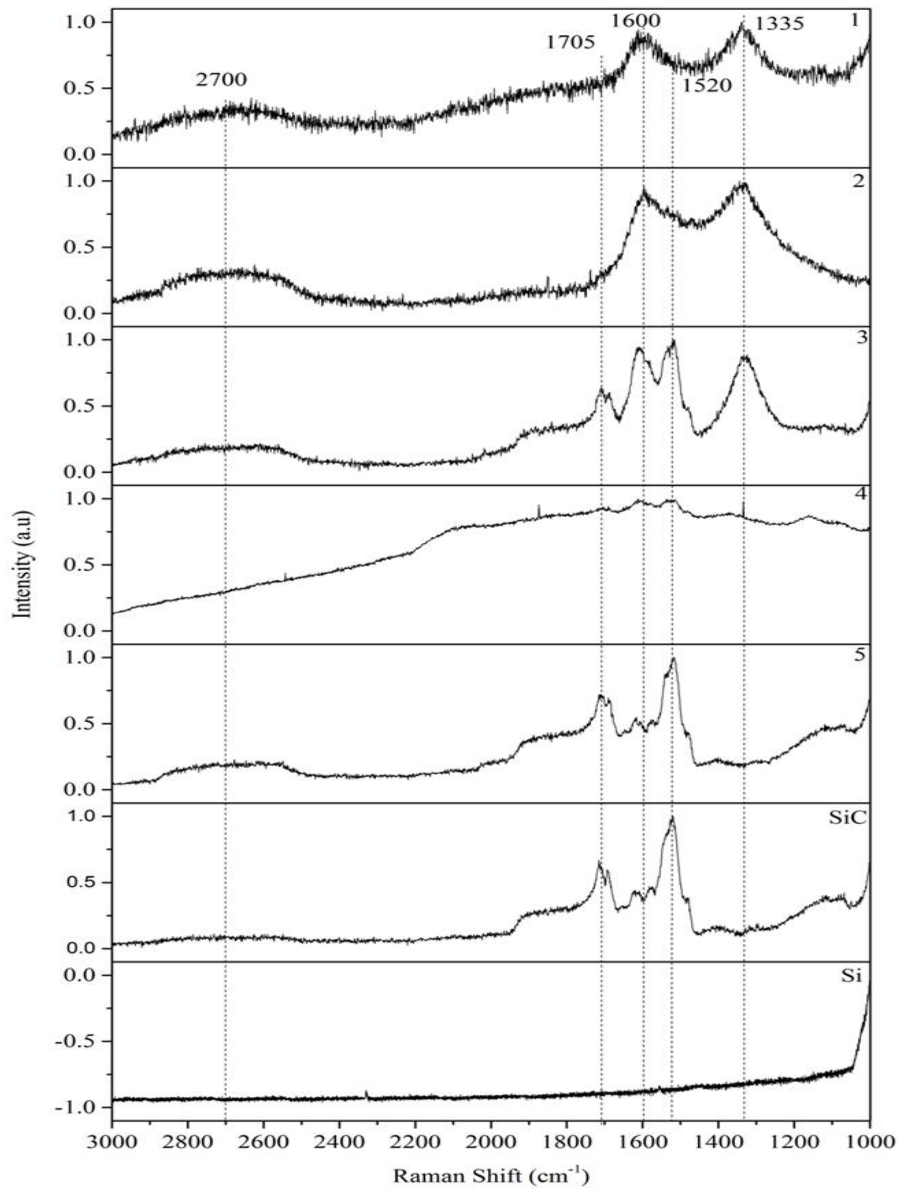

Figure 6.21: Micro Raman spectra of the 193 nm laser irradiated 4H:SiC at a laser fluence 1.65 Jcm^{-2}. The numbers in the right-hand corner correspond to the positions shown in the SEM in. Micro Raman measurements were acquired using an integration time of 300 seconds, and two measurements were averaged. Excitation using a 632.8 nm He-Ne laser at a power of 12 mW and a 100 × microscope objective.

6.1.4.2 Raman Spectra of the Travelling Laser Irradiated SiC.

Raman analysis employed on the scanning laser irradiated SiC to understand the surface decomposition. It was conducted with multi-wavelength Horiba (Jobin Yvon). The applied wavelength was 784.92 nm through a filter to reduce the laser power by 90% on a slit size of 250 µm. Multiple Acquisition was applied to get more precise measurements. This wavelength allows the information to be collected from different depths in the samples according to the relation ($2.3/2\alpha$)[219]. This relation gives the theoretical penetration depth in the sample for the used wavelength depending on the absorption coefficient of the material α and it was integrated from the total scattered light intensity in Raman spectroscopy[219]. Micro Raman reference signature is shown at the bottom of Figure 6.22. The C-C and Si bands were not observed in the spectrum, indicating negligible damage on the surface. The measurements were applied for different locations inside the channel irradiated with 1 Jcm^{-2} at different overlapped laser pulses. It shows that there are two patterns overall the site, the edge area surrounding the pulses projection (inside the spot and at the edge) and the inner of the spot. This was repeated for all sets. For 10 overlapped pulses, the Raman inside the laser spot indicates the same peaks as the un-irradiated SiC, which was expected since our irradiation fluence was near the threshold. While the edge spectra reveal a broadening around the area of Si peak around 450-550 cm^{-1}, this could be related to the Si-O-Si vibration according to the Raman data library provided by Horiba. However, broadening behaviour indicates the amorphous structure. This might be explained as the start of decomposition of the SiC in the air to amorphous silicon and forms of silicon oxide. According to thermal simulation, the temperature here exceeds the melting point of Si, adding the advantage of using high energy of 193 nm laser. In addition, this area receives more energy due to the superposition and diffraction effect of the mask edge. Further increase in the overlapped laser pulses to 100, no other peaks appeared, and a decrease in the SiC peaks took place which cannot be seen due to the normalisation effect, see Figure 6.22 (third layer from bottom). For the 1000 overlapped pulses, determining the pulse edge was challenging, as shown in micrograph of Figure 6.22 (top layer). The collected Raman spectra from the edge were also identical to the SiC peaks. While the Raman spectra inside the track were more complicated and broadened, it is following, with more intense, the same behaviour of the 10 overlapped

pulses (inside the track) with more obvious broadening effect around the 450-550 cm^{-1} and the sharper peak of the C-O-C at 1100 cm^{-1}. In addition to the above behaviour, a further change in the D and G peaks positions appeared. Using origin software find peaks option, peaks at 1325 and a 1590 cm^{-1} were detected. Furthermore, a massive decrease in the SiC peaks was observed, especially the longitudinal optic peak A_1(LO), at 967 cm^{-1}.

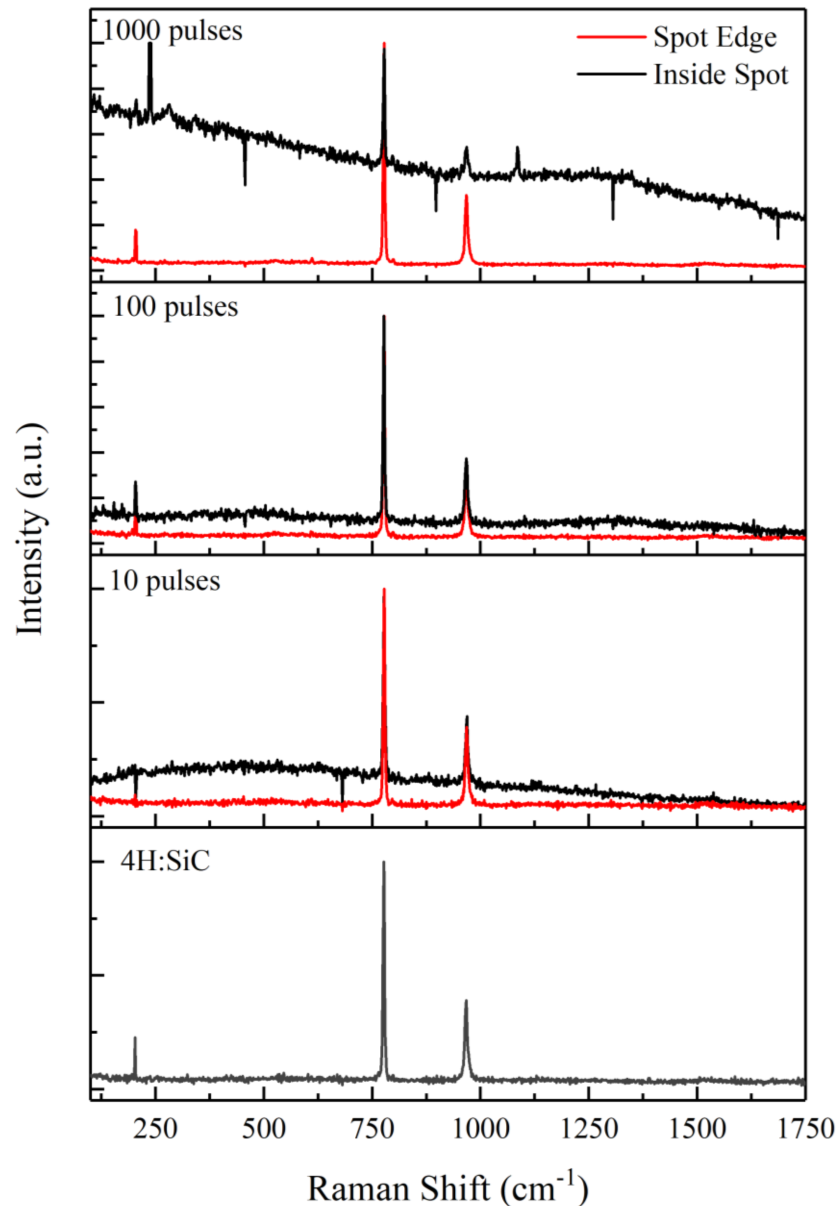

Figure 6.22: Micro-Raman spectra of 193 nm laser irradiated SiC with a fluence of 1 Jcm^{-2} and different overlapped laser pulses during scanning processing (a) 10, (b) 100 and (c) 1000 overlapped pulses. Micro Raman measurements were acquiescing an integration time of 10 seconds, and two measurements were averaged. Excitation using a 784.92 nm at a power of 10 mW and a 50× microscope objective.

Micro-Raman for an applied laser fluence of 1.4 Jcm^{-1} for 10, 100 and 1000 overlapped pulses is shown in Figure 6.23. As always, the (bottom layer) shows the Raman spectra of the 4H:SiC as a reference. Figure 6.23 layers 2, 3 and 4 corresponds to the 10, 100 and 1000 overlapped laser pulses sites, respectively. The measurements were done for the edge and inside the laser spot. The edge spectra of the entire sites were similar to the 4H:SiC reference, especially at the 100 pulses. However, there is an increase in the baseline of the spectra for the other two sites, which is expected to be related to fluorescence, as 784.92 nm excitation wavelength is not entirely free from background fluorescence. With this wavelength, these spectra were collected around the penetration depth of ~400 nm in normal direction on the surface.

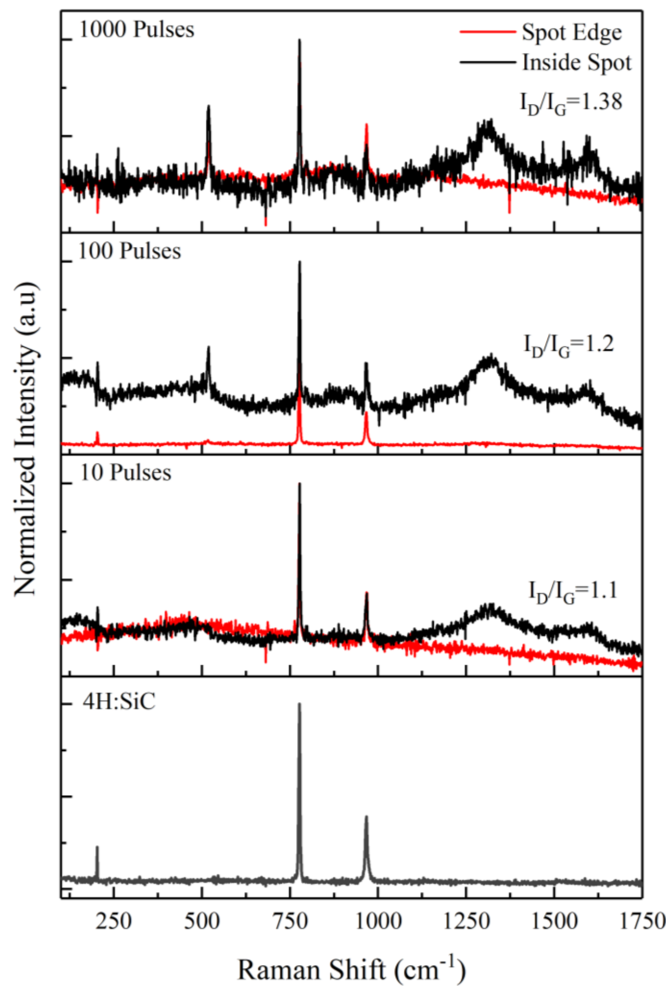

Figure 6.23: Raman spectra of irradiated SiC at 1.4 Jcm^{-2} with different overlapped laser pulses during laser scanning processing starting from bottom to top (1) SiC (2)10, (3) 100 and (4) 1000 overlapped pulses.

In the spot, Raman spectra shows the D and G bands along with the standard 4H:SiC and Si. In all the three samples, the D and G band were available indicating the production of reduced Graphene Oxide (rGO)[229]. The ID/IG ratios were 1.1, 1.2 and 1.38 for overlapped pulses 10, 100 and 1000, respectively. This ratio is less than one in graphene oxide (GO). However, it increases for rGO. It suggests an increase in the sp^2 average size due to the reduction of GO. Further increase in this ratio to 1.49 suggests the formation of 3D-rGO. The applied fluence was simulated using COMSOL and gave a temperature rise above room temperature of ~2300 K. This temperature is higher than the Si melting point, combined with the high laser energy of 6.4 eV. The above combination resulted in the production of graphene oxide (GO) in the first few pulses. However, accumulation of laser pulses was employed to restore the sp^2 groups and in the reduction of GO. Thus, the mechanism of converting SiC to GO or rGO can be understood as a laser-assisted oxidation or reduction process. The absorption of the relatively high-intensity laser by SiC gives rise and increase the temperature in the exposed area or volume, which in turn oxidises the carbon left behind after Si sublimation in the ambient environment by absorbing oxygen in the air. The laser induced temperature rise of SiC is proportional to the laser fluence.

6.2 Discussions

6.2.1 Light-Matter Interaction

Absorption of nanosecond laser pulses rapidly transfers energy into a target material. The optical absorption of 193 nm radiation in SiC is strong with an optical penetration depth of, $l_{Opt} = \alpha^{-1} \sim 7$ nm. The reflection coefficient of SiC at 193 nm wavelength *R*= 0.42. Consequently, electromagnetic radiation is strongly coupled in SiC. Strong coupling viewed as being advantageous in terms of high depth resolution during laser processing. Silicon carbide has a high decomposition temperature, and hence laser processing using ArF excimer lasers that have high pulse energy of 6.4 eV is highly suitable. High intensity used to overcome the initial reflectivity and the absorption process would rise by increasing the material temperature. However, the strong absorption and concomitant high reflectivity and relatively high decomposition temperature can make laser processing

challenging if one is trying to realise clean, well-resolved structures. Nevertheless, this work is more concerned with high depth resolution, so the strong coupling, high depth resolution using a 193 nm laser source is useful for this and future work.

6.2.2 **Laser Ablation**

Of the wide range of lasers that are available, UV lasers offer high photon energies that are useful in laser processing. The photon energy of 193 nm radiation is 6.4 eV and therefore, sufficient to break chemical bonds. Laser ablation can be explained with different models, see chapter three, photochemical, photo-thermal and photomechanical, photophysical, or a combination of these. In this work, the pulse duration is in the nanosecond regime, namely ~11.5 ns, full-width-half-maximum. For the ArF laser used in this work, lattice-heating time is larger than the electron heating time $\tau_h > \tau_e$ so, there is sufficient time for electrons to transfer energy to the lattice. Therefore, appears as a rise in the temperature of the material, which may or may not be sufficient to cause melting or sublimation. Silicon carbide is known to sublime under ambient conditions. However, a melt phase also exists if an external pressure is applied that exceeds~ 35 Bar. During laser ablation, however, the pressure, *P* can increase significantly local to the irradiation site, and non-steady state conditions can exist. The pressure induced by a laser typically follow a $P \sim P_0 I^{\alpha}$ dependency, where P_0 depends on the target material, laser wavelength, pulse duration, and expansion geometry, α is scaling parameter that has a value less than unity, and *I* is the Laser intensity. The time-dependent changes in local pressure, due to the absorption of a high-energy laser pulse over a short duration can result in an associated melt temperature that correlates to some extent with laser fluence. As high heating rates take place typically of $\sim 10^9$ Ks^{-1}, laser ablation pressure can play a significant role in the ablation mechanism.

The transient melt phase of laser irradiated 4H silicon carbide using an XeCl (308 nm) has been studied by time-dependent reflectivity measurements [216]. The authors carried out a detailed study and identified melt and re-crystallisation phase transitions of laser irradiated 4H:SiC. It is therefore of interest to identify the laser ablation threshold and surface modifications of silicon carbide at a wavelength of 193 nm. Identification of the ablation threshold is useful for laser annealing and doping studies that require irradiation

to be below the laser ablation threshold, similarly, the formation of oxides by irradiating below the ablation threshold and other surface modifications. Here, the focus was on the morphological changes (mass transport) occurring to 4H:SiC when irradiated with 193 nm radiation from an ArF laser.

6.2.3 **Heat Transfer**

Of great importance in laser processing are the (HAZ) and the optical and thermal penetration depths. HAZ is quantified by the heat diffusion length, $l_{Therm} = 2\sqrt{D\tau_p} \sim 2.8 \quad \mu m$. Comparing these parameters for 4H:SiC the thermal penetration depth far exceeds the optical absorption depth $l_{Therm} >> \alpha^{-1}$, see SiC properties used for depth calculations in chapter two. Temperature rise for the laser irradiated SiC were calculated numerically and analytically in chapter 5. The heat calculations considered normal to the surface. In this case, it is justified as the imaged spot size is much larger (hundreds of micrometres) than both the optical and thermal absorption depths l_{Opt} and l_{Therm}, respectively.

6.2.4 **Enthalpy Model of Melting**

Incongruent melting of silicon carbide has been reported to occur at a temperature of 3100 ± 40 K at atmospheric pressure. However, at higher pressures, in the GPa regime, silicon carbide has been reported to melt congruently. Between these low and high-pressure regimes, silicon carbide has been reported to melt at 35 atmospheres. Thus, the melt temperature will depend on the local pressure as well as the defects of the crystalline SiC. Recently, it has been reported that irradiation of silicon carbide using pulsed lasers leads to the removal of silicon species from the surface. The surface becomes rich in graphitic domains (size ~2.5 nm) and domains of polycrystalline silicon (size ~5 nm). On absorption of subsequent laser pulses, the irradiated site transforms the carbon-rich domains into multi-layer graphene. The number of graphene layers and the amount of graphite on the surface has been reported to be dependent on the number of laser pulses applied [216]. Therefore, phase separation, the quality of the material (intrinsic defect concentrations) and effects of pressure add to the complexity of understanding the

microscopic decomposition of silicon carbide and quantifying an exact melt temperature, see Enthalpy model in chapter three using equations (3.13), (3.14) and (3.15).

6.2.5 Material Vaporisation

Evaluating the amount of material transported away from a laser irradiated SiC can be approached using a surface vaporisation model. This is justified as opposed to volumetric evaporation due to the very strong absorption of the 193 nm UV radiation with the 4H:SiC, $\alpha^{-1} \sim 7$ nm. We estimate the flux of species transported away from the sample surface using the Hertz-Knudson (H-K) and Clausius-Clapeyron (C-C) equations see chapter three. Using equations (3.20) and (3.21), we assume classical kinetic theory (Maxwell Boltzmann) to calculate the flux of species leaving the surface.

Pinning down a value for the sticking coefficient is non-trivial. Strictly speaking, the H-K equation is valid only under equilibrium conditions but is frequently used for near-equilibrium conditions. It has been debated whether one should assign two coefficients, that is, evaporation and condensation (mass accommodation) coefficients. However, quantifying the coupling mechanism between evaporating and condensing species is non-trivial. In this work, we simplify the analysis and use a single sticking coefficient for the entrapment of species returning to the melt of $\theta_s \sim 20\%$. Acknowledging these simplifications, we estimate the depth of material removed because of absorption of UV laser radiation.

Mass transported away from irradiated materials at a known laser fluence is essential in laser processing and especially the depth of an ablation per laser pulse and is discussed in the previous results.

6.3 Summary

Excimer laser irradiation of SiC leads to a variety of fluence-dependent surface and near-surface alterations. The effects could be the removal of surface oxide, re-ordering, surface graphitization, segregation of the components, and ablation. An excimer laser emitting at a wavelength of 193 nm has been used to investigate the ablation and decomposition of

4H:SiC. An onset of surface modification was seen to take place at a laser fluence of 925 ±80 $mJcm^{-2}$. The etch rate and concomitant surface modification at this fluence are observed as a gentle process and not an abrupt removal of material. The experimentally measured etch rate at threshold corresponds to ~200 pm per laser pulse. These etch rates are close to but above the etch rates calculated using the H-K and C-C relations which are calculated to be ~20 pm per laser pulse. Micro Raman measurements indicate their regions of silicon and carbon on the surface of the laser irradiated 4H:SiC. The actual mechanism of the decomposition process stimulated a more detailed study using Raman microscopy. FEM heat transfer simulations of laser-irradiated silicon carbide have been carried out to calculate the laser induced temperature rise as a function of laser fluence. At laser fluences where significant material is being removed, one observes the growth of micron-sized nodule-like structures on the floor of the ablation crater. SEM measurements clearly show the nodules are decorated with spherical particles and ripple structures are observed on the floor of the ablation crater. These experiments have identified an upper limit of the laser fluence when using 193 nm pulsed nanosecond laser radiation. The preliminary investigations are promising and further work using a laser direct write technique to form carbon-based tracks on 4H:SiC substrates was conducted.

Calculated Raman spectra of irradiated SiC with different crystallite sizes were achieved. The TO peak of a small size shows a small position shift, but the LO peak exhibits a downshift and asymmetrical broadening as the nano-crystallite size decreases. The intensity of the TO and LO modes decreases. The scattering can be spread out over a much broader range of frequencies by varying the nano-crystallite size.

In addition, with relatively high fluence irradiation, the surface tends to oxide changing the surface of the SiC into rGO.

As a binary compound, SiC, would have structural changes due to the total energy difference between two crystallographic structures.

Chapter 7 CO_2 Laser Micromachining of Single Crystalline 4H-SiC

7.1 Introduction

In this chapter, micromachining of single crystalline 4H:SiC wafers and the production of graphene layers by CO_2 laser irradiation was investigated. A range of laser fluences were chosen. Other conditions were studied, such as the pulse duration and the spatial overlapping of laser pulses effect. Scanning, and stationary laser ablation were conducted to investigate the effect of motion on the process. The whole process was performed under an ambient atmospheric environment unless mentioned otherwise. Heating and cooling occurred at standard conditions. The surface topography of the 4H:SiC substrate, as well as the surface coated graphene, was characterised and examined by SEM, AFM and Dektak. Micro Raman spectroscopy analyses were employed to demonstrate the presence of graphene layers on the SiC surface and to study the effect of the laser on the surface.

7.2 Laser Ablation Threshold of SiC by CO_2 Laser

Laser ablation of SiC in the IR region is considered as a photothermal process. Depending on the thermal and optical penetration depth, the thermal length is greater than the optical length inside the 4H-SiC, see Table 7-1. Hence, photothermal is a governing interaction mechanism.

The ablation rate was measured by applying 20 Hz pulse repetition rate with a pulse duration of 150 µsec, as shown in Figure 7.1. Ablation rate greatly depends on the spot size of the laser beam. In Figure 7.1 the ablation rate is clearly divided into two regions. This could be due to different mechanisms involved in each range of pulse energy. In region 1, the ablation rate does not change significantly, where the energy is below 9 mJ. In region 2, the ablation rate increases at a faster rate compared with region 1. No

saturation was observed at the laser fluences measured. The diameters of the ablated sites were determined using an optical microscope. From the gradient of the graph in region one, the laser spot diameter was 49 µm with threshold energy of 4.3 mJ. While for the region two, the slope changed dramatically and the laser spot diameter was found to be 150 µm with a threshold energy of 73 mJ from the intercept.

Table 7-1: Calculated thermal and optical penetration depth of CO_2 laser at room temperature with different pulse durations.

CO_2 pulse duration (µsec)	50	100	150	200
Thermal penetration depth (µm)	189	268	328	370
Optical penetration length (µm)	151	151	151	151

The ablation spot size and the threshold were calculated theoretically. The above process was repeated for different laser pulse durations 50, 100 and 200 µsec to investigate the effect of the pulse duration on the threshold energy. As was expected, more energy was needed with increasing the pulse duration, see Chapter 5. This is considered with respect to the laser spot size with both the optical and the thermal diffusion depth. Figure 7.2 shows an irradiated spot of SiC by CO_2 laser. The spot is circular and surrounded by debris. The laser parameters were set to 150 µsec with 500 Hz pulse repetition rate and laser power of 8.5 W. The damage site seems to be divided into the crater and the surrounding damage site. This could be related more to the debris than the thermal diffusion length. It can be seen that the crater diameter was around 100 µm and the damage site was about 200 µm. While the diffusion length for this pulse duration of 150 µsec should exceed 328 µm as it is shown in Table 7-1. This could be due to the simplification of that model since it neglects any energy losses such as the losses from the plasma formation and reflection.

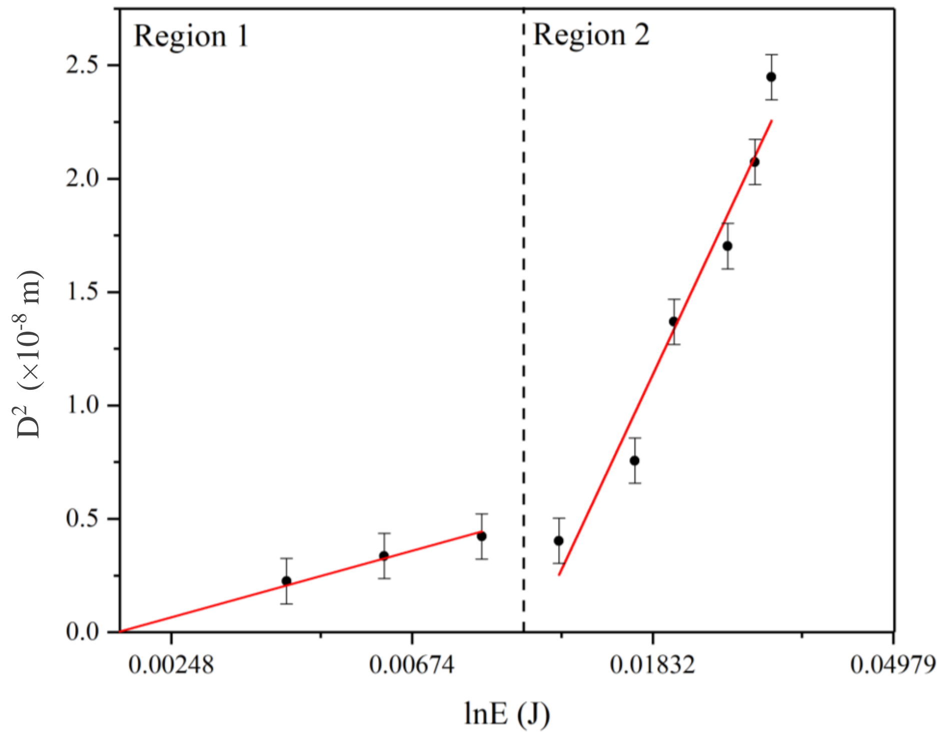

Figure 7.1: The multi-shot of theoretical ablation threshold measurements of SiC irradiated by 10.6 µm CO_2 with 150 µsec pulse duration. The plot represents a natural logarithmic dependence of the squared ablated diameter with the applied laser fluence. The slope shows the minimum laser ablated squared radius. The extrapolation to zero gives the ablation threshold fluence.

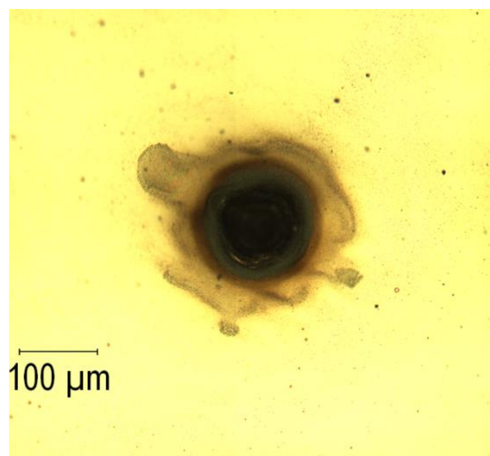

Figure 7.2: A typical irradiated spot of SiC by CO_2 laser at 150 µsec and 500 pulses repetition rate. The attenuator set the applied power to 8.5 W.

7.3 Raman Investigation for Stationary Laser Surface Decomposition of 4H:SiC

Figure 7.3 shows a 4H:SiC irradiated at a fluence of 190 Jcm^{-2}, pulse duration of 100 µsec and laser pulse repetition frequency of 500 Hz. Micro Raman measurements were carried out on the static crater to investigate the decomposition of 4H:SiC. Measurements were recorded at five different spatial locations inside and around the static ablation crater as circulated on Figure 7.3. The topography shows different regions with cracks inside it. The different location corresponds to the Gaussian profile of the laser beam.

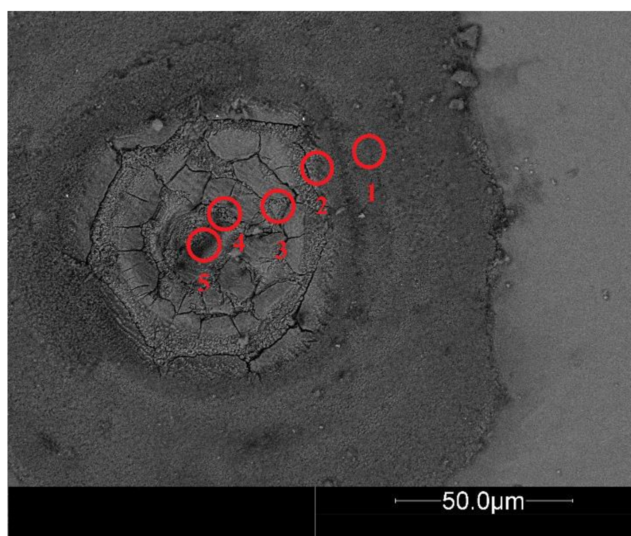

Figure 7.3: SEM micrographs of CO_2 laser ablated 4H:SiC. It was irradiated at a laser power of 4.2 W, pulse duration of 100 µsec and laser pulse repetition frequency of 500 Hz. Positions 1-5 indicate the spatial locations of the micro Raman measurements.

Raman analysis was performed to investigate the possible presence of the different C phases due to the carbon atoms rearrangement after the silicon sublimation. Figure 7.4 shows the average normalised Raman spectra of the synthesised graphene on 4H:SiC surface. The fluence was calculated at each location using laser principles from Siegman[230]. In location 1, which is outside of the site, the laser ablates the substrate and material redeposit over the adjacencies. It shows background behaviour, which is related to the redisposition of the amorphous ablated material. In location 2, at $1/e^2$ of the profile, the 4H:SiC TO peak intensity reduced significantly and a small equivalent peak of 3C:SiC polytype appears. LO band disappears with the rise of both the D, G and weak 2D bands.

These peaks are attributed to the formation of graphene oxide with I_D/I_G of 0.8. However, it is believed to contain many defects due to the rough spectra at the 1100 and 2100 cm^{-1} which corresponds to the C-O-C and C=N stretching, respectively. For location 3, at almost 1/e of the profile, the spectra maintain the 4H:SiC peaks with the presence of 3C:SiC peak, in addition to the D and the G bands with I_D/I_G ratio of 1.25, indicating the presence of rGO. This site received more fluence than location 2; therefore, it is believed to ablate more material. At location 4, Raman spectra was obtained closer to the central region of the site. No sign of the substrate appears in the spectra. However, the peaks of the fundamental vibration modes of graphene appear. The D, G band and 2D peaks are well defined and appear at ~1335, 1582, and ~2665 cm^{-1} respectively. The peaks were fitted to a single Lorentzian curve with the I_{2D}/I_G ratio of 0.55 indicating the formation of multilayer graphene. This could be related to the high power of the CO_2 and also to number of laser pulses. At the centre of the crater in location 5, the Raman spectra shows a typical single layer graphene collected with I_{2D}/I_G of 1.5. The process was conducted at ambient conditions; however, the graphene oxide was absent. The relation between the beam Gaussian profile (fluence) and the ablated vapour explains the spatial behaviour in the spot. When the fluence is large enough for high Si vapour flux, this gas will push away all the ambient gas surrounding the ablated area. For a smaller fluence combined with a relatively high pulse duration, the atmosphere is suitable for the remaining carbon atoms to interact with the oxygen in addition; the obtained graphene always has defects that can be seen in the D peak.

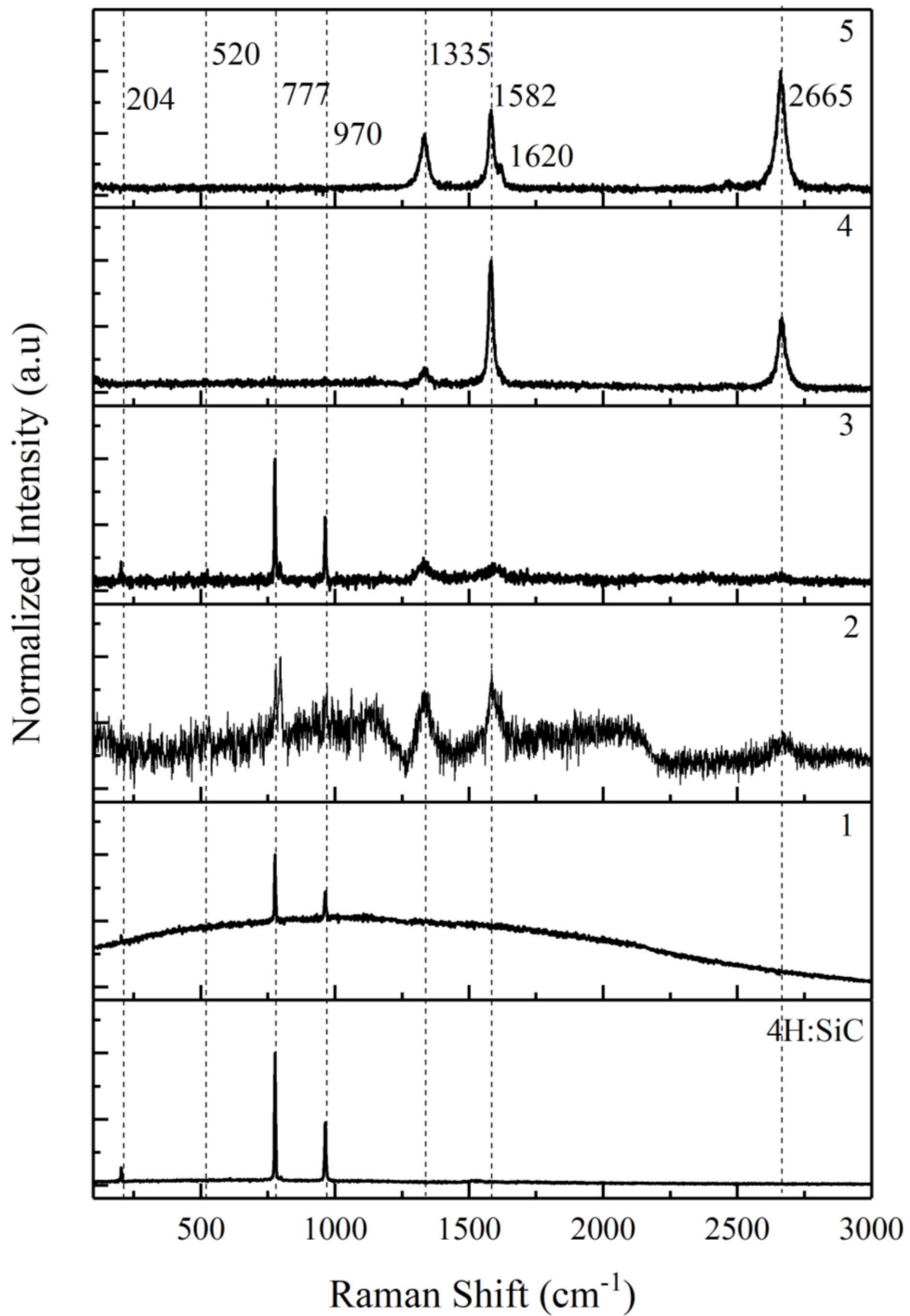

Figure 7.4 Average normalised Raman spectra of irradiated 4H:SiC substrate. It was irradiated at a laser power of 4.2 W, pulse duration of 100 µsec and laser pulse repetition frequency of 500 Hz. Layers attributed to 4H: SiC, location one, location 2, after background subtraction of location 3, location 4 and location 5, respectively as illustrated in Figure 7.3.

7.4 Effect of Laser Pulse Duration on the Structure and Decomposition of SiC

The effect of the applied pulse width, controlled by the pulse generator, on the surface of the irradiated SiC investigated. The sample was irradiated with a different pulse duration of 20, 50, 100, 200 and 400 µsec. Other laser parameters were fixed with a pulse repetition rate of 100, a travel speed of 2 mms^{-1}, and a power around 1.9 W. Both the surface topography and the decomposition behaviour were investigated.

7.4.1 Structural Characteristics

Tilted SEM micrographs demonstrating the effect of the laser pulse duration of 100, 200 and 400 µsec on the irradiated site is shown in Figure 7.5.

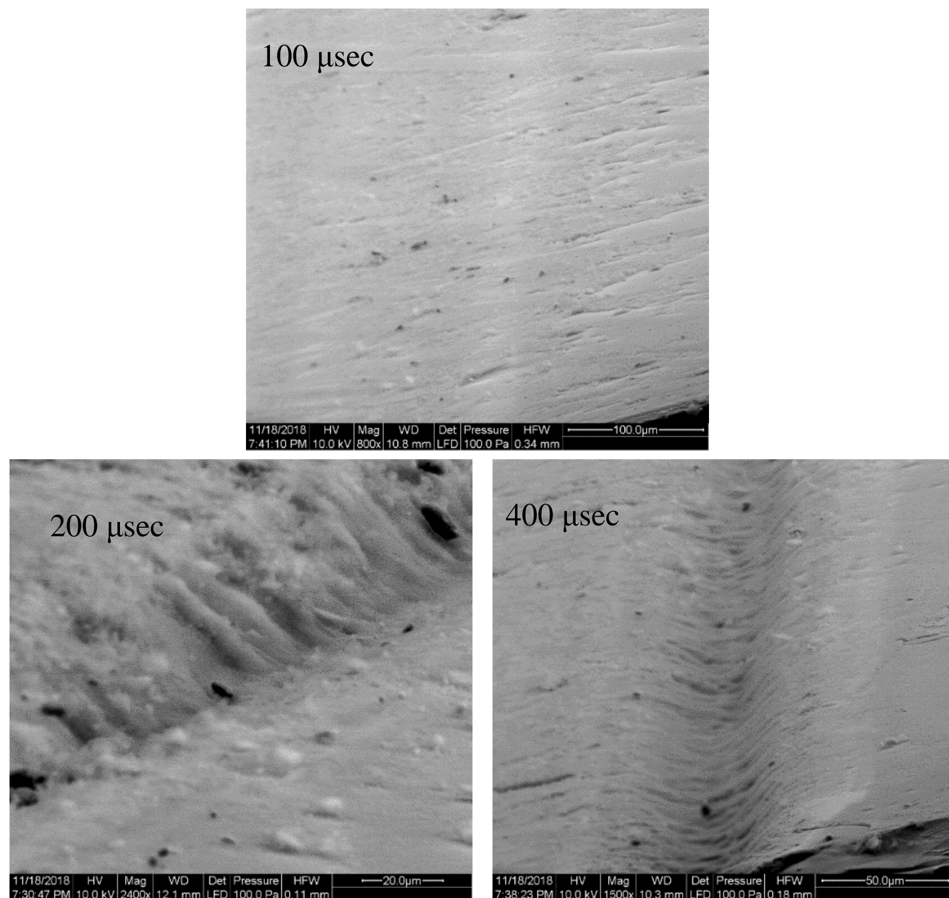

Figure 7.5: Tilted SEM micrographs of the irradiated SiC with different pulse widths of 100, 200 and 400 µsec.

The depth appeared to be a function of the applied pulse width. It can be explained according to the HAZ effect. The depth would increase with increasing the pulse duration. Higher resolution SEM images, as shown in Figure 7.6 and Figure 7.7, were conducted to study the periodic structure formed in the irradiated site. The periodic structures were a feature of all the irradiated samples. The period of the formed ripples (Λ) was always near wavelength (the scattering theory expected the period as in $\Lambda = \lambda/1 \pm \sin\theta$). Where λ is the laser wavelength and θ is the angle of incidence. The periodic structure was classified spatially into two groups; low frequency (Λ, close to the laser wavelength λ or λ/n where n is the refractive index of the material) and high frequency (with $\Lambda < \lambda/2$)[231,232]. The periodic near subwavelength was applied as (Λ/λ) or ($\Lambda/\lambda/n$), and it was in the range 0.8-0.9 for our set of experiments. The ripples formation and dimensions were dependent on the laser parameters, especially the applied laser power and the overlapped number of the laser. The surface shows an increase in ripples with increasing the applied laser power. For the 500 Hz and 8.5 W processing, the overlapped laser pulses were 20 per site, and the ratio Λ/λ were around 0.85, see Figure 7.6. However, when the pulse repetition rate decreased to 100 Hz with a laser power of 1.9 W, two distinct areas could be seen, as shown in the optical micrograph in Figure 7.7. The centre had ($\Lambda/\lambda/n$) ratio of 0.9. Λ was measured using ImageJ software to be 4 μm (where Λ close to λ/n=3.9). The period between two adjacent ripples can slightly decrease toward the edge of the laser channel, following the profile of the laser irradiance, as can be seen in the SEM image in Figure 7.7. This behaviour is believed to be related to the cooling mechanism as it decreases with the applied laser power as shown in Chapter (5)

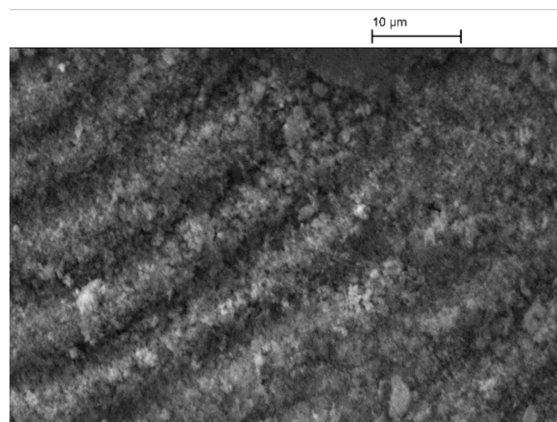

Figure 7.6: SEM micrograph of SiC irradiated with 8.5 W and 500 pulse repetition rate with 150 μsec pulse width. The period of the formed ripples (Λ) was measured using ImageJ software to be 8.5 μm.

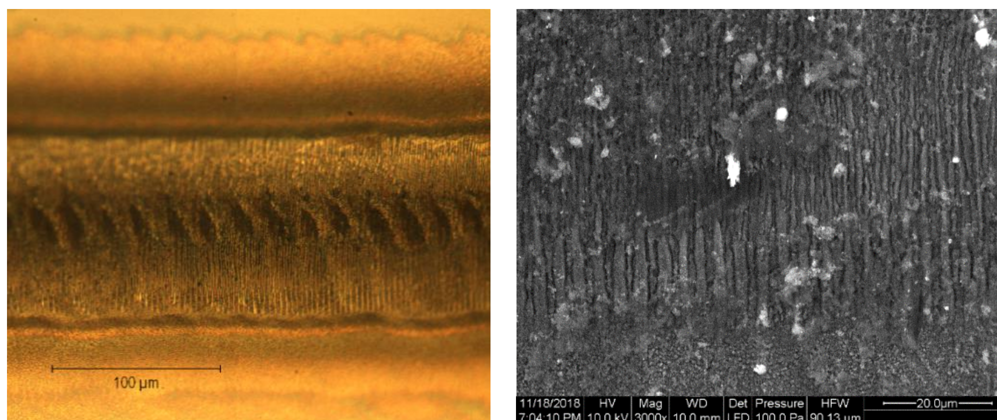

Figure 7.7: Optical and SEM micrograph of 4H:SiC irradiated with 1.9 W and 100 pulse repetition rate with 100 µsec pulse width and stage speed of 2 mms^{-1}. Λ was measured using ImageJ software to be 4 µm.

7.4.2 **Raman Characteristics**

Raman spectra of SiC irradiated with a different laser pulse duration of 20, 50, 100, 200 and 400 µsec was collected as shown in Figure 7.8. The process took place in ambient conditions. The spectra were collected at the centre of the channel and near the channel edge. For 20 and 50 µsec pulse duration, only the Si-C bands appear at 204, 777 and 964 cm^{-1}. The FWHM of the TO peaks varied slightly from 4.7 to 4.4 and 4.3 with 20 and 50 µsec irradiation, respectively. This is indicating an enhancement in the periodicity; thus, an annealing effect was suggested. Furthermore, the C-C bond (G, D and 2D) starts to appear at bands of ~1335, 1582 and 2669 cm^{-1}, respectively. The I_{2D}/I_G ratio of 0.99, indicating the formation of a few layers of graphene. With increasing the pulse width to 200 µsec and 400 µsec, the background signal appears in the spectra. However, the background was subtracted to get the correct information regarding the peak's ratio. The increase in the background could be due to the increase in the roughness of the structure. Interestingly, a change of the 4H:SiC polytype to 3C:SiC took place with the 200 µsec ablation process. Indicating a re-construction of the molten surface to relatively simpler crystalline shape.

Furthermore, the Raman spectrum of 400 µsec did not show any interference signals from SiC indicating the transformation of the sample gradually to graphitic structure and graphene since the laser penetration length increased with the pulse duration as shown in Table 7-1. From the spectra, we can conclude that the graphene was growing on the

surface of the SiC. This was mainly due to the 2D band. For graphene, the 2D band can be fitted with a sharp and symmetric Lorentz peak while that of graphite can be fitted with two peaks. It can be seen in literature that the 2D band becomes broader and blue-shifted when the graphene layers increase to multilayer graphene[233]. The I_{2D}/I_G ratio was calculated to be 0.86, indicating the formation of multilayer graphene. The crystallite size was calculated using Raman spectra. The 400 µsec irradiated samples presented higher concentration of defects, represented in the appearance of a band at 1620 cm^{-1} with a crystallite size of 290 nm, and FWHM of only 33 cm^{-1}. The crystallite size was calculated using Equation (4.7).

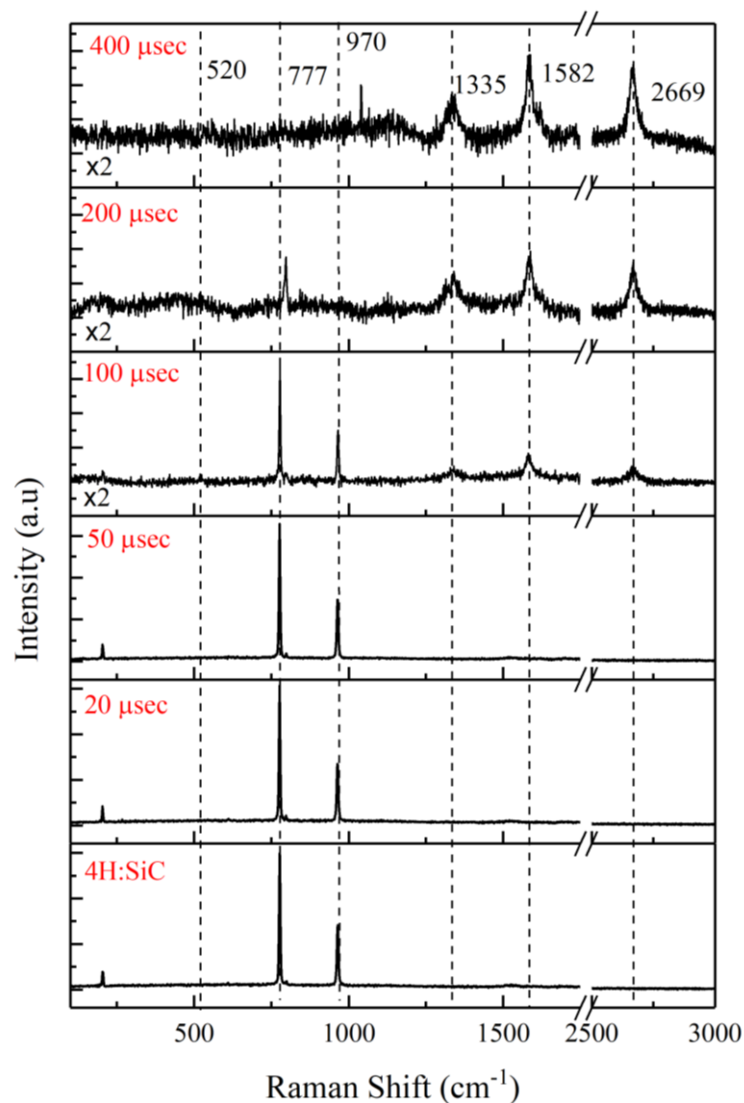

Figure 7.8: Raman spectra of SiC and multilayer graphene are grown on single crystalline 4H-SiC (0001) at a different laser pulse duration of 20, 50, 100, 200, and 400 µsec at the centre of the irradiated channel. The x2 at the above three layers shows double magnification.

Due to the Gaussian behaviour, the edge area corresponding to $1/e^2$ of the power was investigated by Raman scattering spectra for the 100, 200 and 400 μsec pulse durations as shown in Figure 7.9. The spectra, as a function of the applied pulse duration, collected at the channel edge, shows a different composition from the spectra collected in the centre of the channel. We concentrated on the 100, 200 and 400 μsec pulse durations. For 100 μsec pulse, the SiC peaks appears in the spectra with less intensity and all the carbon peaks of D, G and 2D emerged in addition to the Si peak. This can be explained by the decomposition of the SiC into both Si and C. However, the carbon phase can be considered as multilayer graphene with an I_{2D}/I_G ratio of 0.53. For the 200 and 400 μsec pulse duration, the spectra show the 4H:SiC peaks decomposed to amorphous bands along with the appearance of some polytype changes to 3C:SiC. It also shows the presence of the Si peak in both amorphous and crystalline shape with the 200 μsec, and only amorphous Si with 400 μsec. Furthermore, the D, G, and 2D bands appear in the form of reduced graphene oxide with an I_D/I_G ratio of 1.37 and 1.25 in accordance with 200 and 400 μsec, respectively. Finally, a peak at 2100 cm^{-1} was observed. This is related to the C=N stretching. This was explained by the ambient condition and the presence of nitrogen. For the applied fluence, the combination of fluence and relatively high pulse duration provided a suitable atmosphere to the remaining carbon atoms to interact with the nitrogen. In addition, the obtained graphene has defects that can be seen in the D peak. The D-band corresponds to the distortion of sp^2 Crystal structure of graphene. The presence of disorder in sp^2 hybridized carbon systems results in resonance Raman spectra, and thus makes Raman spectroscopy one of the most sensitive techniques to characterize disorder in sp^2 carbon allotropes. An EDX map of the site irradiated with 400 μsec, shows the presence of silicon, oxygen and carbon at the irradiated sample, see Figure 7.10

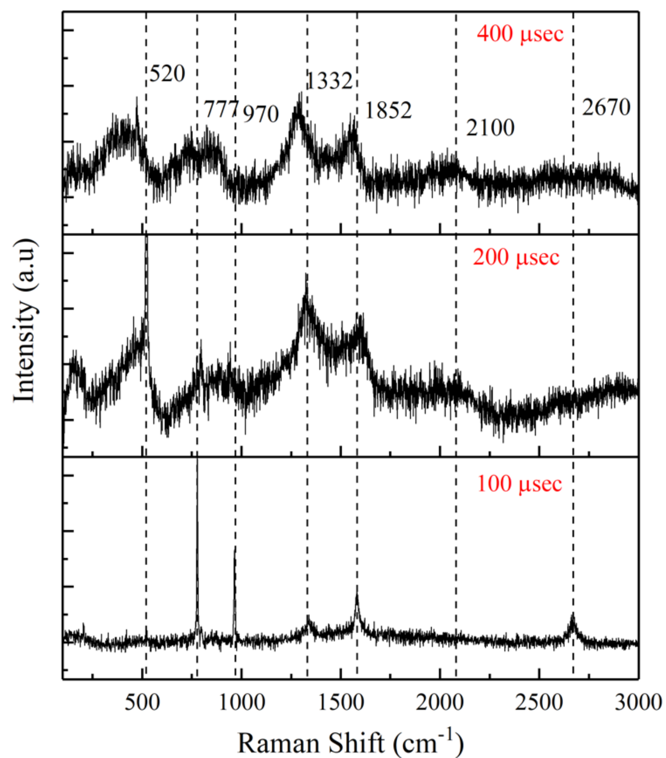

Figure 7.9: Raman spectra of SiC and multilayer graphene and reduced graphene oxide grown on single crystalline 4H-SiC (0001) at a different laser pulse duration of 100, 200, and 400 µsec. The spectra collected at the edge of the irradiated channel.

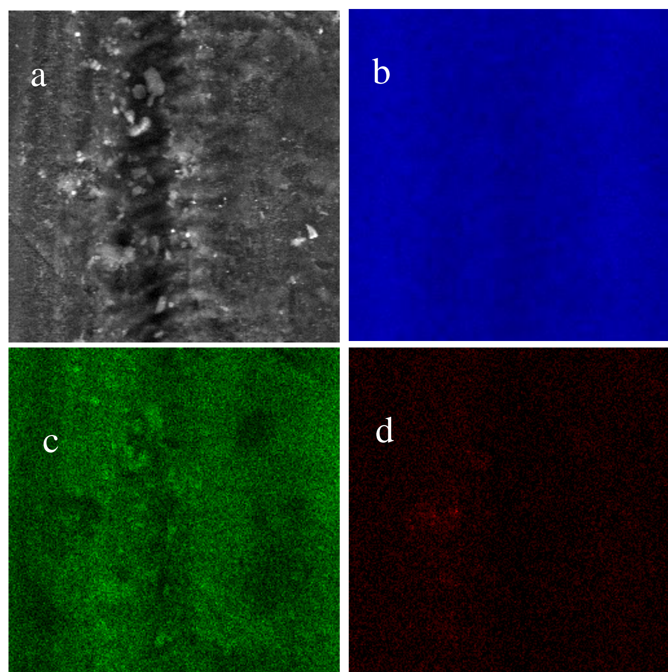

Figure 7.10: SEM micrograph and EDX map of the irradiated site with 1.9 w of 10.6 µm laser at a pulse duration of 400 µsec at 100 Hz frequency (a) SEM, (b) SiK, (c) OK and (d) CK.

7.5 Effect of Laser Power on the Surface of SiC

This section investigates the physical changes on the SiC surface as a function of applied laser power effect. Stationary and scanning processing was conducted. The used power was in the range of 1.5 to 15 W at a pulse duration of 150 μsec, 500 Hz and a stage travel speed of 2 mms^{-1}. The laser power was changed and controlled by the ULO attenuator.

7.5.1 Surface Characteristics

Figure 7.11 shows the depth and the diameter profile of the irradiated spots as a function of the laser power measured using a Leica microscope. The depth profile was measured by focusing on the surface and then on the bottom of the track in the centre and measuring the difference between locations. In both cases, the depth and diameter increased with increasing the applied laser power. Moreover, the same processing conditions applied to produce channels on the SiC surface. Further analysis was conducted to check the profile of the produced track using an image processing function in OriginPro software. Figure 7.12 represents a track produced by 14 W laser power. The profile represents three areas of the sample, the surface, the redeposited material on the edge and the track in which the two lateral lines are above the surface. This was confirmed using the Dektak profilometer, see Figure 7.13. It shows that there is a central crater which is related to the Gaussian behaviour of the laser pulse leading to removing the material in the centre where it contains most of the pulse power. This was shown almost in all the made channels. The structures protruding above the surface of the un-irradiated sample was also measured in all the produced channels.

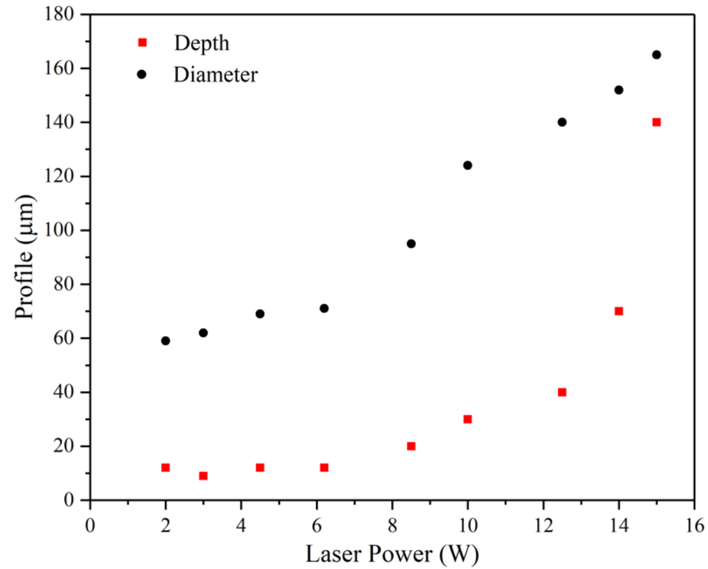

Figure 7.11: Microscopic depth and channel width measurements of the irradiated spots as a function of the applied laser power.

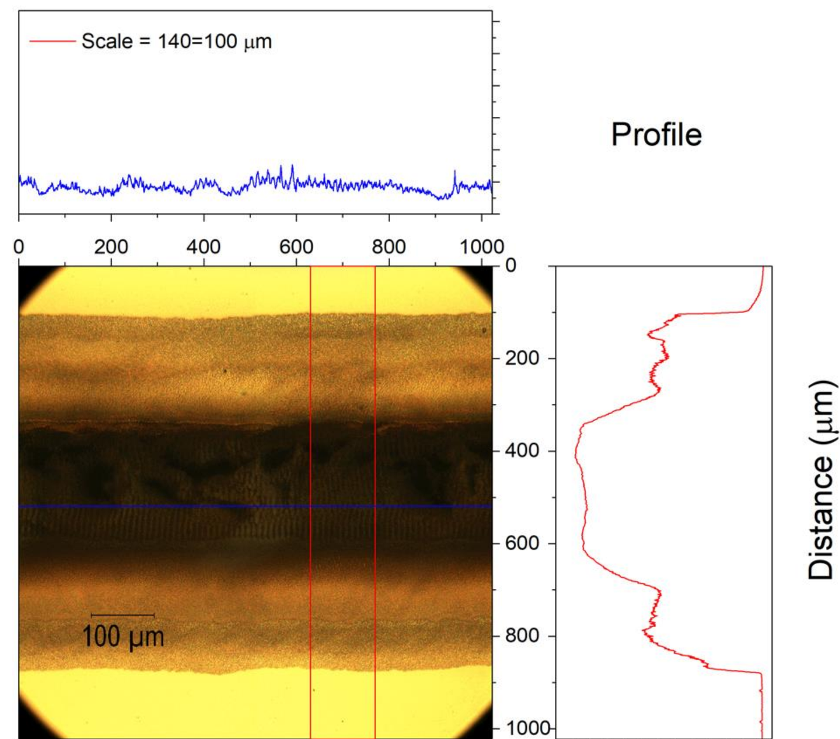

Figure 7.12: A channel produced by 14 W laser power with the processed profile using origin software. Three areas of the sample shows; the surface, the redeposited material on the edge and the track. The two lateral areas are above the surface

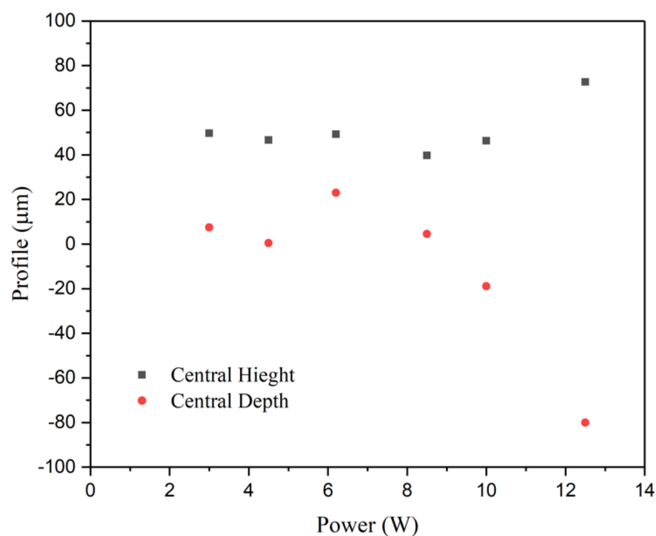

Figure 7.13: Cross-sectional one stylus profile Dektak measurements of laser ablated 4H:SiC channels. Central channel depth and the protruding structure's height above the surface of the SiC surface measured as a function of the applied laser power ranged between 3 and 12.5 W.

The surface topography was investigated under high-resolution SEM. Figure 7.14(a) shows the topography at the centre of channel irradiated at relatively low power of 3 W. A nanostructure with high roughness appears, producing a very high surface area. While Figure 7.14 (b) shows the channel produced with relatively high power of 15 W. Flaky texture with the presence of cracks appears. The images were used to analyse the morphology of the nanostructures showing the shape and size of the sheets. Agglomerated individual sheets were observed through a layered type of structure that were a few micrometres in size. This could be related to the initial surface of the SiC (surface roughness and defects), the Gaussian profile of the laser beam (which causes non-uniform heat distribution on the surface). The presence of defects was expected due to the processing under ambient conditions. Different types of defects were suggested and investigated using Raman by Eckmann[234], this is explained in detail in the next sections.

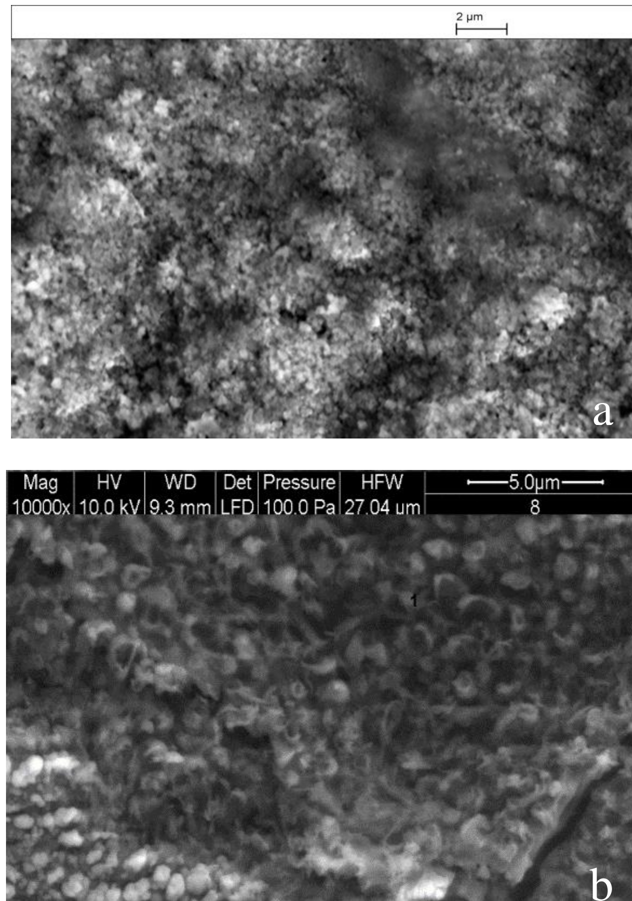

Figure 7.14: SEM micrographs of CO_2 laser-irradiated 4H:SiC surface with 500 Hz pulse repetition rate and 150 µsec pulse width and a different power (a) 3 W and (d) 15 W.

SiC has a native oxide layer, which passivates the surface. The oxide layers are connected directly with the top bilayer of SiC on C-face or make linear Si–O–Si connection on Si-faces of SiC. Thus, the decomposition rate of the SiC is more effective when the oxide layer is disrupted. The latter structure leads to a stronger bonding and thicker oxide layer resulting in a slower decomposition rate of the Si-face. However, the SiO_2 reduction takes place during heating up to ~1400 K in a vacuum and the surface decomposition of SiC starts at this temperature. From COMSOL temperature evaluations, the temperature was enough to disrupt the oxide. The removal of the oxide layer is non-uniform depending on the SiC defects, surface roughness and the acceleration of the evaporated Si atoms. The above would result in local exposure. Thus, non-uniform nucleation of carbon clusters leads to curved and standing graphitic structures[235].

7.5.2 **Raman Investigation**

Figure 7.15 shows the Raman spectra collected from different samples prepared with 3, 6.2, 10 and 15 W at roughly the same location. Other parameters were fixed. The structure and composition of the surface were dependent on the applied laser power. At channels irradiated with 3 W pulses, the surface transforms from high crystallinity 4H:SiC to a rough surface of crystalline silicon (520 cm^{-1}), defected multilayer graphene (1335, 1582, 1620 and 2669 cm^{-1}) and polycrystalline SiC (775, 970 and 1320-1360 cm^{-1}). In addition, there was a C-O-C peak which appeared at 1100 cm^{-1}. The presence of oxygen was detected with EDX in most sites. With increasing the applied laser power to 6.2 W, a surface of amorphous Si, graphite, and a trace of a 3C:SiC polytype was formed. With further increase of the power of the pulse to 10 W, single layer graphene was detected with no trace of Si or SiC substrate. The I_{2D}/I_G ratio was around 2.5 and FWHM ~25 cm^{-1}. These measurements were extracted using a single Lorentzian peak fitting. With 15 W, the peaks were the same but with I_{2D}/I_G ~1 and FWHM ~37 cm^{-1}. These results are believed to be close to the monolayer epitaxial graphene. However, due to the surface topography, it is possible to find monolayers and/or multilayers on the same sample, see Figure 7.16. The FWHM depends on many factors, such as strain, doping, point defects, size, and stacking order[141]. The defect mechanism suggested by Eckmann[234], was employed to investigate the defects in our samples. It depends on the intensity ratio between the D band at 1335 cm^{-1} and the D` height at 1620 $cm^{-1}$ band. The $I_D/I_{D`}$ obtained here was in the range of ~0.71 and ~2.62, see Table 7-2. It is believed to be related to high concentrations of boundary defects.

Table 7-2: The relation between the applied laser power and the defect ratio of $I_D/I_{D`}$.

Applied Laser Power (W)	$I_D/I_{D`}$
3	1.24
6.2	2.62
10	0.71
15	2.12

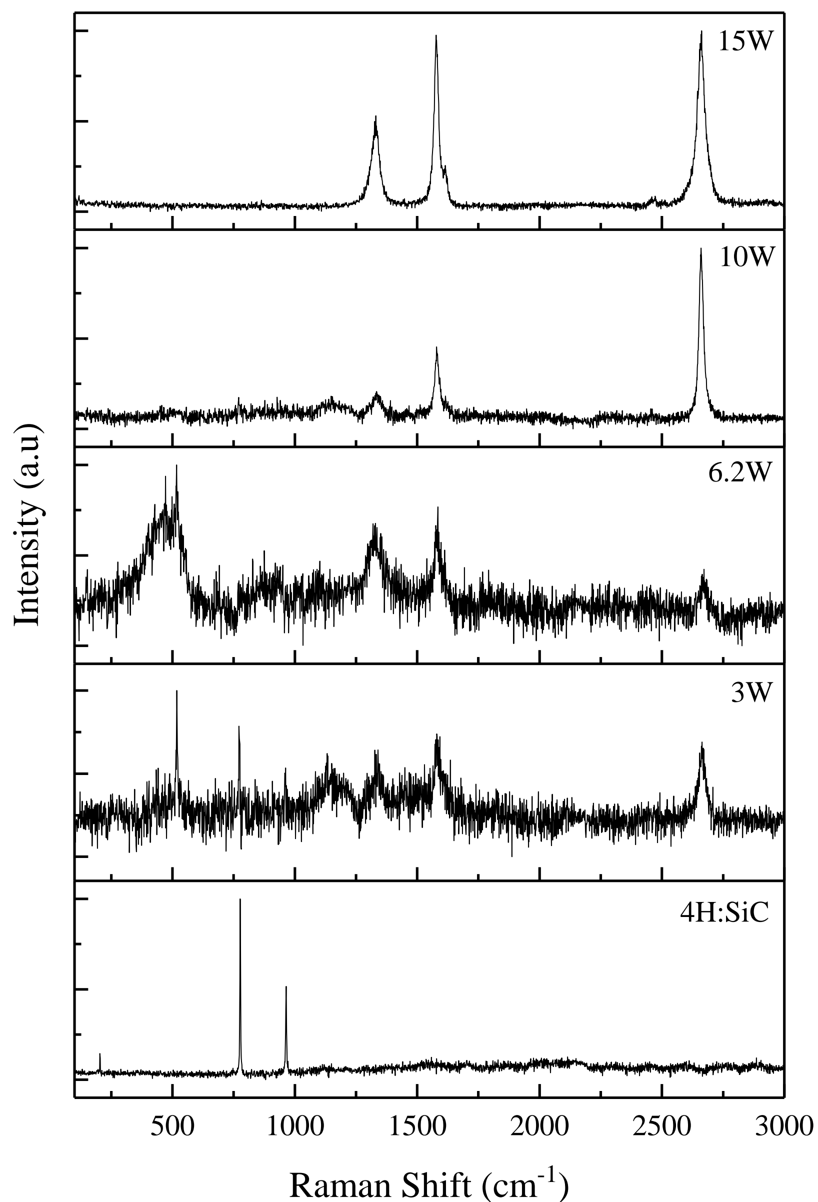

Figure 7.15: Raman spectra of CO_2 irradiated 4H:SiC at different laser power. The bottom layer is a reference 4H:SiC surface, then 3W, 6.2 W, 10 W and 15 W, respectively.

Figure 7.16 represents the spectra taken from the channel centre and near the channel edge. As can be seen, there were several differences observed. The peak profile of the graphene bands has changed. The 2D peak had a sharper profile, with a FWHM of 37 cm^{-1} at the channel centre, while the FWHM of 2D at the edge, changed to 46 cm^{-1}. In addition, SiC peaks appear in the spectra collected near the channel edge, while SiC bands disappeared in the spectra collected from the channel centre. This was related to the

change in the received power by the SiC due to the Gaussian profile of the laser pulse. Moreover, an increase in the defects was observed.

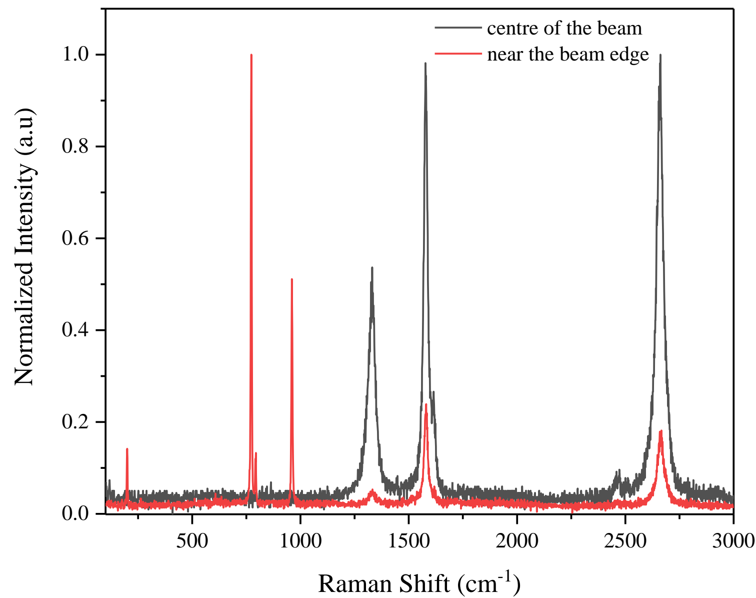

Figure 7.16: Raman spectra of CO_2 ablated SiC at a 15 W with 150 µsec and 500 Hz pulse repetition rate at different locations of the beam. Red colour represents the spectra collected near the edge and the black colour related to the centre of the beam.

7.6 Effect of Travelling Laser Speed on the Surface of 4H:SiC

Laser direct writing channels on 4H:SiC were produced and characterised systematically. The surface was irradiated with fixed laser parameters, but the sample's speed was controlled. Laser parameters were fixed with 10 W power, pulse duration of 150 µsec and 500 Hz Frequency. The Aerotech nano motion stage was used to control the travel speed. The speed was tuned over a wide range from 2 to 21 mms^{-1}.

7.6.1 Surface Characterisation

SEM and an optical microscope were used to investigate the surface. The width profile of the channels as a function of the travel speed appears to decrease with the applied travel speed, as shown in Figure 7.17. Dektak profile measurements on the height of the produced material above the SiC surface conducted as a function of the travel speed of the stage see Figure 7.18. In addition, the debris region and the HAZ were decreasing with increasing the travel speed as it can be seen in Table 7-3.

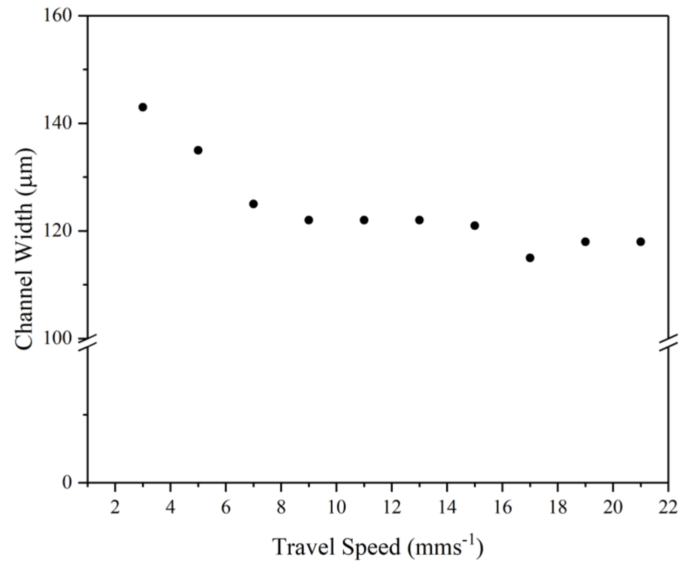

Figure 7.17: Microscopic measurements of the channel width of the irradiated channels as a function of the stage motion.

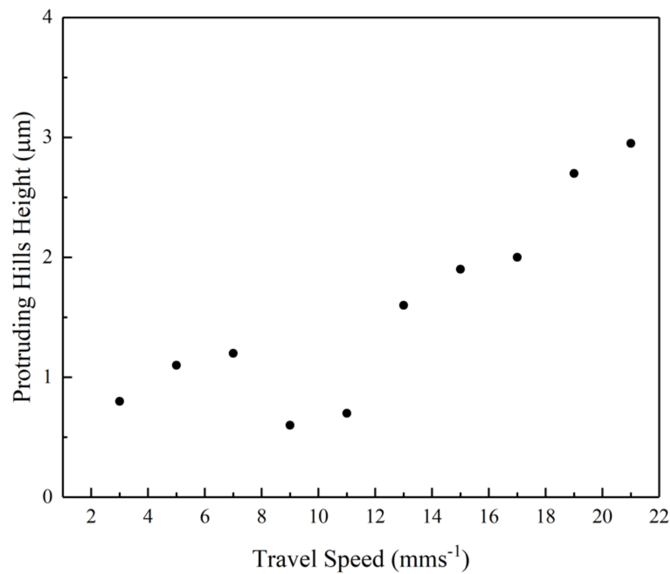

Figure 7.18: Cross-sectional one stylus profile Dektak measurements of protruding height above the surface of the irradiated channels as a function of travel speed ranged between 3 and 21 mms^{-1}.

Table 7-3: Speed effect on the surrounding redisposition at the edge of the irradiated channel.

Speed (mms^{-1})	3	5	7	9	11	13	15	17	19	21
Surrounding Width (µm)	100	103	102	115	108	105	103	97	97	82

Figure 7.19, shows SEM micrographs of different SiC sites irradiated with various travel speed ranging from (a) 5 mms^{-1}, (b) 9 mms^{-1}, (c) 17 mms^{-1} and (d) 21 mms^{-1}. The topography at high power and high-speed processing shows fine structures. In addition, the periodic structure was observed to be the main feature, and it was affected by the travel speed, indicating a relationship between the solidification and cooling rate of the sample while moving.

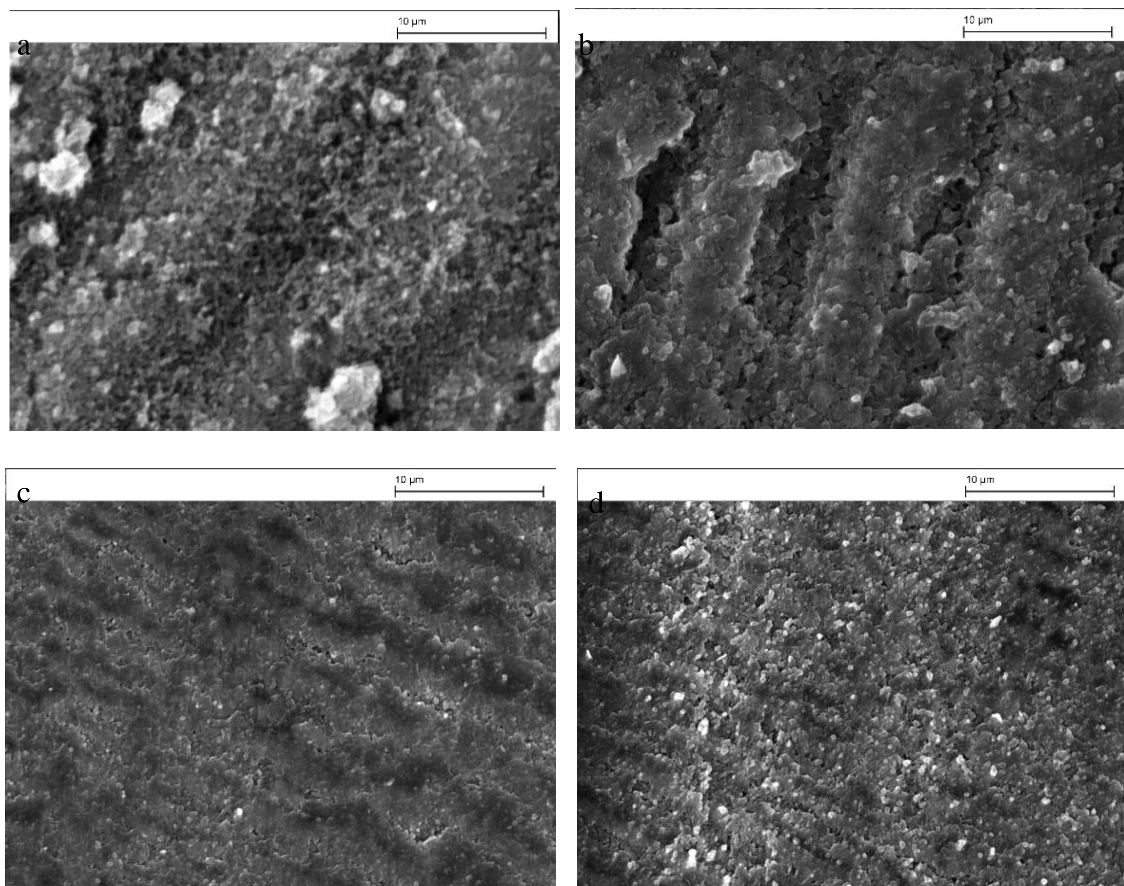

Figure 7.19: SEM micrographs of SiC irradiated with various Aerotech stage speed ranging from (a) 5 mms^{-1}, (b) 9 mms^{-1}, (c) 17 mms^{-1} and (d) 21 mms^{-1}.

The periodic structure shows an identical spacing to the overlapping laser pulses number according to Equation (4.1). As explained in section 7.5. The period of the formed ripples (Λ) was always near subwavelength (the scattering theory expected the period as in $\Lambda = \lambda/1 \pm \sin\theta$). Our results were consistent with a low-frequency periodic structure. (Λ, close to the laser wavelength λ or λ/n).

The periodicity wavelength was applied as (Λ/λ/n), and it was in the range 0.8-0.9 for our set of experiments. The structures were dependent on the laser overlapped number of pulses, i.e. with 5 mms^{-1}; the period was around 10 μm while the number of overlapped pulses was 10. Meaning the period was introduced directly by the spatial profile of the laser. While for 17 mms^{-1}, the period was ~3.5 μm, indicating the formula λ/n. The periodic behaviour was evident with the optical microscope as it can be seen in Figure 7.20.

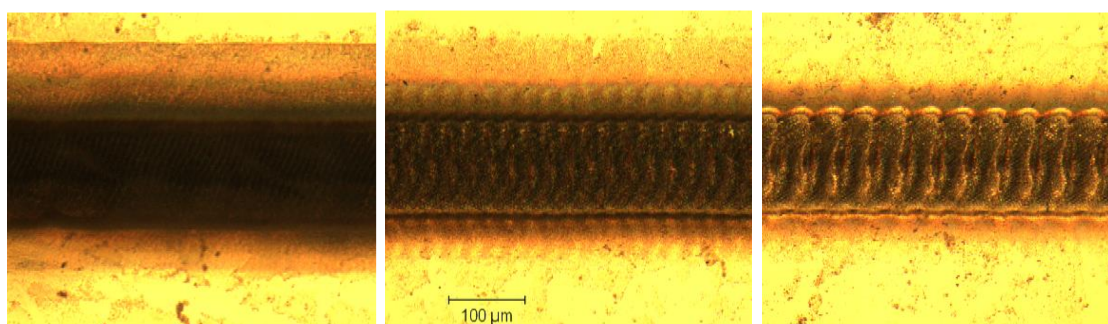

Figure 7.20: Optical micrograph of SiC irradiated at different Aerotech stage speed of 3, 11 and 19 mms^{-1} starting from left to right, respectively.

The above results were from direction laser irradiation on the surface. An interesting effect was noticed during the SEM imaging, where the laser structured the edge of the sample as it can be seen in Figure 7.21. The processing was achieved by passing the laser through the whole sample, crossing the edge of the sample. This led to laser texturing of the sample edges. The morphology at the sample edge was different from the morphology at the top surfaces of the sample. Figure 7.21 represents the cross-sectional view at the bottom edge of (a) un-irradiated 4H:SiC compared with the irradiated SiC at a different travel speed of (b) 21, (c) 19, (d) 17, (e) 11 and (f) 7 mms^{-1}. It starts from fast to slow travelling speed indicating the increase in the overlapped number of pulses received by the sample from 7 to 16.7 pulses per site. Figure 7.21 (b) shows porous formation with nanocrystallite structures on. Decreasing the speed, more pulses were delivered, and the material transforms to a smaller porous structure. Figure 7.21 (e and f) shows a different behaviour as a layer and flake like structures. These pictures confirm the melting of the SiC under laser irradiation. Figure 7.22 shows a higher resolution SEM of the edges presented in Figure 7.21 (f). It clearly shows the layers structure on SiC. For further investigation, Energy Dispersive X-ray analysis (EDX) were collected from the side, see

Figure 7.23. The presence of oxygen, carbon and silicon were the main feature for all the irradiated sites compared to the un-irradiated SiC. It shows an oxygen increase with fast travel speed. Furthermore, the Si/C ratio signals were almost constant, indicating that the carbon on the surface was not depleted by the laser.

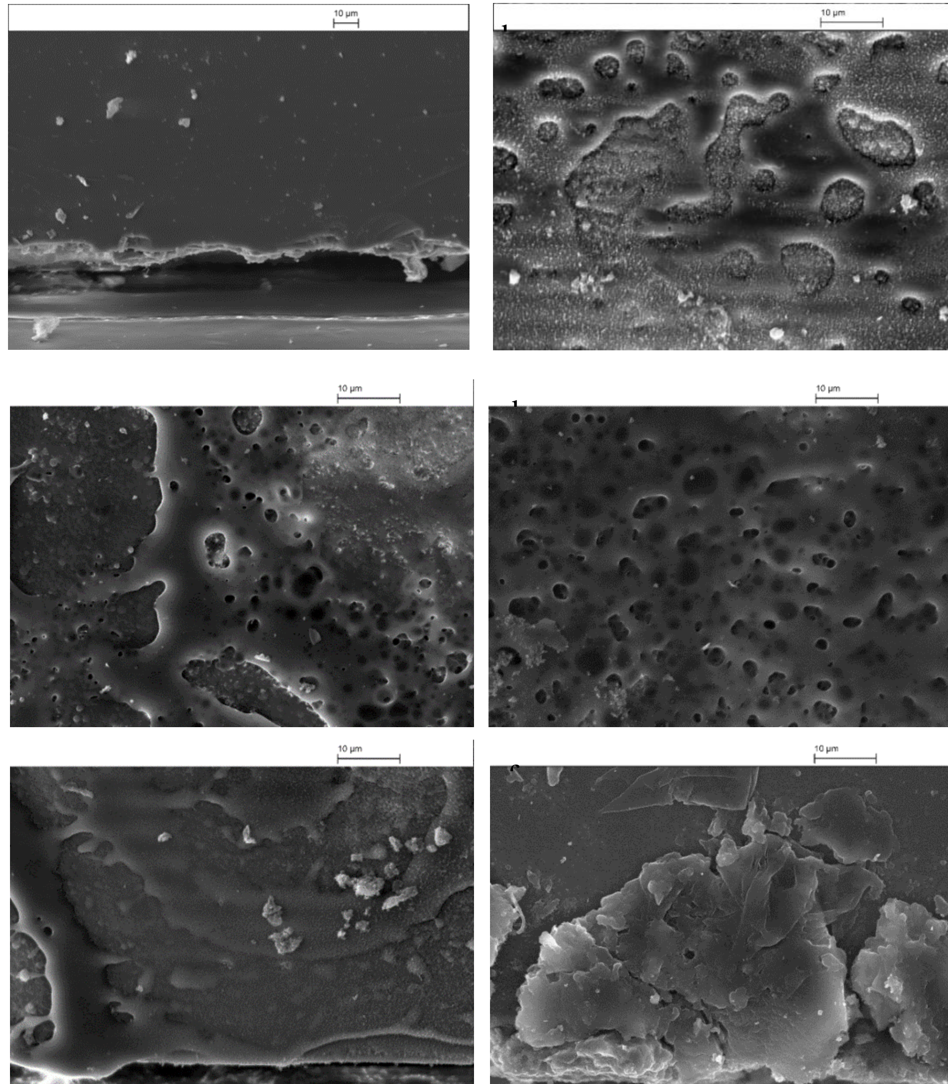

Figure 7.21: Cross-sectional view at the bottom edge of un-irradiated 4H:SiC (a), irradiated SiC with different travel speed at (b) 21, (c) 19, (d) 17, (e) 11 and (f) 7 mms^{-1}.

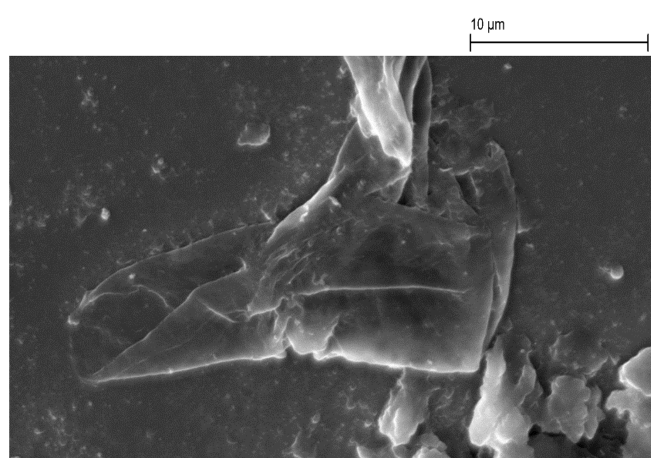

Figure 7.22: SEM micrograph of SiC edge irradiated at 10 W and 7 mms^{-1} speed.

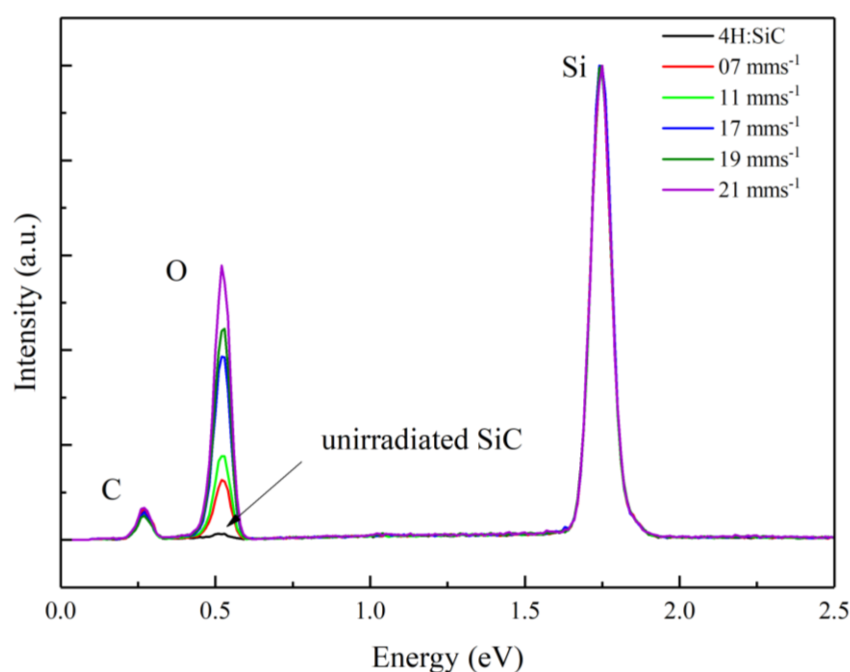

Figure 7.23: EDX of SiC irradiated with different travel speed.

7.6.2 **Raman Characterisation**

Raman spectra of the SiC irradiated with 3, 7, 11, 15, 19 mms^{-1} travel speed was collected as in Figure 7.24. The composition of the surface was dependent on the number of overlapped pulses. The spectra were collected from the same location within the channel roughly at the centre. At 3 mms^{-1}, the surface transforms from high crystallinity SiC to a rough surface highly defected multilayer graphene with Raman peaks at ~ (1334, 1584, 1621 and 2674 cm^{-1}) and 4H:SiC (204, 777 and 965 cm^{-1}). In addition, there was a very

broad band appear at 1100 cm^{-1} of a C-O-C. With increasing the applied travel speed to 7 mms^{-1}, a decomposition of the 4H:SiC takes place to a crystalline Si (520 cm^{-1}) and single-layer graphene with a weaker trace of the substrate as a 4H:SiC. The single layer graphene was characterised with the I_{2D}/I_G ~3.5 and a ~29 cm^{-1} FWHM of Lorentz fitting. With the further increase to 11 mms^{-1}, multilayer graphene was detected on top of SiC surface with a weak trace of very broadening Si peak. I_{2D}/I_G was around 0.53 and 2D FWHM ~47 cm^{-1}. With 15 mms^{-1}, the position of the peak of D, G, D' and 2D were shown with a very weak band of the 4H:SiC. The profile of the peaks shows a formation of single graphene layer with I_{2D}/I_G ~1.52 and 2D FWHM ~30.6 cm^{-1}. These results are believed to be close to the monolayer graphene. At 19 mms^{-1}, I_{2D}/I_G ~0.6 and 2D FWHM ~37 cm^{-1} was measured. Which is in the range of multilayer graphene with no trace of the 4H:SiC substrate.

It must be mentioned here that due to the surface topography, it is possible to have monolayers and or multilayers on the same sample following the Gaussian profile of the applied laser. FWHM depends on many factors, such as strain, doping, point defects, size, and stacking order[141].

In addition, the defect mechanism suggested by Eckmann[234], was employed to investigate the defects in our samples. It depends on the intensity ratio between the D band height at 1335 cm^{-1} and the D' height at 1620 cm^{-1} band. $I_D/I_{D`}$ obtained here were in the range between ~0.75 and ~1.5 as shown in Table 7-4.

Table 7-4: The relation between the applied laser power and the defect ratio of ID/ID`.

Sample travel speed (mms-1)	**ID/ID`**
3	0.95
7	1.45
11	1
15	0.75
19	1.5

Our results are far away from the sp^3 defects which were calculated by Eckmann to be 13 of $I_D/I_{D`}$.

In summary, the fast speed lead to the formation of Graphene without a trace of SiC substrate. By decreasing the speed, the substrate starts to show up again in the Raman spectra. This was believed to be a consequence of increasing the received number of laser pulses by the surface leading to distortion of the SiC substrate or the possibility of an oxide layer formation.

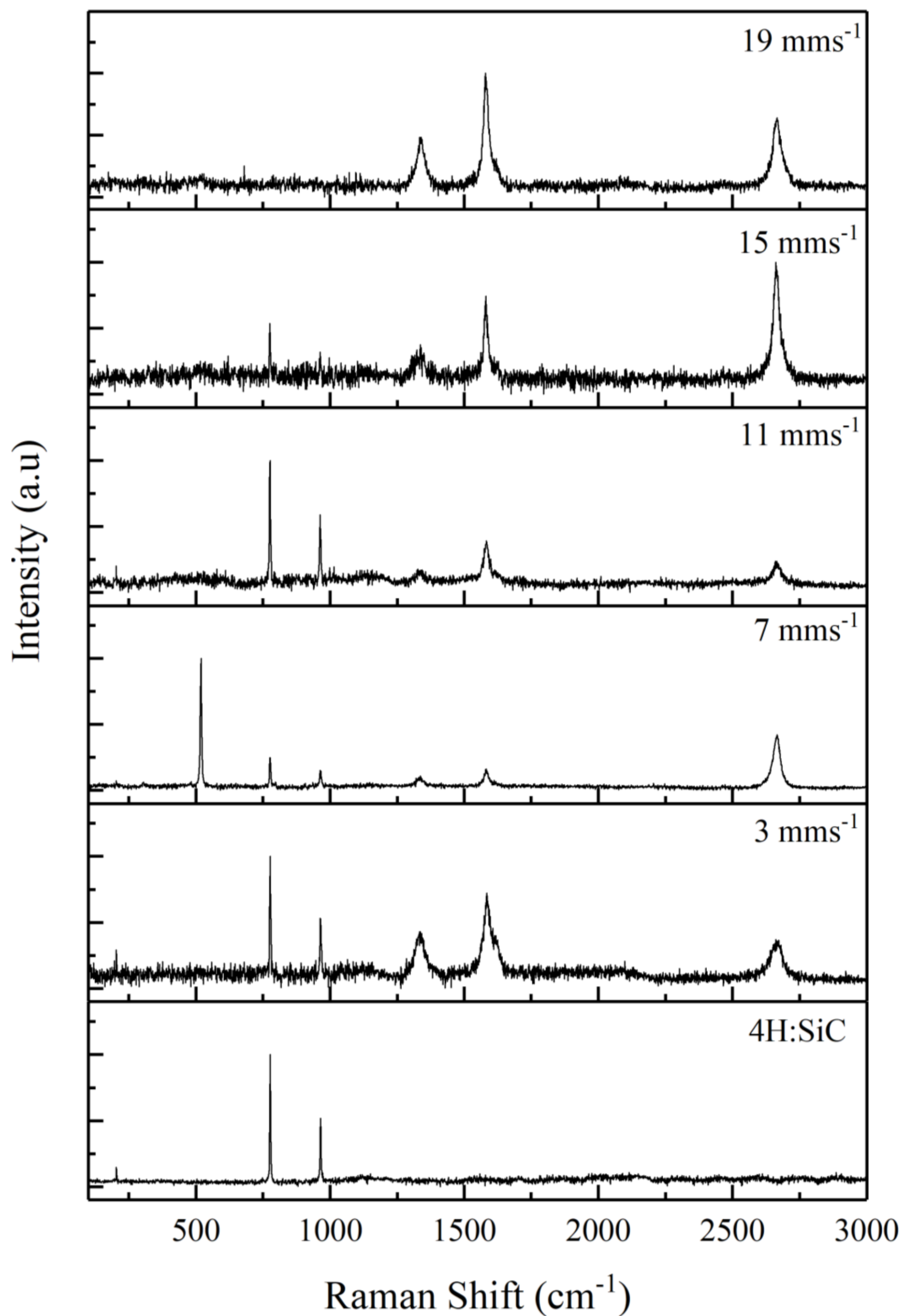

Figure 7.24: Raman spectra of CO2 irradiated 4H:SiC at different travelling sample speed. The bottom layer is an un-irradiated 4H:SiC surface, then 3, 7, 11, 15 and 19 mms^{-1}, respectively. The data were normalised and subtracted.

7.7 Irradiation under Controlled Atmosphere

All the above experiments were conducted in ambient conditions. To understand the effect of air on the processing, a low-pressure chamber was used. A continuous pump-down was in place during the processing. The pressure was measured as a ~1×10^{-4} bar. The sample was processed under applied laser fluence of ~57 Jcm^{-2} with a pulse width of ~100 μsec and a pulse repetition rate of 3 kHz. Figure 7.25 shows the SEM micrograph of the produced structure. The 3D-graphene structure was observed. This could also be suggested as carbon nanotubes. This was believed to be formed due to the gas flow during the pumping processing. The hypothesis was that carbon reconstruction by gas-phase transport at a low partial pressure of oxygen contributes to the growth of nanotubes and 3D-graphene upon decomposition of SiC.

The EDX showa an increase in the atomic percentage of C against Si for both the spot centre and the spot edge.

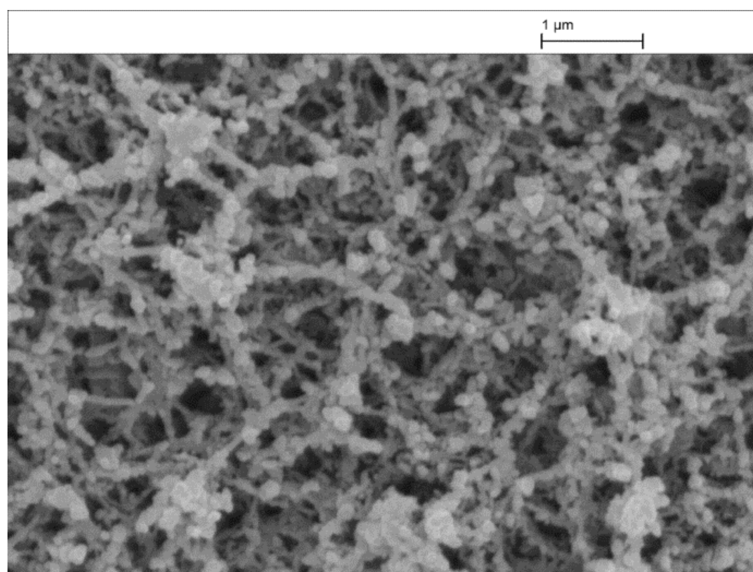

Figure 7.25: SEM micrograph of CO_2 irradiated SiC under controlled atmosphere. The applied laser fluence was ~57 Jcm^{-2} with a pulse width of ~100 μsec and a pulse repetition rate of 3 kHz.

The structure of the stationary spot was investigated by Raman spectroscopy shown in Figure 7.26. The bottom spectrum is of the pristine 4H:SiC. It shows the typical features of (204, 777 and 970 cm^{-1}). The middle layer shows the spectra at the spot centre. The D, G and 2D bands peaked at 1345, 1583 and 2690 cm^{-1}, respectively. In addition to the

above, D`, D+D``, D+2D`and 2D` peaks were found. The wine colour line represents the experimental results, and the other coloured lines show the Lorentzian fitted peaks. An (I_{2D}/I_G) ratio of about 1 and an FWHM of 26 cm^{-1} are presented. The upper spectrum is from the edge area. Apart from all the mentioned peaks above, 4H:SiC band peaks appeared in this region. The G band and 2D band peaks show a slight blue shift to 1585 cm^{-1} and 2692 cm^{-1} compared to the centre spectrum. As mentioned earlier, the appearance of a relatively strong D peak and the D` and the D+D` at 2930 cm^{-1} bands, suggest that the graphene lattice becomes disordered.

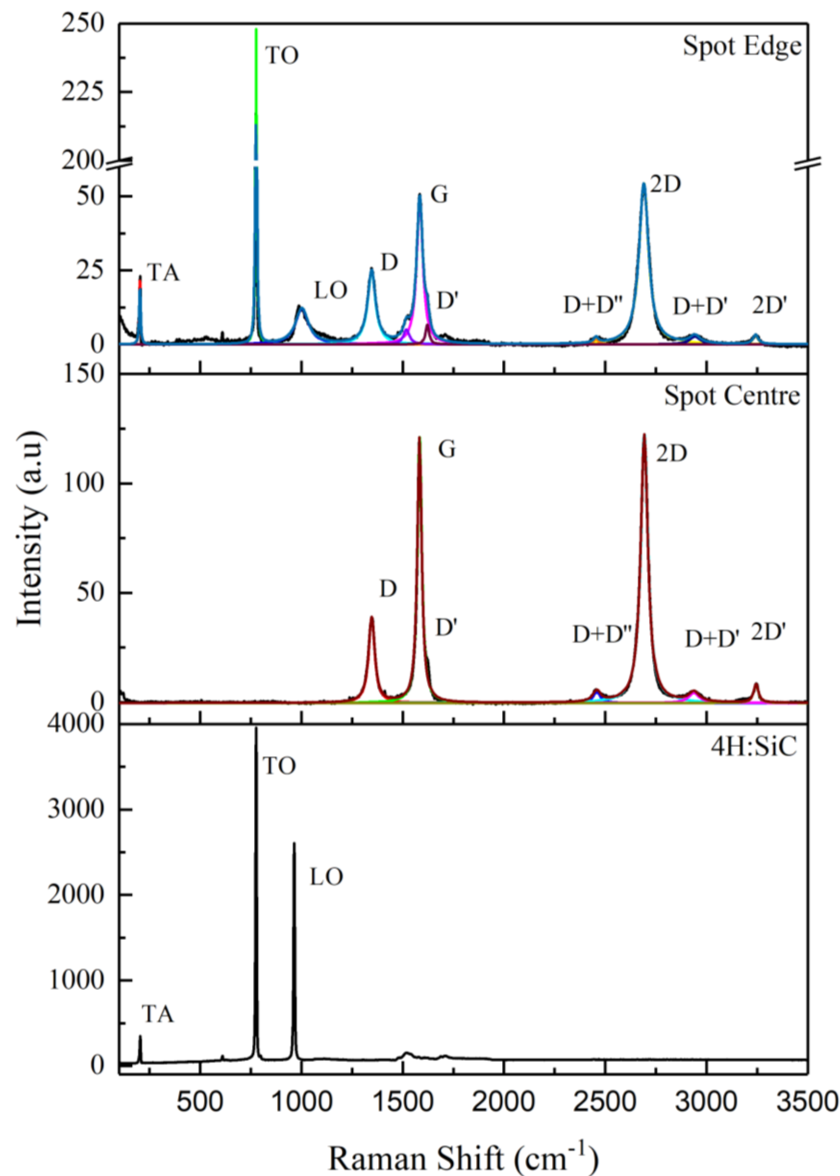

Figure 7.26: Single point Raman spectra of graphene grown on 4H:SiC using CO_2 laser under low pressure at different locations. The bottom layer shows the pristine SiC, middle layer represents the collected Raman from the spot centre and the top layer collected from the spot edge.

7.8 Summary

The laser acts as a heating source, causing a thermal decomposition of SiC, with the formation of graphene and graphene oxide.

To achieve thermal decomposition of SiC, the surface temperatures must be high enough to break the Si-C bands. Thus, Si atoms will be sublimated, and graphitisation takes place. The C atoms left behind on the top of the surface will be rearranged to synthesise the graphene.

Graphene growth on SiC surface with a CO_2 laser in atmospheric pressure was achieved. A 3D graphene structure or nanotubes were produced in a low-pressure atmosphere.

The production of graphene on top of SiC using lasers is fast, simple, cost-effective, viable and promising for different applications.

Micro-Raman spectroscopy proved the formation of graphene on the surface of the SiC substrate. The FWHM, profile and position of the 2D band peaks are in excellent agreement with the range of values found in the literature.

SEM images confirm the formation of graphene layers. It appears as small islands on top of SiC grains, spread all over the substrate surface, or as a continuous layer for a few micrometres.

Graphene, with defects and oxidation, were synthesised. Furthermore, monolayer and multilayer graphene was achieved.

Possible doped graphene was achieved on top of SiC.

Change of the substrate polytype from 4H:SiC to 3C:SiC was achieved.

Chapter 8 Electrical Properties Characterisation of the grown graphene structure on SiC

8.1 Introduction

In previous chapters, we have shown how lasers can be employed to grow graphene and its derivatives on SiC in laser direct writing process (LDW). Microstructural and compositional modifications produced by 193 nm and 10.6 μm lasers were reported. In this chapter, the electric conductance conversion in lasers irradiated SiC were discussed with the effect of different process parameters. Developing a simple, low-cost technique for making conductive tracks on the SiC surface or even p-n junctions or Schottky junctions, the key component in electronic and optoelectronic devices, has proven challenging. Laser processing could present a simple technique for the large-scale patterning of graphitic/SiC junction. “Precise controllability, ease of computer automation to direct a laser beam and its localized intense heating capability make the laser direct-write technique advantageous over the conventional methods for processing wide band gap materials”.

Two-point probe measurements were obtained on the produced graphene-like/SiC wafers. Graphene, graphene oxide and reduced graphene oxide growth on SiC will open new routes for applications, see section 2.7. DLW is a reproducible process, and it can be done directly on the SiC surface with no need to transfer the produced layer. The irradiated samples were characterised using, SEM, AFM, optical microscope and Raman microscopy. Temperature simulations have been performed using the finite element method (FEM) to assist in understanding the dissociation mechanisms of SiC and hence optimise the experimental variables. 2D axis-symmetric FEM calculations predict a surface temperature. Laser-irradiated 4H:SiC is an efficient and controllable method of realising highly reproducible electrically conducting tracks.

8.2 Results and Discussion

8.2.1 Excimer Laser Direct Written Graphitic Channels

193 nm laser processed SiC was investigated electrically due to the production of a graphitic structure. LDW patterns were controlled by overlapping the laser spots using the XYZ nano-resolution controlled stage. It has many advantages; it is an easy method, fast, cost-effective and could be done in an ambient or controlled atmosphere. Most of the electrical measurements were done on semi-insulating v or n doped SiC. Figure 8.1 shows the I-V characterisation of a produced channel. The sample was irradiated with a fluence of 1.56±0.08 Jcm^{-2}, the resistance decreased by nine orders of magnitude in comparison with the non-irradiated SiC area. The resistivity of the un-irradiated SiC was more than 10^7 Ωcm. There was also a linear increase in the resistance by increasing the space between the two probes by 1 mm each time, see Figure 8.2. A linear correlation between the current and voltages was noticed, see Figure 8.1. This indicates the Ohmic behaviour that is typically related to metal samples.

Others reported the conduction properties of the graphitic/SiC junction using femtosecond lasers by measuring the I-V[72,236,237]. A decrease in resistivity of six orders of magnitude was reported compared with non-irradiated surfaces. The decrease is attributed to the drastic increase in electric conductivity on phase separation associated with the formation of traditional laser induced periodic structure. They used the I-V characteristics and the scanning electron microscope observations to confirm their conclusion.

The resistivity (ρ) was measured using Equation (8.1):

$$\rho = \left(\frac{\pi}{\ln 2}\right) tR \tag{8.1}$$

Where t is the irradiated channel thickness, and R is the resistance. Equation (8.1) only works when $t \leq d/2$. Where d is the spacing between the probes (in the above case, 160 nm < 500 μm). A thin film of graphene and graphene oxide is often measured using their

sheet resistance (ρ_s) in units of ohms per square. This can be obtained by dividing the resistivity over thickness $\rho / t = (4.6 \pm 0.5)$ Ω/square. *Graphene derivatives* resistivity is less than the substrate, ensuring that the applied current only flows through the *graphene* layer during the I-V measurements. The SiC substrates resistivity were between 10^5 and 10^7 Ω.cm.

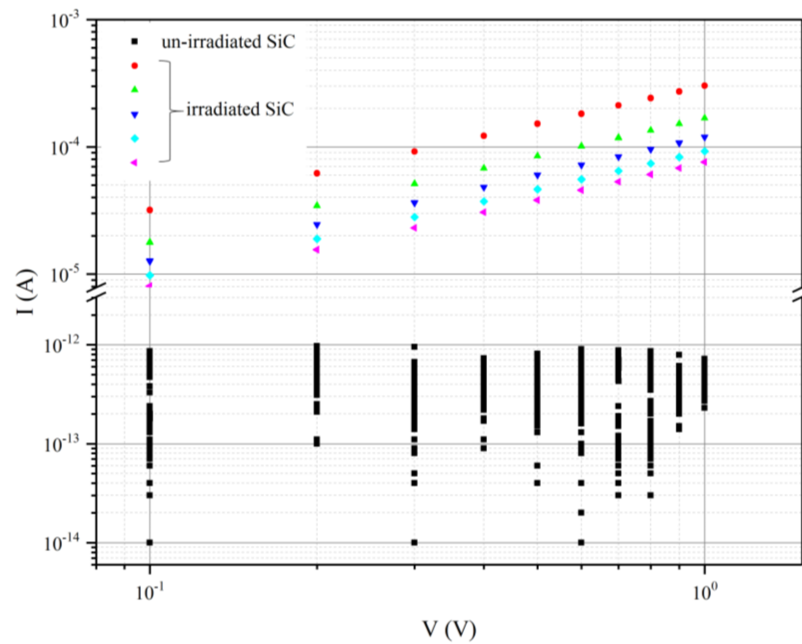

Figure 8.1: I-V characteristic of the graphitic channels produced by 11.5 nsec 193 nm laser at a fluence of 1.56 ± 0.08 Jcm^{-2}. The sample speed was 0.01 mms^{-1} with 5 Hz pulse repetition rate. The black data represent the un-irradiated SiC while the coloured data shows the irradiated channel with probes spacing changing from 1 mm to 5 mm, respectively.

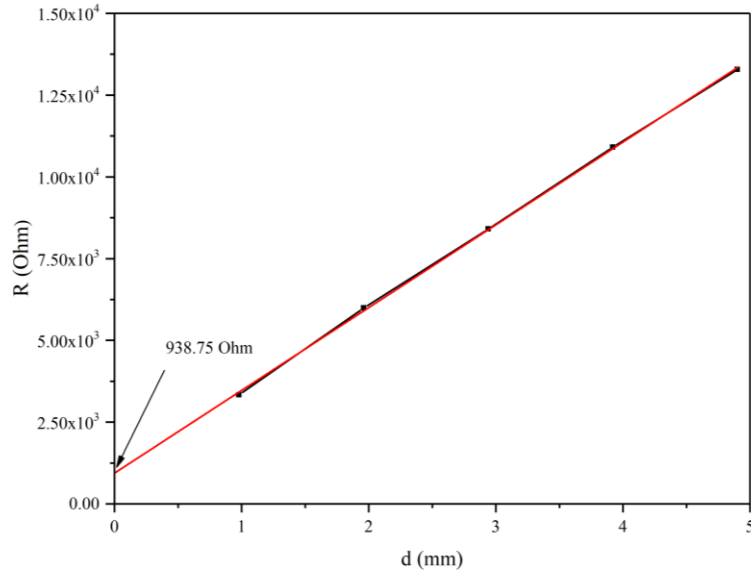

Figure 8.2: The linear relation between the reduced resistance and the changing spacing distance between the probes measured on the channel produced with 1.56 Jcm^{-2}.

Tracks produced with a gap between them were achieved with a 900 nm spacing, see Figure 8.3. A typical I-V curve of graphene or reduced graphene oxide devices was shown as a function of the spacing between the two probes. Figure 8.4 exhibits strong linearity. This was possibly related to the formation of the reduced graphene oxide layer confirmed by Raman spectra. However, when the probes were on one track, the resistance was as measured before, ~940 Ω, while when the probes were located on two tracks, the resistance increased drastically as shown in Figure 8.4.

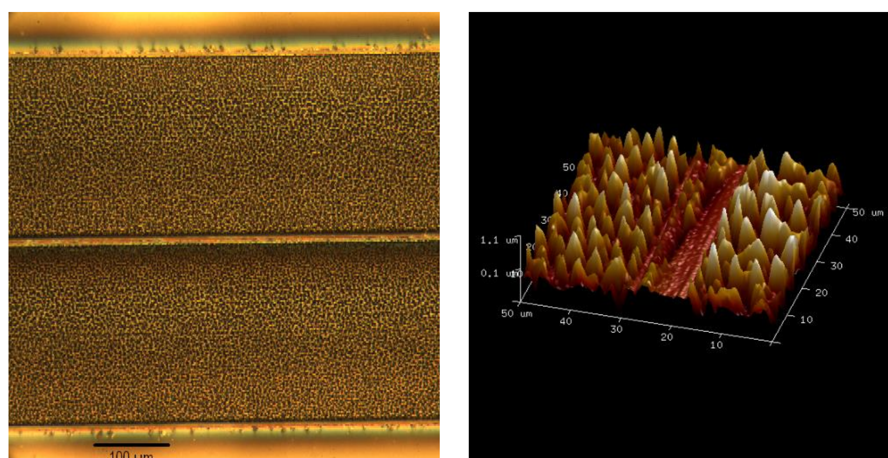

Figure 8.3: Optical micrograph of the gap width between two tracks on SiC (the left) and the corresponding AFM image (right)

To understand the mechanism of producing the graphitic channel, COMSOL™ 5.3 was used (Figure 8.5) to estimate the temperature of the irradiated surface. It shows that the temperature of the 4H:SiC surface reached ~2300 K at the laser pulse duration of 11.5 nsec for the applied fluence of 1.56 Jcm^{-2}. The temperature rise exceeded the melting temperature of Si. This supports the idea of evaporating the Si atoms leaving the carbon behind. However, the high energy of the applied 193 nm laser played a role in the decomposition of the SiC, leading to the decoupling of the Si and the C. In addition, ambient condition processing was believed to play a significant role in the production of graphene oxide which then was processed by further laser irradiation to produce reduced graphene oxide.

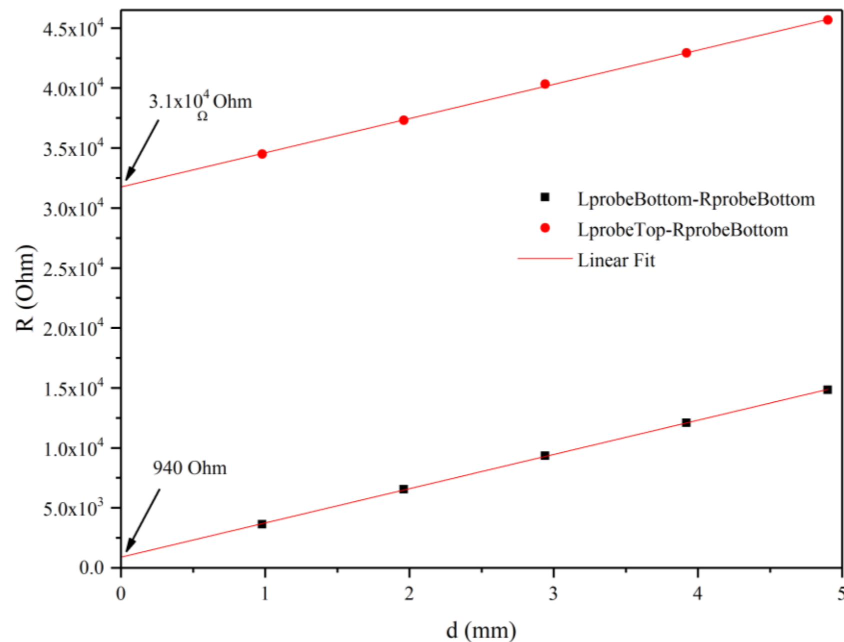

Figure 8.4: The linear relation between the reduced resistance and the changing spacing distance between the probes measured on the channel produced with 1.56 Jcm^{-2}. The probes were either together on one track or each on one track.

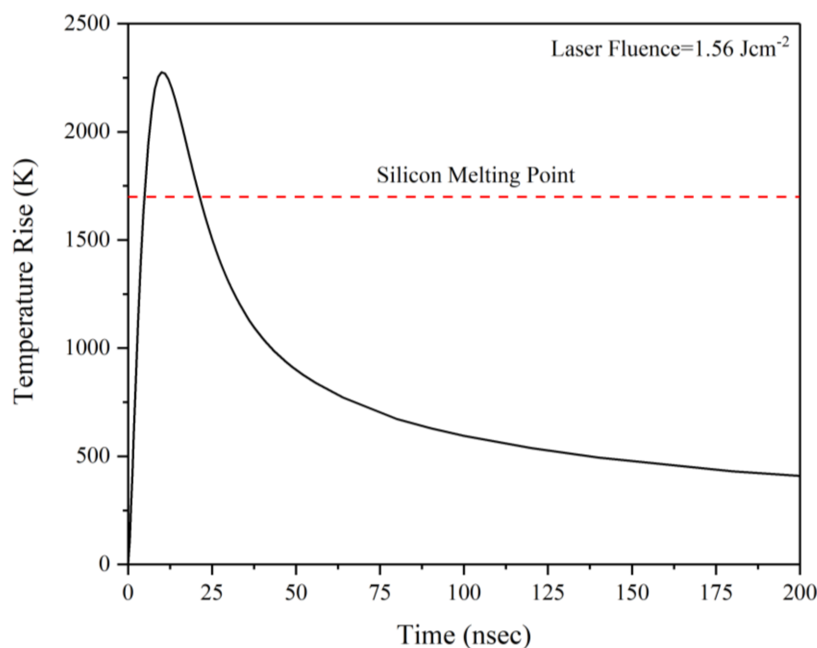

Figure 8.5: Temperature rise as a function of time for the laser fluence 1.56 ±0.08 Jcm^{-2}. It shows that the temperature exceeds 2250 K for the pulse duration of the laser of 11.5 nsec.

Micro-Raman measurements were collected to understand the composition structure (see Figure 8.6). It shows the unirradiated SiC surface as a reference in the bottom layer in Figure 8.6. The peaks were observed at 204, 777, 798 and 970 cm^{-1} which all related to 4H:SiC. In the top layer of Figure 8.6, peak bands of an amorphous and nanocrystalline matrix were found. A trace of the substrate was collected with a broader band due to Si-C optical modes of an amorphous phase and a trace of 3C:SiC polytype. In the range, 400-550 cm^{-1}, both a broad band centred around 480 cm^{-1} and a sharp peak at 520 cm^{-1} were found. The broad peak was related to the optical modes of Si-Si as an amorphous phase. The peak at 520 cm^{-1} indicates the richness in the Si-related to the LO mode of crystalline silicon. Besides, an increase in the C-C bands was detected as a D, and G bands. The D band (defects or disorder) at 1320 cm^{-1} and G (graphite) which spread around 1587 cm^{-1} are both clearly shown and indicate the presence of carbon like material. These peaks indicate a formation of rGO texture on top of SiC. These peaks emerged as a result of a direct laser writing on the surface of SiC. These results are consistent with the SiC decomposition theory of SiC due to 193 nm laser irradiation. It also shows the 4H:SiC peaks decreasing with emerging Si and graphite peaks.

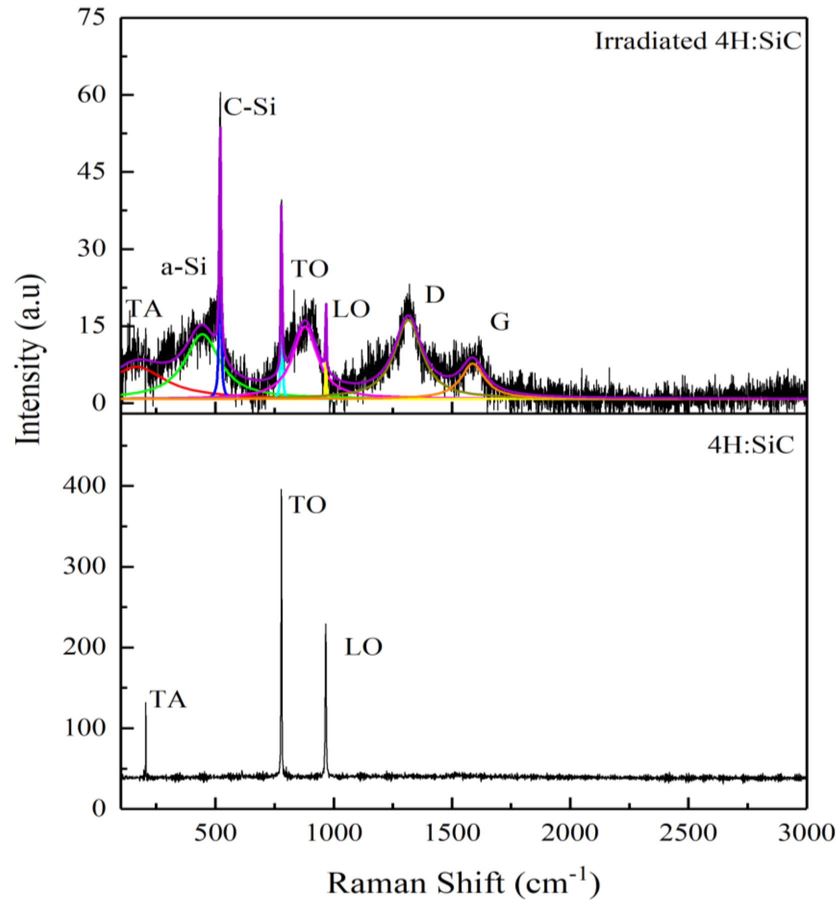

Figure 8.6: Micro-Raman spectra of 4H:SiC before irradiation (top layer) and after irradiation with 193 nm laser (bottom layer). Excitation laser was 784 nm at the power of 1 mW.

It is believed that the reason for some non-linearity in measurements on SiC could be due to the high contact resistance. For the nonlinear relation, the Si and SiC are not dominant, but there is carbon like structure dominating, represented by the G and D band that behave as a graphene or rGO on SiC. While for the site composition of heavy dosage irradiation, it will be mostly Si dominant. So, more voltage will be needed to overcome the energy gap. The topography of the above channel can be seen in Figure 8.7. It shows an interconnected shape of pillars similar to the behaviour shown with spinodal decomposition. The difference between the surface of the 4H:SiC before and after ArF laser irradiation, is shown by an AFM image in Figure 8.8. The hight sensor increased from 4.4 nm to 1.1 μm and the roughness dramatically changed where Ra increased to 130 nm.

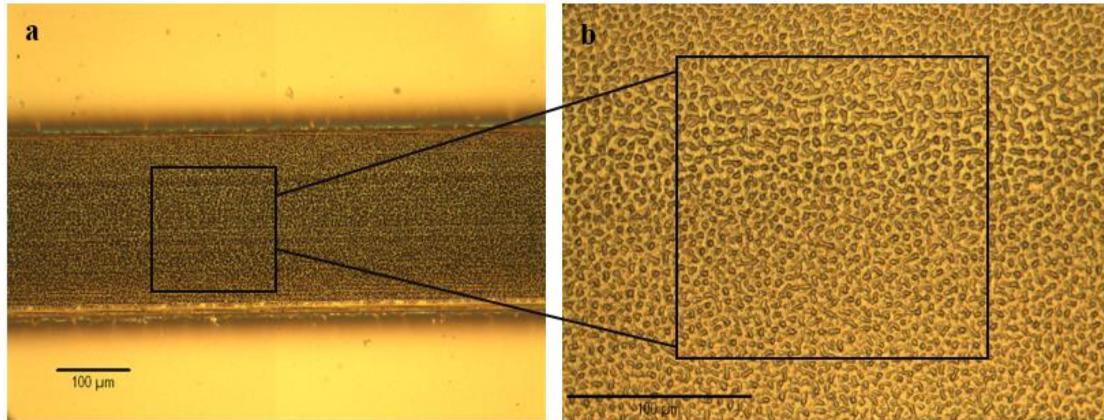

Figure 8.7: Optical micrograph of the irradiated channel by ArF laser with 1.56 Jcm^{-2}. a) is X100 magnification and b) is higher magnification.

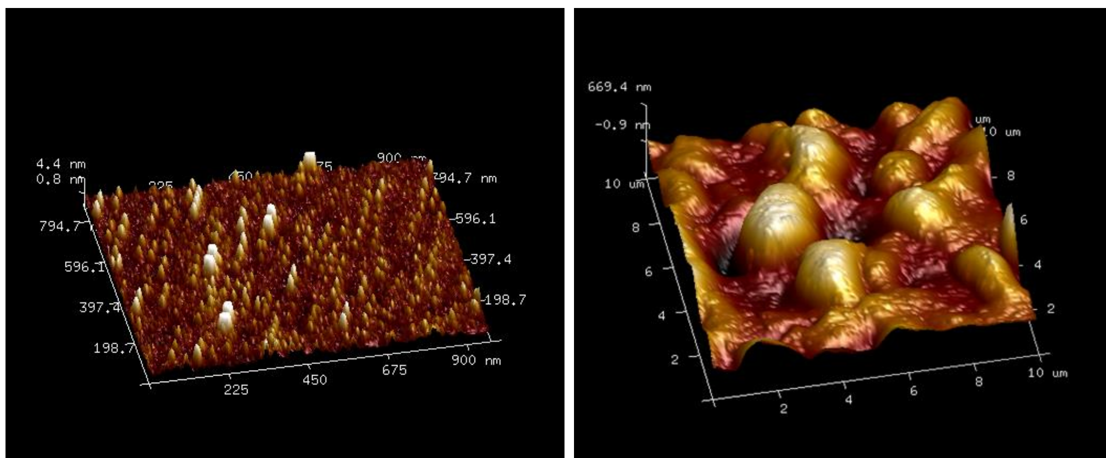

Figure 8.8: AFM images of 4H:SiC before laser processing a) semi-insulating SiC and after 193 nm laser processing, (b) conductive SiC.

8.2.2 Effect of Laser Power and Travelling Speed on the I-V Measurements.

The electrical conductivity of the irradiated sites as a function of the travelling speed was investigated. Figure 8.9 represents the I-V characteristic of irradiated 4H-SiC as a function of the travelling speed of the sample. The samples irradiated with 193 nm laser at ~1.4 Jcm^{-2}, with a laser frequency of 10 Hz. A channel with 155 μm width was achieved. The scanning speed was chosen to give a specific overlapped number of pulses per site. The overlapped pulses were set to 10, 100 and 1000. The I–V data were symmetrical for positive and negative voltages. The two probes I-V measurements were asymmetrically indicating similar behaviour to typical Schottky diode behaviour on the un-irradiated SiC. The I-V data collected by HP4140B source meter unit in the dark, so no light was involved

in the process. For relatively high speed having only 10 pulses per site, there is a linear Ohmic relation with a resistance of 746 Ω and sheet resistance of 3380 Ω/□.

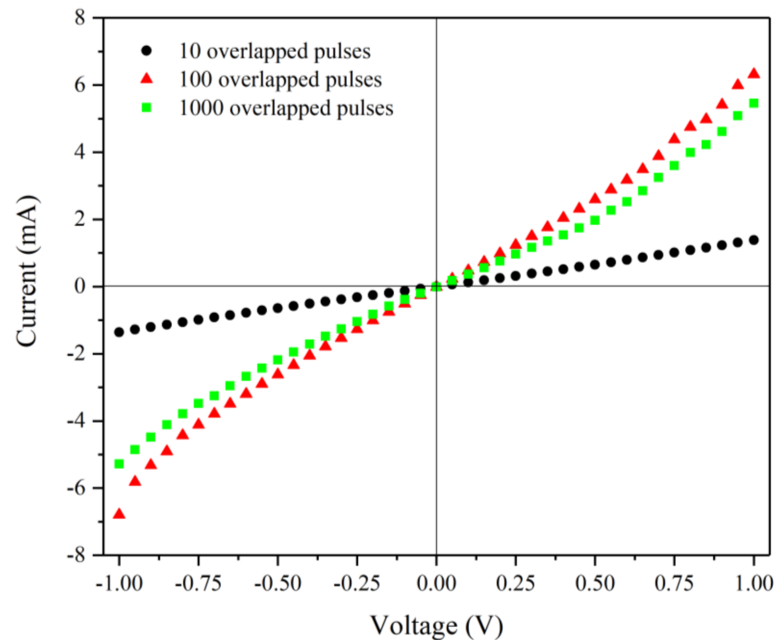

Figure 8.9: I-V measurements of graphitic/SiC junction produced by 193 nm at 1.4 Jcm^{-2} laser fluence with different speed or overlapped dosage.

With increasing the pulses to 100 per site, a dynamic resistance relation appears. Meaning that it is a nonlinear relation, and the resistance will depend on the applied voltage and current at a certain point. However, for low applied voltages ranging between 0 and 0.6 V; the curve has an almost linear behaviour and the resistance range from 170 to 200 Ω. The sheet resistance was measured to be 784 Ω/□. While by further irradiation of the site to 1000 times, the same behaviour continues with higher resistance. This could be related to the fact that when we apply low laser dosage, subsurface interaction with only 29 nm thickness were achieved according to the WLI. Moreover, by increasing the dosage, more interaction took place. Besides, the decomposition mechanism changed, as discussed in Chapter 6.

Different structures formed depending on the overlapped pulses, as shown in the optical micrographs in Figure 8.10(a-c) and the corresponding AFM images in Figure 8.10(d-f).

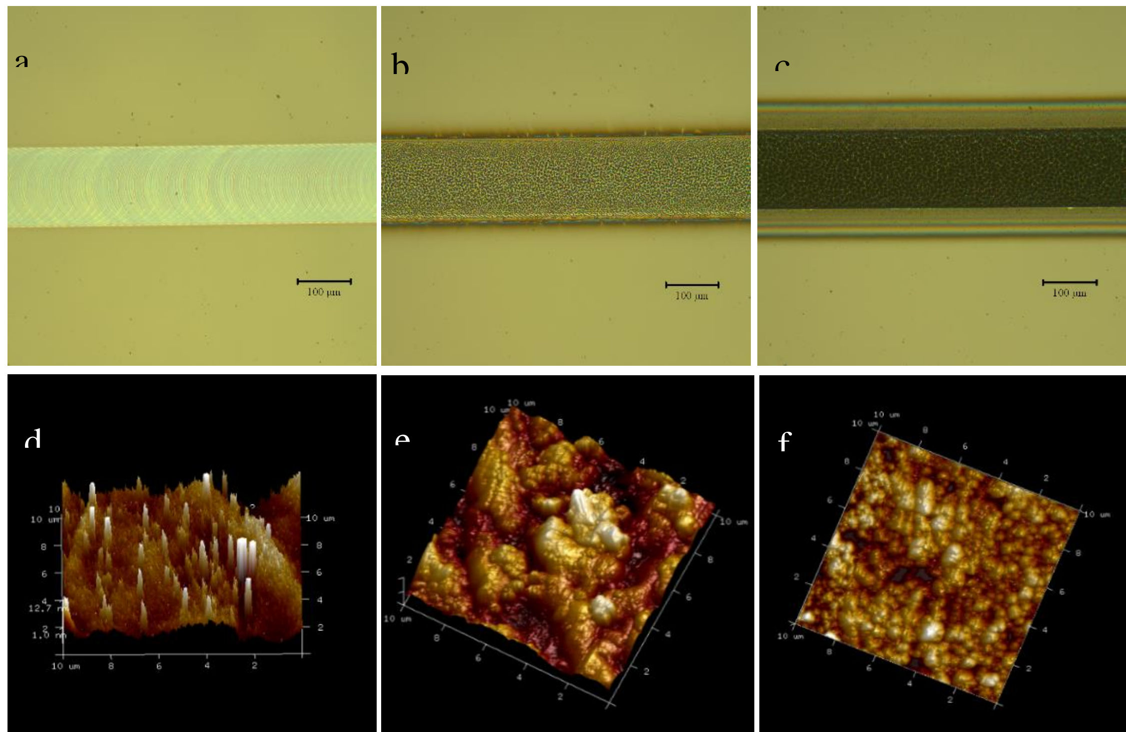

Figure 8.10: Top row represents the optical micrographs, and the bottom row is the AFM graphs of the graphitic structure produced on SiC irradiated by 193 nm laser at 1.4 Jcm^{-2} with different overlapped laser pulses (a, d) 10 pulses (b,e) 100 pulses and (c,f) 1000 overlapped pulses.

The same irradiation conditions were repeated with a laser fluence near the threshold at 1 Jcm^{-2}. The I-V measurements are shown in Figure 8.11.

The I-V curves were close to zero at irradiation with 10 and 100 overlapped pulse with a resistivity of 0.55 Ωcm and 0.0057 Ωcm, respectively. When the direct current bias increased, the reverse leakage current increased rapidly, indicating that severe damage had occurred on the surface. The forward leakage currents also increased with increasing the dc bias.

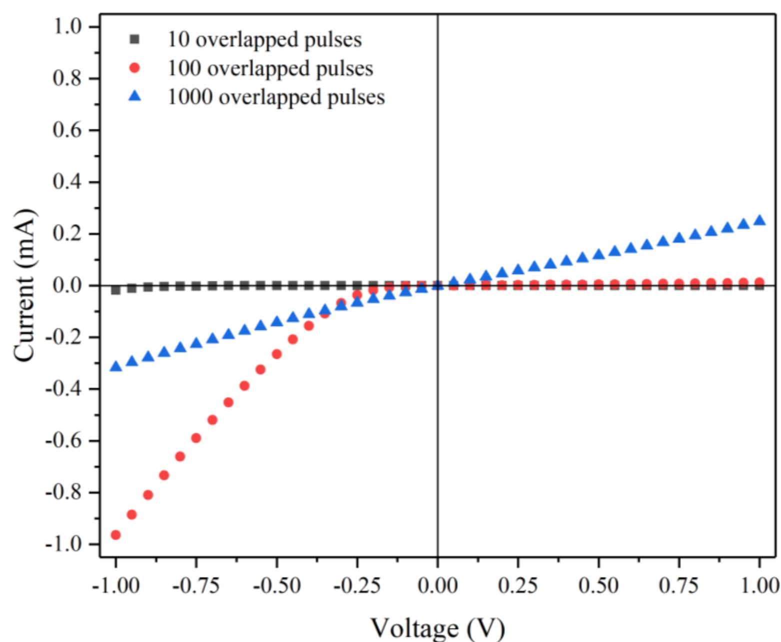

Figure 8.11: I-V measurements of graphitic/SiC junction produced by 193 nm at 1 Jcm^{-2} laser fluence with different speed or overlapped dosage.

8.2.3 CO_2 Laser Direct Written Graphitic Channels

CO_2 Laser processed SiC for the production of a graphitic structure were investigated thoroughly in Chapter 7. The conductivity of the LDW channels was investigated as a function of the applied laser parameters such as the applied power, the travelling speed of the sample and the pulse duration effect. The electrical measurements were conducted on semi-insulating v or n doped SiC with a resistivity of more than 10^7 Ωcm. Investigation of the electric properties of the single and multilayer graphene (synthesised with different applied laser power and confirmed by Raman measurements) were conducted. The I-V properties of the adjacent Ag electrodes were measured at room temperature, see Figure 8.12. The tracks were produced with irradiated laser power of 3, 4.5, 6.2 and 10 W. A non-linear correlation between the current and voltages were noticed, see Figure 8.1. However, the linearity increased with increasing the power of the pulse. This indicates the Ohmic behaviour that typically related to metal samples. The resistance was 130 kΩ at the tracks created with 3 W laser. By increasing the applied power, the resistance decreased to roughly ~30 kΩ. Graphene-SiC I-V could be acts with fluctuations which were correlated to spatial inhomogeneity at the junction due to the roughness, graphene

layer thickness variations, dislocations and grain boundaries, as well as the presence of atomic steps in the SiC as it can be seen in Figure 8.13.

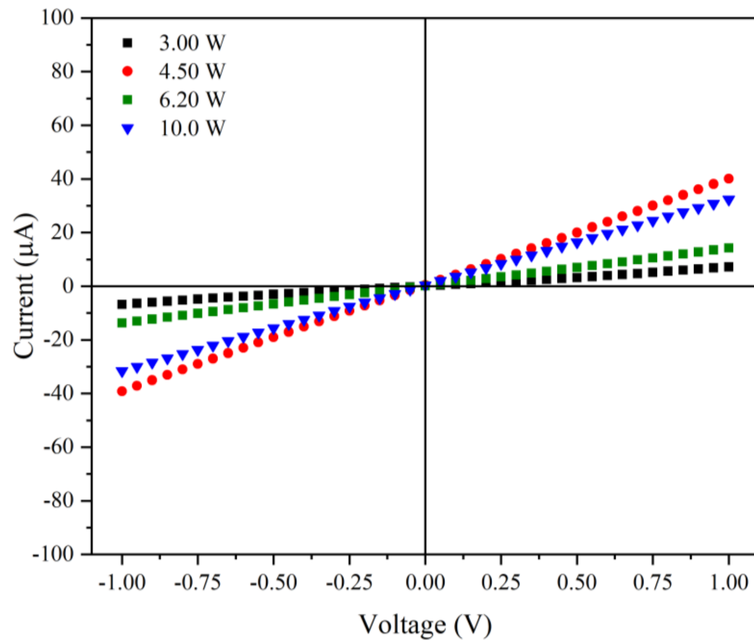

Figure 8.12: I-V measurements of the graphitic/SiC surface produced by CO_2 laser as a function of the applied laser power.

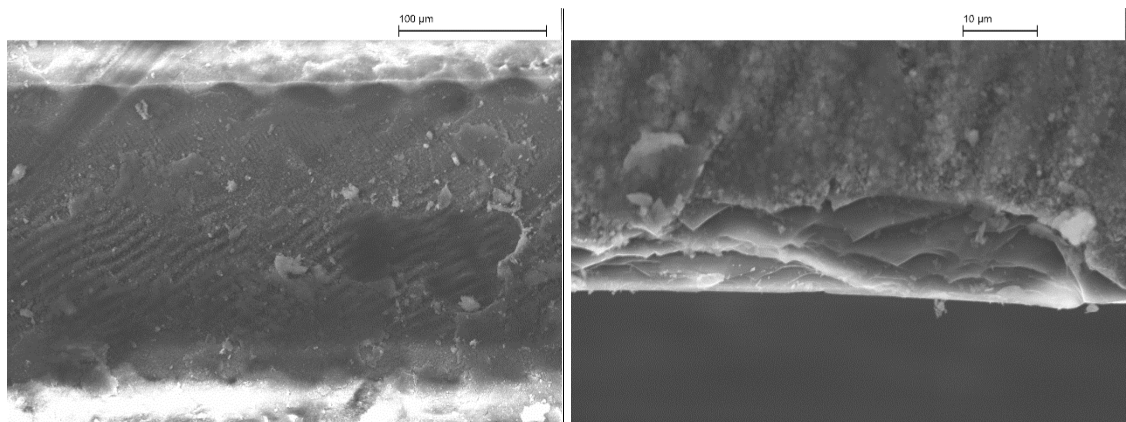

Figure 8.13: SEM micrograph of graphene/SiC junction produced with different laser power (left side) 6.2 W (right side) 14 W

Investigation of the electric properties of the formed graphene (synthesised with a different number of overlapped pulses) was conducted. The I-V properties of adjacent Ag electrodes were measured at room temperature, see Figure 8.14. The tracks were produced with a stage speed of 3, 7, 11, 15 and 19 mms^{-1}. A linear correlation between the current and voltages was noticed, see Figure 8.1. However, the resistance increased with

increasing stage speed. The resistance was 19 kΩ at the tracks created with stage speed of 3 mms^{-1}. By increasing the stage speed, the resistance increased to roughly ~30 kΩ.

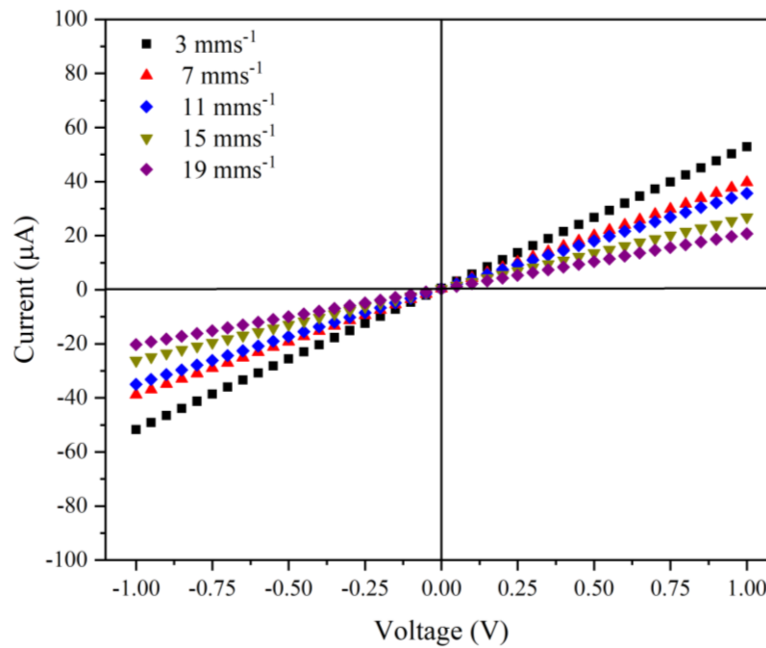

Figure 8.14: I-V measurements of the graphitic/SiC junction produced by CO_2 laser as a function of the travelling speed.

An I-V curve was also measured for graphene/SiC junction produced at different laser pulse durations as shown in Figure 8.15. The figure shows that the resistance decreased from 204 kΩ to 48 kΩ when we increased the pulse duration from 100 µsec to 400 µsec. The surface topography can be seen in Figure 8.16.

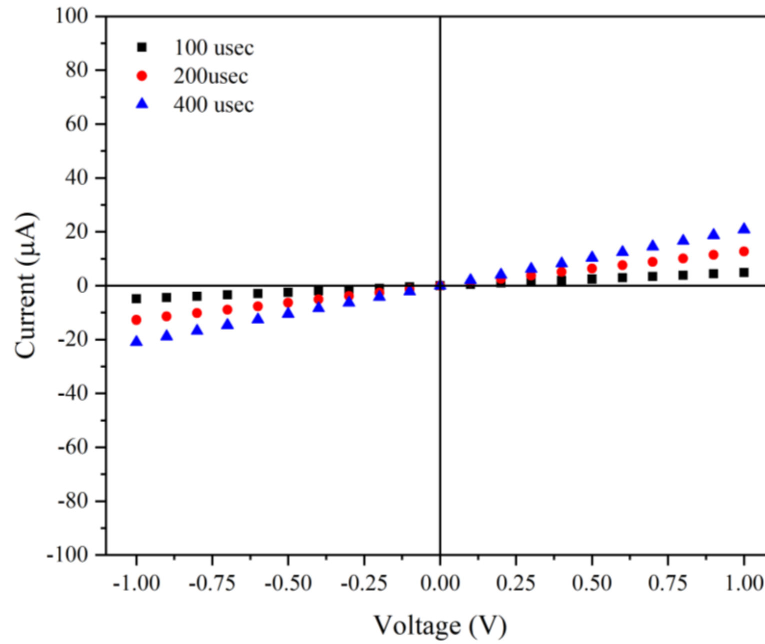

Figure 8.15: I-V measurements of the graphitic/SiC junction produced by CO_2 laser as a function of the applied laser pulse duration.

In general, the I-V characteristics suggest that grown graphene sometimes acts like an Ohmic junction and sometimes act like Schottky junction. Fluctuation of the I-V data with the tracks produced by CO_2 laser was related to the high roughness noticed on the surface of SiC.

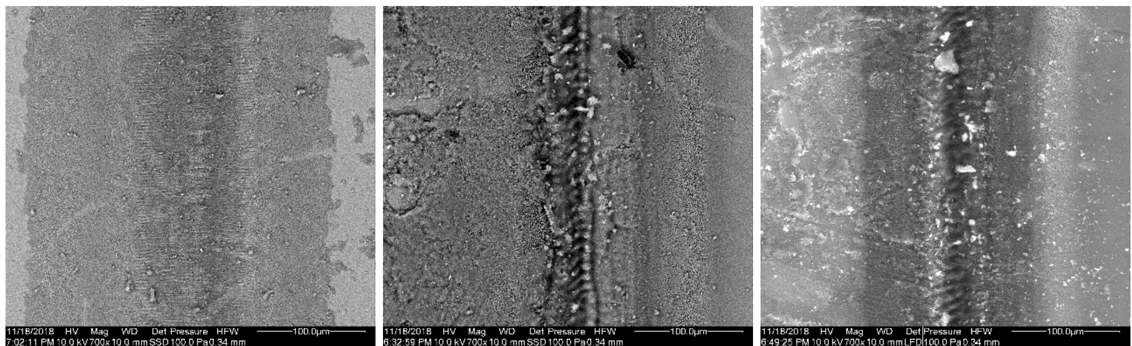

Figure 8.16: SEM micrographs of the graphene derivatives/SiC tracks produced with different laser pulse duration (a) 100 µsec, (b) 200 µsec and (c) 400 µsec.

8.3 Summary

In this work we reported experimental results of 193 nm ArF laser and CO_2 laser irradiated 4H:SiC. Current-Voltage measurements show a decrease of the electrical resistance per unit length by nine orders of magnitude. The lowest resistance per unit length was obtained using a laser fluence of ~1.5 Jcm^{-2} for the 193 nm system, at a pulse repetition frequency of 10 Hz and using a sample translation speed of 0.01 mms^{-1}. Graphene oxide and reduced Graphene oxide were produced using the 193 nm laser.

I-V data showed less decrease in the resistance for the graphene and graphene derivatives/SiC produced by CO_2 laser compared to excimer laser samples.

Mainly, it was showed that it would require very high laser fluence to change and increase the conductivity.

Calculations predict the contact resistance of SiC to be approximately 900 Ω, which is of the order of the input resistance of the voltmeter in our two-point probe measurements. There was almost no change in two-probe I–V curves when the spacing between the probes was changed from 1 mm to 5 mm.

Moreover, the currents of modified lines increased more than nine orders of magnitude when compared with those of the non-irradiated SiC. We conclude that the modification related to the change of the material stoichiometry.

Chapter 9 **Conclusion and Future Work**

9.1 Conclusion

Laser irradiation of 4H:SiC was performed as a function of lasers parameters in the ambient and controlled atmosphere. Different laser systems such as excimer laser with nanosecond pulses and CO_2 laser with microsecond pulses were employed. The ablation threshold and the effects on removal material and thermal damage were investigated.

Analytical and numerical modelling was used to determine the temperature of the sample during and after laser processing. Our measurements and simulations can be efficiently used to describe experiments involving laser heating with minimum limitations. The finite element analysis using COMSOL software was performed to study and predict the temperature distribution on and inside the SiC. The FE simulation models would be highly helpful to select the optimum laser parameters for laser machining.

Numerical results based on less assumption were achieved, resulting in a more accurate temperature rise compared to the analytical version. 1D and 2D-axisymmetric geometry models were applied, and both models gave roughly the same temperature rise. The numerical solutions displayed a robust thermal gradient in the z-direction, which was dependent on the material properties.

The models were built for the excimer laser having a spatial top hat profile and the CO_2 laser with a spatial Gaussian profile. Laser parameters such as laser power (fluence), pulse duration, scanning speed and spot radius was investigated.

With the 193 nm model, the following were concluded: the temperature rises at a laser fluence of 0.97 Jcm^{-2} with 11.5 nsec pulse duration was above the melting point of SiC. The temperature rise was linear with the applied laser fluence. The temperature exceeds the melting point of SiC at a laser fluence of 1.95 Jcm^{-2}. For a laser fluence of 2.6 Jcm^{-2}, the temperature at the surface reached 4000 K, which is close to the melting point of

carbon. The depth temperature profile was in good agreement with the experimental results. For the nanosecond pulses, the substrate effect was negligible. The energy rate deposited is higher in shorter duration leading to more localised distribution in the material.

For a spatial Gaussian CO_2 laser, the energy rate deposition was slower with higher penetration depth. Hence, the heat diffuses into the material, and the cooling plays a dominant effect. The pulse duration of the applied CO_2 laser affected the surface temperature massively. By increasing the pulse duration, the temperature will decrease.

More energy is needed to heat the SiC surface to the same temperature with the CO_2 laser compared to the 193 nm laser. The depth distribution of the heat will increase drastically. The effect of the slow cooling rate means that increasing the number of pulses will affect the temperature rise of the surface and will build up with each pulse. Moreover, the cooling rate would also be affected by the substrate.

An ArF excimer laser emitting at a wavelength of 193 nm has been used to investigate the ablation and decomposition of 4H-SiC. The onset of surface modification is seen to take place at a laser fluence of 925 ± 80 $mJcm^{-2}$. The etch rate and concomitant surface modification at this fluence are observed as a subtle process and not an abrupt removal of material. The experimentally measured etch rate at threshold corresponds to ~200 pm per laser pulse. Etch rates are close to but above the etch rates calculated using the H-K and C-C relations and correspond to ~20 pm per laser pulse. Micro Raman measurements indicate regions of silicon and carbon on the surface of the laser-irradiated 4H-SiC. At laser fluences where the significant material is being removed, the growth of micron-sized nodule-like structures on the floor of the ablation crater was observed. SEM measurements show clearly the nodules are decorated with spherical particles and ripple structures on the floor of the ablation crater. The graphitic and carbon-rich nature of laser irradiated sites has encouraged further investigations using a laser direct-write technique to produce electrically conductive tracks on 4H- SiC substrates.

Spots and channels produced on the SiC surface using stationary and travelling processing with 193 nm and 10.6 μm systems. The channels were made with different moving stage speeds. For the 193 nm processing, the train of pulses effect were independent of the stage

travel speed since the cooling rate was in nanoseconds and the laser repetition rate was in milliseconds. However, in the CO_2 processing, the cooling rates were in microseconds close to the laser pulse durations. In general, increasing the number of overlapped accumulations of material removal takes place. The rearranging of the melted surface was affected directly by the energy deposited in the material.

With the excimer laser, surface texture changed from smooth to rough with small protruding texture on the surface. The protruding dimension increased with increasing fluence. At high fluence such as 5 Jcm^{-2} the ablation effect took place, and the new left surface had a smoother texture with the formation of ripples. SEM imaging of the surface shows a nanocrystallite structure formed on it. While micro Raman analysis proved that the protruding texture was a mixture of Si and SiC. Raman with laser excitation of 532 nm was more of background spectra with sharp SiC bands.

In low fluence regime, the material keeps the original composition of SiC with no trace of graphitic structure. However, accumulation of Si was observed on the edge of the sites. With increasing the fluence, the material suffers decomposition and graphitic structure rearrange on the surface. As a binary compound, SiC would have structural changes due to the total energy difference between two crystallographic structures and the ungorigent melting, the surface would be covered with graphitic structures, and silicon in addition to traces of the substrate was available.

Micro Raman with He-Ne laser excitation showed the detailed structure of the surface. At a fluence of 1.4 Jcm^{-2}, the surface was covered in reduced graphene oxide starting from low to high pulse dosage. This was attributed to the ambient condition and the availability of oxygen. The TO peak is of a small size and shows a small position shift, but the LO peak exhibits a downshift and asymmetrical broadening as the nanocrystallite size decreases. The intensity of the TO and LO modes decreases with decreasing nanocrystallite sizes. The scattering can be spread out over a much broader range of frequencies by varying the nano-crystallite size.

With the CO_2 laser processing, the laser acts as a heating source and causes a thermal decomposition of SiC, with the formation of graphene and graphene oxide. The ablation threshold measurements were divided into two regions indicating different mechanisms

involved. To achieve thermal decomposition of SiC, the high laser power was employed to allow the surface to reach temperatures sufficiently high to break the Si-C bands. Thus, Si atoms will be sublimated, and graphitisation takes place. The C atoms left behind on the top of the surface will be rearranged to synthesise the graphene. Graphene growth on SiC surface with the CO_2 laser in atmospheric pressure was achieved. 3D graphene structure or nanotubes were achieved with vacuum pumping down during the laser processing. The production of graphene on top of SiC using lasers are fast, simple, cost-effective, viable and promising for different application.

SEM images confirm that graphene layers appear as small “islands” on top of SiC grains and small flakes spread all over the substrate surface, and not as a continuous layer. Ripples were also found on the surface in almost all samples. Graphene, free of oxidation and with oxidation, were synthesised with high laser energy density. The mud-like structure was shown in the irradiated sites with roughly 4.2 W. The Spatial Gaussian profile of the pulse has a significant effect on the prepared composition as it was confirmed with Raman spectroscopy. rGO spectra were collected at the edge of the irradiated tracks.

Micro-Raman spectroscopy proved the formation of graphene on the surface of the SiC substrate. The FWHM, profile and position of the 2D band peaks are in excellent agreement with the range of values found in the literature.

Furthermore, monolayer and multilayer graphene was achieved. Possible doped graphene was achieved on top of SiC. Change of the substrate polytype from 4H:SiC to 3C:SiC was achieved.

The mechanism of converting the upper crystalline layers of SiC to graphene (GO or rGO) was achieved by a laser oxidation/reduction process. The absorption of intense laser energy by SiC gives rise to an increase in the temperature in the exposed volume, which in turn oxidises the graphene or the arranged carbon in the ambient environment by absorbing oxygen in the air. The laser-induced rise in the temperature of a material is proportional to the laser fluence. The results reveal a simple and cost-effective alternative for the synthesis of graphene-based structures on SiC.

Current-voltage measurements of the graphitic structure on the SiC surface show a decrease of the electrical resistance per unit length by many orders of magnitude. Nine orders of magnitude were obtained using a laser fluence of ~1.5 Jcm^{-2}, a pulse repetition frequency of 10 Hz and using a sample translation speed of 0.01 mms^{-1}.

Calculations predict the contact resistance of SiC to be approximately 900 Ω, which is of the order of the input resistance of the voltmeter in our two-point probe measurements. There was almost no change in two-probe I-V curves when the spacing between the probes was changed from 1 mm to 5 mm.

The decrease in resistance implies that the observed enhancement of electrical conductivity is proportional to the dosage of the irradiated laser beam. This enhancement is caused by a material phase transition induced by laser irradiation. This drastic change in electrical conductivity is assumed to be associated with the phase transition induced by excimer and CO_2 laser irradiation

I-V data showed a smaller decrease in the resistance for the graphene and graphene derivatives/SiC produced by CO_2 laser compared to excimer laser samples. Mainly, it was shown that it would require very high laser fluence to change and increase the conductivity.

Moreover, the currents of modified lines increased more than nine orders of magnitude when compared with those of the non-irradiated SiC. We conclude that the modification related to the formation of the classical laser-induced periodic structures causes the drastic increase of electrical conductivities.

The resistance of the tracks on SiC, processed with 193 nm, shows a higher reduction compared to the channels produced by the CO_2. This was attributed to the surface texture and the edges and boundary formed on the surface.

9.2 Future Work

This body of research was conducted thoroughly to investigate the graphitisation of SiC using 193 nm laser and 10.6 µm laser. However, other work could be done to gain a better understanding on the phenomena.

- The findings of this work could be expanded into an application of graphene/SiC diodes.
- The findings of the gradient change of the produced structure as a function of the Gaussian profile could be further studied.
- Control of the Gaussian profile of the CO_2 laser could be a subject of interest to produce more homogeneous structures.
- More study could be conducted on controlling the processing environment and producing different doping types to the graphene layers by adding different gases to the vacuum chamber. Producing doped graphene with an energy gap is a subject of interest.
- Specific AFM conductivity measurements for micro and nanoscale devises produced by direct laser writing on SiC could be accomplished.

References

1. British Patent 17. 911. (1892).

2. Kunz G.F. Moissanite. *Am. J. Sci.* **19**, 396–397 (1905).

3. S. Goel, X. Luo, R.L. Reuben, W. B. R. and J. S. . *Key Eng. Mater.* **496**, 150 (2012).

4. Choyke, W. J., Matsunami, H. & and G.Pensl. *Silicon Carbide Recent Major Advances. Growth (Lakeland)* (2004). doi:10.1007/978-3-642-18870-1.

5. V. A. Izhevskyi, L. A. Genova, J. C. Bressiani, A. H. A. B. Review article: Silicon Carbide. Structure, Properties and Processing. *Ceramica* **46**, (2000).

6. M. Sabisch, P. Kruger, J. P. . *Phys. Rev.* **B55**, 10561 (1997).

7. R. Yakimova, M. Syväjärvi, E. J. R. Yakimova, M. Syväjärvi, E. Janzen, Mat. Sci. Forum 264-268 (1998) 159. *Mat. Sci.* **rum 264**-**26**, 159 (1998).

8. Larruquert, J. I. & Keski-Kuha, R. A. Reflectance measurements and optical constants in the extreme ultraviolet for thin films of ion-beam-deposited SiC, Mo, Mg2Si, and InSb and of evaporated Cr. *Appl. Opt.* **39**, 2772–2781 (2000).

9. Zhe Chuan Feng and Jian H.Zhao, Feng, Z. C. & H.Zhao, J. *Silicon Carbide: Materials, Processing, and Devices*. *Taylor & Francis Group* vol. 53 (Taylor & Francis Group, 2004).

10. Zetterling, C.-M. *Process Technology for Silicon Carbide Devices (Materials, Circuits and Devicese)*. (INSPEC, London, 2002).

11. Vasiliauskas, R. Sublimation Growth and Performance of Cubic Silicon Carbide. (2012).

12. Knippenberg, W. F. *Growth Phenomena in SiC*. *Philips Res. Repts* vol. 18 http://scholar.google.com/scholar?hl=en&btnG=Search&q=intitle:Growth+Phenomena+in+Silicon+Carbide#0 (1963).

13. Levinshteĭn, M. E., Rumyantsev, S. L. & Shur, M. S. *Properties of advanced semiconductor materials*. (2001).

14. DULEY, W. W. *UV Lasers: effects and applications in materials science*. *Journal of Chemical Information and Modeling* vol. 53 (Cambridge University Press, 1996).

15. Fedorenko, L. *et al.* Nanostructures on SiC surface created by laser microablation. *Appl. Surf. Sci.* **254**, 2031–2036 (2008).

16. Gray, Theodore, Nick Mann, M. W. http://periodictable.com/Properties/A/LatticeConstants.html. *Wolfram research Inc* (2017).

17. Kim, B., Iida, R., Doan, D. H. & Fushinobu, K. Mechanism of nanosecond laser drilling process of 4H-SiC for through substrate vias. *Appl. Phys. A* **123**, 392 (2017).

18. Torrisi, L. *et al.* Single crystal silicon carbide detector of emitted ions and soft x rays from power laser-generated plasmas. *J. Appl. Phys.* **105**, 4–11 (2009).

19. Cui, Y., Wang, L. & Ren, J. Multi-functional SiC/Al composites for aerospace applications. *Chinese J. Aeronaut.* **21**, 578–584 (2008).

20. Chamberlain, A. & Lane, J. SiC / SiC Ceramic Matrix Composites – A Turbine Engine Perspective Ultra-High Temperature Ceramics Materials for Extreme Environment Applications II. in *Ultra-High Temperature Ceramics: Materials for Extreme Environmental Applications II* (2013).

21. Matejka, V., Lu, Y., Jiao, L. & Huang, L. Effects of silicon carbide particle sizes on friction-wear properties of friction composites designed for car brake lining applications. *Tribol. Int.* **43**, 144–151 (2010).

22. Elasser, A. *et al.* 3000V, 25A pulse power asymmetrical highly interdigitated SiC thyristors. *Conf. Proc. - IEEE Appl. Power Electron. Conf. Expo. - APEC* 1598–1602 (2010) doi:10.1109/APEC.2010.5433445.

23. Singh, R. *et al.* SiC Power Schottky and PiN Diodes. *IEEE Trans. Electron Devices* **49**, 665–672 (2002).

24. Li, H., Yu, R., Zhong, Y., Yao, R. & Liao, X. Design of 400 V Miniature DC Solid State Circuit Breaker with SiC MOSFET. *micromachines* **10**, 1–12 (2019).

25. Andersson, M., Spetz, A. L. & Pearce, R. Recent trends in silicon carbide (SiC) and graphene-based gas sensors. in *From plant genomics to plant biotechnology* 117–158 (Woodhead Publishing Limited, 2013). doi:10.1533/B978-0-85-709866-5.00002.117.

26. Choyke, W. J., Farich, R. F. & Hoffman, and R. A. SiC , a new material for mirrors . 1: High power lasers ; 2: VUV applications. *Appl. Opt.* **15**, 2006–2007 (1976).

27. Shigematsu, I., Kanayama, K., Tsuge, A. & Nakamura, M. Analysis of constituents generated with laser machining of Si3N4 and SiC. *J. Mater. Sci. Lett.* **17**, 737–739 (1998).

28. Kim, S. *et al.* SiC via holes by laser drilling. *J. Electron. Mater.* **33**, 477–480 (2004).

29. Kim, S. *et al.* High-Rate Laser Ablation For Through-Wafer Via Holes in SiC Substrates and GaN/AlN/SiC Templates. *J. Semicond. Technol. Sci.* **4**, 217–221 (2000).

30. Liu, L., Chang, C. Y., Wu, W., Pearton, S. J. & Ren, F. Circular and rectangular via holes formed in SiC via using ArF based UV excimer laser. *Appl. Surf. Sci.* **257**, 2303–2307 (2011).

31. Lee, S. *et al.* Laser-Synthesized Epitaxial Graphene. *ACS Nano* **4**, 7524–7530 (2010).

32. Shafeev, G. A. *et al.* Uncongruent laser ablation and electroless metallization of SiC. *Appl. Phys. Lett.* **773**, 773 (1995).

33. D. SCITI, C. MELANDRI, A. B. Excimer laser-induced microstructural changes of alumina and silicon carbide. *J. Mater. Sci.* **35**, 3799–3810 (2000).

34. Reitano, R., Baeri, P. & Marino, N. Excimer laser induced thermal evaporation and ablation of silicon carbide. *Appl. Surf. Sci.* **96–98**, 302–308 (1996).

35. Gupta, S., Pecholt, B. & Molian, P. Excimer laser ablation of single crystal 4H-SiC and 6H-SiC wafers. *J. Mater. Sci.* **46**, 196–206 (2011).

36. Wu, Y., Ji, L., Lin, Z., Jiang, Y. & Zhai, T. Blue photoluminescence enhancement in laser-

irradiated 6H-SiC at room temperature. *Appl. Phys. Lett.* **104**, 4–8 (2014).

37. Hattori, M. *et al.* Direct growth of graphene on SiC(0001) by KrF-excimer-laser irradiation. *Appl. Phys. Lett.* **108**, 3–8 (2016).

38. Dutto, C., Fogarassy, E. & Mathiot, D. Numerical and experimental analysis of pulsed excimer laser processing of silicon carbide. *Appl. Surf. Sci.* **184**, 362–366 (2001).

39. Desbiens, J. P. & Masson, P. ArF excimer laser micromachining of Pyrex, SiC and PZT for rapid prototyping of MEMS components. *Sensors Actuators, A Phys.* **136**, 554–563 (2007).

40. Duc, D. H., Naoki, I. & Kazuyoshi, F. A study of near-infrared nanosecond laser ablation of silicon carbide. *Int. J. Heat Mass Transf.* **65**, 713–718 (2013).

41. Tong, Y., Bai, S., Zhang, H. & Ye, Y. Laser ablation behavior and mechanism of C/SiC composite. *Ceram. Int.* **39**, 6813–6820 (2013).

42. Sciuto, A., D'Arrigo, G., Mazzillo, M., Torrisi, L. & Calcagno, L. Reversibility of surface damage induced in SiC detectors by low intensity laser plasma. *Mater. Sci. Semicond. Process.* **86**, 36–42 (2018).

43. Kim, B., Iida, R., Kiyokawa, S. & Fushinobu, K. Effect of beam profile on nanosecond laser drilling of 4H-SIC. *J. Laser Appl.* **30**, (2018).

44. C.Palma, M. C. R. and C. S. cw-laser crystallisation of amorphous SiC alloys. *Electron. Lett.* **34**, 1430–1431 (1998).

45. Quintero, F. *et al.* Single-Pass and Multi-Pass Laser Cutting of Si–SiC: Assessment of the Cut Quality and Microstructure in the Heat Affected Zone. *J. Laser Appl.* **19**, 170 (2007).

46. Khuat, V., Si, J., Chen, T., Dao, V. & Hou, X. Simple method for fabrication of microchannels in silicon carbide. *J. Laser Appl.* **27**, 022002 (2015).

47. Zhang, R. *et al.* Micromachining of 4H-SiC using femtosecond laser. *Ceram. Int.* **44**, 17775–17783 (2018).

48. Tóth, S. *et al.* Silicon carbide nanocrystals produced by femtosecond laser pulses. *Diam. Relat. Mater.* **81**, 96–102 (2018).

49. Jandeleit, J., Horn, A., Weichenhain, R., Kreutz, E. W. & Poprawe, R. Micromachining of hard materials by nano- and picosecond laser radiation : Fundamentals and applications. **106**, (1997).

50. Dolgaev, S. I. *et al.* Laser-induced fast etching and metallization of SiC ceramics. *Appl. Surf. Sci.* **109–110**, 559–562 (1997).

51. Chou, S. Y., Chang, Y., Weiner, K. H., Sigmon, T. W. & Parsons, J. D. Annealing of implantation damage and redistribution of impurities in SiC using a pulsed excimer laser. *Appl. Phys. Lett.* **56**, 530–532 (1990).

52. Mizunami, T. & Toyama, N. ArF-excimer-laser annealing of 3C-SiC films - Diode characteristics and numerical simulation. *Opt. Laser Technol.* **35**, 451–456 (2003).

53. Lv, P., Chen, Z. & Zhang, A. H. X. Effect of Laser Annealing on amorphous Silicon Carbide Films Prepared by PECVD. in *Proceedings of the 2009 4th IEEE International*

Conference on Nano/Micro Engineered and Molecular Systems 743–746 (2009). doi:10.1109/NEMS.2009.5068685.

54. Hishida, Y., Watanabe, M., Nakashima, K. & Eryu, O. Excimer Laser Annealing of Ion-Implanted 6H-Silicon Carbide. *Mater. Sci. Forum* **338–342**, 873–876 (2000).

55. Chou, S. Y., Chang, Y., Weiner, K. H., Sigmon, T. W. & Parsons, J. D. Annealing of implantation damage and redistribution of impurities in SiC using a pulsed excimer laser. *Appl. Phys. Lett.* **56**, 530–532 (1990).

56. Key, P. H. *et al.* Infra-red reflectivity of ion-implanted and pulsed excimer laser irradiated 4H-SiC. *Thin Solid Films* **364**, 200–203 (2000).

57. Urban, S. & Falk, F. Laser crystallization of amorphous SiC thin films on glass. *Appl. Surf. Sci.* **184**, 356–361 (2001).

58. Palma, C. & Sapia, C. Laser pattern-write crystallization of amorphous SiC alloys. *J. Electron. Mater.* **29**, 607–610 (2000).

59. García, B. *et al.* Amorphous and excimer laser annealed SiC films for TFT fabrication. *Solid. State. Electron.* **50**, 241–247 (2006).

60. Cheng, Y., Lu, W. Y., Wang, T. & Chen, Z. Z. Fabrication of Ohmic contact on semi-insulating 4H-SiC substrate by laser thermal annealing. *J. Appl. Phys.* **119**, (2016).

61. Silva, M. De *et al.* Formation of epitaxial Ti-Si-C Ohmic contact on 4H-SiC C face using pulsed-laser annealing. **252108**, (2017).

62. Boutopoulos, C. *et al.* Laser annealing of Al implanted silicon carbide: Structural and optical characterization. *Appl. Surf. Sci.* **253**, 7912–7916 (2007).

63. Cho, N. I. *et al.* Laser annealing effect of SiC films prepared by PECVD (plasma enhanced chemical vapor deposition). *Thin Solid Films* **409**, 1–7 (2002).

64. Shafeev, G. A. *et al.* Electroless metallization of SiC after laser ablation. *Surf. Coatings Technol.* **80**, 224–228 (1996).

65. Lyalin, A. A., Obraztsova, E. D., Simakin, A. V & Shafeev, G. A. Pulsed Laser Activation and Electroless Metallizaton of siC Single Crystal. 308–312 (1998).

66. Dong, Y. & Molian, P. Coulomb explosion-induced formation of highly oriented nanoparticles on thin films of 3C-SiC by the femtosecond pulsed laser. *Appl. Phys. Lett.* **84**, 10–12 (2004).

67. Rehman, Z. U. & Janulewicz, K. A. Structural transformations in femtosecond laser-processed n-type 4H-SiC. *Appl. Surf. Sci.* **385**, 1–8 (2016).

68. Zoppel, S. *et al.* Laser micro machining of 3C-SiC single crystals. *Microelectron. Eng.* **83**, 1400–1402 (2006).

69. Marui, D., Ikeda, A., Nishi, K., Ikenoue, H. & Asano, T. Aluminum doping of 4H-SiC by irradiation of excimer laser in aluminum chloride solution. *Jpn. J. Appl. Phys.* **53**, 4–8 (2014).

70. Tian, Z., Quick, N. R. & Kar, A. Laser-enhanced diffusion of nitrogen and aluminum dopants in silicon carbide. *Acta Mater.* **54**, 4273–4283 (2006).

71. Sugioka, K., Meunier, M. & Pique, A. *Laser Precision Microfabrication*. *Springer Series in material Sciences* vol. 53 (Springer, 2010).

72. Deki, M. *et al.* Enhancement of local electrical conductivities in SiC by femtosecond laser modification. *Appl. Phys. Lett.* **98**, (2011).

73. Dong, Y., Zorman, C. & Molian, P. Femtosecond pulsed laser micromachining of single crystalline 3C–SiC structures based on a laser-induced defect-activation process. *J. Micromechanics Microengineering* **13**, 680–685 (2003).

74. Song, J. *et al.* Surface birefringence of self-assembly periodic nanostructures induced on 6H-SiC surface by femtosecond laser. *Appl. Surf. Sci.* **363**, 664–669 (2016).

75. Gemini, L. *et al.* Generation of periodic structures on SiC upon laser plasma XUV/NIR radiations. *Laser Part. Beams* **31**, 547–550 (2013).

76. Matthew J. Allen, Vincent C. Tung, and R. B. K. Honeycomb Carbon A Review of Graphene. *Chem. Rev.* **110**, 132–145 (2010).

77. Wallace, P. R. The band theory of graphite. *Phys. Rev.* **71**, 622–634 (1947).

78. K. S. Novoselov, A. K. Geim, S. V. Morozov, D. Jiang, Y. Zhang, S. V. Dubonos, I. V. Grigorieva, A. A. F. Electric Field Effect in Atomically Thin Carbon Films. *Science (80-.).* **306**, 666–669 (2004).

79. Mishra, N., Boeckl, J., Motta, N. & Iacopi, F. Graphene growth on silicon carbide: A review. *Phys. Status Solidi* **213**, 2277–2289 (2016).

80. Savini, G., Ferrari, A. C. & Giustino, F. First-principles prediction of doped graphane as a high-temperature electron-phonon superconductor. *Phys. Rev. Lett.* **105**, 1–4 (2010).

81. Bae, S. *et al.* Roll-to-roll production of 30-inch graphene films for transparent electrodes. *Nat. Nanotechnol.* **5**, 574–578 (2010).

82. Zhao, X., Zhang, Q., Chen, D. & Lu, P. Enhanced mechanical properties of graphene-based polyvinyl alcohol composites. *Macromolecules* **43**, 2357–2363 (2010).

83. R. R. Nair, P. Blake, A. N. Grigorenko, K. S. Novoselov, T. J. Booth, T. S. & N. M. R. Peres, A. K. G. Fine Structure Constant Defines Visual Transparency of Graphene. *Science (80-.).* **320**, 1308 (2008).

84. Daniel R. Cooper, Benjamin D'Anjou, Nageswara Ghattamaneni, Benjamin Harack, Michael Hilke, Alexandre Horth, NorbertoMajlis, MathieuMassicotte, Leron Vandsburger, EricWhiteway, and V. Y. Review Article Experimental Review of Graphene. *ISRN Condens. Matter Phys.* **2012**, 56 (2012).

85. Michael S. Fuhrer, Chun Ning Lau, and A. H. M. Graphene: Materially Better Carbon. *290 MRS Bull.* **35**, 289–295 (2010).

86. Antonelou, A., Dracopoulos, V. & Yannopoulos, S. N. Laser processing of SiC: From graphene-coated SiC particles to 3D graphene froths. *Carbon N. Y.* **85**, 176–184 (2015).

87. H.P.BoehmR.SettonE.Stumpp. Nomenclature and terminology of graphite intercalation compounds. *Carbon N. Y.* **24**, 241 (1986).

88. Novoselov, K. S. *et al.* A roadmap for graphene. *Nature* **490**, 192–200 (2012).

89. Andrea C. Ferrari, Francesco Bonaccorso, Vladimir Fal'ko, Konstantin S. Novoselov, Stephan Roche, Peter Bøggild, Stefano Borini, Frank H. L. Koppens, Vincenzo Palermo, Nicola Pugno, José A. Garrido, Roman Sordan, Alberto Bianco, Laura Ballerini, Maurizio, T. L. and J. K. Science and technology roadmap for graphene, related two-dimensional crystals, and hybrid systems. *Nanoscale* **7**, 4587–5062 (2015).

90. Bhushan, B. *Scanning Probe Microscopy in Nanoscience and Nanotechnology 2*. vol. 2 (Springer-, 2011).

91. Ray, S. C. *Applications of Graphene and Graphene-Oxide Based Nanomaterials*. (William Andrew is an imprint of Elsevier, 2015). doi:10.1016/B978-0-323-37521-4.00003-0.

92. Murali, R. Graphene transistors. *Graphene Nanoelectron. From Mater. to Circuits* **9781461405**, 51–91 (2012).

93. Lin, Y. *et al.* 100-GHz Transistors from Wafer-Scale Epitaxial Graphene. *Science (80-.).* **327**, 662 (2010).

94. Beshkova, M., Hultman, L. & Yakimova, R. Device applications of epitaxial graphene on silicon carbide. *Vacuum* **128**, 186–197 (2016).

95. Tiras, E., Ardali, S., Tiras, T., Arslan, E. & Cakmakyapan, S. Effective mass of electron in monolayer graphene : Electron-phonon interaction Effective mass of electron in monolayer graphene : Electron-phonon interaction. **043708**, (2013).

96. Zhan, N., Olmedo, M., Wang, G. & Liu, J. Layer-by-layer synthesis of large-area graphene films by thermal cracker enhanced gas source molecular beam epitaxy. *Carbon N. Y.* **49**, 2046–2052 (2011).

97. Choucair, M., Thordarson, P. & Stride, J. A. Gram-scale production of graphene based on solvothermal synthesis and sonication. *Nat. Nanotechnol.* **4**, 30–33 (2009).

98. Trusovas, R. *et al.* Reduction of graphite oxide to graphene with laser irradiation. *Carbon N. Y.* **52**, 574–582 (2013).

99. Jiao, L., Zhang, L., Wang, X., Diankov, G. & Dai, H. Narrow graphene nanoribbons from carbon nanotubes. *Nature* **458**, 877–880 (2009).

100. Van Bommel, A. J., Crombeen, J. E. & Van Tooren, A. LEED and Auger electron observations of the SiC(0001) surface. *Surf. Sci.* **48**, 463–472 (1975).

101. Badami, D. V. Graphitization of α-silicon carbide. *Nature* vol. 193 569–570 (1962).

102. D.V.Badami. X-Ray studies of graphite formed by decomposing silicon carbide. *Carbon N. Y.* **3**, 53 (1965).

103. Kusunoki, M., Suzuki, T., Hirayama, T., Shibata, N. & Kaneko, K. A formation mechanism of carbon nanotube films on SiC(0001). *Appl. Phys. Lett.* **77**, 531–533 (2000).

104. Berger, C. *et al.* Ultrathin epitaxial graphite: 2D electron gas properties and a route toward graphene-based nanoelectronics. *J. Phys. Chem. B* **108**, 19912–19916 (2004).

105. Kim, S., Ihm, J., Choi, H. J. & Son, Y. W. Origin of anomalous electronic structures of epitaxial graphene on silicon carbide. *Phys. Rev. Lett.* **100**, 2–5 (2008).

106. Huang, H., Chen, W., Chen, S., Thye, A. & Wee, S. Bottom-up Growth of Epitaxial. *acsnano* **2**, 2513–2518 (2008).

107. Berger, C., Conrad, E. H. & Heer, W. A. De. Epigraphene : epitaxial graphene on silicon carbide. (2005).

108. Tomás Palacios, Allen Hsu, and Han Wang, M. Applications of Graphene Devices in RF Communications. *NANO-TECHNOLOGY Commun. A* 122–128 (2010).

109. Emtsev, K. V. *et al.* Towards wafer-size graphene layers by atmospheric pressure graphitization of silicon carbide. *Nat. Mater.* **8**, 203–207 (2009).

110. Choi, W., Lahiri, I., Seelaboyina, R. & Kang, Y. S. Synthesis of graphene and its applications: A review. *Crit. Rev. Solid State Mater. Sci.* **35**, 52–71 (2010).

111. Harris, A. J., Vaughan, B., Yeomans, J. A., Smith, P. A. & Burnage, S. T. Surface preparation of silicon carbide for improved adhesive bond strength in armour applications. *J. Eur. Ceram. Soc.* **33**, 2925–2934 (2013).

112. Sadler, L. Y. & Shamsuzzoha, M. Response of Silicon Carbide to High- Intensity Laser Irradiation in a High-Pressure Inert Gas Atmosphere. *J. Mater. Res.* **22**, 147 (2015).

113. Chaika, A. N., Aristov, V. Y. & Molodtsova, O. V. Graphene on cubic-SiC. *Prog. Mater. Sci.* **89**, 1–30 (2017).

114. Stephen E, Saddow and Anant, A. *Advances in Silicon Carbide Processing and Applications*. *Igarss 2014* (2014). doi:10.1007/s13398-014-0173-7.2.

115. Baeri, P., Spinella, C. & Reitano, R. Fast Melting of Amorphous Silicon Carbide Induced by Nanosecond Laser Pulse 1. **20**, 1211–1221 (1999).

116. Bellosi, D. S. and A. Laser Micromachining of Silicon Carbide. *Key Eng. Mater.* **206–213**, 305 (2002).

117. Pehrsson, P., and Kaplan, R., Pehrsson, P. E. & Kaplan, R. Excimer laser cleaning, annealing, and ablation of β–SiC. *J. Mater. Res.* **4**, 1480–1490 (1989).

118. Tian, Z., Salama, I. A., Quick, N. R. & Kar, A. Effects of different laser sources and doping methods used to dope silicon carbide. *Acta Mater.* **53**, 2835–2844 (2005).

119. Yannopoulos, S. N., Siokou, A., Nasikas, N. K., Ravani, F. & Papatheodorou, G. N. CO2 Laser-Induced Laser-Induced Growth of Epitaxial Graphene on 6H-SiC (0001). *Adv. Funct. Mater.* **22**, 113–120 (2012).

120. Ohkawara, Y. *et al.* Synthesis of graphite using laser decomposition of SiC. *J. Mater. Sci.* (2003) doi:10.1023/A:1023909203003.

121. Pecholt, B., Gupta, S. & Molian, P. Review of laser microscale processing of silicon carbide. *J. Laser Appl.* **23**, 012008 (2011).

122. Pecholt, B. F. & Pecholt, B. F. Laser microfabrication and testing of silicon carbide diaphragms for MEMS applications. (2009).

123. Sonde, S. *et al.* Role of graphene/substrate interface on the local transport properties of the two-dimensional electron gas. *Appl. Phys. Lett.* **97**, 5–8 (2010).

124. Salama, I., Kar, A., & Quick, N. Laser Direct-Metallization of Silicon Carbide without

Metal Deposition. in *MRS Proceedings* 764, C2.10 (2003).

125. Kedzierski, J. *et al.* Epitaxial graphene transistors on SiC substrates. *IEEE Trans. Electron Devices* **55**, 2078–2085 (2008).

126. Hwang, W. S. *et al.* Graphene nanoribbon field-effect transistors on wafer-scale epitaxial graphene on SiC substrates. *APL Mater.* **3**, (2015).

127. Avouris, P. & Dimitrakopoulos, C. Graphene: Synthesis and applications. *Materials Today* vol. 15 86–97 (2012).

128. Norimatsu, W. & Kusunoki, M. Growth of graphene from SiC{0001} surfaces and its mechanisms. *Semicond. Sci. Technol.* **29**, (2014).

129. Sarbani Basu, Mu Chen Lee, and Y.-H. W. Graphene-based Electrodes for Enhanced Organic Thin Film Transistors Based on Pentacene. *Phys. Chem. Chem. Phys.* **16**, 16701–16710 (2014).

130. Liu, S. *et al.* Antibacterial activity of graphite, graphite oxide, graphene oxide, and reduced graphene oxide: Membrane and oxidative stress. *ACS Nano* **5**, 6971–6980 (2011).

131. Shalaev, V. *et al.* Wafer-Scale Graphene Integrated Circuit. **332**, 1294–1298 (2011).

132. Panchal, V. *et al.* Small epitaxial graphene devices for magnetosensing applications. *J. Appl. Phys.* **111**, 1–4 (2012).

133. Ciuk, T. & Strupinski, W. Statistics of epitaxial graphene for Hall effect sensors. *Carbon* vol. 93 1042–1049 (2015).

134. Anderson, T. J. *et al.* Ultraviolet detector based on graphene/SiC heterojunction. *Appl. Phys. Express* **8**, 2–4 (2015).

135. Schedin, F. *et al.* Detection of individual gas molecules adsorbed on graphene. *Nat. Mater.* **6**, 652–655 (2007).

136. Pearce, R. *et al.* Epitaxially grown graphene based gas sensors for ultra sensitive NO 2 detection. *Sensors Actuators, B Chem.* **155**, 451–455 (2011).

137. Hwang, H. J. *et al.* Electrical characteristics of wrinkle-free graphene formed by laser graphitization of 4H-SiC. *Appl. Phys. Lett.* (2011) doi:10.1063/1.3629785.

138. Dyer, P. E., Pervolaraki, M. & Lippert, T. Experimental studies and thermal modelling of 1064- And 532-nm Nd:YVO 4 micro-laser ablation of polyimide. *Appl. Phys. A Mater. Sci. Process.* **80**, 529–536 (2005).

139. Wang, X. *et al.* Synthesis of graphene and graphene nanostructures by ion implantation and pulsed laser annealing. *J. Appl. Phys.* **120**, (2016).

140. Galvão, N. *et al.* A Novel Method of Synthesizing Graphene for Electronic Device Applications. *Materials (Basel).* **4**, 1–11 (2018).

141. N. K. Galvão *et al.* Growth and Characterization of Graphene on Polycrystalline SiC Substrate Using Heating by CO2 Laser Beam. *Mater. Res.* **19**, 1329–1334 (2016).

142. Perrone, D. & Maccioni, G. Study on the possibility of graphene growth on 4H-silicon carbide surfaces via laser processing. *Proc. ...* (2009).

143. Luo, T. *et al.* Laser Irradiation-Induced SiC@Graphene Sub-Microspheres: A Bioinspired Core–Shell Structure for Enhanced Tribology Properties. *Adv. Mater. Interfaces* **5**, 1–9 (2018).

144. Choi, I. *et al.* Laser-induced solid-phase doped graphene. *ACS Nano* **8**, 7671–7677 (2014).

145. Aono, Y., Ogawa, K. & Hirata, A. Surface modi fi cation of single-crystalline silicon carbide by laser irradiation for microtribological applications. *Precis. Eng.* **54**, 198–205 (2018).

146. Luo, T. *et al.* Ultrafast synthesis of SiC @ graphene nanocomposites by one-step laser induced fragmentation and decomposition. *Ceram. Int.* **44**, 19028–19032 (2018).

147. Grigoropoulos, C. P. *Transport in laser microfabrication: Fundamentals and applications. Transport in Laser Microfabrication: Fundamentals and Applications* vol. 9780521821 (CAMBRIDGE UNIVERSITY PRESS, 2009).

148. Blatter, M. von A. A. *Laser-Beam Interactions with Materials Physical Principles and Applications*. (Springer-Verlag Berlin Heidelberg GmbH, 1995). doi:10.1007/978-3-642-33848-9.

149. Wooten, F. *Optical Properties of Solids*. (ACADEMIC PRESS, 1972). doi:10.1016/0165-1633(89)90057-9.

150. Jellison, G. E. & Lowndes, D. H. Measurements of the optical properties of liquid silicon and germanium using nanosecond time-resolved ellipsometry. *Appl. Phys. Lett.* **51**, 352–354 (1987).

151. Elton, N. J. the Complex Refractive Index and Reflectometry Versus Ellipsometry. *Surfoptic/Reflectometry Tech. Pap. No. 3* 1–11 (2007).

152. Nichelatti, E. Complex refractive index of a slab from reflectance and transmittance : Analytical solution. *J. Opt. A Pure Appl. Opt* **4**, 400–403 (2002).

153. Jennings, S. G., Pinnick, R. G. & Gillespie, J. B. Relation between absorption coefficient and imaginary index of atmospheric aerosol constituents. *Appl. Opt.* **18**, 1368–1371 (1979).

154. Lucien D. Laude. *Cohesive Properties of Semiconductors under Laser Irradiation*. (1983). doi:10.1007/978-94-009-6890-5.

155. Miller, J. C. *Laser Ablation Principles and Applications*. vol. 28 (Springer-Verlag, 1994).

156. Dutta Majumdar, J. & Manna, I. Laser processing of materials. *Sadhana - Acad. Proc. Eng. Sci.* **28**, 495–562 (2003).

157. Sun, B. K., Zhang, X. & Grigoropoulos, C. P. Spectral optical functions of silicon in the range of 1.13-4.96 eV at elevated temperatures. *Int. J. Heat Mass Transf.* **40**, 1591–1600 (1997).

158. Bäuerle, D. *Laser Processing and Chemistry*. (Springer, 2011). doi:10.1007/978-3-642-17613-5.

159. Phillips, J. C. Covalent and Ionic Bonds. *Bond. Bands Semicond.* 26–56 (1973) doi:10.1016/B978-0-12-553350-8.50006-3.

160. Janzén, E. *et al.* The silicon vacancy in SiC. *Phys. B Condens. Matter* **404**, 4354–4358

(2009).

161. Sörman, E. *et al.* Silicon vacancy related defect in 4H and 6H SiC. *Phys. Rev. B* **61**, 2613–2620 (2000).

162. Baker, A. J. Review of 'Discontinuous Finite Elements in Fluid Dynamics and Heat Transfer'. *AIAA J.* **45**, 1150–1151 (2007).

163. Maul, J. *et al.* Onset of crater formation during short pulse laser ablation. *Appl. Phys. A Mater. Sci. Process.* **82**, 43–47 (2006).

164. Semerok, A., Sallé, B., Wagner, J. & Petite, G. Femtosecond, picosecond, and nanosecond laser microablation Laser plasma and crater investigation. 67–72 (2002).

165. Han, J. & Li, Y. Lasers - Applications in Science and Industry. *Lasers-Applications Sci. Ind.* 109–131 (2011) doi:10.5772/1822.

166. Laude, L. D. *Excimer Lasers*. *Springer -Science + Business Media, B. V.* vol. 265 (Springer Science+Business Media Dordrecht, 1994).

167. Torrisi, L., Borrielli, A. & Margarone, D. Study on the ablation threshold induced by pulsed lasers at different wavelengths. *Nucl. Instruments Methods Phys. Res. Sect. B Beam Interact. with Mater. Atoms* **255**, 373–379 (2007).

168. Dyer, P. Excimer laser polymer ablation: twenty years on. *Appl. Phys. A* **173**, 167–173 (2003).

169. Gower, M. C., Davies, E. & Holmes, A. S. Optical modeling of laser ablated microstructures. *J. Appl. Phys.* **112**, (2012).

170. Zakariyah, S. S. Laser Ablation for Polymer Waveguide Fabrication. *Micromach. Tech. Fabr. Micro Nano Struct.* 109–130 (2012) doi:10.5772/1364.

171. Hauer, M. R. Laser ablation of polymers studied by time resolved methods. (2004) doi:10.3929/ETHZ-B-000225616.

172. Basting, D. & Marowsky, G. *Excimer laser technology*. (Spriger, 2005).

173. Grigoropoulos, C. P. *Laser Ablation and Desorption*. *Experimental Methods in the Physical Sciences* vol. 30 (ACADEMIC PRESS, 1997).

174. Persad, A. H. & Ward, C. A. Expressions for the Evaporation and Condensation Coefficients in the Hertz-Knudsen Relation. *Chemical Reviews* vol. 116 7727–7767 (2016).

175. Ho, J. R., Grigoropoulos, C. P. & Humphrey, J. A. C. Computational study of heat transfer and gas dynamics in the pulsed laser evaporation of metals. *J. Appl. Phys.* **78**, 4696–4709 (1995).

176. Petkov, P. V., Dimov, S. S., Minev, R. M. & Pham, D. T. Laser milling: Pulse duration effects on surface integrity. *Proc. Inst. Mech. Eng. Part B J. Eng. Manuf.* **222**, 35–45 (2008).

177. Dong, Y. & Molian, P. Femtosecond pulsed laser ablation of 3C-SiC thin film on silicon. *Appl. Phys. A Mater. Sci. Process.* **77**, 839–846 (2003).

178. Mehregany, M., Zorman, C. A., Rajan, N. & Wu, C. H. Silicon carbide MEMS for harsh

environments. *Proc. IEEE* **86**, 1594–1609 (1998).

179. Colthup, N. B., Daly, L. H. & Wiberley, S. E. *Introduction to Infrared and Raman Spectroscopy*. *Introduction to Infrared and Raman Spectroscopy* (ACADEMIC PRESS, 1990). doi:10.1016/b978-0-08-091740-5.50003-x.

180. KWTEK. *Raman knowledge* (2016).

181. Heaney, M. B. Electrical_Conductivity_and_Resistivity. 1–14 (2004).

182. Ben-Yakar, A. & Byer, R. L. Femtosecond laser ablation properties of borosilicate glass. *J. Appl. Phys.* **96**, 5316–5323 (2004).

183. Lednev, V. N., Pershin, S. M., Obraztsova, E. D., Kudryashov, S. I. & Bunkin, A. F. Single-shot and single-spot measurement of laser ablation threshold for carbon nanotubes. *J. Phys. D. Appl. Phys.* **46**, (2013).

184. Liu, J. M. Simple technique for measurements of pulsed Gaussian-beam spot sizes. *Opt. Lett.* **7**, 196 (1982).

185. Optics, A. Spot-size measurements of an intense CO2 laser beam. *Appl. Opt.* **31**, 1912 (1992).

186. Tauc, J. Optical properties and electronic structure of amorphous Ge and Si. *Mater. Res. Bull.* **3**, 37–46 (1968).

187. www.COMSOL.com. https://www.comsol.com/release/5.4/application-builder (2019).

188. Machá, P., Fidler, T., Cicho, S. & Mi, L. Synthesis of graphene on SiC substrate via Ni-silicidation reactions. **520**, 5215–5218 (2012).

189. Malard, L. M., Pimenta, M. A., Dresselhaus, G. & Dresselhaus, M. S. Raman spectroscopy in graphene. *Physics Reports* (2009) doi:10.1016/j.physrep.2009.02.003.

190. Frank P. Incropera, David P. Dewitt, T. L. B. and A. S. L. T. L. B. and A. S. L. *Fundamentals of Heat and Mass Transfer*. (Sons, John Wiley &, 2010). doi:10.1109/TKDE.2004.30.

191. Tritt, T. M. *thermal conductivity:theory, Properties, and Applications*. (Kluwer Academic / Plenum Publishers, 2004).

192. LienhardIV, J. H. & LienhardV, J. H. *heat transfer textbook*. (Cambridge, Massachusetts, U.S.A, 2001).

193. Tardu, M. F.-M. S. *Convective Heat Transfer*. (Wiley, 2009). doi:10.1080/03043799408928317.

194. Bejan, A. *Heat Transfer*. (John Wiley & Sons, 1993).

195. Comsol. Comsol Multiphysics User's Guide. *Equation-Based Model.* 803–879, Equation-Based Modeling (2012) doi:10.1016/S0260-8774(99)00111-9.

196. Clarke, A. J. Comparison of calculated and measured temperature fields in laser-heated thin film systems. (2017).

197. Duley, W. . *C02 Lasers Effects and Applications*. (Academic Press, 1976).

198. Carslow, H. S., Jaeger, J. C. & Morral, J. E. *Conduction of Heat in Solids, Second Edition. Journal of Engineering Materials and Technology* vol. 108 (1986).

199. John F. Ready. *Effects High Laser of Power Radiation*. (ACADEMIC PRESS, 1971).

200. Lax, M. Temperature rise induced by a laser beam. *J. Appl. Phys.* **48**, 3919–3924 (1977).

201. Lax, M. Temperature rise induced by a laser beam II. the nonlinear case. *Appl. Phys. Lett.* **33**, 786–788 (1978).

202. El-Adawi, M. K., Abdel-Naby, M. A. & Shalaby, S. A. Laser heating of a two-layer system with constant surface absorption: an exact solution. *Int. J. Heat Mass Transf.* **38**, 947–952 (1995).

203. Bechtel, J. H. Heating of solid targets with laser pulses. *J. Appl. Phys.* **46**, 1585–1593 (1975).

204. S Burnett, D. *Finite element analysis : from concepts to applications*. (Addison Wesley 1987, 2019).

205. Fagan, M. J. *Finite element analysis: theory and practice*. (Pearson Education Limited, 1992).

206. COMSOL. Introduction to COMSOL Multiphysics 5.3. *Manual* 168 (2014).

207. Clarke, A. J. Comparison of calculated and measured temperature fields in laser-heated thin film systems being a Thesis submitted for the Degree of Master of Science in the University of Hull by. (2017).

208. Naftaly, M., Molloy, J. F., Magnusson, B., Andreev, Y. M. & Lanskii, G. V. Silicon carbide—a high-transparency nonlinear material for THz applications. *Opt. Express* **24**, 2590 (2016).

209. Ove Nilsson, Harald Mehling, Ronny Horn, Jochen Fricke, Rainer Hofmann, Stephan G Müller, Robert Eckstein, D. H. Determination of the thermal diffusivity and conductivity of monocrystalline silicon carbide (300-2300 K). *High Temp. Press.* **29**, (1997).

210. Liu, C. J., Lin, S., Zheng, Y., Chen, S. & Shen, P. Pulsed laser synthesis of diamond-type nanoparticles with enhanced Si – C solid solubility and special defects †. *CrystEngComm* **17**, 9142–9154 (2015).

211. J.H. Yu, Temmerman, G. De, Doerner, R. P., Pitts, R. A. & Berg, M. A. van den. The effect of transient temporal pulse shape on surface temperature and tungsten damage. *Nucl. fusion* **55**, (2015).

212. J H Yu, Temmerman, G. De, R P Doerner & M A van den Berg. Study of temporal pulse shape effects on W using simulations and laser heating. *Phys. Scr.* (2016).

213. Küper, S., Brannon, J. & Brannon, K. Threshold behavior in polyimide photoablation: Single-shot rate measurements and surface-temperature modeling. *Appl. Phys. A Solids Surfaces* **56**, 43–50 (1993).

214. Lithography, S. V. G. Mechanism of Laser Induced Compaction. (1995).

215. Scace, R. I. & Slack, G. A. Solubility of carbon in silicon and germanium. *J. Chem. Phys.* **30**, 1551–1555 (1959).

216. Choi, I. *et al.* Laser-induced phase separation of silicon carbide. *Nat. Commun.* **7**, 13562 (2016).

217. Drowart, J., De Maria, G. & Inghram, M. G. Thermodynamic study of SiC utilizing a mass spectrometer. *J. Chem. Phys.* **29**, 1015 (1958).

218. Barin, I. *Thermochemical Data of Pure Substances, 3rd ed.* (1989). doi:10.1016/S0165-2427(96)05632-2.

219. Xu, Z. *et al.* Topic Review: Application of Raman Spectroscopy Characterization in Micro/Nano-Machining. *Micromachines* **9**, 361 (2018).

220. Camassel, A. T. and J. Chapter 2 Raman Imaging in Semiconductor Physics: Applications to Microelectronic Materials and Devices. in *Raman Imaging* vol. 5 337–360 (Springer-Verlag Berlin Heidelberg, 2012).

221. Leme, F. O. *et al.* Effect of pulse repetition rate and number of pulses in the analysis of polypropylene and high density polyethylene by nanosecond infrared laser induced breakdown spectroscopy. *Appl. Surf. Sci.* **258**, 3598–3603 (2012).

222. Bergmann, J. P., Patschger, A. & Bastick, A. Enhancing process efficiency due to high focusing with high brightness lasers- Applicability and constraints. *Phys. Procedia* **12**, 66–74 (2011).

223. Blau P.J. (2013) Asperities. In: Wang Q.J., Chung YW. (eds) Encyclopedia of Tribology. Springer, Boston, MA. https://doi.org/10.1007/978-0-387-92897-5_167.

224. Kundu, S. *et al.* Morphology of thin silver film grown by dc sputtering on Si(001). *J. Phys. D. Appl. Phys.* **31**, 1–6 (1998).

225. Lin, Y. *et al.* Green luminescent zinc oxide films prepared by polymer-assisted deposition with rapid thermal process. *Thin Solid Films* **492**, 101–104 (2005).

226. Fang, Z. B., Yan, Z. J., Tan, Y. S., Liu, X. Q. & Wang, Y. Y. Influence of post-annealing treatment on the structure properties of ZnO films. *Appl. Surf. Sci.* **241**, 303–308 (2005).

227. Rajesh Kumar, B. & Subba Rao, T. AFM studies on surface morphology, topography and texture of nanostructured zinc aluminum oxide thin films. *Dig. J. Nanomater. Biostructures* **7**, 1881–1889 (2012).

228. Sakata, H., Dresselhaus, G., Dresselhaus, M. S. & Endo, M. Effect of uniaxial stress on the Raman spectra of graphite fibers. *J. Appl. Phys.* **63**, 2769–2772 (1988).

229. Fang, S. *et al.* Three-dimensional reduced graphene oxide powder for efficient microwave absorption in the S-band (2-4 GHz). *RSC Adv.* **7**, 25773–25779 (2017).

230. Siegman, A. E. *Lasers*. (1986).

231. Gräf, S., Kunz, C., Engel, S., Derrien, T. J. Y. & Müller, F. A. Femtosecond laser-induced periodic surface structures on fused silica: The impact of the initial substrate temperature. *Materials (Basel).* **11**, 5–7 (2018).

232. Sipe, J. E., Young, J. F., Preston, J. S. & Van Driel, H. M. Laser-induced periodic surface structure. I. Theory. *Phys. Rev. B* **27**, 1141–1154 (1983).

233. Ni, Z., Wang, Y., Yu, T. & Shen, Z. Raman Spectroscopy and Imaging of Graphene. *Nano*

Res **1**, 273 (2008).

234. Eckmann, A. *et al.* Probing the nature of defects in graphene by Raman spectroscopy. *Nano Lett.* **12**, 3925–3930 (2012).

235. Cambaz, Z. G., Yushin, G., Osswald, S., Mochalin, V. & Gogotsi, Y. Noncatalytic synthesis of carbon nanotubes, graphene and graphite on SiC. *Carbon N. Y.* **46**, 841–849 (2008).

236. Ito, T. I. Electrical Conduction Properties of SiC Modified by Femtosecond Laser. *J. Laser Micro/Nanoengineering* **7**, 16–20 (2012).

237. Deki, M. *et al.* Femtosecond laser modification aiming at the enhancement of local electric conductivities in SiC. *AIP Conf. Proc.* **1399**, 119–120 (2011).